A. Shelman, J. Levings, S. Sritharan

Seismic Design of Deep Bridge Pier Foundations in Seasonally Frozen Ground

AUTC Project Number: UAF 08-0033
Submitted to the
Alaska University Transportation Center
Alaska Department of Transportation & Public Facilities

DECEMBER 2010

Final

REPORT

IOWA STATE UNIVERSITY
OF SCIENCE AND TECHNOLOGY

Department of Civil, Construction and Environmental Engineering

Seismic Design of Deep Bridge Pier Foundations in Seasonally Frozen Ground

by

Aaron Shelman
Graduate Research Assistant, Iowa State University

Jared Levings
Former Graduate Research Assistant, Iowa State University

Sri Sritharan
Wilson Engineering Professor, Iowa State University

AUTC Project Number: UAF 08-0033

Final Report to:

Alaska University Transportation Center

Alaska Department of Transportation and Public Facilities

Department of Civil, Construction and Environmental Engineering
Iowa State University
Ames, IA 50011

December 2010

ABSTRACT

In the field of bridge engineering, columns supported on cast-in-drilled-hole (CIDH) shafts are common due to the elimination of a column-foundation connection, simplicity of construction and reduced construction costs. Due to these benefits, this combination of column and foundation is frequently used in high seismic regions. However, the modeling of lateral load behavior of the column-shaft system is a complex matter due to the effects of soil-foundation-structure-interaction (SFSI) and temperature effects. The research presented within this project report identifies numerous challenges associated with the current state of practice of accounting for SFSI in cohesive soils, develops a new method that accounts for SFSI in cohesive soils, examines the current state of cohesionless soil models, examines temperature effects on construction material behavior and provides a design methodology for columns supported by CIDH shafts.

The project undertook an extensive literature review as well as an examination of codes and guidelines to identify the challenges within current practice. Within this task, it was concluded that existing methods are able to capture the behavior of column/shaft systems in cohesionless soils. However, the process also found that although many models exist to simplify the use of the Winkler soil spring concept, none of the simplified models are able to capture both the elastic and inelastic lateral load response of an integrated column/foundation system in cohesive soils. The challenges arose for the following reasons:

1. some models are only applicable in the elastic range;
2. models recommended for use in cohesive soils and cohesionless soils were only verified against experimental data obtained in cohesionless soils;
3. nonlinearity of materials (i.e., soil, concrete and steel reinforcement) was not accounted for in the development of the models; and
4. plastic action within the different methods is generally lower than what actually will be found using a detailed analysis method such as that based on fully implementing the Winkler spring concept.

In addition to the aforementioned shortcomings, the existing methods ignore the effects of seasonal freezing in their development, even though it significantly alters the lateral load response of CIDH shafts. However, it was found this approach is not appropriate, as two-thirds

of the bridges in the United States are affected by seasonal freezing. This problem is only further exacerbated by the fact that half of the bridges in high seismic regions are also affected by seasonal freezing. After identifying these issues, a new method was developed that more accurately predicts the lateral load response of columns supported on CIDH shafts in cohesive soils.

The new approach presented within this report uses a set of three springs to determine a bilinear force-displacement response of the column/foundation system using minimal input parameters about the structure and surrounding soil. The model was developed as a cantilever supported on a flexible base located at the expected maximum moment location. First, a rotational spring and a translational spring were placed at the maximum moment location to capture the behavior of the foundation shaft at and below the location. The final translational spring was located halfway between the maximum moment location and the ground surface to capture the resistance of the soil above the maximum moment location. By basing the system on the maximum moment location, the point at which the most damage will occur is defined. The global response of the system, as well as the local response of the CIDH shaft over the entire lateral loading range, is also captured.

Comparing the alternative method to results from experimental testing performed at Iowa State University and LPILE analyses of several different systems, the new model was found to simulate well the response of the column/foundation system in cohesive soils. The developed method was able to predict the secant stiffness to the first yield location within 10%. Yield and ultimate limit states were within 10% of the detailed analyses performed in LPILE (Reese et al., 2004) and correlated well with the full-scale experimental testing performed by Suleiman et al. (2006). The overall comparisons included multiple displacement and rotation factors, as well as local curvatures developed near the maximum moment location. These aforementioned local comparisons of the CIDH shaft, along with a global comparison of the entire system, were performed to minimize any errors that occurred during model development.

The remaining parts of the project consisted of performing controlled material tests on concrete, steel and soil specimens to examine the effects of seasonal freezing on their behavior. These tests were performed in a laboratory environment in which the temperature during testing was maintained and the results would provide a realistic model. In each case it was determined

that the material properties would experience significant changes when subjected to freezing conditions.

- The materials testing on concrete provided evidence such that an increase in strength and modulus of elasticity occurs when subjected to seasonal freezing. However, the cracking strain of unconfined concrete decreased. The confined concrete specimens experienced an increase in strength, modulus and strain at peak confined compressive stress. This is of key importance to ensure an accurate moment-curvature response of the column and foundation shafts is obtained for design purposes.
- In the steel testing it was discovered that as the specimens undergo freezing, a quadratic increase in the yield and ultimate strengths of the material will occur while experiencing no change in the modulus of elasticity and ultimate strain. This portion of the project provided additional evidence to suggest that strain rate and bar diameter will affect the overall strength gain. All of these results should be accounted for in the design process to ensure that an accurate moment-curvature response of the column and foundation shafts is captured.
- The results of soil testing found that a significant increase in strength could be expected at -1 °C (30.2 °F) and -20 °C (-4 °F). In these cases, it was found the warm weather value could be multiplied by a factor of 10 and 100 to represent the soil unconfined compressive strength at the respective temperatures. This is of great importance as these values will greatly modify the stiffness of the system during times of seasonal freezing, causing an upward shift in the maximum moment location and requiring a larger shear demand to be accounted for in the column/foundation shafts.

The final portion of the project provided a series of flowcharts that should be used during the design of columns supported on CIDH shafts. These charts were constructed such that a detailed computer-based methodology as well as simplified methodologies can be used to account for all seasons of the year during the design process. Therefore, these charts ensure that all possible failure modes are examined and prevented during the seismic design of columns supported on CIDH shafts.

ACKNOWLEDGEMENTS

The study reported herein was made possible through funding provided by the Alaska University Transportation Center (AUTC) along with the Alaska Department of Transportation and Public Facilities (ADOT&PF). Special thanks are due to Billy Connor, AUTC Director; J. Leroy Hulsey, UAF AUTC Associate Director; Kathy Petersen, Grants Manager at AUTC; and Elmer Marx, project manager through the ADOT&PF; Angela Parsons, research project manager at ADOT&PF; Clint Adler, Engineer at ADOT&PF; David Stanley, Chief Engineering Geologist for ADOT&PF.

Additional thanks are required for members of Mueser Rutledge Consulting Engineers (MRCE), who provided their expertise and services in testing frozen soil samples in New York, New York. These persons are Sissy Nikolaou, Associate and Director of Geoseismic Department; James Tantalla, Lab Manager and Engineer; Yesid Ordonez, Lab Technician.

Douglas Wood, structural engineering laboratory manager at Iowa State University, provided a great deal of help with the controlled materials testing of steel and concrete.

In addition, the authors would like to thank the following organizations for donating materials to the project: IPC, Inc. in Iowa Falls, Iowa, for providing a high strength concrete mix for testing; Manatt's in Ames, Iowa, for providing two normal strength concrete mixes typically used for bridge construction.

TABLE OF CONTENTS

ABSTRACT ii
ACKNOWLEDGEMENTS v
TABLE OF CONTENTS vi
TABLE OF FIGURES x
TABLE OF TABLES xix
NOMENCLATURE xxi
CHAPTER 1: INTRODUCTION 1
1.1 Historical Background 1
1.2 Seismic Engineering Practices 1
1.2.1 Seismic Loading 3
1.2.2 Capacity Design Philosophy 4
1.2.3 Behavior of Plastic Hinges 4
1.2.4 Temperature Concerns 7
1.3 Types of Foundations 8
1.3.1 Shallow Foundations 9
1.3.2 Deep Foundations 10
1.4 Soil-Foundation-Structure-Interaction 11
1.4.1 State of Practice 12
1.4.2 Alternative Approach 15
1.5 Scope of Research 17
1.6 Report Layout 17
CHAPTER 2: LITERATURE REVIEW 19
2.1 Introduction 19
2.2 Analytical Investigation 20
2.2.1 Reese and Welch (1975) 20
2.2.2 Crowther (1990) 23
2.2.3 Priestley et al. (1996) 24
2.2.4 Chai (2002) 25
2.2.5 Priestley et al. (2007) 32
2.2.6 AASHTO Specifications 36
2.3 Impact of Seasonal Freezing 38
2.3.1 Effects of Seasonal Freezing 39
2.4 Broad Impacts 46
2.5 Material Behavior 50
2.5.1 Concrete 50
2.5.2 Steel 53
2.5.3 Soil 54
2.6 Sectional Analysis Tool 62
2.7 Pushover Analysis Tool 64

CHAPTER 3: EXAMINATION OF EXISTING METHODS 66
3.1 Introduction 66
3.1.1 Example Problem 66
3.1.2 Moment – Curvature Analysis 66
3.2 Detailed Analysis 68
3.3 Chai (2002) 76
3.3.1 Clay 76
3.3.2 Sand 83
3.3.3 Seasonal Freezing Capability 87
3.4 Priestley et al. (2007) 89
3.5 ATC 32 (1996) 94
3.6 AASHTO (2009) 95
3.7 Summary of Examination 99
CHAPTER 4: DEVELOPMENT OF A NEW SIMPLIFIED MODEL FOR CLAY SOILS 104
4.1 Objective 104
4.2 Background on Model Development 105
4.2.1 Description of New Model 105
4.2.2 Process of Development 107
4.3 LPILE Analyses 107
4.3.1 Analysis Parameters 108
4.3.2 Moment – Curvature Analyses 109
4.3.3 Soil Material Models 110
4.4 Simplified Model for Quantifying Lateral Response 110
4.4.1 Maximum Moment Location 111
4.4.2 Plastic Hinge Length and Zero Moment Location 116
4.4.3 Rotational Spring at Maximum Moment Location 122
4.4.4 Translational Spring 126
4.4.5 Translational Spring Representing the SFSI Effects below Maximum Moment Location 129
4.4.6 Global Bilinear Force-Displacement Response 136
4.5 Model Verification 140
4.5.1 Experimental Verification 140
4.5.2 LPILE Analytical Verification of Concrete Drilled Shafts 145
CHAPTER 5: CONCRETE BEHAVIOR AT FROZEN TEMPERATURES 149
5.1 Introduction 149
5.2 Test Matrix 150
5.2.1 Concrete Selection 150
5.2.2 Testing Plan 151
5.3 Testing Procedures 153
5.3.1 Specimen Construction 153
5.3.2 Load Frame Setup and Instrumentation 156
5.3.3 Loading Protocols 159
5.4 Results 160
5.4.1 Monotonic Testing of Unconfined Concrete 160

5.4.2 Monotonic Testing of Confined Concrete 169
5.5 Conclusions 186

CHAPTER 6: STEEL BEHAVIOR AT FROZEN TEMPERATURES 189

6.1 Introduction 189
6.1.1 Background 189
6.1.2 Previous Research 190
6.2 Experimental Study 192
6.2.1 Sample Preparation 193
6.2.2 Test Setup 194
6.2.3 Loading Protocol 196
6.2.4 Test Matrix 197
6.3 Results and Discussion of Study 199
6.3.1 Temperature Effects 199
6.3.2 Effects of Bar Size 203
6.3.3 Strain Rate Effects 204
6.3.4 Comparison with Previous Recommendations 208
6.3.5 Effects of Cyclic Loading 209
6.3.6 Analysis Model 212
6.4 Recommendations and Conclusions 213

CHAPTER 7: SOIL BEHAVIOR AT FROZEN TEMPERATURES 216

7.1 Introduction 216
7.2 Testing Matrix 216
7.2.1 Soil Selection 216
7.2.2 Testing Plan 217
7.3 Testing Procedures 220
7.3.1 Specimen Preparation 220
7.3.2 Specimen Setup in Chamber 221
7.3.3 Testing Process 223
7.4 Results 224
7.4.1 Typical Results of Experimental Testing 224
7.4.2 Summary of Monotonic Testing 226
7.4.3 Cyclic Testing 236
7.5 Conclusions 238

CHAPTER 8: SUMMARY, CONCLUSIONS AND RECOMMENDATIONS 241

8.1 Introduction 241
8.2 Summary 241
8.3 Conclusions 243
8.4 Design Guidelines and Recommendations 251
8.4.1 Design Guidelines 251
8.4.2 Recommendations for Future Research 260

REFERENCES 262
APPENDIX A: ADDITIONAL INFORMATION FOR PROPOSED NEW MODEL 268
APPENDIX B: ADDITIONAL CONCRETE TESTING INFORMATION 288
APPENDIX C: ADDITIONAL A706 MILD STEEL REINFORCING BAR TEST Data..... 290
APPENDIX D: ADDITIONAL FROZEN SOIL TESTING INFORMATION..... 295

TABLE OF FIGURES

Figure 1-1: Arched pedestrian bridge over I-235 in Des Moines, Iowa (Iowa DOT, 2009) 1

Figure 1-2: Observed earthquake damage: San Fernando (left); Loma Prieta (top right); Northridge (bottom right) [photos accessed through USGS website (2009)] 2

Figure 1-3: 1971 San Fernando earthquake damage, (a) Confinement failure (b) Shear failure within a plastic hinge (Priestley et al., 1996)..... 5

Figure 1-4: Flexural design method based on the equivalent stress block (ACI, 2008)..... 6

Figure 1-5: Cyclic load testing results (Suleiman et al., 2006)..... 8

Figure 1-6: Typical configuration of a spread footing..... 9

Figure 1-7: Different deep foundation systems 10

Figure 1-8: Typical bridge bent with a continuous column to cast-in-drilled-hole (CIDH) shaft cross-section down longitudinal axis..... 11

Figure 1-9: Typical lateral load response of a column supported on a CIDH shaft 13

Figure 1-10: Fixed base cantilever with moment and deflection profiles 13

Figure 1-11: Comparison of equivalent cantilevers with expected response 14

Figure 1-12: Alternative approach to accounting for SFSI..... 16

Figure 2-1: Winkler foundation model 21

Figure 2-2: Beam-column element used in differential equation derivation 22

Figure 2-3: (a) Plastic hinge length; (b) depth to plastic hinge location [Reproduced from Budek et al., 2000]..... 24

Figure 2-4: Equivalent fixed-base cantilever (after Chai 2002) 25

Figure 2-5: Subgrade coefficient and effective friction angle of cohesionless soils (ATC-32, 1996)..... 28

Figure 2-6: Assumed perfectly plastic response between yield and ultimate conditions 30

Figure 2-7: Assumed equivalent plastic hinge length of concrete CIDH shafts (after Chai, 2002)..... 31

Figure 2-8: Moments in pile/column system (after Priestley et al., 2007) 33

Figure 2-9: Basic strain wedge theory model in a uniform soil (Ashour et al., 1998) 37

Figure 2-10: Cross-section details of column-shafts (after Sritharan et al., 2007); (1 in. = 25.4 mm = 2.54 x 10^{-2} m) 40

Figure 2-11: Measured force-displacement response (after Sritharan et al., 2007)..... 41

Figure 2-12: Frost depth, maximum moment location and plastic hinge length at ultimate condition for column-foundation shafts with dimensions of SS1 and SS2 (Sritharan et al., 2007)..... 44

Figure 2-13: Global force-displacement response as temperatures decrease for a column-foundation shaft system with SS1 and SS2 dimensions (Sritharan et al., 2007) 44

Figure 2-14: Comparison of the force-displacement characteristics at the column top for the monotonic and cyclic Ruaumoko models (a) SS1; (b) SS2 45

Figure 2-15: Cyclic force-displacement responses for (a) SS1 column top; (b) SS2 column top; (c) SS1 column base; (d) SS2 column base. 46

Figure 2-16: Frozen soil depth contours produced for a two-year return period by DeGaetano and Wilks (2001) 47

Figure 2-17: Average winter temperatures for Japan's larger cities (Japanese Meteorological Agency, 2009) 47

Figure 2-18: Statewide distribution of bridges in the United States (Bureau of Transportation Statistics, 2007) 48

Figure 2-19: USGS seismic hazard map (2002) overlaid with frost depth contours shown in Figure 2-16 49

Figure 2-20: Seismic activity of Japan near Hokkaido Island circa year 2000 50

Figure 2-21: Percentage increase of concrete strength with reduction in temperature (after Sehnal et al., 1983) 51

Figure 2-22: Yield and ultimate strength increase generated from the works of Sloan (2005) 54

Figure 2-23: Typical curves of unfrozen water content against temperature (after Williams, 1988) [Harris, 1995] 57

Figure 2-24: Temperature dependence of unconfined compressive strength for several frozen soils and ice (after Sayles, 1966) [Andersland and Anderson, 1978] 58

Figure 2-25: Ultimate compressive strength of frozen soils as a function of their total moisture content: (1) sand; (2) sandy loams; (3) clay (51% content of 0.005 mm fractions); (4) silty clay (63% content of fraction < 0.005 mm). [Tsytovich, 1975] 60

Figure 2-26: Stress-strain curves for uniaxial compression of a remoulded silt (after Zhu and Carbee, 1984) [Harris, 1995] 61

Figure 2-27: Modulus of normal elasticity E, kg/cm^2, of frozen ground at constant pressure σ = 2 kg/cm^2. (1) Frozen sand; (2) frozen silty soil; (3) frozen clay. (Tsytovich, 1975) 62

Figure 2-28: Comparison of the measured and calculated force-displacement response envelopes of the column-foundation systems at different temperatures (Sritharan et al. 2007) 65

Figure 3-1: Details of experimental test units SS1 and SS2 (after Sritharan et al., 2007); (1 in. = 25.4 mm = 2.54 x 10^{-2} m) 67

Figure 3-2: Moment-curvature response of SS1 cross-sections without soil confinement 68

Figure 3-3: Soil profile with depth (a) CPT tip resistance (after Sritharan et al., 2007); (b) Undrained shear strength (GWT = Ground Water Table) 70

Figure 3-4: Laboratory testing for development of soil springs at Spangler test site from Sritharan et al. (2007) 71
Figure 3-5: Moment-curvature analyses revised after adjusting the effects of soil confinement for the foundation cross-section A-A 73
Figure 3-6: Global lateral load response of LPILE analyses compared to experimental results of Suleiman et al. (2006) 74
Figure 3-7: Idealized moment-curvature analysis for Chai's method 78
Figure 3-8: Global response based on Chai's method to those from experimental testing and detailed models containing nonlinear soil springs 79
Figure 3-9: Moment-curvature comparison for non-cohesive soil example 84
Figure 3-10: Global response comparison of experimental data with other modeling approaches 86
Figure 3-11: Global response comparison of seasonally frozen system in cohesionless soil 88
Figure 3-12: Bilinear idealized moment-curvature response 91
Figure 3-13: LPILE detailed analysis results (a) moment profile; (b) shear profile 96
Figure 4-1: Proposed new simplified model 105
Figure 4-2: Definition of critical parameters used in the proposed simplified model 106
Figure 4-3: Structural behavior of the column and foundation shafts used in model development 110
Figure 4-4: Location of the maximum moment at the first yield and ultimate limit states at 5% ALR 113
Figure 4-5: Location of the maximum moment with second order polynomial trendlines 114
Figure 4-6: Soil coefficient relationships used to locate the point of maximum moment (1 psi = 6.895 kPa) 115
Figure 4-7: Comparison of maximum moment location using the developed equation and detailed analysis results 116
Figure 4-8: Analytical plastic hinge length in terms of L_{mb} for all aboveground column heights at the ultimate limit state as a function of c_u 118
Figure 4-9: Normalized zero moment location as a function of undrained shear strength at the ultimate limit state for a column shaft system with a 5% axial load ratio 119
Figure 4-10: Normalized zero moment location with the established power series trend lines at the ultimate limit state 120
Figure 4-11: Coefficient and exponent relationships used for locating the first zero moment location below the maximum moment location 121
Figure 4-12: Comparison of normalized zero moment location using Equation 4-5 and detailed analyses 122

Figure 4-13: Comparison of normalized plastic hinge lengths where the solid filled bars are L_{pb}/D and the colorless bars are L_{pa}/D 124
Figure 4-14: Data and trends obtained for the elastic rotation at the maximum moment location due to the elastic curvature below the maximum moment location occurring 125
Figure 4-15: Description of bilinear moment rotation spring located at the point of maximum moment 126
Figure 4-16: Description of soil spring located halfway between the maximum moment location and ground surface 128
Figure 4-17: Average first yield to ultimate subgrade reaction comparison including data points and best fit trend line 129
Figure 4-18: Normalized translation at first yield and ultimate limit states versus normalized length L_{mb}/D 131
Figure 4-19: Linear trend lines associated with the yield and ultimate limit state translation at the point of maximum moment 132
Figure 4-20: Soft soil correction information for coefficient ψ to account for deviation from the linear trend specified in Equation 4-16 (Note: ψ = Adjustment factor) 134
Figure 4-21: Soft soil adjustment factor data and a linear fit curve 134
Figure 4-22: Graphical verification of proposed translation equations at the maximum moment location with $\psi = 1.0$ 135
Figure 4-23: Description of the bilinear translational spring located at the point of maximum moment 136
Figure 4-24: Spangler soil profile with depth in the unfrozen and frozen state (GWT = Ground Water Table) 141
Figure 4-25: Moment-curvature section analyses of test units SS1 and SS2 of Suleiman et al. (2006) for foundation section A-A (see Figure 2-10) 142
Figure 4-26: Global response comparison obtained from the new model with the experimental response and that established from a detailed LPILE analysis of SS1 at 23 °C (73.4 °F) ... 143
Figure 4-27: Global response comparison obtained from the new model with the experimental response and that established from a detailed LPILE analysis of SS2 at -10 °C (14 °F) 143
Figure 4-28: Global response comparison obtained from the new model with that established from a detailed LPILE analysis at $c_u = 48.3$ kPa (7 psi) and $L_{col}/D = 0$ 146
Figure 5-1: Idealized stress-strain behavior of confined and unconfined concrete subjected to an axial loading 149
Figure 5-2: Experimental testing of a confined concrete specimen with $\rho_s = 0.7\%$ subjected to monotonic and cyclic loading (after Thiemann 2009) 152
Figure 5-3: Details of specimens used for testing of confined and unconfined concrete 154
Figure 5-4: Constructed concrete cylinder molds prior to placement of concrete 154

Figure 5-5: Loading frame setup for testing of cylindrical concrete specimens: (a) front schematic view; (b) actual view of testing apparatus 157
Figure 5-6: Axial and bending failure of confined concrete cylinder when upper head rotated after damage to the confined specimen 157
Figure 5-7: Clamping system for concrete cylinder tests 158
Figure 5-8: Concrete experimental instrumentation setup: (a) original; (b) modified..... 159
Figure 5-9: Comparison of SGF obtained from experimental testing for Man AB concrete mix, a linear best fit curve and trendlines established in past studies 161
Figure 5-10: Average value comparison of experimental concrete study and past research..... 163
Figure 5-11: Recommended strength increase curve for unconfined concrete with average test data..... 163
Figure 5-12: Change in ε_{co} of Man AB mix as temperature decreases..... 164
Figure 5-13: Comparison of recommended ε_{co} and experimental results of Man AB mix 165
Figure 5-14: Comparison of the recommended curve with experimental results for strain at peak compressive stress of the Man C and IF concrete mixes 166
Figure 5-15: Comparison of experimental modulus of Man AB mix with trends established from previous unconfined concrete research..... 167
Figure 5-16: Comparison of RV for experimental modulus of Man AB concrete mix to recommended equations 169
Figure 5-17: Comparison of strength RV of Man AB confined cylinders with the ISU unconfined recommendation and Mander et al. (1988)..... 171
Figure 5-18: Effect of cold temperature on Poisson's ratio of concrete [reproduced from Lee et al. (1988b)]..... 172
Figure 5-19: Comparison of Mander et al. (1988) and experimental $f'_{cc}/f'_{c,avg20}$ data at 20 °C (68 °F) for the ManAB concrete mix..... 173
Figure 5-20: Effect of reinforcement ratio on $f'_{cc}/f'_{cc,avg20}$ 174
Figure 5-21: Confined concrete strength ratio deviation with temperature..... 175
Figure 5-22: Comparison of the proposed equation for the increase in confined compressive strength against the test data for the Man AB confined concrete specimens 177
Figure 5-23: ε_{cc} values obtained from experimental testing of Man AB confined specimens ... 179
Figure 5-24: Comparison of theoretical ε_{cc} from Mander's et al. (1988a) with average experimental results at 20 °C (68 °F) for the Man AB concrete mix..... 180
Figure 5-25: Experimental results of ε_{cc} plotted against ρ_s at freezing temperatures..... 181
Figure 5-26: Verification of equations for strain at peak confined concrete stress 182
Figure 5-27: Ultimate confined strain capacity of the Man AB mix test specimens..... 183

Figure 5-28: Modulus of elasticity experimental data points for confined and unconfined concrete at the four testing temperatures 185
Figure 5-29: Experimental concrete stress-strain curves of the Man AB concrete mix tested at 20 °C (68 °F) 186
Figure 6-1: Yield and ultimate tensile strength increases reported for A706 steel by Sloan (2005) 191
Figure 6-2: Aluminum sleeves used to ensure uniform grip at bar ends 194
Figure 6-3: Milled specimen for cyclic loading 194
Figure 6-4: Setup used for testing A706 specimens within an environmental chamber 196
Figure 6-5: Idealized stress-strain curve for A706 mild steel reinforcement 200
Figure 6-6: Effects of cold temperature on the yield strength of A706 mild steel reinforcement established from monotonic testing 201
Figure 6-7: Effects of cold temperature on the ultimate tensile strength of A706 mild steel reinforcement established from monotonic testing 202
Figure 6-8: Comparison between yield and ultimate tensile strength increases obtained for tow bar sizes subjected to monotonic loading 204
Figure 6-9: Modulus of elasticity vs. strain rate at -1°C (30.2°F) and -20°C (-4°F) 205
Figure 6-10: Effects of strain rate on the yield strength of A706 mild steel reinforcement at -1°C (30.2°F) and -20°C (-4°F) 205
Figure 6-11: Effects of strain rate on the yield plateau length of A706 mild steel reinforcement at -1°C (30.2°F) and -20°C (-4°F) 206
Figure 6-12: Dissipation of yield plateau length due to strain rate of a milled #8 A706 mild steel reinforcing bar at -20°C (-4°F) 207
Figure 6-13: Effects of strain rate on the ultimate strength of A706 mild steel reinforcement at -1°C (30.2°F) and -20°C (-4°F) 208
Figure 6-14: Comparison of proposed A706 temperature effects to those found in the literature for A572, CSA G30.16, and A706 209
Figure 6-15: Initial cyclic buckling problem for A706 mild steel reinforcement 210
Figure 6-16: Comparison of planned and actual loading path used for cyclic testing 211
Figure 6-17: Effects of cyclic loading on stress-strain behavior of A706 mild steel reinforcement at -1°C (30.2°F) and at 0.03 /min. 211
Figure 6-18: Effects of cyclic loading on stress-strain behavior of A706 mild steel reinforcement at -20°C (-4°F) and at 0.03 /min 212
Figure 6-19: Validation of proposed temperature effect strength increase equations for A706 mild steel reinforcement 213
Figure 7-1: Sample compaction process: (a) loosely placing soil in mold; (b) using a plunger to compact soil; (c) placing compacted soil and molds in storage freezer 221

Figure 7-2: Final soil sample preparation: (a) extrusion of sample from mold; (b) fully prepped sample ready to be tested 222
Figure 7-3: Modified triaxial chamber setup for testing of frozen soils at MRCE 222
Figure 7-4: Experimental stress-strain curve for a Type I soil at -20 C (-4 F) and a 15% moisture content 223
Figure 7-5: Stress-strain response of a Type I soil subjected to monotonic loading and temperatures between 20 °C (68 °F) and -22.8 °C (-9 °F) 224
Figure 7-6: Experimental cyclcic stress-strain response of a Type I soil 225
Figure 7-7: Failure strengths of analyzed soils at 20 °C (68 °F) [Note: 1 tsf = 95.8 kPa; 1 pcf = 0.157 kN/m^3] 226
Figure 7-8: Increase in the ultimate compressive strength of a Type I soil with respect to warm temperature at 20 °C (68 °F) 227
Figure 7-9: Increase in ultimate compressive strength of the five soil types specified in Table 7-2 tested at -1 °C (30.2 °F) with respect to the ultimate compressive strength at 20 °C (68 °F) 228
Figure 7-10: Increase in ultimate compressive strength of the five soil types specified in Table 7-2 tested at -20 °C (-4 °F) with respect to the ultimate compressive strength at 20 °C (68 °F) 229
Figure 7-11: Effects of temperature on the strain at the ultimate compressive strength of a Type I: Alluvial soil 230
Figure 7-12: Effects of temperature on the soil modulus of elasticity under monotonic loading 231
Figure 7-13: Effects of density on undrained shear strength of a CH soil at -20 °C (-4 °F) 232
Figure 7-14: Effects of moisture content on the undrained shear strength of a CH soil at -20 °C (-4 °F) 233
Figure 7-15: Effect of strain rate on the ultimate compressive strength of a Type I soil tested at -20 °C (-4 °F) 234
Figure 7-16: Effect of strain rate on the strain at the ultimate compressive strength of a Type I soil tested at -20 °C (-4 °F) 235
Figure 7-17: Effect of strain rate on the secant modulus of elasticity to the undrained shear strength of a Type I soil tested at -20 °C (-4 °F) 235
Figure 7-18: Experimental cyclic stress-strain results of a Type I soil subjected to subzero temperatures and a loading rate of 1% strain per minute 236
Figure 7-19: Experimental strain rate effects on the cyclic stress-strain response of a Type I soil tested at -20 °C (-4 °F) 237
Figure 8-1: Initial design flow chart for the seismic design of CIDH shafts 252
Figure 8-2: Sophisticated design method flowchart in all soil types 253
Figure 8-3: Simplified method design flowchart in cohesive soils 254

Figure 8-4: Description of the terminology used within the simplified method for cohesive soils provided in Figure 8-3 255
Figure 8-5: Final bilinear force-displacement response attained using the simplified method for cohesive soils 257
Figure 8-6: Simplified method design flowchart in cohesionless soil 258
Figure 8-7: Flowchart for defining concrete, steel and soil material properties at cold temperatures 259
Figure A-1: Global response comparison of new methodology with additional analytical verification #1 273
Figure A-2: Global response comparison of new methodology with additional analytical verification #2 275
Figure A-3: Global response comparison of new methodology with additional analytical verification #3 277
Figure A-4: Global response comparison of new methodology with additional analytical verification #4 279
Figure A-5: Global response comparison of new methodology with additional analytical verification #5 281
Figure A-6: Global response comparison of new methodology with additional analytical verification #6 283
Figure A-7: Global response comparison of new methodology with additional analytical verification #7 285
Figure A-8: Global response comparison of new methodology with additional analytical verification #8 287
Figure B-1: Comparison of SGF obtained from experimental testing of Man C concrete mix and past studies 288
Figure B-2: Comparison of SGF obtained from experimental testing of IF concrete mix and past studies 289
Figure C-1: Modulus of elasticity vs. temperature obtained at a strain rate of 0.001896 ε/min. 290
Figure C-2: Yield plateau length vs. temperature obtained at a strain rate of 0.001897 ε/min. for all tested bar sizes 291
Figure C-3: Ultimate strain vs. temperature at a strain rate of 0.275 ε/min. 291
Figure C-4: Ultimate strain vs. strain rate at various temperatures 292
Figure C-5: Strain-hardening strength increase equation 6-5 validation at 20 °C (68 °F) 292
Figure C-6: Strain-hardening strength increase equation 6-5 validation at 5 °C (41 °F) 293
Figure C-7: Strain-hardening strength increase equation 6-5 validation at -1 °C (30.2 °F) 293
Figure C-8: Strain-hardening strength increase equation 6-5 validation at -20 °C (-4 °F) 294

Figure C-9: Strain-hardening strength increase equation 6-5 validation at -40 °C (-40 °F) 294
Figure D-1: Refernce value comparison for failure strength on a Type II soil..... 295
Figure D-2: Reference value comparison for failure strain on a Type II soil..... 295
Figure D-3: Reference value comparison for failure strength on Type III soil 296
Figure D-4: Reference value comparison for failure strain on Type III Soil..... 296
Figure D-5: Reference value comparison for failure strength on Type IV soil 297
Figure D-6: Reference value comparison for failure strain on Type IV soil 297
Figure D-7: Reference value comparison for failure strength on Type V soil 298
Figure D-8: Reference value comparison for failure strain on Type V soil 298

TABLE OF TABLES

Table 2-1: Studies on lateral loading of drilled shafts 19

Table 2-2: Ultimate strength of frozen soils in uniaxial compression (after Tsytovich, 1975) 59

Table 2-3: Instantaneous and ultimate long-term tensile strengths of frozen soils (after Tsytovich, 1975) 59

Table 2-4: Values of Poisson's coefficient for frozen soils (after Tsytovich, 1975) 62

Table 3-1: Loading and material properties used for moment-curvature analyses of SS1 cross-sections (see Figure 3-1) 67

Table 3-2: Primary soil profile chosen for soil springs in LPILE analysis 70

Table 3-3: Secondary soil profile chosen for soil springs in LPILE analysis based on laboratory testing modifications 71

Table 3-4: Lateral load response of SS1 at the critical conditions 74

Table 3-5: Localized responses of final models at the ultimate condition 75

Table 3-6: Local response comparison between Chai's method and the nonlinear soil spring methods 80

Table 3-7: Sensitivity of Chai's (2002) plastic rotation on the ultimate displacement capacity of SS1 82

Table 3-8: Detailed comparison of experimental values with Chai's analytical model 87

Table 3-9: Comparison of detailed analysis method with Chai's methodology (2002) in seasonally frozen ground 88

Table 3-10: Results of detailed analysis of modified SFSI system using LPILE 90

Table 3-11: Global comparison between LPILE and Priestley models 92

Table 3-12: Localized comparison between LPILE and Priestley models 92

Table 4-1: Mathematical verification of the proposed translation equations at the maximum moment location for c_u = 48.3 kPa (7 psi) 136

Table 4-2: Bilinear idealization obtained for shafts from moment-curvature analyses 142

Table 4-3: Comparison of critical parameters of SS1 at the ultimate limit state 144

Table 4-4: Comparison of critical parameters of SS2 at the ultimate limit state 144

Table 4-5: Comparison of critical parameters at the ultimate limit state obtained from the new model with that established from a detailed LPILE analysis at c_u = 48.3 kPa (7 psi) and L_{col}/D = 0 147

Table 5-1: Concrete strength, reinforcement type and horizontal reinforcement ratios of cylindrical test specimens 151

Table 5-2: Test Matrix used for Cylindrical Concrete Specimens 152

Table 5-3: A summary of concrete batch testing results 155

Table 6-1: Cyclic test target strains for A706 mild steel reinforcement 197
Table 6-2: Monotonic test matrix used to study the effects of temperature, bar size and strain rate on A706 mild steel reinforcement 198
Table 6-3: Cyclic test matrix used to study the effects of temperature on A706 mild steel reinforcement 199
Table 6-4: Adjusted parameters to define the stress-strain behavior of A706 mild steel reinforcement at warm temperatures 213
Table 7-1: Five main soils types and expected temperature and moisture content ranges 217
Table 7-2: Summary of Completed Soil Tests 218
Table 7-3: Target strains for cyclic loading of Type I: Alluvial Soil at strain rates of 1% per minute and 10% per minute 219
Table 7-4: Numerical results of the Type I soil stress-strain curves depicted in Figure 7-5 225
Table A-1: Input parameters for additional analytical verification #1 272
Table A-2: Comparison of critical parameters at the ultimate limit state for additional analytical verification #1 272
Table A-3: Input parameters for additional analytical verification #2 274
Table A-4: Comparison of critical parameters at the ultimate limit state for additional analytical verification #2 274
Table A-5: Input parameters for additional analytical verification #3 276
Table A-6: Comparison of critical parameters at the ultimate limit state for additional analytical verification #3 276
Table A-7: Input parameters for additional analytical verification #4 278
Table A-8: Comparison of critical parameters at the ultimate limit state for additional analytical verification #4 278
Table A-9: Input parameters for additional analytical verification #5 280
Table A-10: Comparison of critical parameters at the ultimate limit state for additional analytical verification #5 280
Table A-11: Input parameters for additional analytical verification #6 282
Table A-12: Comparison of critical parameters at the ultimate limit state for additional analytical verification #6 282
Table A-13: Input parameters for additional analytical verification #7 284
Table A-14: Comparison of critical parameters at the ultimate limit state for additional analytical verification #7 284
Table A-15: Input parameters for additional analytical verification #8 286
Table A-16: Comparison of critical parameters at the ultimate limit state for additional analytical verification #8 286

NOMENCLATURE

Abbreviations

AASHTO = American Association of State and Highway Transportation Officials
ALR = P/f'_cA_g = axial load ratio
ASTM = American Society for Testing and Materials
ATC = Applied Technology Council
CIDH = cast-in-drilled-hole
CPT = cone penetration test
CRSI = Concrete Reinforcing Steel Institute
PTC = Parametric Technology Corporation
SFSI = soil-foundation-structure-interaction
UHPC = ultra-high performance concrete
USCS = Unified Soil Classification System
USGS = United States Geological Service
VSAT = Versatile Section Analysis Tool
ult = ultimate limit state
yld = first yield limit state

Symbols

C_1 = coefficient dependent on end fixity condition (Priestley et al., 2007)
C_3 = coefficient for changing moment pattern (Priestley et al., 2007)
D = column or pile shaft diameter
D' = effective core diameter for a circular concrete shaft
D^* = reference pile diameter = 1.83 m (6 ft) (Priestley et al., 1996)
E_p = pile modulus of elasticity
E_s = soil modulus of elasticity
E_s = Young's modulus of elasticity for mild steel reinforcement (Chapter 6)
EI = flexural stiffness of foundation (Reese et al., 1975)
EI_{eff} = effective flexural stiffness term
H = height of column above ground
H_{cp} = height to contraflexure point from top of column
H_{IG} = distance to in-ground plastic hinge from top of column
I_e = effective moment of inertia for pile cross-section
I_p = soil plasticity index
I_w = weak axis moment of inertia for foundation shaft
K = soil subgrade modulus in units of force per length cubed
K_{sp} = stiffness of soil-pile system when subjected to lateral loading
K_c = stiffness of a cantilever column when subjected to lateral loading
L = overall length of column-pile shaft
L_a = above ground column height
L_a^* = normalized above ground column height
L_{cant} = equivalent cantilever length from column top to effective fixity location
L_f = depth to effective fixity from ground surface
L_f = length of foundation shaft

L_m = depth to the maximum moment location from ground surface
L_m^* = normalized depth to maximum moment location from the ground surface
L_{col} = height of column above ground surface
L_{ma} = distance to point of maximum moment from top of column
L_{mb} = distance below maximum moment to first point of zero moment
L_{m0} = distance to first point of zero moment from top of column
L_{sp} = idealized strain penetration length
L_p = analytical plastic hinge length
L_{pa} = analytical length of plastic hinge above the maximum moment location
L_{pb} = analytical length of plastic hinge below the maximum moment location
$L_{p,actual}$ = actual length of plastic hinge from detailed analysis
$L_{p,IG}$ = analytical plastic hinge length due to in-ground hinging
M = moment
M_{max}^* = normalized flexural strength of foundation shaft
M'_y = first yield moment capacity of shaft cross-section corresponding with ϕ'_y
M_y = yield moment capacity of shaft cross-section corresponding with ϕ_y
M_u = ultimate moment capacity of shaft cross-section corresponding with ϕ_u
N_k = bearing capacity factor used in a CPT test
P = axial load applied to column-pile shaft system
R_c = characteristic length of column-pile shaft = $\left(EI_{eff}/k_h\right)^{1/4}$
T = temperature of material
V = lateral force applied at top of column-pile shaft
V_s = soil shear force at location of soil spring
V_{sy} = soil shear force at the yield limit state
V_{su} = soil shear force at the ultimate limit state
V_t = corrected lateral load at the top of the column
V_{t1} = uncorrected lateral load at the top of the column
V_y = first yield lateral load at top of column
V_u = ultimate lateral load at top of column
V_u^* = normalized lateral strength of soil-pile system (Chai, 2002)
b = width of foundation in Reese et al. (1975)
b = exponent in p-y curve development using Reese et al. (1975) suggestions
c = neutral axis depth in concrete shaft for a given curvature
c_u = undrained shear strength of soil
d_b = nominal diameter of deformed reinforcing bar
d_{bl} = diameter of longitudinal reinforcing bar
f'_c = specified ultimate concrete compressive stress
f'_{ce} = expected ultimate concrete compressive stress
$f'_{c,avg20}$ = average ultimate concrete compressive stress at 20 °C (68 °F)
$f'_{c,exp}$ = experimental ultimate concrete compressive stress
f'_t = concrete tensile stress
f_y = specification yield steel stress of reinforcing bars
f_y = yield strength of longitudinal mild steel reinforcement (Chapter 6)
f_{ye} = expected yield steel stress of reinforcing bars
f_{su} = ultimate tensile strength of longitudinal mild steel reinforcement
f_u = ultimate steel stress of reinforcing bars

g = acceleration due to gravity
h_s = height of soil between the maximum and zero moment locations
k = coefficient in L_p equation for a fixed head condition (Priestley et al., 2007)
k = initial p-y modulus used in LPILE analyses in units of force per length cubed
k_h = constant modulus of subgrade reaction in units of force per length squared
p = soil subgrade reaction per unit length of pile
p_u = ultimate soil subgrade reaction per unit length of pile
q_u = unconfined compression strength of soil
s_u = maximum unconfined compressive strength of soil
w/c = water to cement ratio
x = depth from ground surface to location of soil spring in Reese et al. (1975)
x = distance from bottom of pile to a point along length of column-pile shaft
y = displacement of soil/pile according to Reese et al. (1975) at depth z
y_{50} = displacement of soil/pile at one-half the ultimate soil subgrade reaction
z = depth below ground surface
Δ = displacement of column-shaft system at top of column
Δ_D = design displacement of column-shaft system at top of column
Δ_e = elastic displacement of column-shaft system at top of column
Δ_{ea} = corrected elastic displacement of system at top of column from cantilever action above the maximum moment location
Δ_{ea} = uncorrected elastic displacement of system at top of column from cantilever action above the maximum moment location
Δ_{eb} = elastic displacement of system at top of column from elastic rotation below the maximum moment location
Δ_g = displacement of column-CIDH shaft at ground level
Δ_{La} = above ground cantilever lateral displacement at column tip
Δ_p = plastic displacement of column-shaft system at top of column
Δ_{pu} = plastic displacement of column-shaft system at top of column for the ultimate limit state
$\Delta_{p,IG}$ = plastic displacement of column-shaft system at top of column due to in-ground hinging
Δ_{sp} = lateral displacement of soil-pile system at column tip
Δ_t = translation of foundation shaft at the maximum moment location
Δ_{trans} = displacement of the system at the maximum moment location
Δ_{ty} = translation at the maximum moment location for the first yield limit state
Δ_t = translation at the maximum moment location for the ultimate limit state
Δ_y = yield displacement of system at top of column
$\Delta_{y,F}$ = yield displacement of system at top of column due to fixed head condition
$\Delta_{y,IG}$ = yield displacement of system at top of column due to in-ground hinging
Δ_u = ultimate displacement of system at top of column
$\Delta f_y(\%)$ = percent increase in yield strength with respect to 20 °C (68 °F)
$\Delta f_{su}(\%)$ = percent increase in ultimate tensile strength with respect to 20 °C (68 °F)
$\Delta f_{0.03}(\%)$ = percent increase in strength at 0.03 strain with respect to 20 °C (68 °F)
α_{ma} = coefficient for computing the maximum moment location
α_{m0} = coefficient for computing the first zero moment location

β_{ma} = coefficient for computing the maximum moment location
β_{m0} = coefficient for computing the first zero moment location
χ_{ma} = coefficient for computing the maximum moment location
ε = soil strain from laboratory testing
ε_c = concrete strain
ε_{co} = concrete cracking strain
ε_{cu} = ultimate strain of concrete
$\varepsilon_{dc,c}$ = damage control strain for concrete
$\varepsilon_{dc,s}$ = damage control strain for steel reinforcing bars
ε_{sh} = strain in mild steel reinforcement at the onset of the strain hardening
ε_{su} = ultimate strain of mild steel reinforcement corresponding to f_{su}
ε_y = yield strain of mild steel reinforcement corresponding to f_y
ε_{50} = soil strain at fifty percent of maximum principal stress
ϕ = curvature of shaft cross-section
ϕ_e = elastic curvature of shaft cross-section
ϕ_{ls} = limit state curvature of shaft cross-section
$\phi_{ls,c}$ = damage control limit state curvature of shaft cross-section for concrete failure
$\phi_{ls,s}$ = damage control limit state curvature of shaft cross-section for steel failure
ϕ'_y = first yielding curvature of shaft cross-section
ϕ_y = idealized elasto-plastic yield curvature of cross-section used in Chai (2002)
ϕ_y = yield curvature of shaft cross-section
ϕ_p = plastic curvature of shaft cross-section
ϕ_u = ultimate curvature of shaft cross-section
γ = effective unit weight of soil
γ_m = effective moist unit weight of soil
η = coefficient to modify the ultimate soil shear force to a yield condition
λ_p = normalized analytical plastic hinge length
μ_Δ = displacement ductility of system
μ_ϕ = curvature ductility of foundation shaft
θ_{eb} = elastic rotation from effects below the maximum moment location
θ_{eby} = elastic rotation from effects below the maximum moment location at first yield
θ_{ebu} = elastic rotation from effects below the maximum moment location at ultimate
θ_g = rotation of column-pile shaft at ground level
θ_p = plastic rotation of column-pile shaft
θ_{pa} = plastic rotation above point of maximum moment
θ_{pb} = plastic rotation below point of maximum moment
θ_y = yield rotation of column-pile shaft at the maximum moment location
θ_u = ultimate rotation of column-pile shaft at the maximum moment location
ρ_l = longitudinal reinforcement ratio
ρ_s = transverse (spiral) reinforcement ratio
$\pm\sigma$ = percent increase standard deviation from Δf_y(%)
$\pm\sigma$ = percent increase standard deviation from Δf_{su}(%)
ξ_a = coefficient for locating the above ground height (Chai, 2002)
ξ_f = coefficient for locating the equivalent depth to fixity (Chai, 2002)

ψ	= soft soil modification factor in translation computations for new method
~	= approximately

Units

cm	= centimeter (1 cm = 0.01 m)
ft	= feet
in.	= inch
kN	= kilonewton (1 kN = 1000 N)
kip	= 1000 pound-force
kPa	= kilopascal (1 kPa = 1000 Pa)
ksi	= kip per square inch (1 ksi = 1000 psi)
ksf	= kip per square foot (1 ksf = 1000 psf)
lb	= pound-force
m	= meter
mm	= millimeter (1 mm = 0.001 m)
MN	= meganewton (1 MN = 1E+06 N)
MPa	= megapascal (1 MPa = 1E+06 Pa)
Pa	= pascal (1 Pa = 1 N/m^2)
psi	= pound-force per square inch
psf	= pound-force per square foot
°C	= degrees Centigrade
°F	= degrees Fahrenheit

CHAPTER 1: INTRODUCTION

1.1 Historical Background

A bridge, by definition, is a time, place, or means of connection or transition (Merriam-Webster, 2008). In ancient times, this may have been as easy as a log that had fallen across a river or as complicated as a Roman arch bridge. As the years passed, the design of bridges became more complicated due to the desire to provide functionality along with an artistic appearance, such as the pedestrian bridges located in Des Moines, Iowa (Figure 1-1). With the ever changing demands on designers, significant advancements of knowledge within structural behavior and construction materials have been made to further advance the innovation in bridge design.

Figure 1-1: Arched pedestrian bridge over I-235 in Des Moines, Iowa (Iowa DOT, 2009)

1.2 Seismic Engineering Practices

Structural engineering is an expanding field based on knowledge ascertained over the decades. In the specialized field of seismic engineering, the design of structures has been constantly evolving as knowledge about earthquakes and their effects on structural response progresses. The earliest records of earthquakes go back as far as 1831 BC, in the Shandong province of China (USGS, 2009). However, China is not the only location in the world to have recorded early earthquakes. In the United States, European settlers experienced earthquakes as

early as 1663 AD (USGS, 2009). From this point in time, earthquakes within the United States have been steadily recorded in time histories.

One of the more significant sets of earthquakes in the history of the United States is the New Madrid Series of 1811 – 1812. This series contained three earthquakes with a magnitude of at least 8 and had devastating effects on structures in the central United States due to the efficiency of the geological features to propagate seismic energy (USGS 2009). As time progressed, more information was gained about dynamics and structural behavior, as well as characteristics of earthquakes from when a full earthquake ground acceleration record was collected during the 1940 Imperial Valley earthquake. This information allowed structures to be designed to target ground accelerations using a force-based approach that related to the ground accelerations measured during past earthquakes. However, it was not until the 1980s when engineers began to realize that a force-based approach combined with an allowable stress method would not be a sound approach for the seismic design of structures (Priestley et al., 2007). The problem with a force-based approach without emphasizing adequate displacement capacities became prevalent with damage caused by the 1971 San Fernando earthquake, the 1989 Loma Prieta earthquake and the 1994 Northridge earthquake to name a few (see Figure 1-2). Today, an approach that relies on the final performance of structures when subjected to different intensities of earthquakes is slowly taking over. This method ensures an appropriate design is created such that the desired performance of the structure is met over the lifespan of the structure.

Figure 1-2: Observed earthquake damage: San Fernando (left); Loma Prieta (top right); Northridge (bottom right) [photos accessed through USGS website (2009)]

1.2.1 Seismic Loading

Since the first full record of ground accelerations were first captured during the 1940 Imperial Valley earthquake, the understanding of seismic loading has been constantly evolving. This evolution in seismic loading has generally come from two different sources. The first source of evolution is the improvement of data acquisition systems over the years, which has led to more data collections with enhanced accuracy in capturing seismic accelerations across the entire world. The increased amount of data collected has led to maps and time history data files able to provide more localized accelerations based on previously recorded events as well as the geology of the areas. The second major point of evolution is the continuously learned knowledge of structural behavior and its effects on the seismic design process. A key component of this evolution is the understanding of material behavior and how the nonlinearity in the material properties can be used to ensure a structure that performs as desired when subjected to earthquake excitation. By using the nonlinearity of material properties, structures are now designed to form a hinge point and essentially deform in a ductile manner while losing minimal capacity. This evolution of design also led to a better understanding of hysteretic damping and how it may be used to dissipate the seismic energy applied to a structure.

Although a great deal of evolution has occurred with data collection and understanding of structural behavior, the analysis methods used for determining the final seismic loading have been relatively unchanged. The analysis methods are generally classified into two areas—a full dynamic analysis and a simplified analysis. The full dynamic analysis will use a previously recorded or artificially generated earthquake time history in a numerical integration method that will generate the full response of the structure, forces and displacements, due to the energy imparted by an earthquake ground motion. The simplified method uses an approximation based on the period of the structure to establish a design base shear force that is then distributed to the different levels of the structure using the appropriate modal shapes of the structure. These distributed shear values are then used to determine the design forces for individual members of the structure. No matter what method is chosen for determining the seismic loading, the response of the structure should be understood in the design process to ensure an adequate response during a seismic event.

1.2.2 Capacity Design Philosophy

In high seismic regions of the United States, such as California, Alaska and South Carolina, structures are now designed to ensure an adequate response to seismic loading. To maintain a satisfactory performance, structures are designed in accordance with standards as specified by the owning agency. The standards within the high seismic regions generally follow a design philosophy that uses capacity design principles (Priestley et al., 1996). These principles as stated by Priestley et al. (1996) are summarized as follows:

- the structure is allowed to respond inelastically through flexural yielding and formation of plastic hinges under design-level earthquakes;
- plastic hinge locations are pre-determined and carefully detailed to ensure that ductile response of the structure can occur; and
- undesirable mechanisms (e.g., shear failure) are prevented throughout the structure by the provision of a suitable strength margin.

Currently, the capacity design principles are not widely used around the United States (Priestley et al., 2007) even though the principles can be used within a force-based design. The future of earthquake engineering, however, is steadily progressing toward the principles of capacity design as the performance-based method of design takes over by ensuring all possible scenarios, including seismic events, are accounted over the lifespan of the structure. Designs will be further improved, as well, since the capacity design principles will ensure other modes of lateral loading shall not collapse the structure.

1.2.3 Behavior of Plastic Hinges

The predetermined placement of plastic hinges is vital in seismic design. Plastic hinges are designed and detailed to dissipate energy by responding inelastically during a seismic event without experiencing significant strength degradation (Priestley et al., 1996). The locations are determined by identifying the critical section of the flexural members. These plastic hinges can be positioned in a structure to allow for a bridge superstructure to perform elastically or to provide redundancy in buildings to protect human life during a seismic event. If designed properly, the catastrophic failures depicted in Figure 1-3 and the collapse of the entire structure can be prevented.

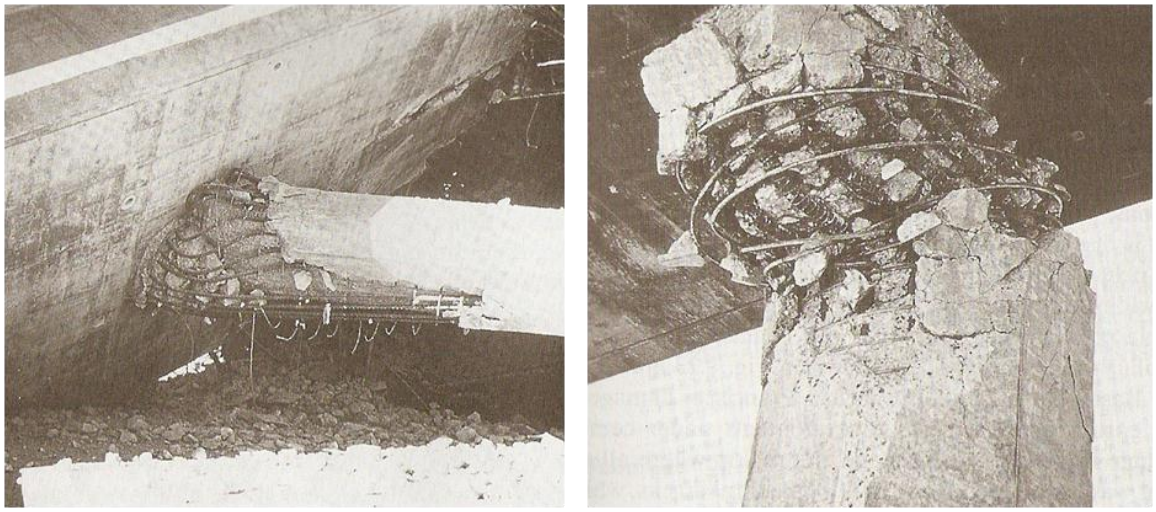

(a) **(b)**

Figure 1-3: 1971 San Fernando earthquake damage, (a) Confinement failure (b) Shear failure within a plastic hinge (Priestley et al., 1996)

In addition, flexural members containing the plastic hinges must be designed in such a way that they meet the displacement or displacement ductility requirements at the ultimate limit state as specified in the code of practice (e.g., ACI, AASHTO, etc.). To attain this displacement ductility, the preselected hinges undergo inelastic deformation during the design seismic event. The flexural members should also be designed so undesirable failure modes, such as shear and buckling, do not dictate the member's performance during the structure's design life.

The current procedure to design for the ultimate limit state for seismic condition is presented by the AASHTO LRFD Bridge Design Specifications with interim revisions and/or the ACI-08 code (ACI, 2008; AASHTO, 2007). Both sources, ACI-08 Chapter 21 and AASHTO Section 5.7.2.2, use the equivalent stress block method to determine the flexural capacity of a flexural member and provide provisions on transverse reinforcement near the ends of these members to incorporate ductility. The equivalent stress block method, as shown in Figure 1-4, recreated from ACI-08 Section 10.2, assumes the non-uniform concrete compressive stress contour provides a total force that can be represented as a stress block with dimensions $0.85*f_c'$ by B_1*c, where B_1 is the factor relating depth of compressive block to neutral axis depth, c is the neutral axis depth and f'_c is the concrete compressive stress. All mild steel within the section is assumed to be at yield, f_y, or at the nominal flexural capacity, f_{ps}, in prestressed sections (ACI-08 Section 18.7.1 and AASHTO Section 5.7.3.1). From these assumptions, one can determine the ultimate flexural capacity of the section. The AASHTO code allows for the $0.85*f_c'$ concrete strength to

be modified for sections if experimentation can prove the new value accurate and dependable (AASHTO, 2007).

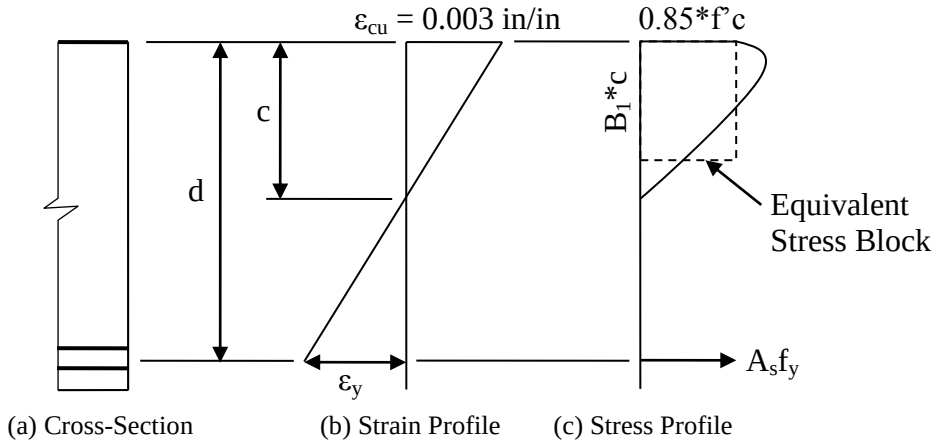

Figure 1-4: Flexural design method based on the equivalent stress block (ACI, 2008)

The equivalent stress block method has limitations and disadvantages. This method tends to be conservative (Priestley et al., 1996), leading to more costly sections. The underestimation of flexural strength may lead to additional funds spent on retrofitting of existing structures where a more precise method of analysis may deem the section adequate. The equivalent stress block method cannot accurately depict the true flexural capacity of the section because the resultant compressive force location varies based on the assumed material behavior of the cross-section. This includes the concrete compressive strength which changes based on confined or unconfined concrete behavior. An inaccuracy in the section's flexural resistance may cause undesirable failures, such as shear failure, to occur because the demand is too high. Finally, the designer has no control over the ductility of the system because it cannot be determined with the information provided.

In Section 8.4 of the newest AASHTO Design guide, *AASHTO Guide Specifications for LRFD Seismic Bridge Design*, a moment-curvature approach for designing sections is provided (AASHTO, 2009). This approach is more consistent with the Capacity Design Philosophy and also contains information on material models that can be used in lieu of material test data. This design guide was created in response to the vulnerability of columns with inadequate transverse reinforcement and anchorage of longitudinal reinforcement evidenced in the 1989 Loma Prieta and 1998 Northridge earthquakes (AASHTO, 2009). The material models provided in this

document allow mild steel reinforcement, concrete and prestress steel responses to be captured. However, utilizing this material information may lead to errors in the moment-curvature response if the data used in the field is not adequately represented by the models (e.g., the strain hardening region not being fully captured).

Upon the completion of designing for the ultimate limit state, the service limit state should be checked. After an event, no remedial action should be required at this state as no crushing of concrete, extensive cracks that require injection grouting, or spalling of the concrete should form under service and/or minor earthquake loading. Currently, this is satisfied in codes and guidelines by extra provisions, such as crack control reinforcement spacing or deflection check requirements.

To better estimate the actual behavior and capacity of flexural members for ultimate and service limit states while maintaining the most cost effective section, a moment-curvature approach can be used. The stress quantifications are refined to more accurately predict moment capacities and an idealized force-displacement response can be found. However, the LRFD method indirectly specifies the maximum displacement possible for a section, as the ductility is empirically integrated into the equations for most structures, while other standards require a pushover analysis (Caltrans, 2006).

1.2.4 Temperature Concerns

The capacity design principles, as stated above, heavily rely on allowing flexural yielding and preventing undesirable effects in the structure; however, little research has been performed on the effects of seasonal cold temperatures on ductile behavior of structures when subjected to a seismic event. This is a major deficiency in the field of earthquake engineering, as some of the largest earthquakes (e.g., 1811-1812 New Madrid Series and the 1964 Great Alaska earthquake) actually occurred in the earthquake affected regions of the United States during winter months that cause ground freezing. It has been shown in an exploratory research program by Sritharan et al. (2007) that the seasonally frozen effects can cause brittle failure of bridges designed to respond in a ductile manner unless their effects are accounted for in seismic design. The effects of cold temperature are further exacerbated by the unknown effects caused to the moment-curvature response of a critical member section, an important element in determining flexural yielding. The significance of these two issues are made even more critical as they are in direct violation of the capacity design principles. These principles state the designer should allow

flexural yielding while preventing an undesirable failure mode, such as a brittle failure. In the exploratory research that examined the performance of continuous columns supported on drilled shaft foundations, Suleiman et al. (2006) drew the following conclusions regarding the lateral load response of a full-scale test in wintry conditions with respect to the response of an identical system in warm conditions:

- effective elastic stiffness increased by 170%,
- lateral load resistance increased by 44%,
- maximum moment location shifted upwards by 0.84 m (33 in.),
- plastic region length reduced by 64% in the foundation shaft, and
- gap opening at the base of the column reduced by 60%.

Results for the cyclic responses of the two column-shaft systems are presented in Figure 1-5. The results demonstrate the drastic difference between seasonal wintry conditions and summer conditions where one can see a significant difference in the lateral force at a comparable displacement between the two experiments. Due to the large variation in the lateral response of the system, any new development in the seismic design process of an integrated column-foundation shaft should give consideration to this issue.

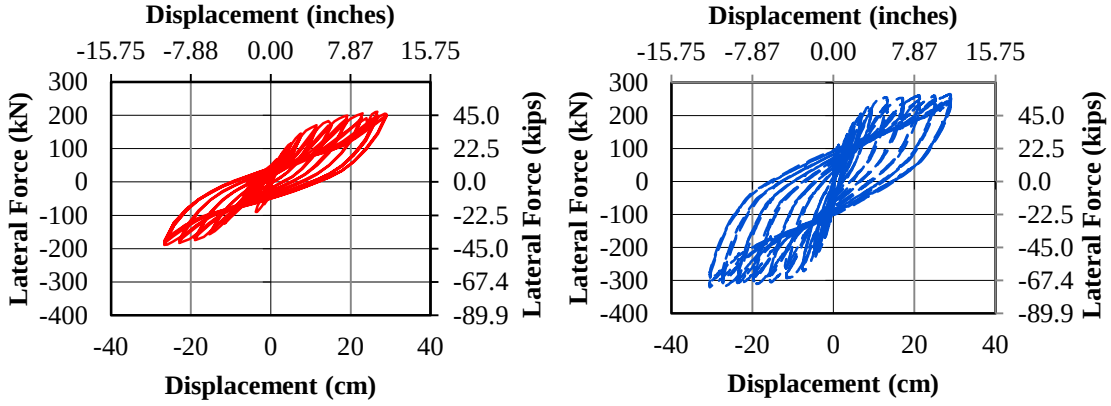

(a) SS1 at 23 °C (b) SS2 at -10 °C

Figure 1-5: Cyclic load testing results (Suleiman et al., 2006)

1.3 Types of Foundations

Over the years bridge superstructures have undergone many changes in seismic regions for both artistic and structural reasons. However, bridge substructures have essentially remained unchanged and can be classified into two main groups: those utilizing shallow foundations and those utilizing deep foundations. Shallow foundations are foundations located on competent

soils that are able to support the structure directly through bearing for vertical loads. Shallow foundations require a large enough base to prevent overturning and sliding to handle lateral seismic loading. When the soil is not competent enough to support the structure or a shallow foundation is not cost effective, deep foundation systems are used.

1.3.1 Shallow Foundations

Shallow foundations are typically referred to as spread footings and consist of a rectangular pad of concrete that bears directly on the soil as depicted in Figure 1-6. This method of foundation construction generally requires less excavation and no specialized equipment, making this a cost-effective foundation on competent soils. Although a spread footing is easy to construct and can lessen building costs, the cross-section of the spread footing may be inefficient because the footing must be extremely large to prevent a failure due to bearing capacity, overturning or sliding, especially under seismic loading. Inefficiency also appears within the spread footing because of how seismic loads are handled. When dealing with seismic loads, the typical method of design for a shallow foundation is to allow inelastic action to occur within the bridge column for ease of inspection, repair and design. By allowing the inelastic action to occur in the column, conversely, extensive amounts of reinforcement are generally required to keep the response of the footing elastic due to large shear demands at the interface between the column and footing in both the vertical and horizontal directions. Therefore, this type is not commonly used in seismic bridge design practice. Another disadvantage to the spread footing is that the footing must be placed on a competent soil that will not cause significant settlement. Spread footings cannot be used in most bridge locations due to site constraints and the availability of competent soils to support the structure.

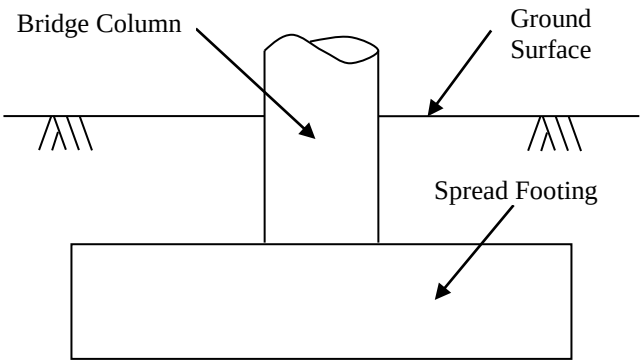

Figure 1-6: Typical configuration of a spread footing

1.3.2 Deep Foundations

When spread footings are not a suitable substructure support, deep foundations are used. Deep foundations use piles or shafts to transmit vertical and horizontal loads to the soil, respectively, through the development of skin as well as tip resistance and passive lateral earth pressure. Deep foundation systems come in many different forms and materials, as depicted in Figure 1-7, with specific advantages and disadvantages to each. For example, pile supported spread footings are generally assumed to maintain elastic behavior below the ground surface unlike a continuous column-foundation shaft, known as drilled or cast-in-drilled-hole (CIDH) shafts, which are typically designed to form inelastic plastic hinges below the ground surface. Differences between types of piles also occur within the placing methods (i.e., driven versus cast-in-place). Unlike driven piles, cast-in-place concrete piles are able to develop an extremely high axial load, as the piles are designed for the ultimate condition. The steel non-displacement driven pile disturbs less soil area during placement, allowing for a better characterization of soil properties and a more economical design. In general, both driven and cast-in-place piles are very advantageous in areas where:

- environmental concerns prohibit excavation,
- weak soils cause excessive settlement,
- spread footings are not cost effective, and
- bridge locations, where deemed appropriate.

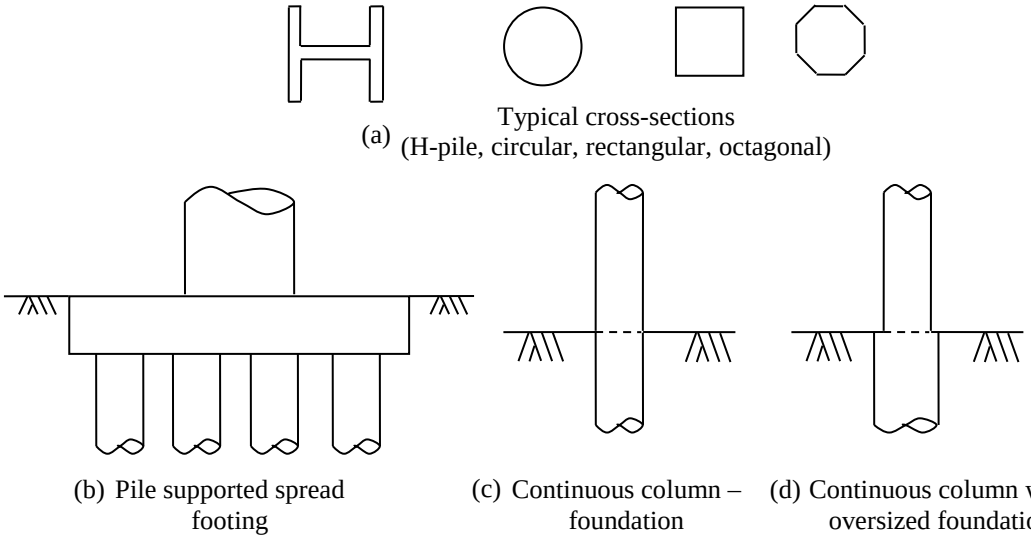

Figure 1-7: Different deep foundation systems

Currently, columns that extend into the ground as cast-in-drilled-hole (CIDH) shafts, as depicted in Figure 1-8, are a common column and foundation system due to the simplicity of construction, elimination of a column to foundation connection and reduced construction costs. The aforementioned benefits continue to make the continuous column-foundation system more desirable to engineers in the bridge design community. Since the nature of the research performed during this project focuses on columns supported by drilled shafts, this foundation type will be the focus for the remainder of the report.

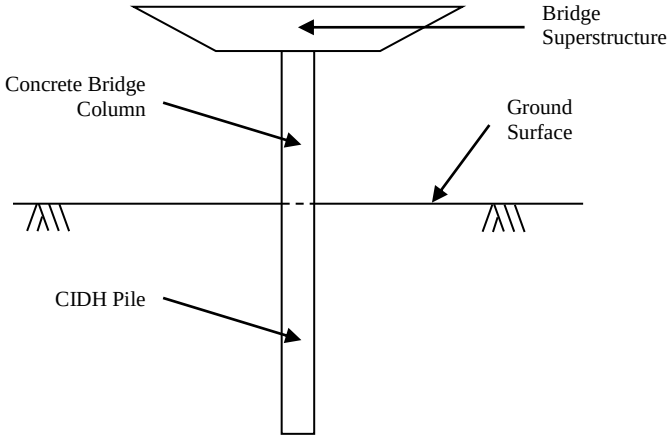

Figure 1-8: Typical bridge bent with a continuous column to cast-in-drilled-hole (CIDH) shaft cross-section down longitudinal axis

1.4 Soil-Foundation-Structure-Interaction

When performing seismic design, accounting for the effects of lateral loading is a critical portion of the design process and must be examined correctly. During the design process of integrated column-foundation systems, such as the one depicted in Figure 1-8, the effects of soil-foundation-structure-interaction (SFSI) further complicate the lateral loading analysis and thus the design methodology. SFSI complicates the process for multiple reasons, but all hinges on one issue—how to correctly model the effects of the soil onto the structural design. A satisfactory approach to capture these effects is by a numerical analysis method that models the soils using nonlinear springs and determines the force-displacement response of piles subjected to lateral loading in soil as well as the overall structural response.

In addition to the complexity of this analysis, soil properties involved in SFSI, especially those near the ground surface, greatly influence the response of a CIDH shaft and the column that it is supporting. Soil located near the ground surface has the greatest influence on the

response of the system, as this is where the soil is providing the largest amount of resistance to lateral movement. The amount of resistance provided within this critical region is the largest area of variability due to the depositional nature of soil, the type of soil present, the stiffness of the soil and the environmental surroundings (e.g., temperature). In addition to providing resistance to lateral movement, soil stiffness along the foundation depth dictates the global and local displacements of the system, the local curvature demand and much more.

The influence of SFSI on the design of continuous column-foundation systems subjected to lateral loading has been researched by numerous people [e.g., Reese et al. (1975), Priestley et al. (1996), Budek et al. (2000), Chai (2002) and Priestley et al. (2007)]. In these studies, researchers were typically looking for a way to better define the response of these systems subjected to a monotonic lateral loading. For example, Reese et al. (1975) improved on the definition of soil springs in cohesive soils; whereas, Chai (2002) expanded the definition of the flexural strength and ductility of an extended pile shaft. No matter what research was undertaken, the end goal was to obtain an accurate representation of the expected lateral response of the column-foundation-soil system. A typical column-pile shaft with its expected displacement, expected moment profile and critical locations is presented in Figure 1-9. The critical locations identified are (1) the maximum moment location, the surrounding area needs the most confinement in seismic design, and (2) the typical fixity point, current models assume the foundation shaft is fully fixed against all deformation at this point.

1.4.1 State of Practice

Today's practice suggests simple and complex methods to account for the effects of SFSI. Although the complex methods involving nonlinear material models and analyses are generally able to capture the realistic lateral load response, they take a considerable amount of time to complete and require a great deal of information about the structure and soil surrounding the foundation shaft. In this approach, it is especially important to accurately represent the soil, as this dictates the response on local and global levels. To reduce the amount of information and time required to account for SFSI, simplified methods [e.g., Chai (2002), Priestley et al. (2007), etc.] are suggested for use in current guidelines and specifications (AASHTO, 2007 and 2009). These simplified methods generally establish an equivalent fixed base cantilever loaded laterally at the column tip without the presence of soil between the fixity location and ground surface. Even though this approach to modeling allows for simple calculations that can be performed in

significantly less time than a more complex approach, these simplified methods do not capture the realistic response depicted in Figure 1-9 and described in Chapter 3.

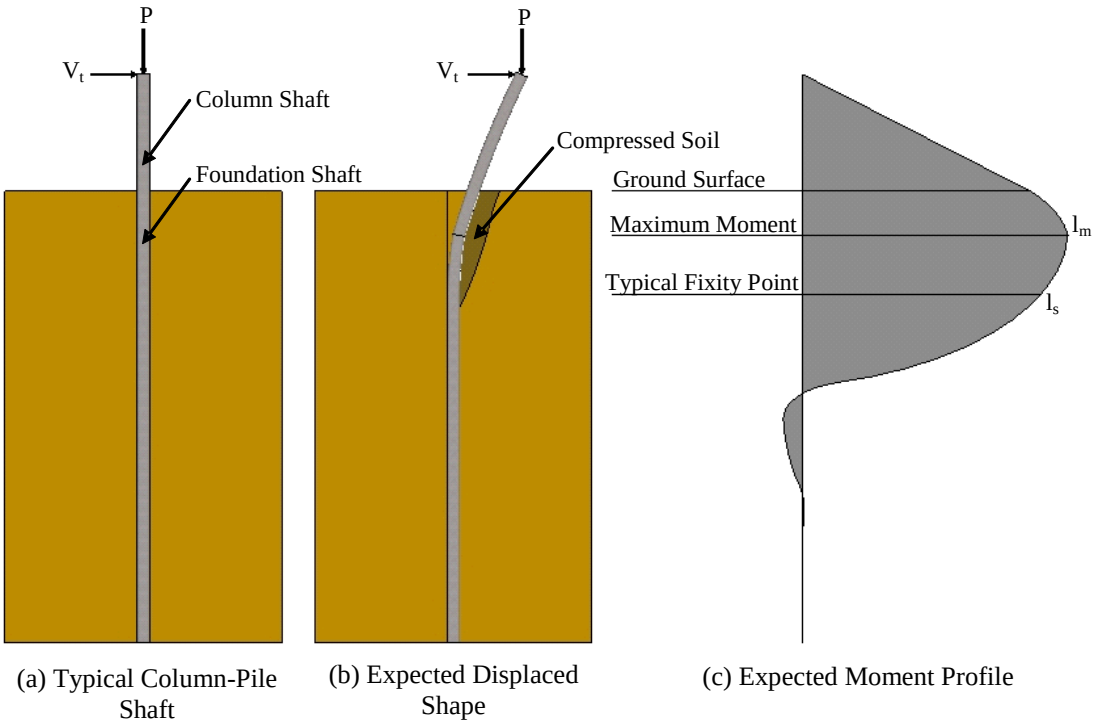

Figure 1-9: Typical lateral load response of a column supported on a CIDH shaft

The first reason why a realistic response is not captured is due to the fact that the base is assumed to be completely fixed against deformation (Figure 1-10). The fully fixed base implies the maximum moment location occurs at this point, and no forces or displacements will occur below this point along the length of the foundation shaft. These implications, however, are not an accurate representation of the system, as forces and displacements are expected to occur at and below this location and must be accounted for correctly (see Figure 1-9 and Figure 1-11).

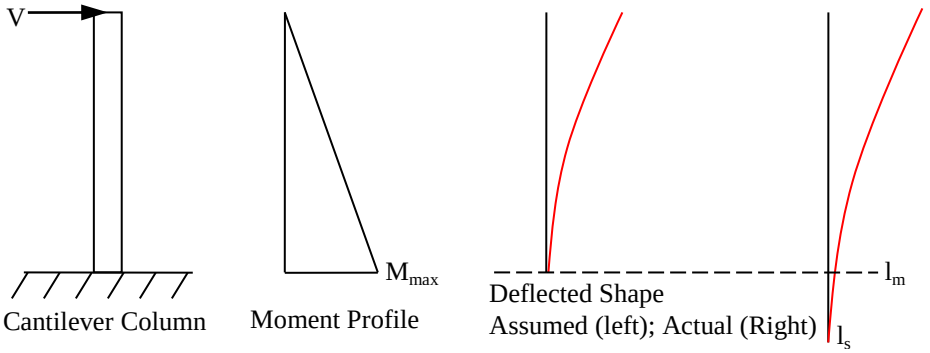

Figure 1-10: Fixed base cantilever with moment and deflection profiles

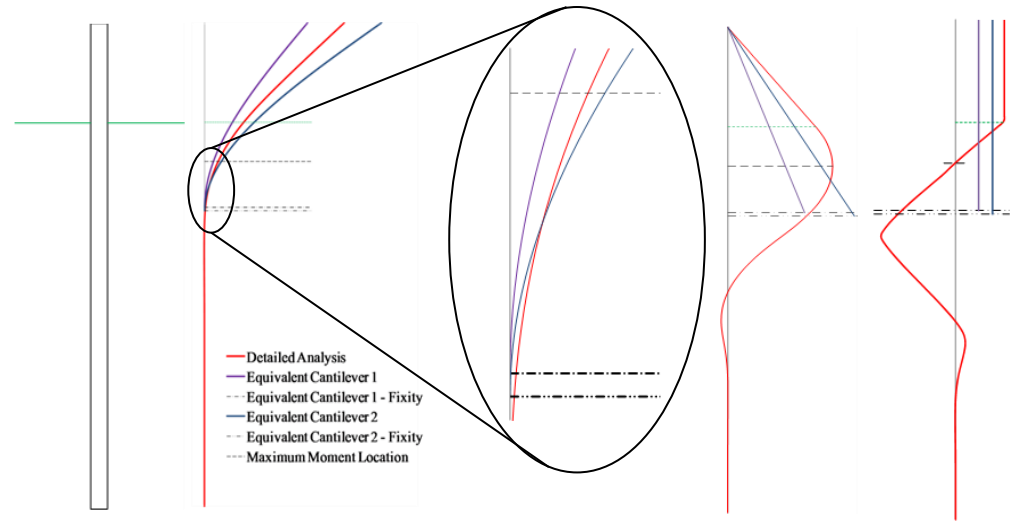

(a) Integrated Shaft (b) Deflection Profile (c) Moment Profile (d) Shear Profile

Figure 1-11: Comparison of equivalent cantilevers with expected response

Besides the challenges associated with capturing the displacement and forces along the length of the column and foundation shafts correctly (see Figure 1-11), a number of other challenges arise in the development and use of models in existence today. The first one stems from the way in which the different models were developed and verified for use in different soil types. The major issue that arises within the verification area is that although the models were developed for both cohesive and cohesionless soils, they were only verified against cohesionless soil experiments. Verifications were performed in this manner due to the ability of a researcher to better control the high variability of soil material properties. Even though the different methods were verified in this manner, they were still suggested for use in cohesive soils although they do not capture the lateral response of integrated systems tested in clay soils (more details in Chapter 3). In addition, verifications were performed in a column of uniform soil which is not a realistic assumption in actual field conditions.

A second challenge associated with the models appears in the defining of the lateral response of a CIDH shaft. The model presented by Chai (2002) suggests that a perfectly plastic response between the yield and ultimate limit states will provide a good estimation of lateral response. This, however, is not accurate as seen in Figure 1-5, where an increase between the yield and ultimate limit states occurs. The increase comes from the combined effects of material nonlinearity in soil, concrete and steel when the column is pushed past the first yield state. In the method suggested by Priestley et al. (2007), the lateral shear forces applied at the top of the

column are not easily determined, since a significant amount of information is needed about damping and the design level earthquake. The last point made within this area is that some of the methods (e.g., AASHTO 2009) are only applicable when all of the materials behave within an elastic manner.

A third concern associated with the development of the existing models is that none of the researchers gave consideration to the effects of seasonal freezing in the construction of their approaches. Although ignored in the development, it is clear that wintry conditions significantly alter the effects of SFSI and they cannot be easily accounted for in the existing models. The effects were previously mentioned with the quick overview of the research performed by Suleiman et al. (2006) and Sritharan et al. (2007) at Iowa State University. These challenges, as well as others, are expanded on in the report that follows in the literature review provided in Chapter 2 and the examination of common methods used in practice provided in Chapter 3.

1.4.2 Alternative Approach

When performing a design or analysis in engineering, a free-body diagram (FBD) is typically used to represent a system and simplify the force and displacement calculations based on known constraints in the system. Using this approach, a FBD was constructed for a column supported on a CIDH shaft (see Figure 1-12a). In this diagram, the effective height of the system, L_{ma}, was taken to be the distance from the column tip to the maximum moment location. This point was chosen for the following reasons:

1. the maximum moment will occur here and this point must be defined for analysis and design purposes,
2. the most confinement will be placed in the area immediately surrounding this point to allow plastic action to form once the foundation shaft exceeds the yielding capacity, and
3. the point is the simplest location to cut the system without having to define multiple locations to account for plastic action and soil stiffness.

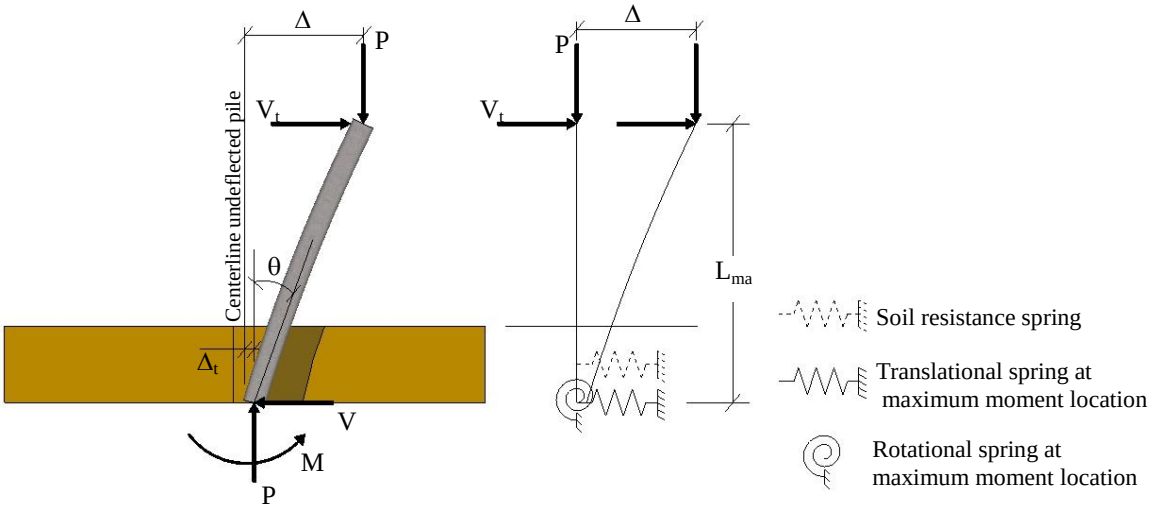

(a) Free-Body-Diagram (b) Proposed Model

Figure 1-12: Alternative approach to accounting for SFSI

By constructing a FBD for this system, one can see that a flexible foundation system and the inclusion of a soil spring, as shown in Figure 1-12b, is more applicable to account for the effects of SFSI. In this approach, the rotational spring located at the maximum moment location would account for the elastic rotations occurring below this point as well as all of the plastic rotations, above and below this point, within the system. The translational spring, as part of the flexible foundation, accounts for the fact that the column-pile shaft system does not experience zero lateral displacement at the maximum moment location. By including this spring, the displacement that forms due to the curvature of the pile below the maximum moment is included in addition to the possibility of a variable shear force along the shaft. The second translational spring accounts for the resistance of the soil to lateral movement above the maximum moment location, providing a more realistic representation. Although one soil spring is depicted, this could be replaced by multiple springs to better define soil properties in this critical region more accurately. Through the inclusion of springs into the proposed model, the effects of soil stiffness are included into their definitions. In the springs at the flexible foundation, for example, the rotation and the lateral displacement will decrease when compared with an equivalent system pushed to the same force at the column tip in a softer soil. In addition, the soil spring would create a larger resistance to lateral movement, causing the global displacement to decrease.

1.5 Scope of Research

In the current state of practice of designing bridges subjected to lateral loading, numerous deficiencies were identified (more details provided in Chapters 2 and 3) at Iowa State University (ISU), especially in the cohesive soil models. The literature review within the current study has found that deficiencies in practice are located in the range of applicable soils, the model verifications, the handling of seasonal temperature effects and the lateral response over the full elastic and inelastic range. Based on the deficiencies noted within today's practices, the current project was undertaken with the overall scope being the development of a simplified model suitable for determining the lateral load response of deep bridge pier foundations in clay that is also able to account for seasonal temperature effects. In order to develop the simplified model, the project focuses on the following objectives:

1. A detailed examination of the current SFSI practice through a literature review.
2. A verification of existing models presented in current codes and the literature review.
3. The development of a simplified equation-based model to capture local and global responses of a continuous column-foundation system in clay with the inclusion of seasonal temperature effects.
4. Modification to existing sand models to account for temperature effects.
5. Ensure that shafts encompassed by steel shells may be adequately handled in the design process.
6. A systematic study on the effects to temperature to the behavior of material properties. This includes an examination of concrete, ASTM A706 steel and soil typical to the state of Alaska.
7. To formulate design and analysis recommendations suitable for continuous column-foundation systems in all soil types while ensuring the ability to handle seasonal temperatures.

1.6 Report Layout

The remainder of the report discusses in detail the aforementioned project. The discussion began with the introduction to the project in this chapter by providing background information and the scope of the research undertaken in this study. The second chapter presents a detailed literature review of the current state of practice for the design and analysis of drilled shafts

subjected to lateral loading during all seasons of the year. Using the information provided within the second chapter, the third chapter provides a comparison of the different methods through example column-foundation systems. The fourth chapter of the report presents a new simplified methodology for the seismic design of drilled shafts in clay soils along with its verification. Chapters five through seven present experimental materials testing performed on concrete, steel and soil in freezing conditions. The eighth chapter provides the design guidelines suggested for use in the design of drilled shafts subjected to a design-level or greater seismic event in seasonally frozen ground. The ninth and final chapter of this report provides the conclusions and recommendations determined upon completion of the project.

CHAPTER 2: LITERATURE REVIEW

2.1 Introduction

In the seismic design and analysis of columns supported on CIDH shafts, SFSI is a component that must be included in any modeling technique. Over the years, researchers are constantly improving the methods of accounting for SFSI through experimental and analytical studies, Table 2-1. The goal of each study normally falls within two categories—improvement or simplification of the soil spring concept (described in Section 2.2.1) used in today's practice.

Table 2-1: Studies on lateral loading of drilled shafts

Researcher	Year	Type of Study	Study Overview
Reese and Welch	1975	Experimental	Development of soil subgrade reaction-displacement curves (p-y curves) in clay soils for use in the Winkler soil spring concept
Crowther	1990	Experimental	Modification of curves by Reese and Welch for use in frozen clay soils
Priestley et al.	1996	Analytical	Determination of inelastic rotation and ductility of a column/foundation shaft in cohesionless soils
Budek et al.	2000	Analytical	Parametric study on the inelastic seismic response of reinforced concrete bridge column/pile shafts in non-cohesive soils to simplify Winkler model. Verified against experimental and in-situ testing.
Chai	2002	Analytical	Analytical model for the flexural strength and ductility of drilled shafts subjected to lateral loads in cohesive and non-cohesive soils
Chai and Hutchinson	2002	Experimental	Experimental testing on full scale drilled shafts in cohesionless soils. Used to verify the analytical model proposed by Chai (2002)
Suleiman et al.	2006	Experimental	Experimental testing on full scale integrated column/foundation systems in cohesive soil to examine the effects of seasonal freezing on the lateral response.
Suarez and Kowalsky	2007	Analytical	Parametric study on cohesive and non-cohesive soils for the displacement-based seismic design of drilled shafts. Verified against experimentation by Chai and Hutchinson (2002)
Sritharan et al.	2007	Analytical	Parametric study to examine the effects of seasonal freezing in clay soils.

Although multiple studies have been performed, a lack of accurate simplified lateral loading models in cohesive soils exists, even though these are typical soils around deep foundations in many parts of the United States, including some regions of Alaska. Concerns with today's methods are due to the way cohesive soil models were verified, their inability to capture seasonal freezing effects, omission of nonlinear material properties after yielding, and the inability to capture the global and local lateral response of CIDH shafts over the elastic and inelastic regions expected at design-level and greater seismic events. The verifications, for example, have been performed using experimentation in cohesionless soils due to the ability of the researcher to better control material properties, although the models are still recommended for cohesive soils. Besides the verification concern, seasonal freezing is a major issue as continuous bridge column/foundation shafts may experience cold temperatures as low as -40 °C (-40 °F) and still need to perform as stipulated by the capacity design principles during a seismic event. Based on the nature of this project and challenges associated with current methods of accounting for SFSI, this chapter will examine today's state of design, analysis and overall behavior of continuous column-foundation systems in a soil medium subjected to seismic loads during all seasons of the year.

2.2 Analytical Investigation

During the examination of the current state of practice, an investigation into the multiple methods available for determining design displacements and the lateral response of bridge columns supported by CIDH shafts was performed. The investigation found that these methods range from simple to complex in both the amount of information needed and the number of steps needed to execute the methods. The remainder of this analytical investigation section will examine in detail some of the more common methods [e.g., Reese et al. (1975), Crowther (1990), Priestley et al. (1996), Applied Technology Council (ATC, 1996), Budek et al. (2000), Chai (2002), Priestley et al. (2007) and American Association of State and Highway Transportation Officials (AASHTO, 2007 and 2009)] used for determining the lateral response of continuous column/foundation systems.

2.2.1 Reese and Welch (1975)

The Winkler foundation method is a very common detailed method in foundation engineering that uses a series of soil springs placed along the shaft length, as depicted in Figure

2-1, to determine the lateral response of drilled shafts. This method breaks down the column/foundation shaft into a series of equal length beam-column elements. Each element is then characterized by specifying the moment resistance and corresponding flexural stiffness, E_cI_{eff}, where E_c is the concrete modulus of elasticity and I_{eff} is the effective moment of inertia of the section. The resistance of the soil surrounding the foundation shaft is then modeled as a series of nonlinear compression-only springs located at the mid-height of each beam-column element. The springs are characterized by a p-y curve in which p defines a soil subgrade reaction (force/length) for a given displacement, y, of the soil. After defining these parameters along with the loading conditions, a finite difference or direct stiffness method is typically followed to complete the numerical calculations. The methods use a numerical iteration process to handle the nonlinear material properties and ensure that equilibrium is obtained between the lateral soil springs, foundation element displacements and foundation element forces. A key component within these methods is to accurately define the resistance of the soil surrounding the foundation shaft through the use of p-y curves. Although soil is highly variable in nature, many researchers have attempted to quantify the lateral resistance of different soils. In clay soils for example, an accepted method to represent the lateral behavior of soil was provided by Reese and Welch (1975).

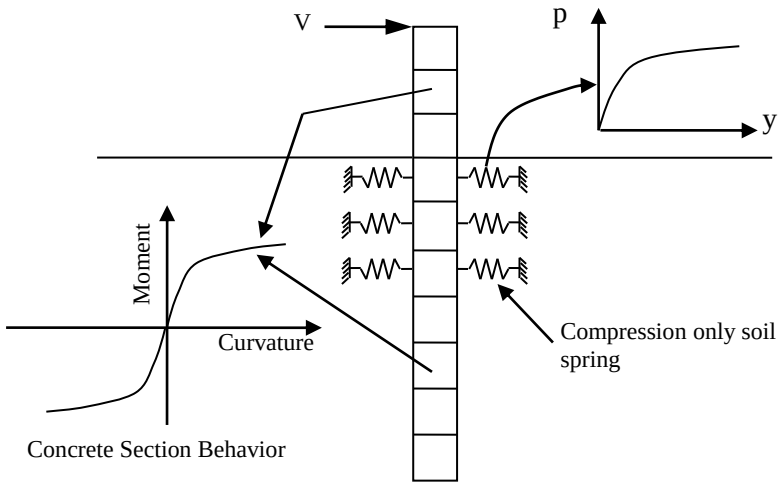

Figure 2-1: Winkler foundation model

In 1975, Reese and Welch performed experimental testing on full scale drilled shafts in a stiff to very stiff red clay (Beaumont clay). The goal of the project was to determine a soil modulus value that could be used in the well known differential equation (Hetenyi 1946), Equation 2-1,

which relates the soil and structure for use in the Winkler foundation system when a deep foundation is loaded laterally. The differential equation is based off of structural equilibrium in the beam-column element shown in Figure 2-2, where M is the applied moment and V_v is the horizontal shear force.

$$EI\frac{d^4y}{dx^4} + P\frac{d^2y}{dx^2} - p = 0;\ p = -E_s y \tag{2-1}$$

where, EI = flexural stiffness of foundation;
y = lateral deflection of beam-column element and soil;
x = length along foundation;
P = axial load on column/foundation shaft
E_s = soil modulus; and
p = soil subgrade reaction.

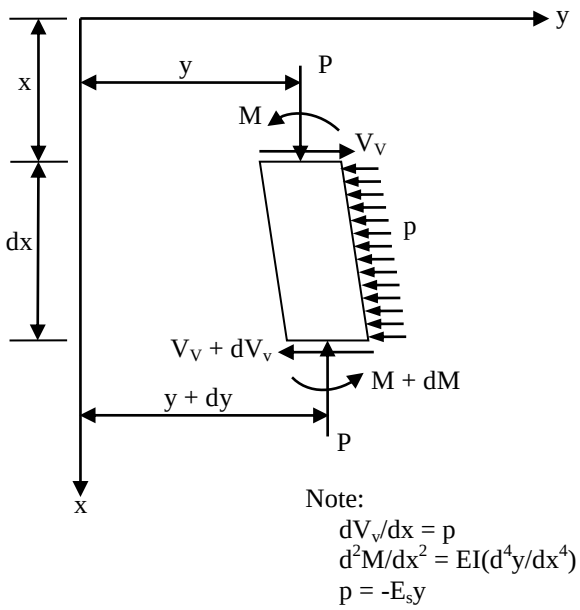

Figure 2-2: Beam-column element used in differential equation derivation

In order to obtain a relationship for the soil modulus, experimental testing was performed ensuring the moment profile along the length of the shaft could be determined. Using the computed moment value, a lateral deflection of the soil and foundation shaft could be determined with a soil reaction at differing depths using standard beam theory from mechanics and numerical iteration processes. After completing analysis of the data, Reese and Welch (1975) found that a power series with the soil reaction, p, normalized with respect to the ultimate soil reaction, p_u, and the soil deflection, y, normalized against the deflection at one-half the ultimate

soil reaction, y_{50}, would provide a good representation of the horizontal soil resistance. Using this relationship, the following procedures were suggested to determine the short-term static p-y curves in clay soils:

1. Obtain the best estimate of variation of undrained shear strength, c_u or s_u, effective unit weight, γ, and strain corresponding to one-half the maximum principal stress difference, ε_{50}, along the length of shaft. If ε_{50} is unavailable, use a value of 0.005 or 0.010 with the larger value being more conservative.
2. Compute the ultimate soil resistance per unit length using the smaller of Equations 2-2 and 2-3.

$$p_u = \left(3 + \frac{\gamma x}{c_u} + 0.5\frac{x}{b}\right) c_u b \quad (2\text{-}2)$$

where, x = depth from ground surface to point of spring
b = width or diameter of foundation

$$p_u = 9 c_u b \quad (2\text{-}3)$$

3. Compute the deflection at one-half the ultimate soil subgrade reaction using Equation 2-4

$$y_{50} = 2.5 b \varepsilon_{50} \quad (2\text{-}4)$$

4. Compute the points describing the p-y curve using Equation 2-5. (Note: $p = p_u$ for all values of y beyond $y = 16y_{50}$)

$$\frac{p}{p_u} = 0.5\left(\frac{y}{y_{50}}\right)^{1/4} \quad (2\text{-}5)$$

A second method was also presented in conjunction with the above procedure, if laboratory testing was performed on soil samples taken from the site. The idea being that the p-y curve can be derived on the basis that it will follow the same shape as the soil stress-strain curve. Using this concept, the p-y curve could be constructed using the relationship shown in Equation 2-6 to find the lateral deflection of the soil, where the exponent z is taken to be one-quarter and Equation 2-5 to find the corresponding soil subgrade reaction.

$$\left(\frac{y}{y_{50}}\right)^{z} = \left(\frac{\varepsilon}{\varepsilon_{50}}\right)^{1/2} \quad (2\text{-}6)$$

2.2.2 Crowther (1990)

A key part in constructing the p-y curves for soils is to ensure that an appropriate exponent is used on the deflection criteria in the model produced by Reese and Welch (1975). Crowther

(1990) examined the prediction of lateral displacements in frozen layered soils. The investigation included the use of data obtained from testing performed by Weaver and Morgenstern (1981) as well as Sayles and Haines (1974). During the study, Crowther demonstrated that by modifying the exponent, z, in Equation 2-6, to a value of 0.33, a satisfactory performance could be obtained in frozen clays. This modification is important to this project as the new methodology must be able to handle seasonally cold temperatures.

2.2.3 Priestley et al. (1996)

Priestley et al. (1996) suggested the plastic hinge length and depth of plastic hinge follow a hyperbolic trend related to a normalized value based on the flexural stiffness, EI_{eff}, of the foundation shaft and a soil subgrade modulus, K. The graphs, Figure 2-3, presented in this reference were an initial portion of the work that would be later published by Budek et al. (2000). Although the trends were initially suggested for soils, in general, the research published later states that the trends were developed and verified only for cohesionless soils. The aforementioned graphs, therefore, are not recommended for use in the modeling of a cohesive soil. Additionally, the text in which these graphs were presented does not suggest a method on their use in the design of continuous column/foundation systems. The only suggestion provided for handling a bridge column that extends into the ground as a CIDH shaft was to perform an elastic analysis and shift the location of the maximum moment towards the ground surface. The upwards shift was stated to be 30% of the total depth predicted by an elastic analysis.

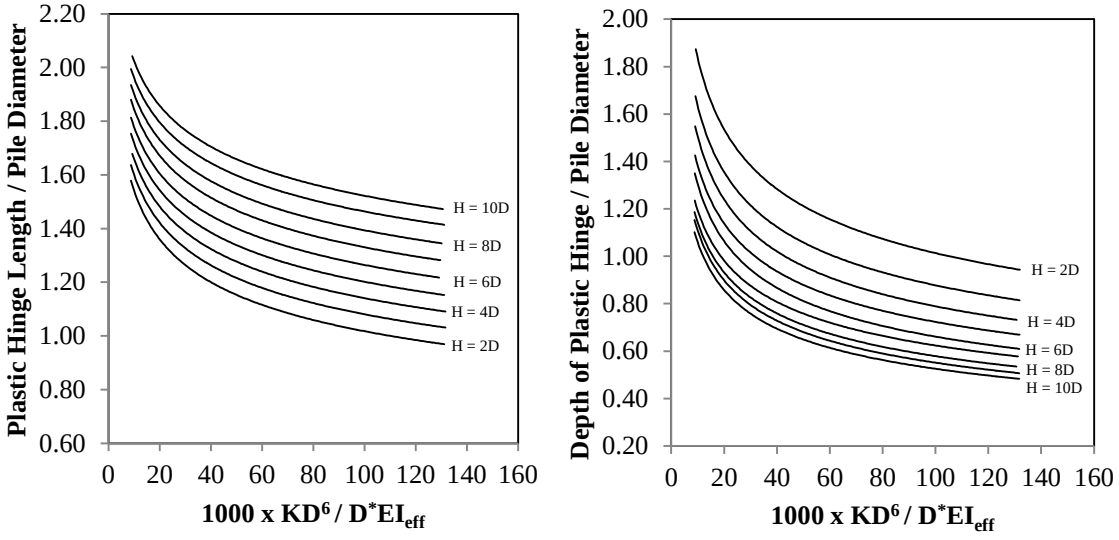

Figure 2-3: (a) Plastic hinge length; (b) depth to plastic hinge location [Reproduced from Budek et al., 2000]

2.2.4 Chai (2002)

Chai proposed a model to determine the lateral response of extended pile shafts while accounting for the effects of soil. The model relies on the use of two points, fixity and maximum moment, along the length of the system in order to determine the systems flexural strength and ductility. A visual representation of the model and the two points defining the fixity and the maximum moment locations used to determine the lateral loading and displacements of the column/foundation system in a uniform layer of soil, cohesive or non-cohesive, are shown in Figure 2-4.

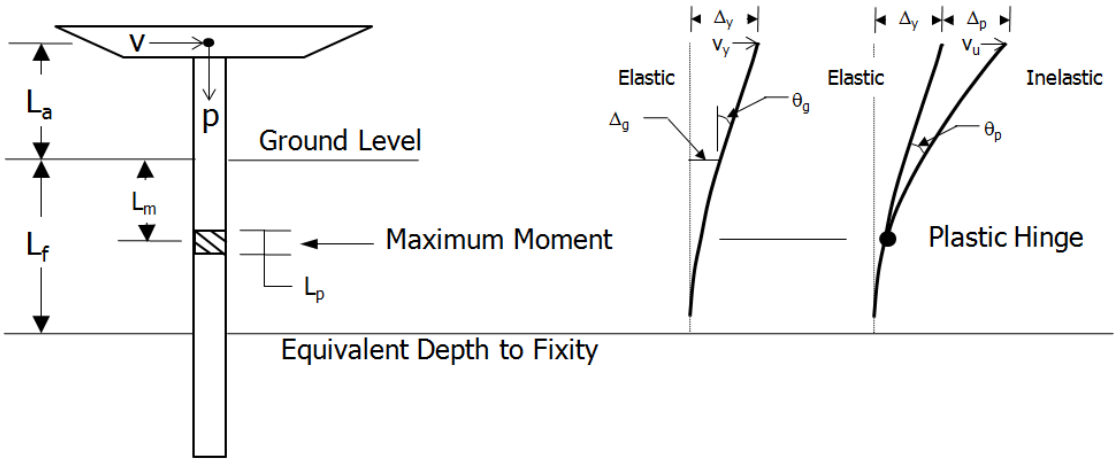

Figure 2-4: Equivalent fixed-base cantilever (after Chai 2002)

Chai began the development of the model by determining the point of fixity over the elastic and inelastic regions, which would relate the stiffness of a soil-pile system, K_{sp}, to the stiffness of an equivalent fixed-base cantilever, K_c. The stiffness of the cantilever is defined as the shear force, V, applied at the top of the column divided by the lateral displacement at the top of the cantilever, Δ. The stiffness expression was further expanded into Equation 2-7 using principles of mechanics.

$$K_c \equiv \frac{V}{\Delta} = \frac{3EI_e}{(L_f + L_a)^3} \qquad (2\text{-}7)$$

where, EI_e = effective flexural rigidity of the cantilever;
L_f = equivalent depth-to-fixity; and
L_a = above ground height of the column.

Cohesive Soil

In order to relate the equivalent cantilever system to the soil-pile system in a cohesive soil the closed form solution to ground movement (see Equations 2-8 and 2-9) of a long pile subjected to lateral loading produced by Poulos and Davis (1980) was used.

$$\Delta_g = displacement\ at\ ground\ level = \frac{V(L_a+\sqrt{2}R_c)}{k_h R_c^2} \tag{2-8}$$

where, $R_c = pile\ characteristic\ length = \sqrt[4]{\frac{EI_e}{k_h}}$; and

$k_h = constant\ modulus\ of\ subgrade\ reaction = 67 s_u$

$$\theta_g = rotation\ of\ pile\ at\ ground\ level = \frac{V(\sqrt{2}L_a+R_c)}{k_h R_c^3} \tag{2-9}$$

The closed form solution was added to the above ground cantilever displacement, Δ_{La}, to develop Equation 2-10, which defines the total displacement of the soil-pile system, Δ_{sp}, within the elastic region.

$$\Delta_{sp} = \Delta_g + \theta_g L_a + \Delta_{L_a} \tag{2-10}$$

where, $\Delta_{L_a} = \frac{VL_a^3}{3E_c I_e}$; and

I_e = effective moment of inertia of the foundation shaft.

After obtaining the total displacement of the soil-pile system, its lateral stiffness can be determined. At this point, K_c and K_{sp} are set equal to one another, thus locating the equivalent point of fixity. In order to efficiently equate the two stiffness terms, the above ground height and depth to fixity were defined in terms of the characteristic length of the pile (i.e., $L_a = \xi_a R_c$ and $L_f = \xi_f R_c$, where ξ_a and ξ_f are coefficients for the above ground height and equivalent depth-to-fixity, respectively). The soil-pile system stiffness can be written as shown in Equation 2-11 with the coefficient for the equivalent depth-to-fixity being computed through Equation 2-12.

$$K_{sp} = \frac{3k_h R_c}{3\sqrt{2}+6\xi_a+3\sqrt{2}\xi_a^2+\xi_a^3} \tag{2-11}$$

$$\xi_f = \sqrt[3]{4.24 + 6\xi_a + 4.24\xi_a^2 + \xi_a^3} - \xi_a \tag{2-12}$$

Once the point of fixity is located, the maximum moment location is also needed in order to determine the ductility capacity of the system. Using a modified version of Broms (1964a) soil pressure distribution acting on the pile (see Equation 2-13), shear and moment relationships are

developed based off of static equilibrium of horizontal forces and bending moments. The shear and moment relationships are presented in Equation 2-14 and Equation 2-15, respectively.

$$p_u(z)=\begin{cases}\frac{1}{27}c_u\left[54+84\frac{z}{D}-7\left(\frac{z}{D}\right)^2\right] & \text{for } z\leq 6D \\ 11.3c_u & \text{for } z>6D\end{cases} \quad (2\text{-}13)$$

where, z = depth below the ground surface; and
D = pile diameter

$$V_u^* = 2L_m^* + \frac{14}{9}L_m^{*\,2} - \frac{7}{81}L_m^{*\,3} \quad for \;\; L_m^* \leq 6 \quad (2\text{-}14)$$

where $L_m^* = normalized\ depth\ to\ maximum\ moment = \frac{L_m}{D}$; and

$$V_u^* = normalized\ lateral\ strength\ of\ soil - pile\ system = \frac{V_u}{c_u D^2};$$

$$M_{max}^* = 2L_a^* L_m^* + \left(1 + \frac{14}{9}L_a^*\right)L_m^{*\,2} + \frac{7}{81}(12 - L_a^*)L_m^{*\,3} - \frac{7}{108}L_m^{*\,4} \; for \; L_m^* \leq 6 \quad (2\text{-}15)$$

where, $L_a^* = normalized\ aboveground\ height = \frac{L_a}{D}$; and

$$M_{max}^* = normalized\ flexural\ strength\ of\ pile = \frac{M_{max}}{c_u D^3}$$

The normalized depth to maximum moment and ultimate lateral strength of the system can now be determined using an idealized elasto-plastic moment-curvature response established for the cross-section of the foundation shaft.

Cohesionless Soil

Similar to the cohesive soil model, Chai produced a cohesionless soil model using the work of Poulos and Davis (1980) in non-cohesive soils to relate the stiffness of the soil to that of an equivalent cantilever system. This was done through the closed form solution proposed in Poulos and Davis (1980) that relates ground movement and ground rotation to lateral load (see Equations 2-16 and 2-17)

$$\Delta_g = displacement\ at\ ground\ level = \frac{V}{EI_e}[2.40R_n^3 + 1.60R_n^2 L_a] \quad (2\text{-}16)$$

where, $R_n = pile\ characteristic\ length = \sqrt[5]{\frac{EI_e}{n_h}}$; and

$$n_h = rate\ of\ increase\ of\ modulus\ of\ horizontal\ subgrade\ reaction = k_h/z$$

$$\theta_g = rotation\ of\ pile\ at\ ground\ level = \frac{V}{EI_e}[1.60R_n^2 + 1.74R_n L_a] \quad (2\text{-}17)$$

Using the process described in the cohesive soil section, the soil-pile system stiffness and the coefficient for the equivalent depth to fixity are defined in Equations 2-18 and 2-19.

$$K_{sp} = \frac{EI_e}{R_n^3} \frac{1}{\left[2.4+3.2\xi_a+1.74\xi_a^2+\xi_a^3/3\right]} \quad (2\text{-}18)$$

$$\xi_f = \sqrt[3]{7.2 + 9.6\xi_a + 5.22\xi_a^2 + \xi_a^3} - \xi_a \quad (2\text{-}19)$$

where, $L_f = \xi_f R_n$ and $L_a = \xi_a R_n$

In order to complete these computations the rate of change of the horizontal modulus of subgrade reaction must be known. Chai (2002) suggested the use of a chart presented in ATC-32 (1996), provided herein as Figure 2-5. This figure establishes the coefficient as a function of the relative density, D_r, and the friction angle, ϕ_{bar}, of cohesionless soil. Based on the assumption this value should be determined at the working load, the chart value was suggested to be divided by a value of four for larger seismic considerations.

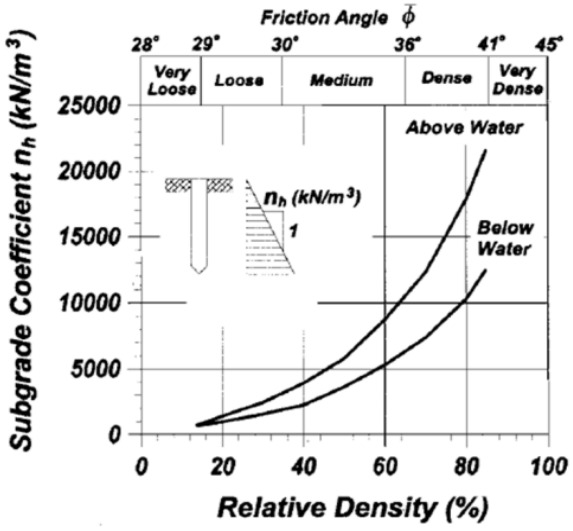

Figure 2-5: Subgrade coefficient and effective friction angle of cohesionless soils (ATC-32, 1996)

Once the effective point of fixity has been established, the maximum moment location is defined to establish the ductility capacity of the system. This process was undertaken by using the soil pressure distribution along the length of the pile suggested by Broms (1964b) (see Equation 2-20) and the principles of static equilibrium. The principle of horizontal equilibrium and zero shear force at the maximum moment location defines Equation 2-21; while the principle of bending moment equilibrium defines Equation 2-22. By solving these two equations

simultaneously, the normalized depth to maximum moment and lateral strength are obtained (see Equations 2-23 and 2-24)

$$p_u(z)=C\sigma_v^{'}(z)K_p \tag{2-20}$$

where, C = coefficient suggested by Broms (1964b) = 3

K_p = Rankine lateral earth pressure coefficient = $\frac{1+\sin(\emptyset_{bar})}{1-\sin(\emptyset_{bar})}$

σ'_v = vertical effective overburden stress = γ'*z

γ' = effective unit weight of the soil

z = depth to point of examination below ground surface

$$L_m=\sqrt{\frac{2V_u}{CK_p\gamma^{'}D}} \tag{2-21}$$

where, L_m = depth to maximum moment

V_u = lateral strength of pile-shaft system

D = foundation shaft diameter

$$M_{max}=V_uL_a+\sqrt{\frac{8V_u^3}{9CK_p\gamma^{'}D}} \tag{2-22}$$

where, M_{max} = maximum flexural strength of foundation shaft

$$L_m^* = \frac{1}{2}\left[\frac{(L_a^*)^2}{p} - L_a^* + p\right] \tag{2-23}$$

where, L_m^* = normalized depth-to-maximum moment = L_m/D

L_a^* = normalized aboveground height = L_a/D

$$p = \sqrt[3]{\frac{12}{C}M_{max}^* - (L_a^*)^3 + \sqrt{\frac{24}{C}M_{max}^*\left(\frac{6}{C}M_{max}^* - (L_a^*)^3\right)}}$$

$$M_{max}^* = M_{max}/K_p\gamma' D^4$$

$$V_u^* = \frac{C}{2}(L_m^*)^2 \tag{2-24}$$

where, $V_u^* = V_u/K_p\gamma' D^3$

Kinematic Model

After defining the critical locations and ultimate lateral strength of the soil-pile system, the kinematic model was developed. In this model, Chai (2002) proposed that a perfectly plastic response between the yield and ultimate conditions be assumed for the force-displacement response of the equivalent fixed-base cantilever as shown in Figure 2-6. Using the aforementioned assumptions, the displacement ductility, μ_Δ, of the system and curvature ductility, μ_ϕ, of the foundation shaft are related, allowing the curvature demand for the

foundation shaft to be determined based off of the desired displacement ductility of the system. To determine the yield displacement, Δ_y, for use in finding the ductility, two relationships for the ultimate lateral force, V_u, were equated and rearranged to find the lateral yield displacement. They are presented below as Equations 2-25 and 2-26.

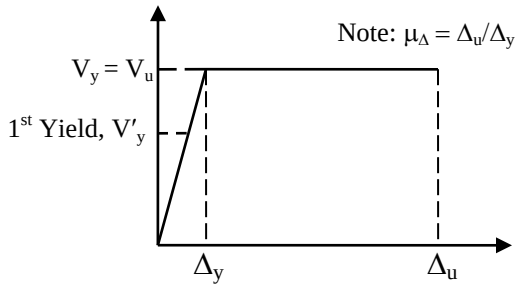

Figure 2-6: Assumed perfectly plastic response between yield and ultimate conditions

$$V_u = \begin{cases} \frac{3EI_e}{\left(L_a^* + L_f^*\right)^3 D^3}\Delta_y \\ \frac{M_{max}}{M_{max}^* D} V_u^* \end{cases} \quad (2\text{-}25)$$

$$\Delta_y = \frac{\phi_y}{3}\frac{\left(L_a^* + L_f^*\right)^3 V_u^* D^2}{M_{max}^*} \quad (2\text{-}26)$$

where, ϕ_y = equivalent elasto-plastic yield curvature.

The plastic displacement, Δ_p, of the system is the final portion needed to determine the ultimate displacement, Δ_u, and therefore the displacement ductility of the system. The plastic action is found by assuming that all of the plastic rotation, θ_p, is concentrated at the maximum moment location and equal to the plastic curvature, ϕ_p, multiplied by the length of the plastic hinge, L_p. The plastic curvature is defined as a curvature, ϕ, beyond the yield point minus the idealized yield curvature. Chai then normalized the plastic displacement equation with respect to the column diameter leading to the final relationship depicted in Equation 2-18.

$$\Delta_p = \theta_p(L_a + L_m) = \lambda_p \phi_p (L_a^* + L_m^*) D^2 \quad (2\text{-}27)$$

where, $\theta_p = (\phi - \phi_y)L_p = \phi_p L_p$; and

λ_p = normalized plastic hinge length = L_p/D

Using the yield and plastic displacements, the displacement ductility of the system was related to the demand curvature ductility. The final relationship for the displacement ductility suggested by Chai (2002) is presented in Equation 2-19.

$$\mu_\Delta = 1 + 3\lambda_p\left(\mu_\phi - 1\right)\frac{\left(L_a^* + L_m^*\right)}{\left(L_a^* + L_f^*\right)^3}\frac{M_{max}^*}{V_u^*} \tag{2-28}$$

The normalized plastic hinge length in the model is a key component within the analysis, since this plays a significant role in determining the ultimate displacement of the soil-pile system. As stated in Section 2.2.3, previous research found the plastic hinge length varies with the lateral stiffness of the soil surrounding the foundation shaft; however, this was shown to be inaccurate in a companion paper to the analytical model presented by Chai (2002). This companion paper by Chai and Hutchinson (2002) found that the plastic hinge length was insensitive to the lateral stiffness of the soil through an experimental investigation. The experimental investigation was performed on four full-scale columns to drilled shaft systems in cohesionless soils of different densities and as shown later in Chapter 4. During the analysis of the data, the plastic hinge length was found to primarily depend on the aboveground height of the column. Using the results of this experimentation, Chai suggests that a plastic hinge length varying from 1.0D at ground level to 1.6D at an aboveground column height of L_a = 6D. After this point, the plastic hinge length is assumed to be constant for all other aboveground column heights. The suggested relationship for both cohesive and cohesionless soils is shown as a function of the normalized aboveground height in Equation 2-29 and graphically in Figure 2-7.

$$\lambda_p = \frac{L_p}{D} = \begin{cases} 1 + 0.1\frac{L_a}{D} \quad for\ \frac{L_a}{D} \le 6 \\ 1.6 \quad for\ \frac{L_a}{D} > 6 \end{cases} \tag{2-29}$$

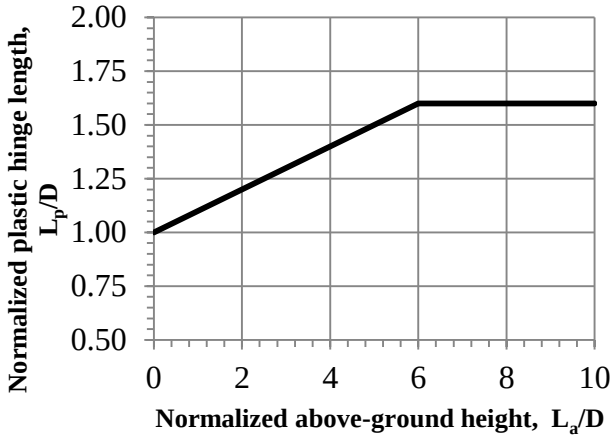

Figure 2-7: Assumed equivalent plastic hinge length of concrete CIDH shafts (after Chai, 2002)

Although Chai's model was verified experimentally by Chai and Hutchinson (2002), some limitations are noted for this model and its verifications. The first limitation with the model is the verification was performed only within a uniform layer of experimentally constructed cohesionless soils, although recommended for both cohesive and non-cohesive soils. This would ensure the model accurately represents a cohesionless soil, but it does not verify the validity of the cohesive soil model. The making of the soil properties in the testing chamber is a point of concern, as this does not represent a realistic field application. The second challenge associated with the model is that a perfectly plastic response between the yield and ultimate conditions was assumed for the lateral response of the system. The perfectly plastic response is an inaccurate representation of actual conditions because it does not account for the strength gains accrued due to the combined effects of soil and material nonlinearity in the plastic region of lateral loading. The third limitation noted is that multiple locations, apparent fixity and maximum moment, are needed to define the global response of the system. By needing multiple points to define the system, the model cannot be easily input into a structural analysis program and used as part of the full analysis of the structure when dealing with the formation of nonlinear components during a seismic event. If the model is input into structural analysis software, the maximum moment will form at the fixity location and cause the plastic displacements components to be located from this point. This, however, is an inaccurate representation and is the reason two points were used to define the overall response of the system. Further examination of this model is presented in Chapter 3 to identify other challenges associated with the use of this model.

2.2.5 Priestley et al. (2007)

In 2007, Priestley et al. published a textbook on displacement-based seismic design of structures. The book covers multiple types of structures, steel to concrete and buildings to bridges, including the topic of bridge columns that extend into the ground as CIDH shafts. During the presentation of the aforementioned topic area, a model was introduced by Priestley et al. (2007) to determine the design displacement of a column/foundation system, including the effects of SFSI, which is discussed in detail in the remainder of this section. A visual depiction of the terminology used within this method is presented in Figure 2-8, where $H_{cp} = 0$ when a pinned connection to the superstructure exists.

The method introduced in Figure 2-8 for handling soil-structure-interaction is a variation of the displacement-based design model suggested by the authors for use in a bridge column

supported on an isolated footing. For a shaft supported bridge column, the design displacement is determined by adding the yield displacement to the plastic displacement. The yield displacement for a shaft supported column is presented in Equation 2-30, where C_1 is a constant dependent on end-fixity; H is the effective height of the column; and L_{sp} is a length used to account for the effects of strain penetration when appropriate.

$$\Delta_y = C_1 \phi_y \left(H + L_{sp}\right)^2 \tag{2-30}$$

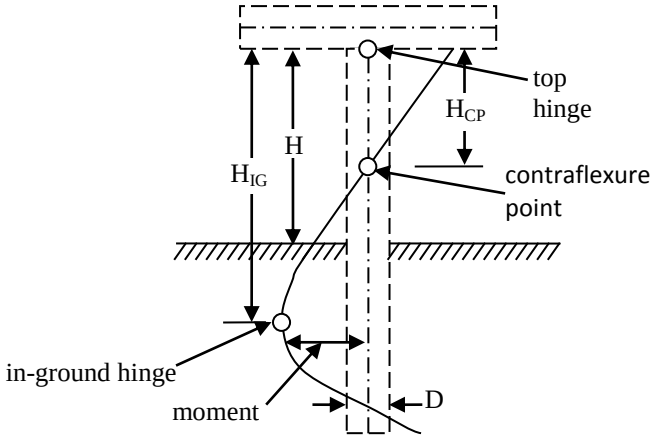

Figure 2-8: Moments in pile/column system (after Priestley et al., 2007)

Priestley et al. (2007) suggested the yield displacement is modified such that strain penetration is conservatively neglected and the effective column height is taken as the distance from the in-ground plastic hinge to the top of the column in a pinned connection to the superstructure, Equation 2-31.

$$\Delta_{y,IG} = C_1 \phi_y H_{IG}^2 \tag{2-31}$$

If a fixed connection is present at the level of the superstructure, the top hinge will dictate the design displacement and modifications must be made to Equation 2-30. These modifications include changing the coefficient for end fixity conditions to account for the superstructure flexibility of a fixed superstructure, replacing the effective height of the system with the depth to the point of in-ground hinging, and using strain penetration effects. The new relationship is presented below as Equation 2-32.

$$\Delta_{y,F} = C_1 \phi_y \left(H_{IG} + L_{sp}\right)^2 \tag{2-32}$$

The modifications to the pier supported system were proposed based off of an analytical parametric study performed by Suarez and Kowalsky (2007) on the effects of SFSI on drilled shafts. For cohesive soils, two different undrained shear strengths, c_u = 20 kPa and 40 kPa (420 psf and 840 psf), were examined. An analysis of the data led to Equation 2-33, for locating the in-ground hinge, as well as Equation 2-34, for modifying the coefficient that accounts for end-fixity conditions, based off of the undrained shear strength parameter and head fixity. In addition to the cohesive soil, two types of cohesionless soils were investigated. These analyses were performed in soils with an effective friction angle of $\phi = 30°$ and $\phi = 37°$. By examining the results, the authors developed Equation 2-35 for locating the in-ground hinge and Equation 2-36 for modifying the coefficient that accounts for end-fixity conditions based on the effective friction angle.

$$\frac{H_{IG}}{D} = \begin{cases} 6.38 + 0.69\frac{H}{D} & for\ c_u = 20kPa\ (420\ psf) \\ 4.96 + 0.71\frac{H}{D} & for\ c_u = 40kPa\ (840\ psf) \end{cases} \quad (2\text{-}33)$$

$$C_1 = \begin{cases} 1.840 - 0.363ln\left(\frac{H}{D}\right) & for\ c_u = 20kPa\ (420\ psf) \\ 1.767 - 0.360ln\left(\frac{H}{D}\right) & for\ c_u = 40kPa\ (840\ psf) \\ 0.447 - 0.055ln\left(\frac{H}{D}\right) & for\ fixed\ head \end{cases} \quad (2\text{-}34)$$

$$\frac{H_{IG}}{D} = \begin{cases} 4.39 + 0.82\frac{H}{D} & for\ \emptyset = 30° \\ 3.40 + 0.84\frac{H}{D} & for\ \emptyset = 37° \end{cases} \quad (2\text{-}35)$$

$$C_1 = \begin{cases} 1.187 - 0.223ln\left(\frac{H}{D}\right) & for\ \emptyset = 30° \\ 1.137 - 0.230ln\left(\frac{H}{D}\right) & for\ \emptyset = 37° \\ 0.310 - 0.030ln\left(\frac{H}{D}\right) & for\ fixed\ head \end{cases} \quad (2\text{-}36)$$

After determining the modifications as presented above, the design displacements are computed for the column/foundation system using the following procedures:

1. Locate the in-ground plastic hinge using Equation 2-33 or Equation 2-35.
2. Determine the yield and ultimate limit state curvatures of the foundation shaft, ϕ_y and ϕ_u, using equations presented by Priestley et al. (2007) for the yield limit state and damage-control limit strains of concrete and steel to find the appropriate ultimate limit state curvature, ϕ_{ls}.

3. Find the analytical plastic hinge length, L_p, based off the head fixity conditions. For a pinned condition, use the plastic hinge length presented in Section 2.2.4 as suggested by Chai (2002). For a fixed head condition, use Equation 2-37.

$$L_p = kH_{cp} + L_{sp} \geq 2L_{sp} \quad (2\text{-}37)$$

where, $k = 0.2\left(\frac{f_u}{f_y} - 1\right) \leq 0.08$;

$$L_{sp} = \begin{cases} 0.022 f_{ye} d_{bl} & for\ f_{ye}\ in\ MPa \\ 0.15 f_{ye} d_{bl} & for\ f_{ye}\ in\ ksi \end{cases};$$

f_u = ultimate stress of flexural reinforcement;
f_y = yield stress of flexural reinforcement;
f_{ye} = expected yield stress of CIDH shaft longitudinal reinforcement; and
d_{bl} = diameter of CIDH shaft longitudinal reinforcing bars.

4. Determine the end-fixity coefficient, C_1, using Equation 2-34 or Equation 2-36.
5. Find the yield displacement using Equations 2-31 and 2-32 depending on head fixity conditions.
6. Find the design displacement, Δ_D, using Equation 2-38 for the pinned head condition or Equation 2-39 for the fixed head condition.

$$\Delta_D = \Delta_{y,IG} + (\phi_{ls} - \phi_y) L_p H_{IG} \quad (2\text{-}38)$$

$$\Delta_D = \Delta_{y,F} + C_3(\phi_{ls} - \phi_y) L_p H_{IG} \quad (2\text{-}39)$$

where, C_3 = coefficient to account for changing moment pattern = 1.54

The method presented within this section appears to have limitations. The first limitation of this model for cohesive soils is that it is only applicable to soils in a limited range of undrained cohesive strengths, c_u = 20 kPa (420 psf) and 40 kPa (840 psf). The limited range is a concern as stiff cohesive soils could reach undrained shear strengths as high as 400 kPa (8350 psf). In addition, the cohesionless soil model is only applicable to the two effective friction angles of ϕ = 30° and ϕ = 37°. Although these are typical extremes, no information is presented as how to handle soils with effective friction angles between these two extremes. The next challenge associated with this method is the verification of the model was performed by Suarez and Kowalsky (2007) only for cohesionless soils by using the experimental data produced by Chai and Hutchinson (2002), which used a uniform Nevada sand as the soil media with a friction angle of 38°. The third limitation arises because the lateral shear demands at the top of the

column are not easily produced by the model, unless information regarding the viscous damping of the soil is known. The lack of this information means that a bilinear force-deflection curve cannot be easily established.

2.2.6 AASHTO Specifications

In the United States of America, bridge design is generally governed by the current specifications and interim revisions published by the American Association of State and Highway Transportation Officials (AASHTO). The code being used in this report, based on the start time of this project, was published in 2007 with interim revisions updated yearly to maintain changes while the next code is being developed. Within the AASHTO specifications (2007), two methods are deemed appropriate to ensure an adequate displacement capacity is provided for laterally loaded foundation shafts. Both methods require an extensive knowledge about the subsurface surroundings as well as an iterative process that is not easy to perform using hand calculations.

The first of the two methods is to perform an analysis using the Winkler foundation method previously presented in Section 2.2.1. The second method suggested for use is the strain wedge model. This model uses an iterative process to relate the one-dimensional beam on an elastic foundation to that of an envisioned three-dimensional passive wedge of soil that will form on the front of a pile (see Figure 2-9) when pushed laterally (Ashour et al., 1998). Although both methods have been shown to accurately represent the behavior of laterally loaded CIDH shafts, the models require knowledge about the pile and surrounding soil (e.g., moist unit weight, friction angle, material strengths, pile dimensions, etc.) to complete numerous iterations to within the inelastic displacement range.

In an attempt to update the specifications used for the LRFD seismic design of bridges, AASHTO recently published guidelines (AASHTO, 2009) that may be used in conjunction with the previously discussed specifications. The new guidelines present multiple methods, from simple to complex, for determining the lateral response of pile foundations based on site location, bridge design and site importance. Many of the models suggested in the main guidelines and commentary have already been discussed. Within the main commentary, the detailed method suggested for use is the Winkler foundation system presented in Section 2.2.1. The simple methods presented within the commentary were those proposed by Chai (2002) and Priestley et al. (2007), and they were previously discussed in Sections 2.2.4 and 2.2.5,

respectively. Despite the limitations and shortcomings of these methods, each method was suggested for use in both cohesive and non-cohesive soils as specified by the authors.

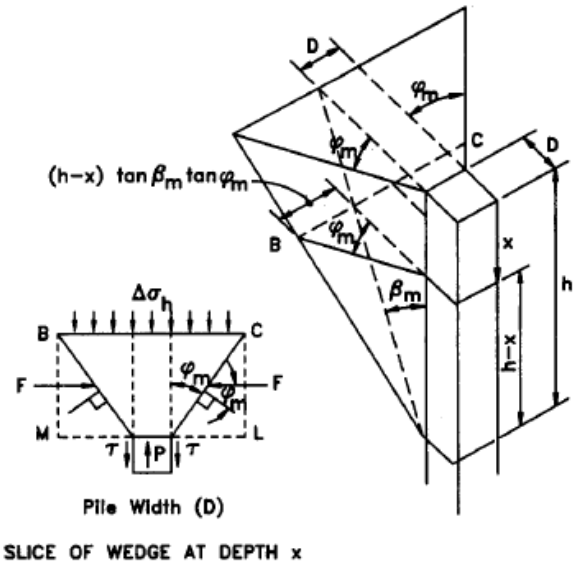

Figure 2-9: Basic strain wedge theory model in a uniform soil (Ashour et al., 1998)

The final method presented within the new guidelines is to determine the effective point-of-fixity for the soil-shaft system to establish an elastic system void of any soil above the fixity location. This method is suggested within the main guidelines and uses an empirical equation to locate the effective point-of-fixity which can then be related to an equivalent cantilever system modeled without any surrounding soil and the base being fully constrained from deformation similar to Chai (2002). The top of the equivalent cantilever system is modeled based on the constraints imposed by the bridge superstructure. In order to locate the equivalent point of fixity, Equation 2-40 was proposed for use in a uniform layer of cohesive soil. A second approach is suggested for a uniform layer of cohesionless soil, but is not presented here. The empirical equation was found based on the research performed by Davisson and Robinson (1965).

$$L_f = 1.4\left(\frac{E_p I_w}{E_s}\right)^{0.25} \quad (2\text{-}40)$$

where, E_p = modulus of elasticity of pile (ksi);
E_s = soil modulus for clays = $0.465c_u$ (ksi);
I_w = weak axis moment of inertia for pile shaft (ft^4); and
c_u = undrained shear strength of clays (ksf).

The main limitation associated with the effective fixity model is the maximum moment will develop at the point of fixity and is only applicable within the elastic range of loading. However, the maximum moment will not occur at the point of fixity but rather between this point and the ground surface. The location of the maximum moment is critical, as this will determine the region at which the most damage will occur within the system and where confinement reinforcement is required to maintain an adequate response of the concrete foundation shaft due to seismic loading. Furthermore, the moment profile of the point of fixity models will not be the same as that expected for the soil-foundation-structure system, leading to erroneous information about lateral displacements. When compared with Chai (2002) and Priestley et al. (2007), this method is much simpler to perform, but it is only applicable in the elastic region of loading experienced by the column/foundation system (i.e., when displacement demands are being determined).

2.3 Impact of Seasonal Freezing

As noted previously, some of the largest earthquakes recorded in the history of the United States and the world have taken place during winter months. Examples include the New Madrid earthquake sequence of 1811-1812, the Great Alaska earthquake of 1964 (M_L = 9.2), the Nisqually earthquake of 2001 (M_L = 6.9) in Washington, and several large magnitude Hokkaido earthquakes in Japan. Although the occurrence of major future earthquakes cannot be predicted, seasonal temperature variations across the United States are well known. In areas expected to seasonally freeze, the following temperature variations are expected:

- Alaska: from -40 °C to 20 °C (variation of 110 °F),
- Midwest: from -20 °C to 20 °C (variation of ~75 °F),
- Eastern seismic region: from -20 °C to 20 °C (variation of ~75 °F), and
- Western seismic region: from -20 °C to 15 °C (variation of ~60 °F).

Despite these drastic temperature changes, they are not accounted for in routine design although SFSI and to a certain extent structural behavior will be greatly influenced. Understanding the influences of cold temperatures on the response of SFSI systems are critical within the field of seismic engineering to prevent undesirable failure modes in accordance with the capacity design philosophy.

2.3.1 Effects of Seasonal Freezing

In order to understand the effects of seasonal freezing on deep bridge pier foundations, Sritharan et al. (2007) undertook an exploratory research program into the lateral response of integrated bridge column/foundation systems with a CIDH shaft subjected to seasonal freezing. The exploratory research program consisted of analytical and experimental components. Following completion of the experimental investigation (Suleiman et al., 2006), analytical studies were performed by Sritharan et al. (2007) and Wotherspoon et al. (2010 a&b)

The experimental investigation was performed on three full-scale integrated bridge column-foundation systems located on the grounds of Iowa State University in Ames, Iowa. Using multiple cone penetration tests (CPTs), the soil present at the site was further classified as low plasticity clay according to the Unified Soil Classification System (USCS). As part of the experimental investigation performed on this site, two of three specimens were identical and were constructed as continuous bridge columns that extended into the ground as drilled shaft foundations to examine the effects of seasonal freezing in a lateral loading situation. The third specimen, which will not be discussed within this report, consisted of a bridge column supported on an oversized drilled shaft foundation.

The two identical systems, SS1 and SS2, had 0.61 m (24 in.) diameter sections for the column and foundation shafts with column heights of 2.69 m (106 in.) and shaft lengths of 10.36 m (410 in.). The systems were reinforced longitudinally with a two percent longitudinal reinforcement ratio, ρ_l, along the entire column length, as this represents an average steel ratio for columns in high seismic regions (Priestley et al., 1996) and bridge columns in the Midwest, which are generally not designed for seismic events. The aforementioned steel ratio was obtained by using twenty number six bars [d_b = 19 mm (0.75 in.), d_b = diameter of bar] as the longitudinal reinforcement. The transverse reinforcement ratio, ρ_s, was designed in accordance with codes for seismic regions and found to be eight tenths of a percent in the critical plastic hinge region. In order to obtain this transverse steel ratio, number three bar [d_b = 9.5 mm (0.375 in.)] in a spiral reinforcement pattern with a spacing of 63 mm (2.5 in.) was used along the entire column length and top two-thirds of the foundation shaft. The remaining portion of the foundation shaft, a non-critical region, contained a number three bar spiral with spacing of 152 mm (6 in.). The cross-section details are presented graphically in Figure 2-10 below.

As a part of this investigation, material testing was performed to identify changes caused by seasonal freezing. Material testing consisted of unconfined compressive strength tests for the concrete, unconfined compression stress-strain test on soil and cone penetration tests in the field near the test specimens [additional information available in Sritharan et al. (2007) and Chapter 3]. The differences noted from the cone penetration testing were that the tip resistance differed markedly near the ground surface from an unfrozen state to a frozen state. In addition to the differences in tip resistance near the ground surface, a frozen soil layer of 0.75 m (~30 in.) was identified from temperature readings taken in the soil surrounding the foundation shafts. The unconfined compressive strength testing found that the concrete strength increased during the frozen state as opposed to the unfrozen state. To ensure that the correct deviation in material properties was determined, the aforementioned testing was performed at the same ambient temperatures as the testing of SS1 and SS2, 23 °C and -10 °C (73.4 °F and 14 °F) respectively.

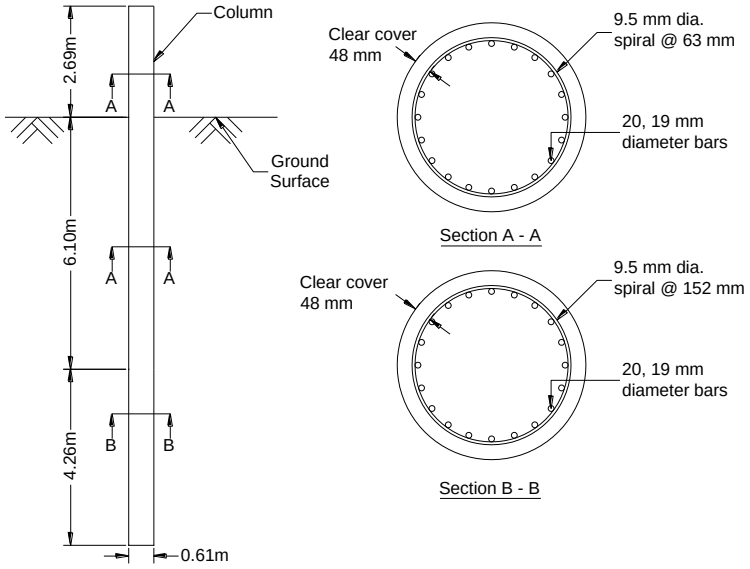

Figure 2-10: Cross-section details of column-shafts (after Sritharan et al., 2007); (1 in. = 25.4 mm = 2.54 x 10^{-2} m)

The lateral loading of the columns consisted of repeated fully reverse cyclic motions with respect to a reaction column in a quasi-static manner. One load cycle was used until the theoretical displacement for first yielding was reached. After this point, three loading cycles per target displacement were used. This method of loading was performed to effectively capture the effects of degradation that will occur after the initial loading to a specified target displacement.

The testing continued in this manner until the limitations of the actuator were obtained, which was about 280 mm (11 in.) in the push direction and 290 mm (11.5 in.) in the pull direction. The final force-displacement response of the two systems is depicted in Figure 2-11, in which the solid line is SS1 and the dashed line is SS2.

Based on the experimental data, a number of conclusions were drawn on the effects of seasonal freezing to the lateral loading of integrated column/foundation systems. The following conclusions were reported in Suleiman et al. (2006):

1. As expected, the continuous shaft increased the flexibility of the system due to the maximum moment forming below the ground surface.
2. With respect to SS1, SS2 experienced the following changes in the lateral load response:
   - increased effective elastic stiffness by 170%,
   - increased lateral load resistance by 44%,
   - upward shift of the maximum moment location by 0.84 m (~33 in.),
   - reduced plastic region length by 64% in the foundation shaft, and
   - reduced the gap opening at the base of the column by 60%.
3. Seasonal wintry conditions must be accounted for in the seismic design of continuous column to drilled shaft foundations because of the drastic changes seen in the lateral response of these systems.

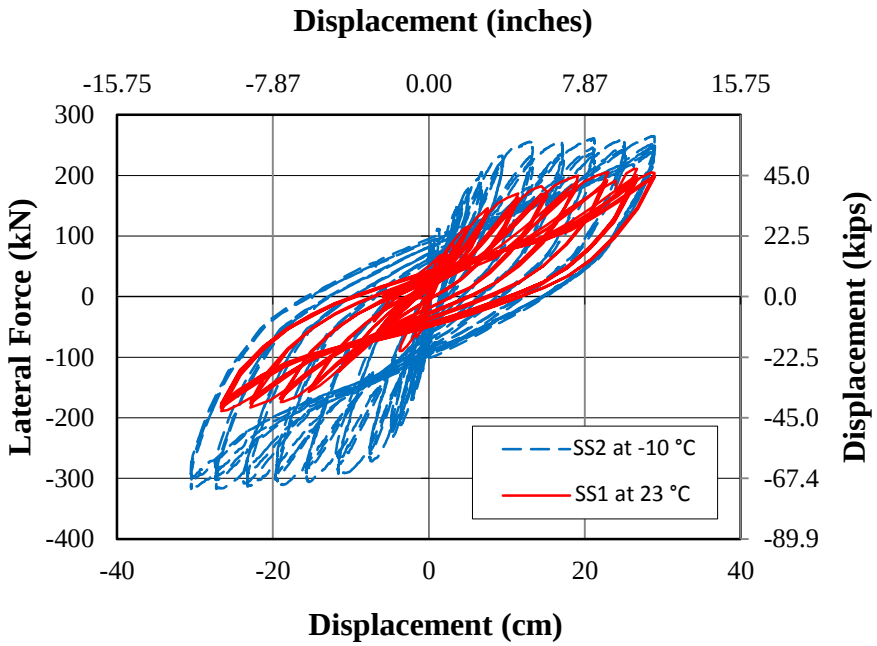

Figure 2-11: Measured force-displacement response (after Sritharan et al., 2007)

The analytical investigation undertaken by Sritharan et al. (2007) examined the generalized effects of freezing temperatures and associated design implications on integrated column/foundation systems. LPILE (2004), which uses the finite difference method and the Winkler soil spring concept, was used to complete the analytical portion. To account for the effects of seasonally wintry conditions, material properties were modified as needed.

The response of the soil springs was of significant importance, as this response will greatly dictate the lateral loading behavior of the column-shaft system. To modify the soil springs, unconfined compression stress-strain data were generated through laboratory experiments on glacial till specimens at -1 °C (30.2 °F), -7 °C (19.4 °F), -10 °C (14 °F) and -20 °C (-4 °F). Using these data sets, the p-y curves were generated using the procedure suggested by Reese and Welch (1975). The aforementioned method was modified based off of the work performed by Crowther (1990) with an exponent of 0.43 and experimental data to ensure the model accurately captured the frozen soil response. The depth of frozen soil for the analyses at -1 °C (30.2 °F), -7 °C (19.4 °F), -10 °C (14 °F)and -20 °C (-4 °F) were found to be 0.076 m (3 in.), 0.46 m (18 in.), 0.76 m (30 in.) and 1.2 m (47 in.), respectively For a direct comparison with the experimental testing, the soil profile produced by the cone penetration test (CPT) was used to generate the p-y curves at 23 °C (73 °F) and -10 °C (14 °F). To do this, the unconfined compressive strength of the soil was found using the recommendations of Robertson and Campanella (1983) with a bearing capacity factor, N_k, of fifteen. The final portions needed for the computer program, a soil subgrade modulus and strain at fifty percent of the soil strength, were found for the laboratory and CPT curves based on the recommendations of Reese et al. (2000).

The final modifications for the analysis were made to the concrete and steel properties. Concrete compressive strength properties were modified based on the research performed by Lee et al. (1988), in which it was found that the concrete strength and elastic modulus would increase by 22% and 10%, respectively, at -20 °C (-4 °F) when compared to the properties at 0 °C (32 °F). Reinforcing steel properties for the wintry conditions were modified following the research performed by Filiatrault and Holleran (2001). This research found that the strength of steel would increase by 4.5% at -20 °C (-4 °F) when compared to the strength at 23 °C (73.4 °F). Using these modifications, the moment-curvature analyses were performed to accurately represent the flexural stiffness of the shaft as a function of temperature.

Using the above modifications, the analyses were run and compared to the experimental results as appropriate. These comparisons concluded that the modeling would accurately capture the effects of seasonally frozen conditions, allowing the remaining analyses at different temperatures to be legitimized. A number of conclusions were drawn from this study, which are as follows:

1. A 2-D model that uses beam-column elements to represent the column and foundation shafts and compression only springs satisfactorily captured the measured response of the column/foundation system in warm and freezing conditions. This correlates well with the design recommendations presented in AASHTO (2007 and 2009) in which a method involving soil springs is the primary recommendation.
2. With respect to warm weather conditions, the response of a column to drilled shaft system at -1 °C (30.2 °F) to -20 °C (-4 °F) will change the lateral response as follows:
   - increase the effective lateral stiffness by 40% - 188%,
   - reduce the lateral displacement capacity by 17% - 63%,
   - increase the lateral load resistance and shear demand in the column by 25% - 30%,
   - increase the shear demand in the foundation shaft by 25% - 80%,
   - shift the maximum moment location upwards by 0.54 m - 0.82 m, and
   - reduce the length of plastic action in the foundation shaft by 19% - 68%.
3. The change in soil stiffness plays a more significant role in dictating the lateral response of column/foundations systems than the change in concrete and steel properties.
4. The depth of frozen soil and axial load do not greatly alter the response of the system in the frozen state (see Figure 2-12).
5. Seasonal freezing will significantly alter the seismic response of integrated bridge column-foundations systems. Therefore, unless these effects are accounted for in design, they will have serious implications in areas where seasonal freezing occurs around the world (see Figure 2-13).

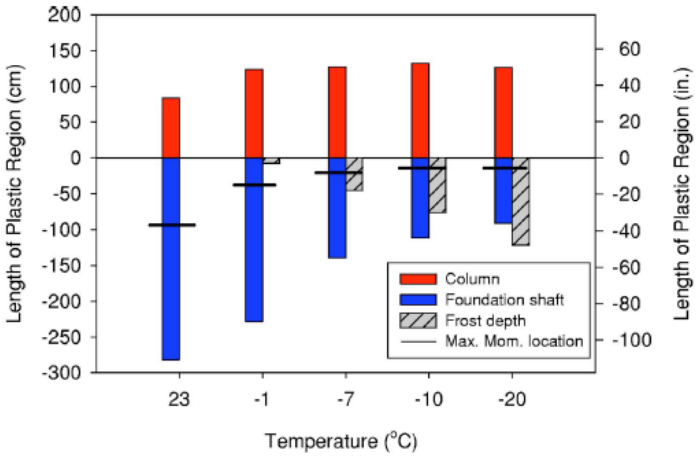

Figure 2-12: Frost depth, maximum moment location and plastic hinge length at ultimate condition for column-foundation shafts with dimensions of SS1 and SS2 (Sritharan et al., 2007)

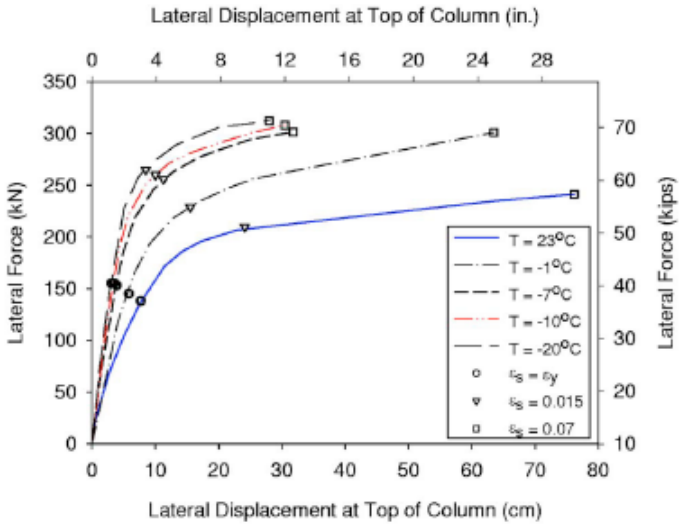

Figure 2-13: Global force-displacement response as temperatures decrease for a column-foundation shaft system with SS1 and SS2 dimensions (Sritharan et al., 2007)

In addition to the monotonic analytical modeling performed by Sritharan et al. (2007), analytical investigations were conducted by Wotherspoon et al. (2010 a&b) to construct a full cyclic model of the lateral force-displacement response of the two systems examined by Suleiman et al. (2006). The research was conducted using Ruaumoko (Carr 2005) and the Winkler soil spring concept. The springs in this method were established as a series of detachable springs so the gap opening and reattachment occurs during the cyclic loading would be accurately captured. Each soil spring response was uniquely defined using the methodology

of Reese and Welch (1975), since CPT and experimental soils testing data was provided in Sritharan et al. (2007). The structural behavior of the reinforced concrete column and foundation shafts were modeled using experimental material properties through the use of moment-curvature responses constructed using a fiber based approach available in OpenSees. Cyclic loading was applied to the top of the column based on the experimental testing by applying increasing target displacements with no less than three cycles at each target displacement.

Wotherspoon et al. (2010a) concluded that through the use of elements available in Ruaumoko, the full-scale cyclic response of a column/foundation shaft could successfully capture the outdoor testing in both summer and winter conditions. This was accomplished by modeling structural nonlinearity, gap development and soil nonlinearity in compression. Each model was verified using multiple output parameters on the global and local level to ensure accuracy of the model. Global force-displacement comparisons used in the model validation are provided herein as Figure 2-14 and Figure 2-15. The modeling in Ruaumoko further validated the findings of Sritharan et al. (2007) in which the range of temperatures experienced by the system must be included in the design process to ensure adequate response during a seismic event.

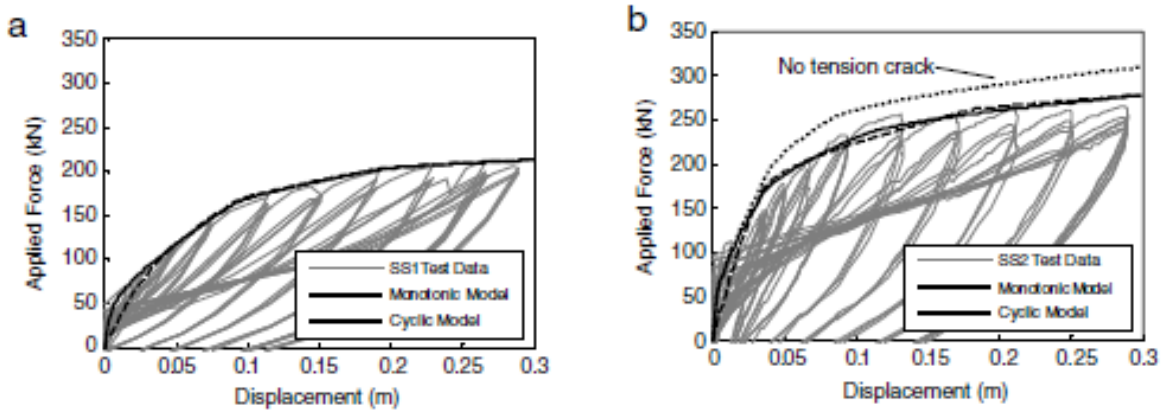

Figure 2-14: Comparison of the force-displacement characteristics at the column top for the monotonic and cyclic Ruaumoko models (a) SS1; (b) SS2

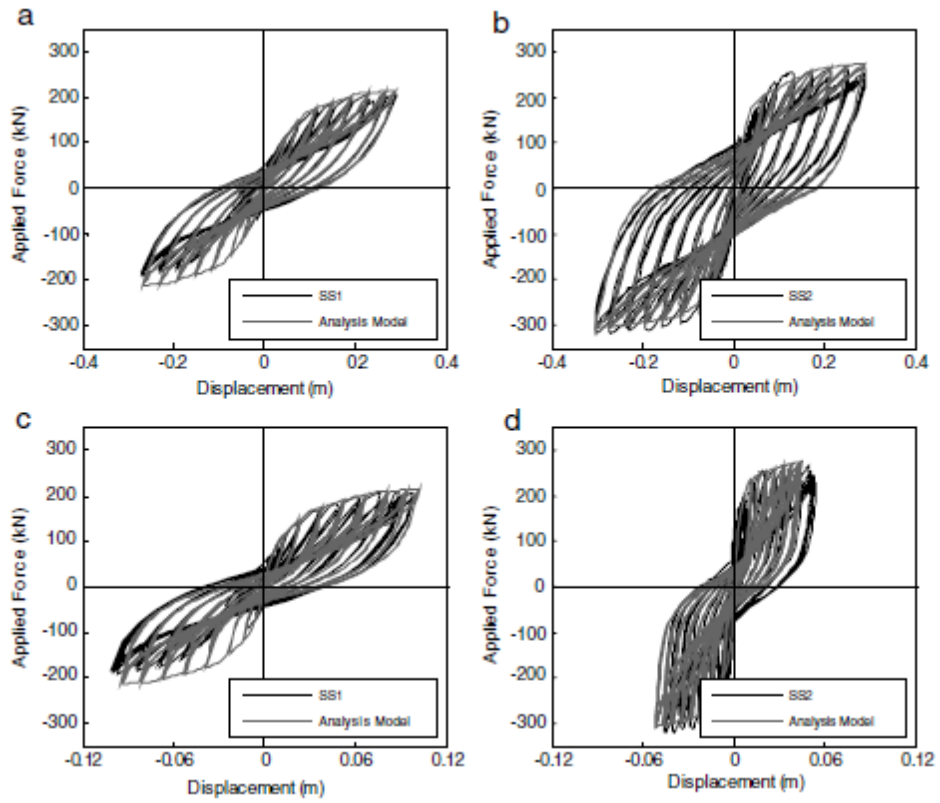

Figure 2-15: Cyclic force-displacement responses for (a) SS1 column top; (b) SS2 column top; (c) SS1 column base; (d) SS2 column base.

2.4 Broad Impacts

To better understand the broad impacts of seasonal freezing, an investigation was undertaken to examine the potential of seismic events and seasonal freezing to occur simultaneously within the United States and Japan (Sritharan and Shelman, 2008). In the United States, one commonly assumes that a significant freezing condition would only occur within the Central and Eastern United States and Alaska, but this is not an accurate assumption. In fact, a depth as small as 10 cm (4 in.) can alter the lateral loading response of integrated bridge column/foundation systems according to Sritharan et al. (2007). DeGaetano and Wilks (2001) suggested a depth of this nature can be expected in the seismic region of the western United States including the northeastern part of California (see Figure 2-16). In Japan, the northern portion of Honshu Island and the Island of Hokkaido should experience seasonal freezing and high seismic activity as well (see Figure 2-17).

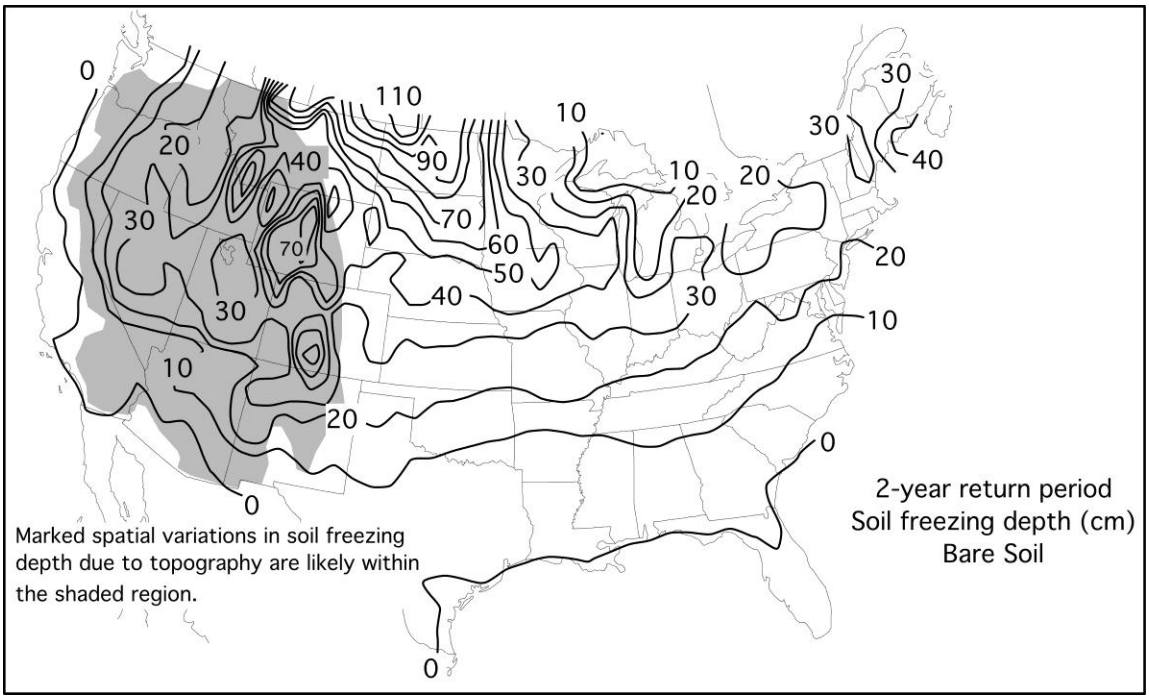

Figure 2-16: Frozen soil depth contours produced for a two-year return period by DeGaetano and Wilks (2001)

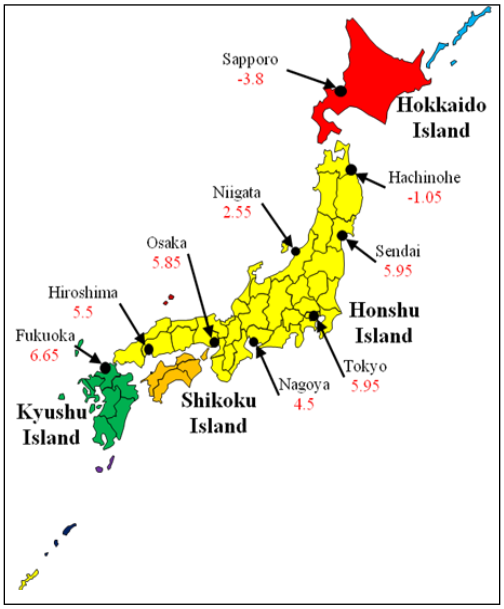

Figure 2-17: Average winter temperatures for Japan's larger cities (Japanese Meteorological Agency, 2009)

Despite the presence of frozen ground in winter months, all seismic regions of the United States, Japan and other countries around the world ignore the effects of seasonally frozen conditions on SFSI and the seismic response of bridges. To better understand the significance of

soil freezing and the seismic response of bridges, an impact study was performed for the United States and Japan.

For the United States, the number of bridges within each state was determined and then compared to the frost depth contour map in Figure 2-16 and a seismic hazard map. Due to a lack of information, it was assumed the number of bridges shown in Figure 2-18 were uniformly distributed within each state. The chosen seismic map for this study was the 0.2-second spectral acceleration map with a 10% probability of exceedance in 50 years as published by the United States Geological Survey (2002). With a limiting criterion that the bridges should experience at least 0.2g spectral acceleration at a period of 0.2-second, 66,000 bridges were estimated to be in the seismic region. To examine how many of these bridges would be affected by seasonally frozen conditions, the frost contours were overlaid on the seismic hazard map, as shown in Figure 2-19, and the number of bridges that may experience both a minimum of 10 cm (~ 4 in.) of frost depth and 0.2g spectral acceleration was estimated. This combination showed that seismic response of approximately 50% of the 66,000 bridges in active seismic regions would be affected by seasonal freezing, which is a significant finding. When only the minimum frost depth condition was used (i.e., the bridge site should experience a frost depth greater than or equal to10 cm [~ 4 in.]), over 400,000 bridges or two-thirds of all bridges in the U.S. were found to be affected by seasonally frozen conditions, yet this issue is seldom addressed in routine design methods.

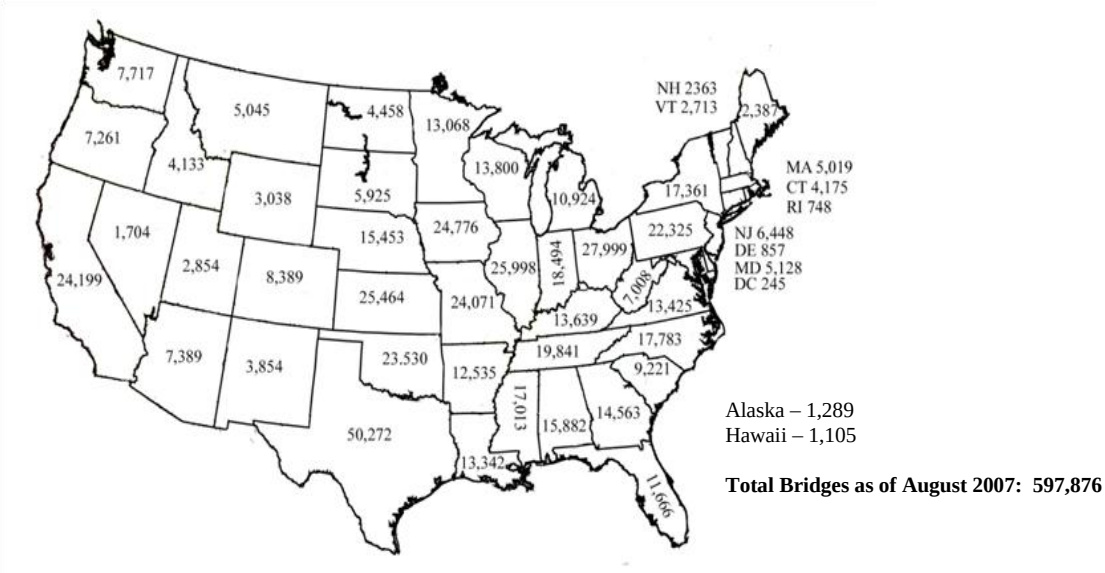

Figure 2-18: Statewide distribution of bridges in the United States (Bureau of Transportation Statistics, 2007)

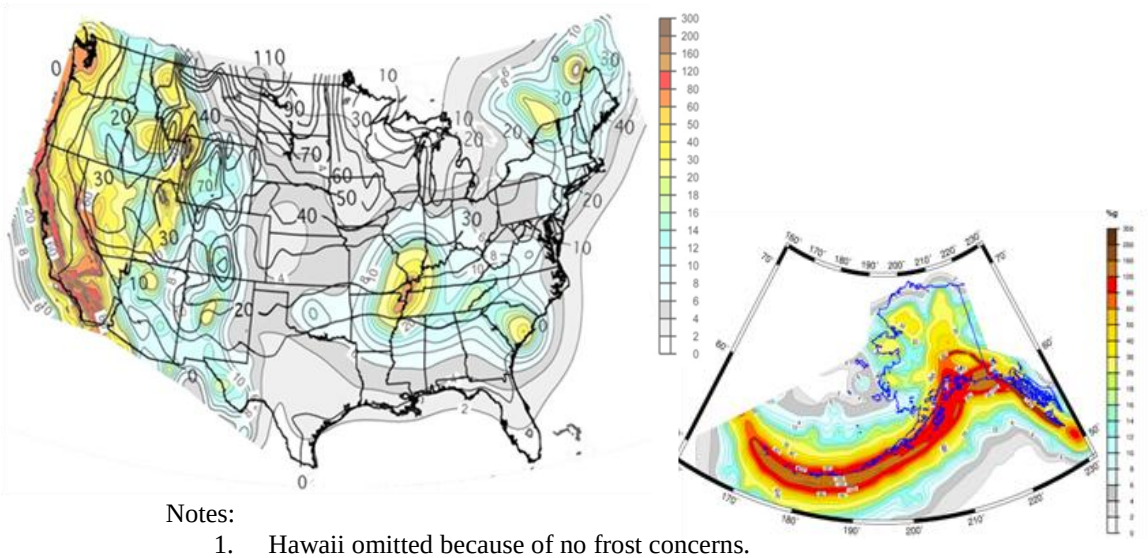

Notes:

1. Hawaii omitted because of no frost concerns.
2. Entire State of Alaska would experience greater than 10cm frost depth

Figure 2-19: USGS seismic hazard map (2002) overlaid with frost depth contours shown in Figure 2-16

The broad impact study of Japan consisted of examining the average winter temperatures and comparing the locations of possible frozen soils to seismic hazards and population distribution. Figure 2-17 demonstrated the locations for possible frozen soils were Hokkaido Island and the northern part of Honshu Island. Within this region, seismic hazards were found, using the National Earthquake Information Center's historical and present data, and compared with the frozen soils area. With this information, the population distribution was examined to provide a qualitative risk estimate, as bridge locations were unavailable. It was noted that some major cities were located within this region, such as Sapporo. A final map correlating with Figure 2-17 was produced that shows the population distribution and seismic events in the area in Figure 2-20. It appears that bridges in four major cities and the south-eastern part of the island may be affected by both earthquakes and seasonally frozen conditions.

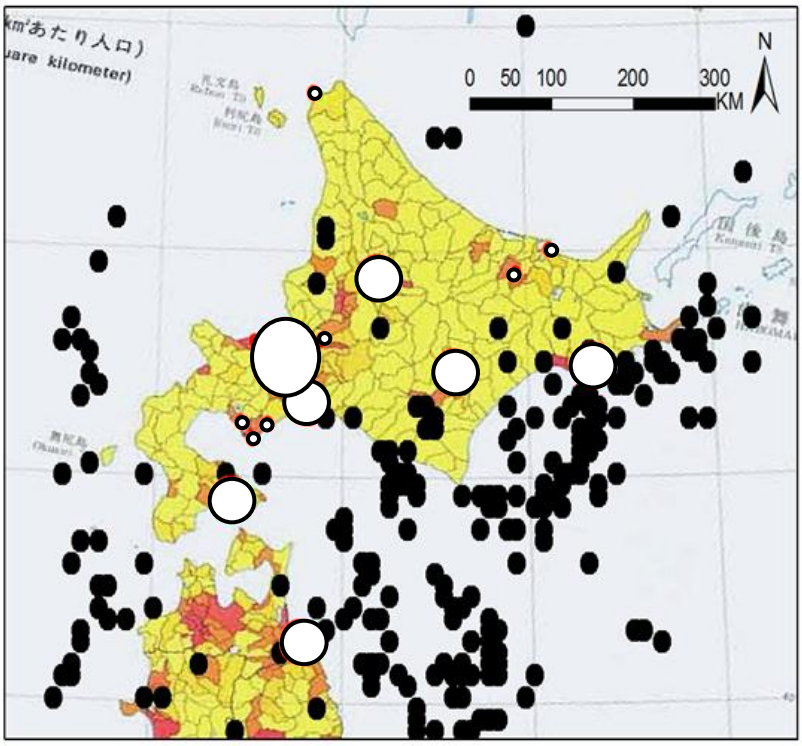

Key:

1. Small black circles are magnitude 5.5 or greater earthquakes
2. Open circles are population centers of 35,000 to 1.8 million persons

Figure 2-20: Seismic activity of Japan near Hokkaido Island circa year 2000

2.5 Material Behavior

When examining the lateral response of columns supported on CIDH shafts, the material behavior must be defined for concrete, soil and steel. These definitions are even more critical during times of seasonal freezing in which material properties are markedly different from warm weather conditions. The section below provides information on the studies performed in freezing conditions. These studies are critical to understand the local response of a confined concrete member so the moment-curvature response is correctly captured. By accounting for the freezing effects in the moment-curvature response and the soil parameters, the development of the new methodology presented in Chapter 4 will provide consideration to all seasons of the year.

2.5.1 Concrete

Sritharan et al. (2007) demonstrated in an exploratory research program that concrete material properties will change as temperature decreases. Although they state that these changes

in the material properties do not cause as significant an impact as the change in soil properties, they must be accounted for to correctly handle the effects of seasonal freezing in design. Currently, a limited amount of research is present to show the influence of cold temperatures, as warm weather conditions are generally used for the design process. The following section will discuss prior research that has been completed on the effects of cold temperatures to concrete material properties.

Sehnal et al. (1983)

Prior research in material testing of concrete has shown that as temperature decreases the compressive strength, elastic modulus and bond strength of concrete increases. Sehnal et al. (1983) demonstrated that as temperature decreased, concrete compressive strength increased according to a polynomial curve in normal strength concrete. The curve produced by this study, reproduced in Figure 2-21, showed that between 20 °C (68 °F) and -25 °C (-13 °F) an increase of 25% in compressive strength could be expected. Although experimentation was performed on 41.4 MPa (6 ksi) concrete, it was assumed that this was applicable over varying strengths as the testing was performed on plain Type II Portland cement concrete for a w/c ratio of 0.6 which is high for typical bridge designs throughout Alaska and the United States. They also provided evidence, based on statistical modeling, that the rate at which concrete test specimens were cooled to testing temperature was independent of the compressive strength (1983).

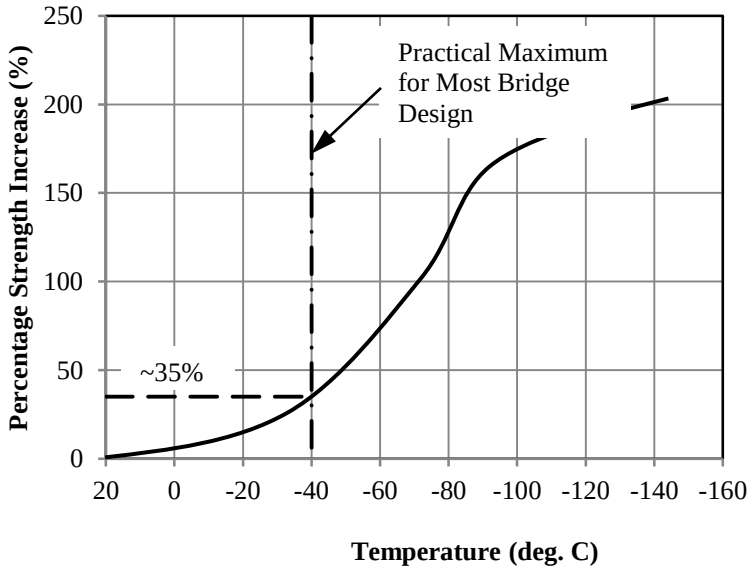

Figure 2-21: Percentage increase of concrete strength with reduction in temperature (after Sehnal et al., 1983)

Lee et al. (1988)

The information provided by Sehnal et al. (1983) was furthered in 1988 by Lee et al. (1988a). This research demonstrated the compressive strength increased in a polynomial manner as suggested by Sehnal et al. (1983). Lee et al. (1988a) further concluded the modulus of elasticity and bond strength would increase at lower temperatures. These researchers noted that the increase in modulus of elasticity occurred at a slower rate than the rate of increase of concrete compressive strength (e.g., at -70 °C [-94 °F] the compressive strength increased by 151.3% compared with the elastic modulus increase of 114.7%). This rate of decrease is as expected, as most codes suggest E_c is a function of the square root of the unconfined compressive strength. The bond strength in confined concrete was also noted to increase with lower temperatures, since bond strength is correlated with the unconfined compressive strength of concrete. In the study it was found that at -70 °C [-94 °F] the bond strength would increase by 145.1% compared with the 128.6% increase of the concrete compressive strength. The data also demonstrate a non-uniform increase of bond strength was experienced as temperature decreased from ambient room temperature.

In a follow-up paper published by Lee et al. (1988b), the effects of high strength concrete at low temperatures provided conclusions in terms of compressive strength, modulus of elasticity and bond strength. The main conclusions drawn were that the respective properties increased at a similar rate to that of normal strength concrete; however, the percent of increase tended to be lower than those of normal strength concrete at similar temperatures. This difference may be due to the variation in water to cement ratio between the normal strength, w/c = 0.48, and high strength, w/c = 0.35, tests; however, the authors do not provide any reasons for the differences experienced between the two types of concrete.

In the two papers published by Lee et al. in 1988 (a & b), the researchers expanded the information available on Poisson's ratio. They reported that the past studies conclude Poisson's ratio should be taken to be approximately 0.20 regardless of compressive strength and that Poisson's ratio will decrease as the compressive strength of the concrete increases. This suggests that no matter the temperature of concrete a constant value of 0.20 should be used for Poisson's ratio in concrete. However, Lee et al. (1988a, 1988b) has shown in both normal strength concrete and high strength concrete that as temperature decreases and unconfined compressive strength increases, the Poisson's ratio will increase. The researchers provide data that suggest

that at a temperature as low as -70 °C [-94 °F], Poisson's ratio will increase by approximately 50% in normal strength concrete and 25% in high strength concrete with interpolation required to attain increases at other subzero temperatures.

2.5.2 Steel

Understanding the behavior of steel at low temperatures is the other key component needed to perform a moment-curvature analysis to account for the effects of seasonal freezing on the section response. Although a key component, very little research has been performed in this area. This section presents a brief overview of previous studies on the effects of steel reinforcing behavior at cold temperatures. Additional information may be found in Chapter 6.

Filiatrault and Holleran (2001) completed experiments on CSA 30.16 reinforcing steel and found the yield and ultimate tensile strengths would increase by 20% and 10%, respectively, at -40 °C (-40 °F) when compared to 20 °C (68 °F). In addition, the research concluded that Young's modulus and the ultimate tensile strain were unaffected by temperature. Another study performed by Bruneau et al. (1997) on American Society for Testing and Materials (ASTM) A572 Grade 50 steel found the yield and ultimate tensile strengths increased by 9% and 5%, respectively, at -40 °C (-40 °F) when compared to 20 °C (68 °F). Bruneau et al. (1997) also noted the ultimate tensile strain and Young's modulus would not be affected when temperature decreases. These results, although comparable, were not performed on steel reinforcing bars that are now commonly used in high seismic regions (i.e., ASTM A706 Grade 60 steel).

Sloan (2005) conducted testing on A706 mild steel reinforcement at temperatures of 22 °C (71.6 °F) and approximately -20 °C (-4 °F), the temperature after cooling the samples with dry ice, as supplemental research on the examination of the performance of reinforced concrete members subjected to low temperatures. The specimens were placed in a cooler with dry ice until they were ready to test, quickly removed, placed into the grips of the Materials Testing Systems (MTS) fatigue machine, and tested. The results of the testing were compiled into graphical form by the authors of this report in Figure 2-22 and noted that a large scatter in the data existed with the trend appearing to be an increase in both the yield and ultimate steel stresses as temperature decreased.

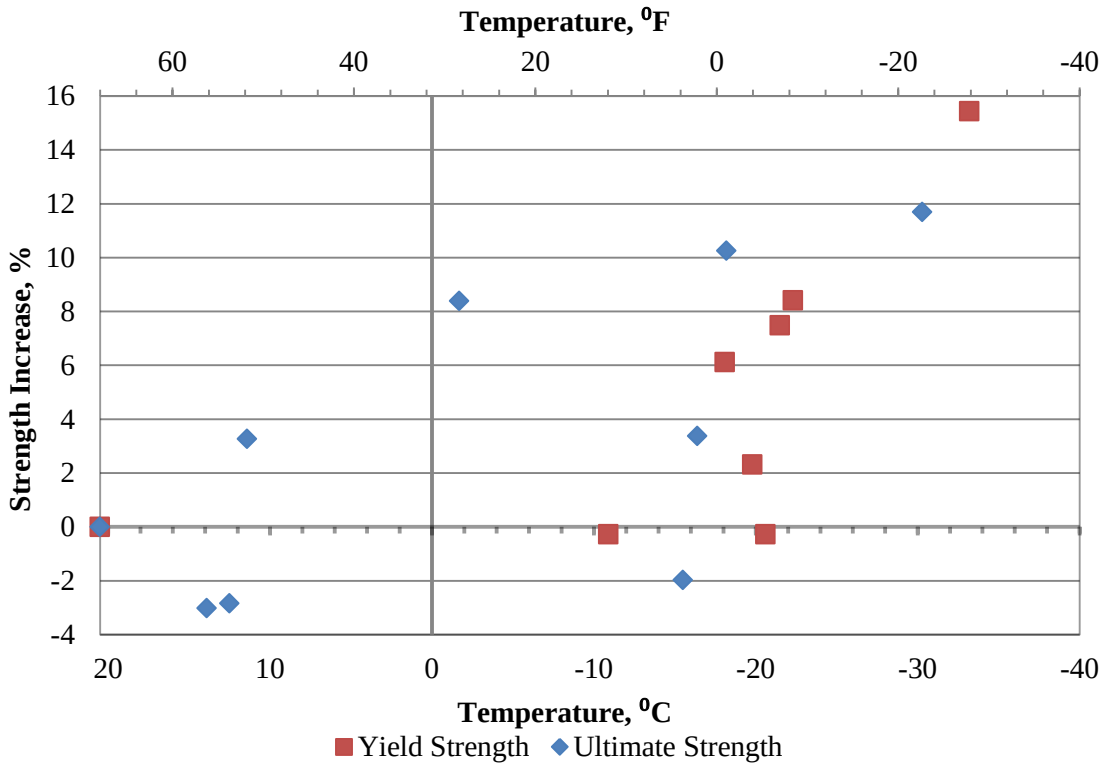

Figure 2-22: Yield and ultimate strength increase generated from the works of Sloan (2005)

Some of the challenges associated with this testing program arose due to the use of dry ice to cool the test samples rather than placing the sample in a controlled environment. The first of these challenges was that a thermocouple was attached to the exterior of each sample during cooling with the sample being tested upon reaching the desired temperature (Sloan, 2005). It is believed this method may have caused the temperature inside the sample to be different than the reported value. Second, the samples were removed from the dry ice for testing (Sloan, 2005). Sloan (2005) stated the warming of the samples made it difficult to correctly quantify the cold temperature stresses during testing. Finally, failure of the deformed bar specimens were experienced near the grips due to rapid warming, likely due to heat transfer (Sloan, 2005). Milled samples were only used toward the end of testing to resolve this phenomenon.

2.5.3 Soil

Frozen soil can be both an advantage and disadvantage when designing or constructing a structure in civil engineering projects. This is the case, as the inherent impervious nature of ice within the frozen soil construct allows for weak and soft soils to be bridged temporarily for stabilizing slips, underpinning structures, sampling weak or non-cohesive soils, temporary roads,

protecting sensitive equipment and many other advantages (Harris, 1995). All of these benefits rely on the stiffening of soil which is a concern for the seismic design of columns supported on CIDH shafts as previously shown in Section 2.3. Thus, the mechanical properties of the soil must be adequately established.

To define engineering properties correctly, the effects of moisture content and ice on the unconfined compressive strength of concrete must be understood. According to Tsytovich (1975), the range in which water experiences a significant phase transformation, the factors determining the strength of frozen soils, both seasonally and permanently, are the overall amounts of ice and unfrozen water and how they vary with temperature. The range discussed in Tystovich (1975) was suggested as 0 °C to -0.5 °C (32 °F to 31.1 °F) for sandy soils and 0 °C to -5 °C (32 °F to 23 °F) for clayey soils. The variation of unfrozen water content with temperature for different soils was examined during a project undertaken by Williams (1988). The data attained during this investigation, Figure 2-23, demonstrate that between 0 °C to -5 °C (32 °F to 23 °F) the amount of unfrozen water in a soil specimen will change rapidly as the water undergoes a phase change from a liquid to a solid. In addition, the information provided suggests the rate of change in the unfrozen water content is a function of the soil type which is most likely due to the variation in the molecular structures.

After understanding the formation of ice in soil, the next step is to examine how the overall freezing of the soil affects engineering properties (e.g., compressive strength and modulus of elasticity). In 1978, Andersland and Anderson provided a summary of the work conducted by Sayles (1966 and 1968) on the effects of temperature on the unconfined compressive strength of soils. This summary was provided graphically and is provided here as Figure 2-24. Figure 2-24 shows that as temperature decreases from 0 °C (32 °F) to approximately -150 °C (-238 °F) an overall increase in the unconfined compressive strength of the soil occurs. In addition to the soil curves, three curves representing the increase in compressive strength of ice were provided to demonstrate the hardening that takes place with temperature. The combination of soil and ice curves demonstrates the influence of ice forming within the pores of the soil contributes to the overall unconfined compressive strength gain. However, the figure also provides evidence suggesting that as temperatures decreases, the influence of ice reduces and the contact between the microscopic particles has a direct impact on the unconfined compressive strength of soil.

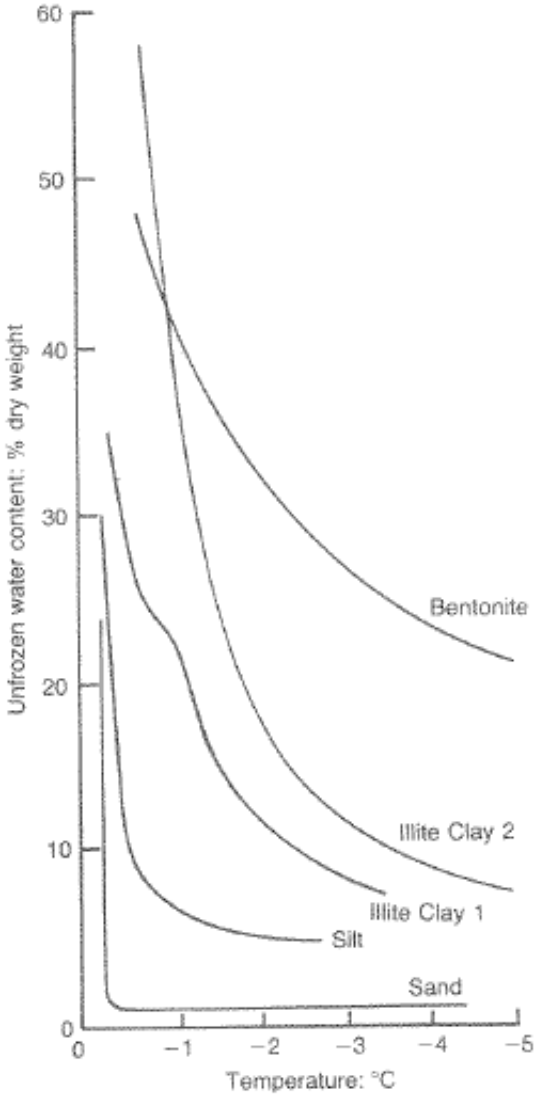
60
50
40
30
20
10
0
Unfrozen water content: % dry weight
Bentonite
Illite Clay 2
Illite Clay 1
Silt
Sand
0
−1
−2
−3
−4
−5
Temperature: °C

Figure 2-23: Typical curves of unfrozen water content against temperature (after Williams, 1988) [Harris, 1995]

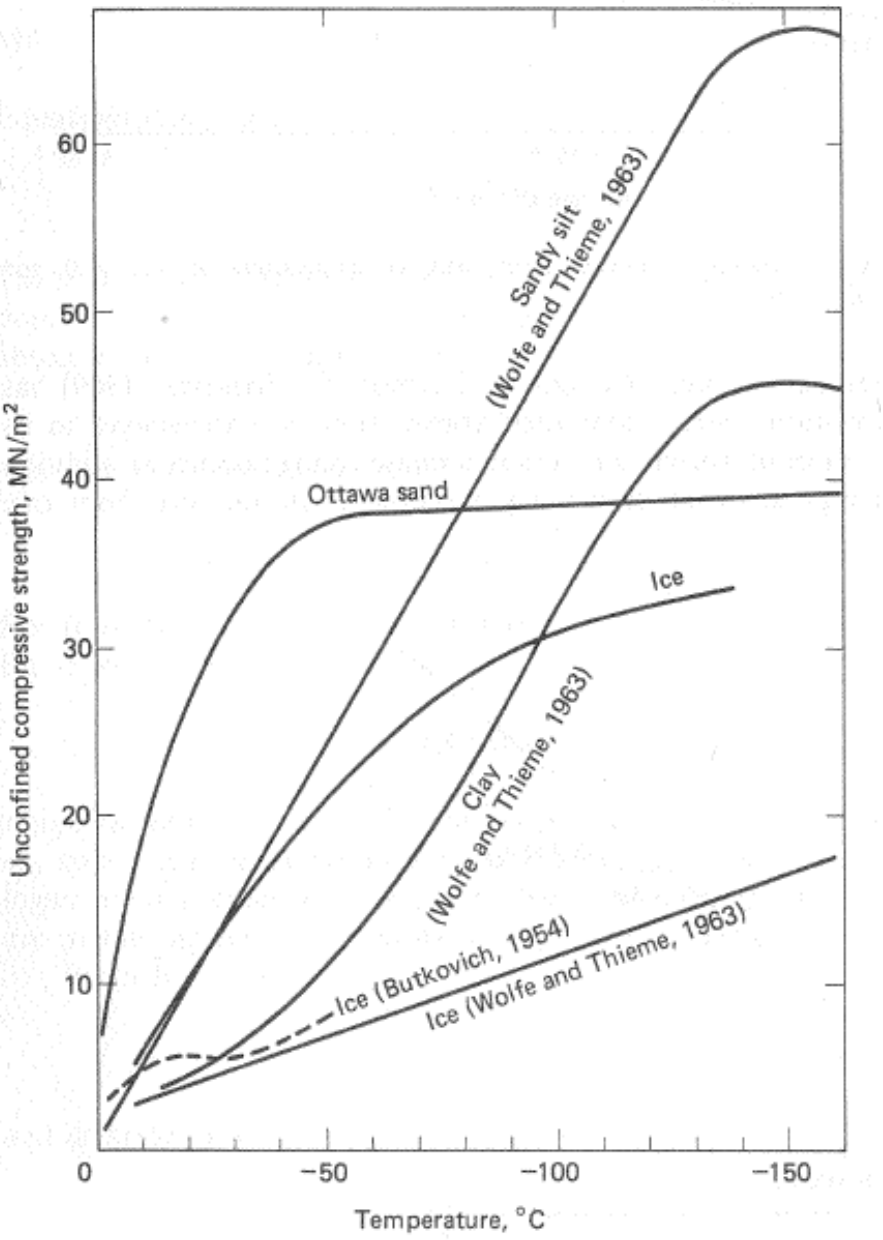

Figure 2-24: Temperature dependence of unconfined compressive strength for several frozen soils and ice (after Sayles, 1966) [Andersland and Anderson, 1978]

Besides the work performed by Sayles (1966), Tsytovich (1975) provided a table, Table 2-2, on past investigations that noted the increase in ultimate compression strength of soil when subjected to freezing temperatures. Additional information was provided by Tsytovich (1975) on the temperature effects on the strength of permafrost, but the data sets have not been included due to the focus of the report being on seasonally frozen ground.

Table 2-2: Ultimate strength of frozen soils in uniaxial compression (after Tsytovich, 1975)

Designation of Soil	Total Moisture W_d, %	Temperature °C (°F)	Strength σ_{ul}, MPa (tsf)	Investigator
Quartz sand (100% content of 1 – 0.05 mm fraction	14.7 14.3 14.0 14.1 14.9 14.3	-1.8 (28.8) -3.0 (26.6) -6.0 (21.2) -9.0 (15.8) -12.0 (10.4) -20.0 (-4)	6.08 (63.5) 7.65 (79.9) 9.71 (101.4) 11.57 (120.8) 13.14 (137.2) 14.91(155.7)	N. A. Tystovich (1930)
Silty sandy loam (61.2% of 0.05 – 0.005 mm fraction; 3.2% < 0.005 mm)	21.6 23.1 22.1 21.3	-0.5 (31.1) -1.8 (28.8) -5.1 (22.8) -10.3 (13.5)	0.88 (9.2) 3.53 (36.9) 7.65 (79.9) 12.55 (131.1)	N. A. Tystovich (1940)
Clay (50% content of < 0.005 mm fraction)	34.6 36.3 35.0 35.3	-0.5 (31.1) -1.6 (29.1) -3.4 (25.9) -8.2 (17.2)	0.88 (9.2) 1.27 (13.3) 2.26 (23.6) 4.41 (46.1)	N.A. Tystovich (1940)
Quartz sand (100% content of 1 – 0.05 mm fraction	16.7	-20.0 (-4)	14.71 (153.6)	N. K. Pekarskaya (1966)
Cover Clay (44.3 content of < 0.005 mm fraction)	32.0	-20.0 (-4)	8.92 (93.2)	N. K. Pekarskaya (1966)

Tsytovich (1975) furthered the information on frozen soils through an examination of the tensile strength of soil, both instantaneously and long term. This data set, Table 2-3, suggests that as temperature decreases the tensile strengths of soil will increase. Therefore, when a system is subjected to a lateral load during a time of seasonal freezing, larger tensile cracks will form, decreasing the soil confinement on the foundation shaft.

Table 2-3: Instantaneous and ultimate long-term tensile strengths of frozen soils (after Tsytovich, 1975)

Designation of Soil	Total Moisture W_d, %	Temperature °C (°F)	Strength, σ_{inst} MPa (tsf)	Strength, σ_{lt} MPa (tsf)	Investigator
Clay (45% content of fraction < 0.005 mm)	19.4 19.4 19.4	-1.2 (29.8) -2.5 (27.5) -4.0 (24.8)	0.96 (10.0) 1.65 (17.2) 2.12 (22.1)	-- -- --	N. A. Tsytovich (1952)
Cover Clay	32.0	-2.0 (28.4)	1.13 (11.8)	--	N. K. Pekarskaya

	32.0 32.0	-5.0 (23.0) -10.0 (14.0)	1.35 (14.1) 2.60 (27.1)	-- --	(1966)
Heavy loam (22.5% content of fraction < 0.005 mm)	31.8	-3.0 (26.6)	1.18 (12.3)	0.25 (2.7)	S.E. Grechishchlev (1963)
Heavy sandy loam	34.0	-4.0 (24.8)	1.67 (17.4)	0.20 (2.0)	N. A. Tsytovich (1952)
Quartz Sand	17.0 17.0 17.0	-2.2 (28.0) -5.0 (23.0) -10.0 (14.0)	0.62 (6.5) 0.77 (8.1) 1.57 (16.4)	-- -- --	N. K. Pekarskaya (1966)

In addition to the temperature being a significant contributor to the ultimate compressive strength of the soil, the total moisture content of the soil will influence the strength. Tsytovich (1975) found that as the moisture content increases the ultimate compressive strength of the soil will increase until just short of complete water saturation and decrease thereafter, similar to unfrozen soil. Tsytovich's figure is provided within this report as Figure 2-25.

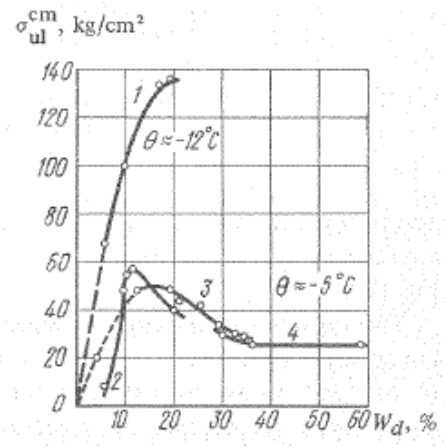

Figure 2-25: Ultimate compressive strength of frozen soils as a function of their total moisture content: (1) sand; (2) sandy loams; (3) clay (51% content of 0.005 mm fractions); (4) silty clay (63% content of fraction < 0.005 mm). [Tsytovich, 1975]

Harris (1995) further expanded on the strength of frozen soil by providing information on the work of Zhu and Carbee (1984) performed on frozen silt (Plasticity Index, $I_p = 4$). The work concluded that as the strain rate applied to the specimens increased the strength of the soil increased, as shown in Figure 2-26. Additionally, Figure 2-26 shows the failure mode of the silt switched from a ductile failure at slower rates of loading to a more brittle failure at the higher rates of loading. A closer examination of the data provided evidence to suggest that the sharp

bend in the stress-strain curves at less than 1% strain is most likely due to the cracking of the ice matrix.

The elastic modulus of soil is a major component when determining the deformation of the soil, as this property dictates the initial portion of a p-y curve. Tsytovich (1975) examined the effects of negative temperatures on the modulus of elasticity of soil. This investigation found that as temperature decreased the elastic modulus would increase as expected, since the soil modulus of elasticity is proportional to soil strength. Tsytovich found that the modulus could be predicted by a power series or a third order polynomial function, as depicted by the data shown in Figure 2-27. However, if the temperature of the specimen is not within the phase changing range of water a linear approximation can be used with coefficients determined using experimental means. It was also noted that the applied external pressure will influence the coefficients used to determine modulus of elasticity through the suggested relationships.

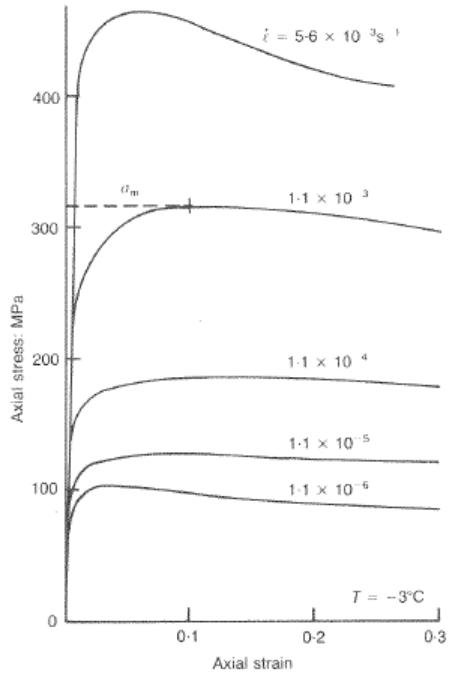

Figure 2-26: Stress-strain curves for uniaxial compression of a remoulded silt (after Zhu and Carbee, 1984) [Harris, 1995]

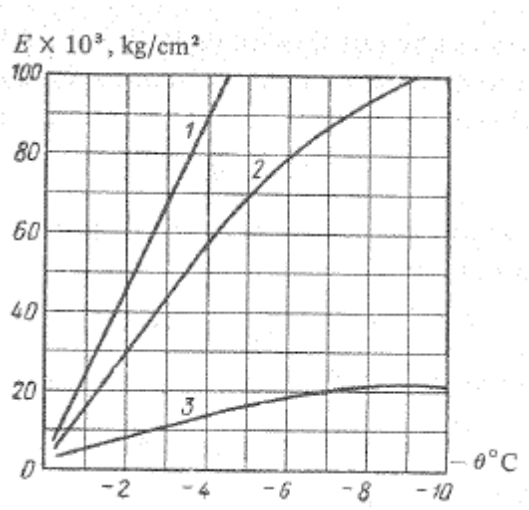

Figure 2-27: Modulus of normal elasticity E, kg/cm^2, of frozen ground at constant pressure σ = 2 kg/cm^2. (1) Frozen sand; (2) frozen silty soil; (3) frozen clay. (Tsytovich, 1975)

Another deformation component examined by Tsytovich (1975) was Poisson's coefficient to examine the effects of temperature on the lateral elastic deformation of soil. This examination was performed using direct measurements of experimental test specimens. Data retrieved from this testing, Table 2-4, show that as temperature decreases Poissson's ratio will substantially reduce. In addition, the data demonstrate that as the temperature approaches 0 °C (32 °F) the coefficient approached 0.5, similar to an ideal plastic body at lower temperatures.

Table 2-4: Values of Poisson's coefficient for frozen soils (after Tsytovich, 1975)

Designation of Soil	Total Moisture W_d, %	Temperature °C (°F)	Axial Stress, σ_t MPa (tsf)	Poisson's Coefficient
Frozen Sand	19.0	-0.2 (31.6)	0.20 (2.0)	0.41
	19.0	-0.8 (30.6)	0.59 (6.1)	0.13
Frozen Silty Loam	28.0	-0.3 (31.5)	0.15 (1.5)	0.35
	28.0	-0.8 (30.6)	0.20 (2.0)	0.18
	25.3	-1.5 (29.3)	0.20 (2.0)	0.14
	28.7	-4.0 (24.8)	0.59 (6.1)	0.13
Frozen Clay	50.1	-0.5 (31.1)	0.20 (2.0)	0.45
	53.4	-1.7 (28.9)	0.39 (4.1)	0.35
	54.8	-5.0 (23.0)	1.18 (12.3)	0.26

2.6 Sectional Analysis Tool

In an attempt to handle the multiple issues associated with determining the moment-curvature behavior of a confined concrete section, such as the column and foundation shafts, a

section analysis tool was developed at ISU by Levings (2009). The program, Versatile Section Analysis Tool (VSAT), was designed to include the following features: 1) permitting different cross-sections; 2) allowing both normal strength and ultra-high performance concrete (UHPC) material behavior; 3) enabling mild steel and prestress reinforcing steel; 4) allowing the confining effects of soil pressure; 5) including a steel shell circular section; and 6) accounting for low temperature effects on concrete and steel behavior. Upon selecting the appropriate features, VSAT would define the moment-curvature the chosen section.

The geometry of the cross-section is a major contributor to the moment-curvature response; therefore, VSAT was designed to handle different sections. Typical cross-sections, such as circular and rectangular sections, used in the seismic design of reinforced concrete as well as well as some unusual sections, including circular concrete filled steel shells and H-shaped ultra high performance pile sections, are available. Each of these sections can be subjected to a compressive or tensile external axial load and/or prestress forces during the analysis.

Simplified normal strength concrete and UHPC models exist in VSAT to allow the user to accurately define the behavior of concrete with a minimal number of variables. Both the tensile and compressive concrete stress-strain profiles can be modeled in VSAT to allow for a more accurate depiction of how concrete contributes to the section's performance. A more complex normal concrete model, as discussed in Levings (2009), is also available to account for the varying confinement as the transverse reinforcing steel behaves in an elastic, plastic and strain hardening manner.

In addition to the concrete models, the stress-strain behavior of mild steel and prestress reinforcing, along with their ASTM diameters and areas, can be defined within VSAT. This lessens the input required by the user during the analysis definition stage. The user may, however, opt to enter their own for bar sizes with areas calculated assuming a circular cross-section.

The inclusion of soil pressure and/or an exterior steel shell alter(s) the section's performance during loading. VSAT models these effects as a secondary confining pressure that confines all concrete within the section and inhibits the section from spalling cover concrete during loading.

The effects of low temperatures on steel and concrete have also been included in VSAT. The user may enter both an analysis temperature and a temperature at which the material properties are known to eliminate further experimentation that would otherwise be required.

Steel temperature effects are determined based off of the conclusions of this report, as presented in Chapter 6; whereas, the concrete temperature effects are handled based off of data found through a literature review in Levings (2009) which presented data consistent with the experimental study completed in Chapter 5.

2.7 Pushover Analysis Tool

To conduct the numerous pushover analyses within this project, the fifth version of a computer software package entitled LPILE (Reese et al. 2004) was selected. The program takes the specified pile/shaft system and creates a series of beam-column elements as shown in Figure 2-1 to solve Equation 2-1 using the finite difference method. In order to discretize the system into its elements, the user specifies the number of elements along with the material properties and applied loadings. The software then takes the applied loadings and uses the finite difference method to iterate until equilibrium within the displacements, slope, moments and shears of the system are attained. LPILE allows the user to perform a full nonlinear analysis, since the user is able to specifically input a moment-curvature response of the structural shaft and full p-y curves for the soil. This allows the plastic deformation of the system to be captured as the program is iterating using the input moment-curvature response generated in a separate package, such as the tool discussed in Section 2.6. Additionally, the program takes into account the pile/shaft systems boundary conditions (i.e., fixed head or pinned head) during the iteration process to find equilibrium. It is noted, however, that these constraints do not take into consideration the effects of strain penetration.

As part of the study performed by Sritharan et al. (2007) at ISU, LPILE was used to expand the experimental results of Suleiman et al. (2006) to a broader temperature range as discussed in Section 2.3. Prior to using the program for this purpose, a verification of its capabilities was performed using the experimental test results of Suleiman et al. (2006) and the known properties of both the shaft and the surrounding site based on field and laboratory measurements. These properties were then input into LPILE and the system was analyzed to provide a comparison between the field results and the software package. The analysis found the localized critical locations were adequately captured (details in Chapter 3). Additionally, the global response compared well between the field test and computer simulation results as shown in Figure 2-28.

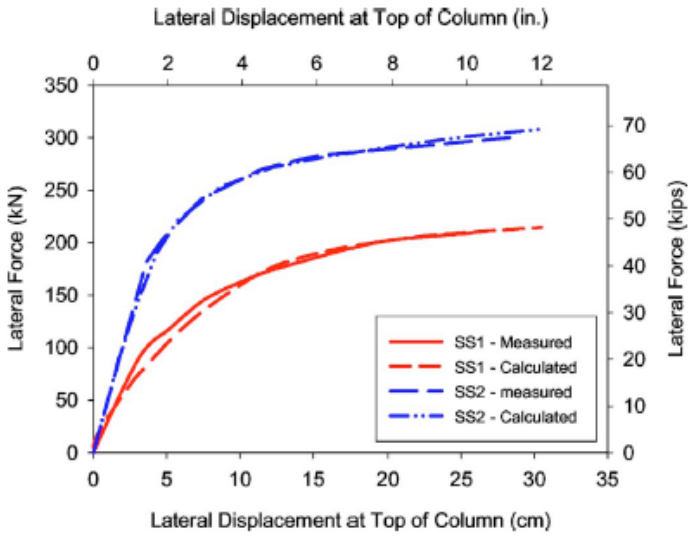

Figure 2-28: Comparison of the measured and calculated force-displacement response envelopes of the column-foundation systems at different temperatures (Sritharan et al. 2007)

CHAPTER 3: EXAMINATION OF EXISTING METHODS

3.1 Introduction

In today's engineering practice, many models are available for use in the design and analysis of drilled shafts subjected to lateral loading. Several of the models currently recommended for seismic design and analysis were introduced in Chapter 2: Literature Review. This chapter illustrates in detail that each of these methods uses different procedures and techniques to account for the effects of SFSI. To better understand the models and the underlying rationale, this section further examines the different methods presented within the literature review through an example problem of a continuous bridge column supported by a CIDH shaft.

3.1.1 Example Problem

In order to compare the different methods to an experimental baseline, the identical full-scale systems (i.e., SS1 and SS2) used in the exploratory research program by Suleiman et al. (2006) and Sritharan et al. (2007) were chosen as the integrated column-shaft system. The column and foundation shafts, depicted in Figure 3-1, were originally designed taking into consideration the average column and foundation reinforcement details used in the Midwest and high seismic regions, as well as the seismic design recommendations included in the Applied Technology Council (ATC) 32 guidelines (1996) and AASHTO (1998). Due to the limitations of the different models, soil profiles were varied based on the method being examined and are presented in the respective sections below.

3.1.2 Moment – Curvature Analysis

To create an accurate analytical model that can characterize the nonlinearity in the system, moment-curvature analyses must be performed for the different cross-sections depicted in Figure 3-1. To perform these analyses, VSAT (Levings, 2009) was used with the loadings and material properties provided in Table 3-1. The material properties and loadings were taken from the analytical study performed by Sritharan et al. (2007) for the warm weather integrated column-shaft system, SS1. The results of the moment-curvature analyses are provided in Figure 3-2 and idealized later, depending on the requirements of the specific model being examined. The longer lines within Figure 3-2 are for the two foundation cross-sections and are nearly identical. Although soil confinement pressure alters the moment-curvature response, it is ignored in the

initial detailed analyses and therefore ignored in this section. The effects of soil confinement and how they were included in the analysis, however, are described in the sections that follow to help develop a more accurate analytical model.

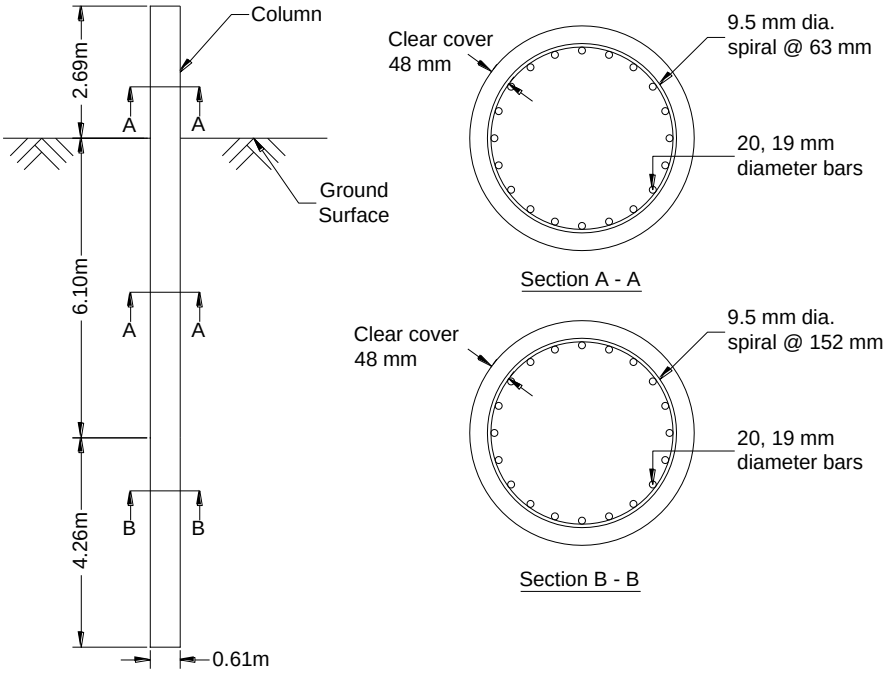

Figure 3-1: Details of experimental test units SS1 and SS2 (after Sritharan et al., 2007); (1 in. = 25.4 mm = 2.54 x 10^{-2} m)

Table 3-1: Loading and material properties used for moment-curvature analyses of SS1 cross-sections (see Figure 3-1)

	Location (Cross-Section)		
Material Property	**Column (A-A)**	**Foundation (A-A)**	**Foundation (B-B)**
Axial load, P [kN (kip)]	0 (0)	0 (0)	0 (0)
Concrete compressive strength, f'_c [MPa (ksi)]	57.9 (8.4)	56.5 (8.2)	56.5 (8.2)
Concrete cracking strain, ε_{co}	0.002	0.002	0.002
Ultimate concrete strain, ε_{cu}	0.01367	0.01386	0.0086
Concrete tensile strength, f'_t	$7.5(f'_t)^{0.5}$		
Steel yield stress, f_y [MPa (ksi)]	471.5 (68.4)		
Steel ultimate stress, f_u [MPa (ksi)]	748.4 (113.8)		
Ultimate steel strain, ε_{su}	0.12		

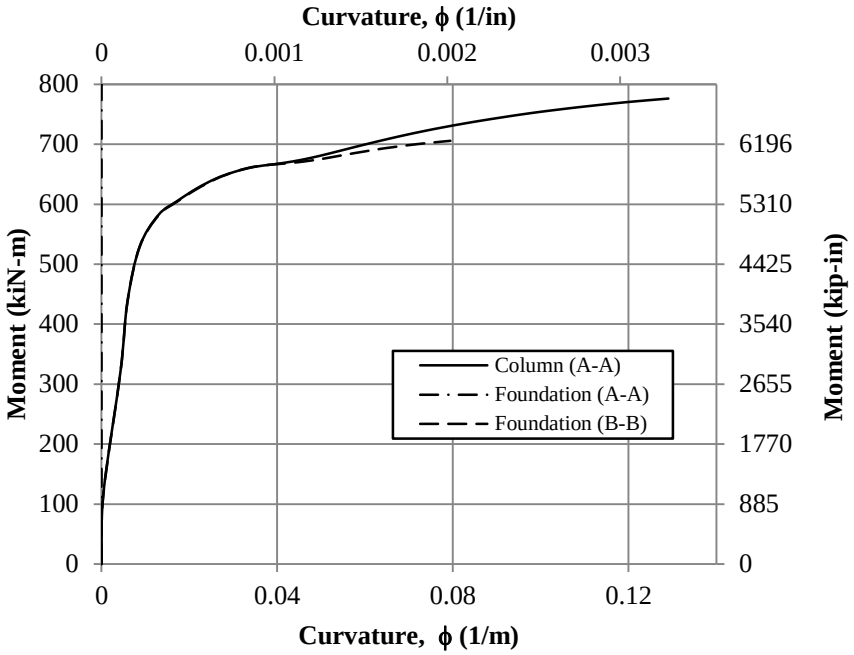

Figure 3-2: Moment-curvature response of SS1 cross-sections without soil confinement

3.2 Detailed Analysis

The current bridge design specifications in use today, AASHTO (2007 and 2009), suggest that a detailed analysis involving soil springs is a more appropriate means to correctly model the lateral load response of drilled shafts in soil. To use this method, a computer program, such as LPILE (Reese et al., 2004) or FB-Pier (UF, 2009), is needed to perform a numerical analysis that will find the structural equilibrium at a given loading condition, force or displacement. These computer programs require a significant amount of information about the site to complete the analysis and have limitations when examining nonlinear shaft/pile response. This section will further discuss the needs of such a detailed method by examining the use of LPILE (2004) in determining the lateral response of the example column/foundation system presented in Section 3.1. As a basis of comparison, analysis results obtained for a model of SS1 in LPILE will be compared with the experimental results of this system as reported by Suleiman et al. (2006).

To use a computer program such as LPILE, the first step in determining the lateral behavior of a drilled shaft foundation is to define the type of analysis needed for the project. For the example problem, a full nonlinear static analysis was chosen to represent the inelastic action expected within the foundation shaft due to the lateral loading. After defining the type of analysis to be used by the program, the integrated column/foundation system and surrounding

soil properties must be defined. The first step in this process was to define the structural parameters of the shafts (e.g., cross-sectional area, moment of inertia and stiffness).

A key component in defining the structural parameters was the modeling of the shaft stiffness. In LPILE, the full moment-curvature results of the column and shaft section are used to accurately represent the stiffness of the SFSI system when performing a full nonlinear analysis. The inputs needed for this are the flexural rigidities and moments of the different cross-sections along the length of the shaft. The values taken for this step were initially specified within Section 3.1.2. After manually inserting these data sets generated from other software, the next step is to define the soil parameters at the site.

Since the basis of comparison for this analysis was with the experimental research completed by Suleiman et al. (2006), the soil profile obtained for the field test location at the Spangler testing facility on the ISU campus was directly used in the analysis; however, the soil profile was later modified to meet the capabilities of the approach being examined. Accordingly, the site contained a glacial till composed mostly of low plasticity clay with a permanent water table at 8.2 m (26.9 ft) below the ground surface. To better define the entire soil profile along the length of the shaft, the CPT data established in this research project are reproduced in Figure 3-3a. The undrained shear strength, c_u, of the soil was then computed by using the method presented by Robertson and Campanella (1983) with a soil unit weight of 21.2 kN/m^3 (0.078 lb/in^3), Figure 3-3b. To input the soil profile into LPILE, the graphs were broken into piecewise linear portions and the resulting data were used to define the soil parameters needed for the selected soil models. The soil model chosen for this analysis was Reese's stiff clay model with and without free water as needed by the ground conditions. The soil parameters used by this method included the soil's effective unit weight, γ, undrained shear strength, strain at fifty percent of the maximum compressive stress and a p-y modulus, k, as needed. The p-y modulus and fifty percent strain value were chosen based on recommendations by Reese et al. (2004). The final points and parameters chosen for the analysis are provided in Table 3-2.

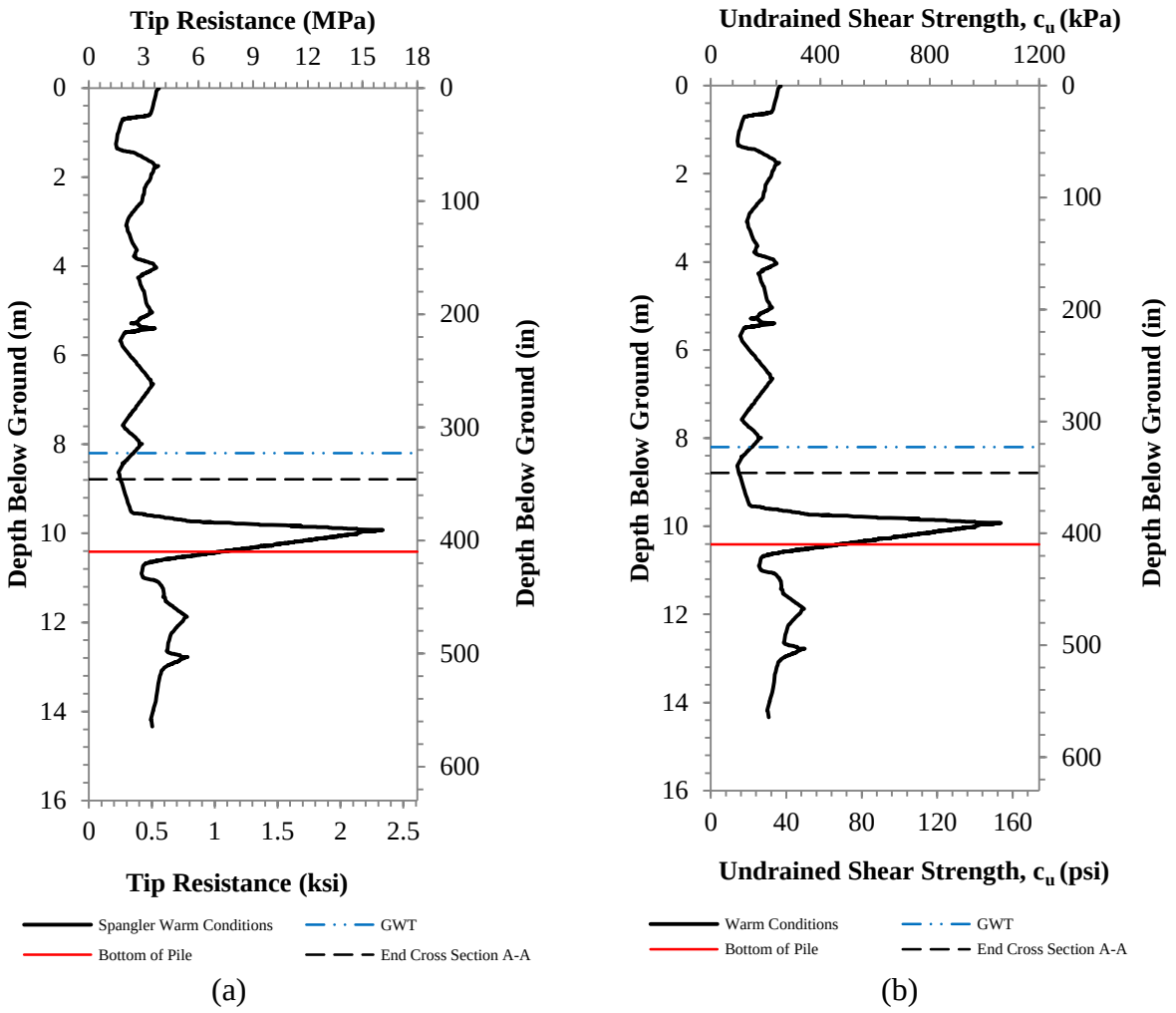

Figure 3-3: Soil profile with depth (a) CPT tip resistance (after Sritharan et al., 2007); (b) Undrained shear strength (GWT = Ground Water Table)

Table 3-2: Primary soil profile chosen for soil springs in LPILE analysis

Depth Below Ground Surface	Water Present	γ	c_u	ε_{50}	k
m (in.)		kN/m^3 (lb/in^3)	kPa (lb/in^2)	in/in	MN/m^3 (lb/in^3)
0 (0)	No	21.2 (0.078)	253 (36.7)	0.0045	N/A
0.61 (24)	No	21.2 (0.078)	193 (28)	0.005	N/A
1.22 (48)	No	21.2 (0.078)	96.5 (14)	0.007	N/A
1.40 (55)	No	21.2 (0.078)	115 (16.7)	0.005	N/A
5.33 (210)	No	21.2 (0.078)	186 (27)	0.005	N/A
8.23 (324)	Start GWT	21.2 (0.078)	152 (22)	0.005	271.5 (1000)
8.79 (346)	Yes	21.2 (0.078)	100 (14.5)	0.007	135.7 (500)
10.41 (410)	Yes	21.2 (0.078)	345 (50)	0.004	542.9 (2000)

Note: GWT = Ground Water Table

As part of the comparison, a secondary soil profile was created based off of the laboratory soils testing completed for this field experiment. In Sritharan et al. (2007), stress-strain curves obtained from unconfined compression tests on soil samples were provided for the Spangler test site (see Figure 3-4a) as a function of temperature. Using this information along with the CPT, p-y curves were generated (see Figure 3-4b) using Reese and Welch's methodology (1975) for approximately the first two pile diameters below the ground surface, since the soils closest to the ground surface play a significant role in the lateral response of an integrated column-shaft system. The second soil profile is shown in Table 3-3.

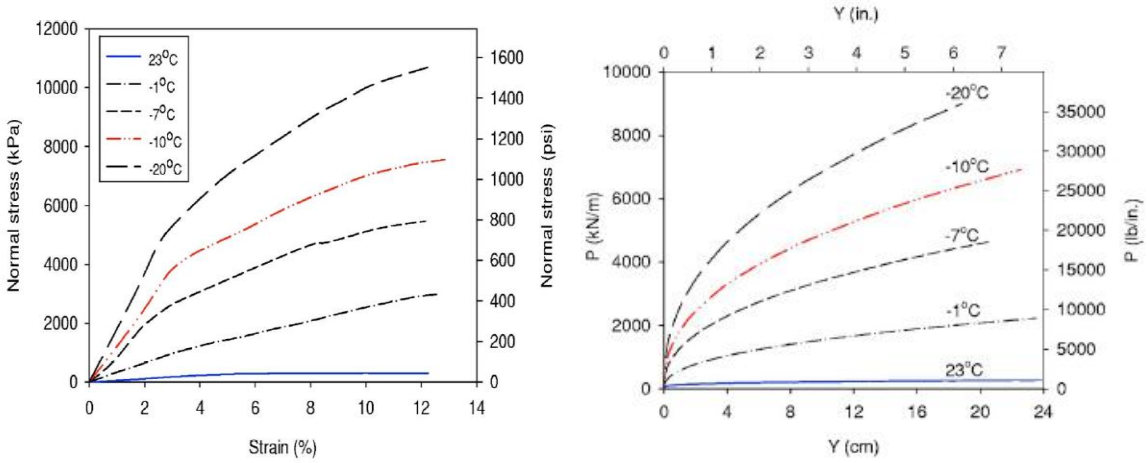

(a) Unconfined compression stress-strain curves (b) p-y curves

Figure 3-4: Laboratory testing for development of soil springs at Spangler test site from Sritharan et al. (2007)

Table 3-3: Secondary soil profile chosen for soil springs in LPILE analysis based on laboratory testing modifications

Depth Below Ground Surface	Water Present	γ	c_u	ε_{50}	k
m (in.)		kN/m^3 (lb/in^3)	kPa (lb/in^2)	in/in	MN/m^3 (lb/in^3)
0 (0)	No	p-y curve			
0.61 (24)	No	p-y curve			
1.22 (48)	No	p-y curve			
1.40 (55)	No	p-y curve			
5.33 (210)	No	21.2 (0.078)	186 (27)	0.005	N/A
8.23 (324)	Start GWT	21.2 (0.078)	152 (22)	0.005	271.5 (1000)
8.79 (346)	Yes	21.2 (0.078)	100 (14.5)	0.007	135.7 (500)
10.41 (410)	Yes	21.2 (0.078)	345 (50)	0.004	542.9 (2000)

Note: GWT = Ground Water Table

The final major step prior to completing the analysis of the integrated column-shaft system in warm weather conditions, SS1, was to define the boundary conditions enforced at the top of the column. Depending on the analysis program selected, these conditions may be defined in a manner of different ways (e.g., shear and moment, shear and rotation, displacement and moment, pinned, fixed, etc.). The main boundary condition specified for the example problem was that a pinned connection was present between the superstructure and bridge column. With this as the basis, a pushover analysis was performed using the following criteria:

- the pushover analysis should be run incrementally by increasing the boundary conditions at the top of the column whether through force or preferably displacement means;
- first occurrence of the extreme compression fiber in the concrete reaching a strain, ε_c, of 0.002. This value is important in the soil confinement process as this is where the unconfined and confined concrete curves begin to deviate from one another; and
- ultimate lateral displacement occurs when the ultimate curvature, ϕ_u, of a cross-section is reached (typically within foundation shaft). This curvature assumes that a flexural failure in the system occurs at the in-ground hinge when a pinned superstructure is present in the analysis.

After running an initial analysis on the drilled shaft system, an iterative process that included changing the target pile head displacements was used to locate the second and third points listed in the above criteria. These points were critical to the analysis in that they are used to define the amount of soil pressure acting as confinement to the foundation shaft based on the study performed by Sritharan et al. (2007), and should be included in the moment-curvature analysis. Using the procedure suggested by these authors, the average soil pressure experienced by the foundation shaft was found to be 372.3 kPa (54 psi) and 296.5 kPa (43 psi) for the primary and secondary soil profiles, respectively. These pressures were applied along the length of the foundation shaft in which the concrete strain exceeded 0.002 at the ultimate condition, since this is where the response of the shaft would be altered. This point typically occurred before the change in reinforcement properties and was therefore only applied to the foundation shaft of cross-section A-A. Although a non-uniform soil pressure more accurately represents the soil confinement, a uniform pressure was specified for the different soil profiles based on the limitations of VSAT. Using these soil pressures, the moment-curvature analysis was repeated and the results indicated an increase in the ultimate moment and ultimate curvature for the

foundation shaft. The ultimate moment and curvature of the foundation section increased by 3.7% and 7.5% in the primary soil profile analysis; whereas, an increase of 2.9% and 5.9% was experienced in the secondary soil profile analysis. The results of the moment-curvature analysis for the foundation shaft with cross-section A-A are shown in Figure 3-5.

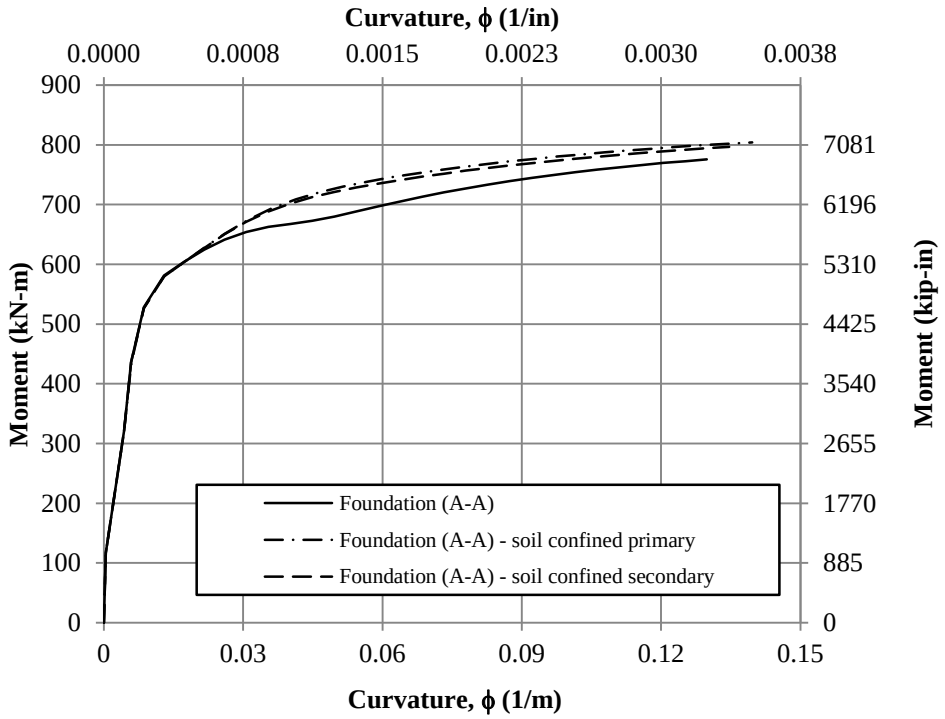

Figure 3-5: Moment-curvature analyses revised after adjusting the effects of soil confinement for the foundation cross-section A-A

Upon completion of the second moment-curvature analyses, LPILE was reconfigured with the new structural parameters and run again using an iterative process to determine the lateral force-displacement response of the system. The results of two critical conditions, the point of first yielding and the ultimate point, are presented within Table 3-4 for the different soil profile models. The overall global lateral force-displacement responses of the final models are compared to the experimental data from Suleiman et al. (2006) in Figure 3-6.

Figure 3-6 includes the global results of a third analysis, for use in later comparisons, in which the soil profile was created to be a uniform soil along the length of the foundation shaft. The parameters of the uniform soil were found by using a weighted average of the unconfined compressive strength of the soil within the first six pile diameters below the ground surface.

Table 3-4: Lateral load response of SS1 at the critical conditions

		Soil Profile	
Critical Value	**Experimental**	**Primary (CPT)**	**Secondary (Lab)**
First yielding lateral load	137.75 kN (30.97 kip)	147.4 kN (33.14 kip)	138.15 kN (31.1 kip)
First yielding column head displacement	6.25 cm (2.45 in.)	5.54 cm (2.18 in.)	6.65 cm (2.617 in.)
Ultimate lateral load	Not pushed to failure	270.5 kN (60.80 kip)	252.6 kN (56.78 kip)
Ultimate displacement	Not pushed to failure	64.62 cm (25.44 in.)	78.87 cm (31.05 in.)
Max. moment location from top of column	3.69 m (145.28 in.)	3.32 m (130.72 in.)	3.67 m (144.48 in.)

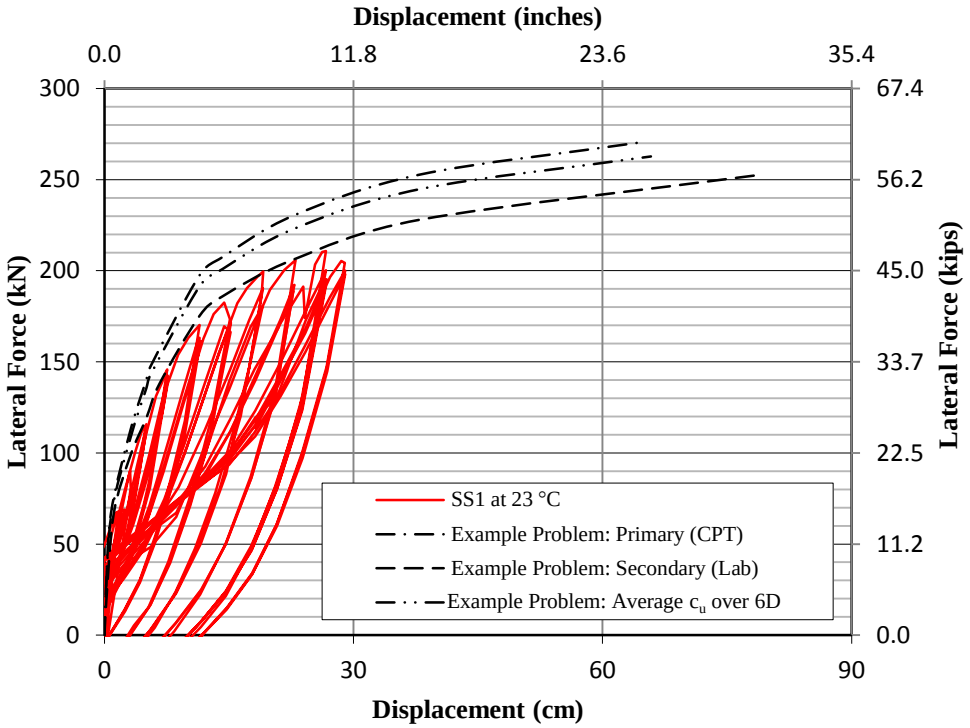

Figure 3-6: Global lateral load response of LPILE analyses compared to experimental results of Suleiman et al. (2006)

Besides the global responses mentioned above, a computer program using the Winkler soil spring method also provides information regarding the localized responses. This is possible as the method employed internally by LPILE uses a numerical process (i.e., the finite difference method) to find structural equilibrium along the length of the column-foundation shaft. Some of the more critical localized responses are provided in Table 3-5 for the primary and secondary soil profiles.

Table 3-5: Localized responses of final models at the ultimate condition

	Soil Profile	
Local Response Values	**Primary (CPT)**	**Secondary (Lab)**
Elastic Curvature, ϕ_e	0.0098/m (0.0002486/in.)	0.011/m (0.0002749/in.)
Plastic Curvature, ϕ_p	0.13/m (0.003294/in.)	0.127/m (0.00322/in.)
Elastic Rotation below Max Moment, θ_{eb}	0.01783 rad	0.01987 rad
Plastic Rotation below Max Moment, θ_{pb}	0.08220 rad	0.08942 rad
Total Plastic Rotation, θ_p	0.15737 rad	0.17386 rad
Translation at Max Moment Location, Δ_{trans}	5.42 cm (2.132 in.)	6.07 cm (2.39 in.)
Length to First Zero Moment after Max, L_{m0}	6.84 m (269.35 in.)	7.19 m (283.13 in.)
Analytical Plastic Hinge Length, L_p	1.21 m (47.78 in.)	1.37 m (53.99 in.)
Actual Plastic Hinge Length, $L_{p,actual}$	3.77 m (148.48 in.)	3.85 m (151.37 in.)

The method discussed above, although it provides more detailed results with good accuracy, has several challenges associated with its use in design practice, as follows:

1. A significant amount of information is required about the structure and surrounding soil to create an accurate model that represents real world conditions. This information includes the drilled shaft and column dimensions, reinforcing details along the length of the entire system, axial and lateral loading conditions, and boundary conditions at the column superstructure interface. The main issue, however, is detailed information about the surrounding soil (e.g., CPT and laboratory testing) is needed to accurately capture the lateral load response. In most cases, a designer may only be able to blindly predict the behavior of the system within about 15%.
2. The selected soil profile, especially near the ground surface, alters the overall response of the system significantly. This is prevalent within Figure 3-6, where the soil profile based off of laboratory testing near the ground surface provided a more realistic soil response and, therefore, a more accurate lateral load behavior. This can be further emphasized by examining the global lateral displacement from the different curves generated for the system for a given lateral force, especially in the 200 kN (45 kip) to 250 kN (56 kip) range. Taking for example an inertial force of 200 kN (45 kip), the lateral displacement demand shows a variation of approximately 60%, which can cause an undesirable failure mechanism depending on the method chosen, leading to a potential violation of the assumption made within the capacity design principles. This variation is significant in

seismic design, where the displacements experienced by a system are extremely important to ensure an adequate performance is maintained over the lifespan of the structure. Therefore, one may conclude that the model will only be as good as the information used during its creation.

3. The number of iterations needed to ensure the equilibrium of the SFSI system at a given loading condition for these methods typically requires an expertise in software, such as LPILE (2004) or FB-Pier (2009), since the computations are not easily performed by hand.
4. Every time a structural or soil parameter is modified, a new model must be constructed in the appropriate computer software. This leads to numerous models being constructed, so an accurate representation of the lateral load response of a column supported on a CIDH shaft is obtained. New models must be created to ensure the new system will effectively maintain the desired performance and adhere to the capacity design principles stated in Chapter 1.
5. The design process using this method will require a significant amount of time to complete. More time is required than with other methods due to the creation of multiple models because of the inherent iterative process between the foundation engineering and structural design.
6. The effects of wintry conditions were not considered in this section or the AASHTO specifications used for this project, but Sritharan et al. (2007) addressed this concern. In the study, the researchers found that seasonal freezing could be modeled using LPILE when soil and structural parameters were modified for these conditions.

3.3 Chai (2002)

3.3.1 Clay

Since the method of designing and analyzing drilled shafts proposed by Chai (2002) was suggested for use in the AASHTO guidelines for seismic design (2009), an attempt was made to compare the model Chai provided to that of the more detailed soil spring model verified in Section 3.2 as well as the experimental data from Suleiman et al. (2006). Two modifications to the soil and structural parameters were necessary to undertake Chai's method for use in the verification process. The first modification was that the soil needs to be represented as a single

uniform layer, and the second modification was the moment-curvature analysis needs to be idealized to provide an elasto-plastic response. The remainder of this section discusses how these modifications were made and compares the results with the experimental data found from Suleiman et al. (2006) and the detailed soil spring model shown in Section 3.2 to the response of the model suggested by Chai (2002).

To provide a realistic verification, the CPT data shown in Figure 3-3 were used to determine the properties of the uniform soil layer using properties within the first six pile diameters of the ground surface due to the models development (Chai 2002). Although the CPT data did not provide the closest lateral response in Section 3.1, these data were considered the best option for computing average soil properties. By using this information, the soil profile was the same as the primary profile presented in Table 3-2. The uniform soil layer was then constructed by finding a weighted average of the undrained shear strength of the soil within the first six diameters of the ground surface. This length was chosen in the range for which Chai's method would be applicable. The final soil profile was found to be a soil with a unit weight of 21.2 kN/m^3 (0.078 lb/in^3) and an undrained shear strength, c_u, of 150.2 kPa (21.79 psi).

The structural parameters used for the model were modified by relating the area under the moment-curvature response with soil confinement effects for the primary condition depicted in Figure 3-5 to that of an idealized elasto-plastic response. Similar to the detailed analysis, only the foundation with cross-section A-A was examined, as this section develops the plastic action and, therefore, will dictate the inelastic response of the total system. The area under the curve was determined by generating a cubic function in Mathcad 14 (PTC 2007) that represents the moment-curvature response. This function was then integrated over the entire curvature spectrum to find an area that may be related to the elastoplastic response. Using this area, an elastoplastic response was found, in which the yield moment, M_y, was 739.9 kN-m (6549 kip-in), the corresponding yield curvature, ϕ_y, equals 0.00985/m (0.000255/in.) and the ultimate curvature, ϕ_u, equals 0.1396/m (0.003546/in.) at an ultimate moment equivalent to M_y. The idealized elasto-plastic response is compared to the more accurate response shown in Figure 3-7, where it is noted that the idealized curve goes through the first yield point.

Upon determining the aforementioned modifications, Chai's model was completed following the procedures described in Section 2.2.4. The results found using this method are as follows:

- modulus of horizontal subgrade reaction, k_h = 10.06 MPa (1459.7 lb/in^2);

- shaft characteristic length, R_c = 164.54 cm (64.78 in.);
- coefficient for aboveground height and depth to fixity, ξ_a and ξ_f = 1.636 and 1.464;
- depth to point of fixity, L_f = 240.84 cm (94.82 in.);
- normalized aboveground height and depth to fixity, L_a^* and L_f^* = 4.42 and 3.95;
- normalized maximum moment, M_{max}^* = 21.744;
- normalized depth to maximum moment location, L_m^* = 1.160;
- depth to maximum moment from the ground surface, L_m = 70.72 cm (27.84 in.);
- normalized ultimate shear at top of column, V_u^* = 4.28;
- ultimate shear at top of column, V_u = 238.84 kN (53.693 kip);
- yield displacement, Δ_y = 14.33 cm (5.64 in.);
- normalized plastic hinge length, λ_p = 1.442;
- plastic hinge length, L_p = 87.88 cm (34.6 in.);
- plastic curvature, ϕ_p = 0.13/m (0.003291/in.);
- plastic rotation at ultimate condition, θ_p = 0.1139 radians;
- plastic displacement at ultimate, Δ_p = 38.71 cm (15.24 in.); and
- total lateral displacement at column top, Δ_u = 53.03 cm (20.88 in.).

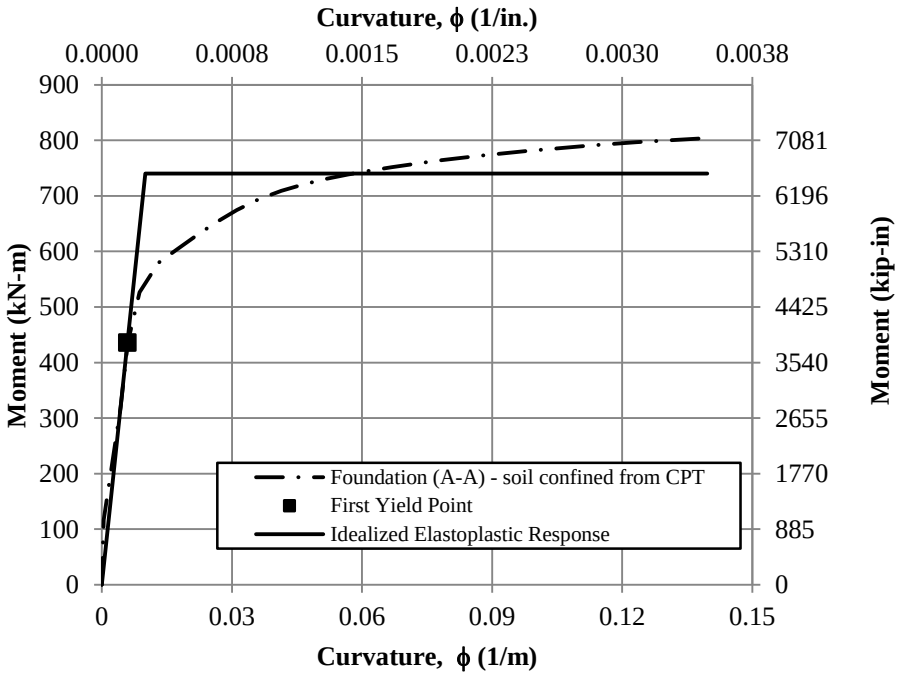

Figure 3-7: Idealized moment-curvature analysis for Chai's method

Based on the analysis results presented above, the local and global responses of the example problem were compared. Chai's method provides an initial secant stiffness to the first yield point as 1667.2 kN/m (9.52 kip/in) compared with experimental results of 2213.6 kN/m (12.64 kip/in) a difference of 24.7%. If yielding for the experimental data is approximated at a displacement of 10 cm (3.94 in.) and a lateral force of 177.93 kN (40 kip) for a bilinear idealization, Chai's model over predicts the displacement and force at yield by 43.3% and 34.2%, respectively. At the ultimate condition, Chai's model under predicts the displacement and force by 32.8% and 5.4% when compared to the detailed analysis using the secondary soil profile. The global response comparison is presented in Figure 3-8. When compared to a soil spring method or experimental data the model over predicts the yield point, but the ultimate condition appears to be within about 15% of the experimental data. The results of the local responses of the detailed analyses and Chai's model are compared in Table 3-6, in which the data demonstrate the inelastic range of the lateral loading is not accurately predicted. The maximum moment location, a localized parameter that can be compared with the experimental data, was under predicted by 29.3%; thus, stating that the point at which the most damage will occur is closer to the ground surface than where it actually occurred.

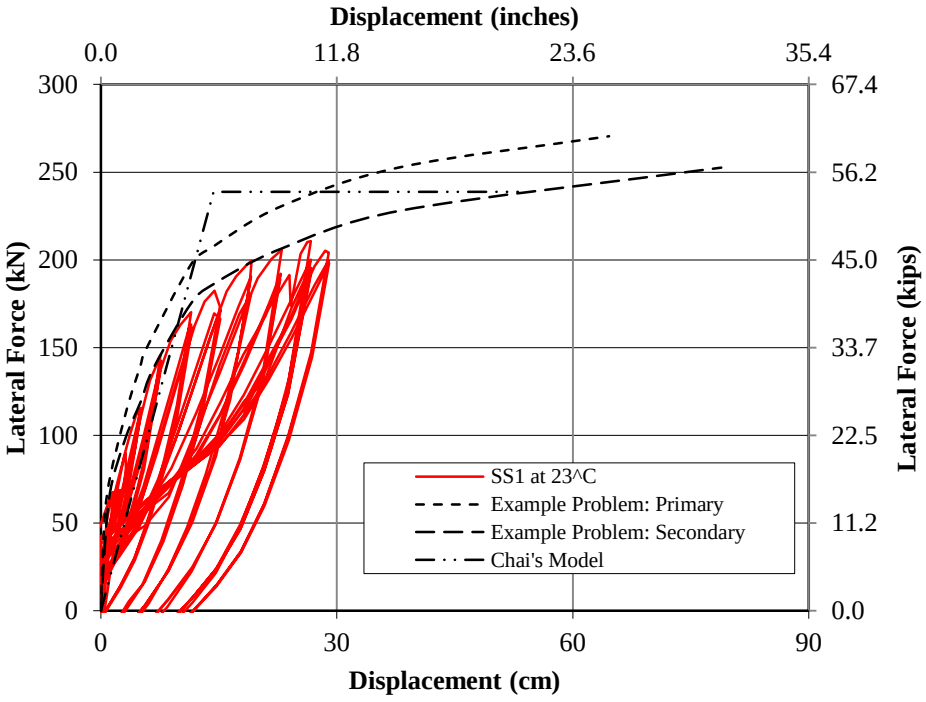

Figure 3-8: Global response based on Chai's method to those from experimental testing and detailed models containing nonlinear soil springs

Table 3-6: Local response comparison between Chai's method and the nonlinear soil spring methods

Local Values	Soil Spring Method		Chai Method	% Difference	
	Primary (CPT)	Secondary (Lab)		Primary (CPT)	Secondary (Lab)
ϕ_e	0.0098/m (0.0002486/in.)	0.0108/m (0.0002749/in.)	0.0098/m (0.00025/in.)	0.56%	9.06%
ϕ_p	0.1297/m (0.003294/in.)	0.1268/m (0.00322/in.)	0.1296/m (0.003291/in.)	0.09%	2.20%
L_m	0.628 m (24.72 in.)	0.977 m (38.48 in.)	0.707 m (27.84 in.)	12.62%	27.65%
θ_p	0.15737 rad	0.17386 rad	0.1139 rad	27.62%	34.49%
Δ_{trans}	5.42 cm (2.132 in.)	6.07 cm (2.39 in.)	Cannot Compute	Cannot Compute	
L_p	1.21 m (47.78 in.)	1.37 m (53.99 in.)	0.879 m (34.6 in.)	27.58%	35.91%
$L_{p,actual}$	3.77 m (148.48 in.)	3.84 m (151.37 in.)	Cannot Compute	Cannot Compute	

Chai's method demonstrated that a fairly good representation of a bilinear response of the SFSI system can be attained. Although the ultimate condition appears to be more accurately captured, the yield location is of great importance for both force and displacement responses, since this dictates when the plastic hinge in the foundation shaft starts to form. In this model the yield force and displacement are over predicted by approximately 40%. The verification of Chai's model has demonstrated some shortcomings associated with the use of this approach when applied to CIDH shafts in cohesive soils. The challenges associated with the method are believed to be mostly due to the fact that the model was verified against data from full-scale testing in cohesionless soils. The concerns associated with this method of predicting the local and global responses of CIDH shafts in cohesive soils are as follows:

1. The use of an elasto-plastic moment curvature response assumption introduces larger errors, as it ignores the nonlinear behavior of reinforcing steel and to a larger extent that of soil, leading to a perfectly plastic force-displacement response between the yield and ultimate limit states. The perfectly plastic response, however, does not seem to capture the experimental response of SS1 in which a second slope occurs between the yield and ultimate limit states.

2. The maximum moment location is over predicted by 12.6% when compared directly to the detailed analysis performed in LPILE using just the CPT data. The location was also under predicted by 27.7% when compared with the detailed analysis using the soil profile with p-y curves generated from laboratory testing. In addition, the maximum moment location was found to be under predicted by 29.3% when compared with the experimental data produced by Suleiman et al. (2006). These differences in the maximum moment location alter the total displacement, although not as significantly as the other parameters, of the system as the plastic rotation is assumed to be concentrated at this location.
3. When compared to the primary and secondary soil profile analyses in LPILE, the plastic rotation in the system was under predicted by 24% and 31%, respectively. Although conservative in a design process, this approach may lead to a higher cost of construction due to the increase in materials needed to obtain the appropriate lateral response of the system. Additionally, variation in the plastic rotation value in this manner under predicts the plastic displacement of the system and the displacement capacity, which is of primary interest in the design of these SFSI systems.
4. The analytical plastic hinge length was also largely under predicted by 24.5% and 32.5%. This value dictates the amount of plastic rotation concentrated at the maximum moment location and, therefore, the lateral plastic displacement of the system at the top of the column. The difference in plastic rotation caused the final displacements to differ by 13.4% and 27.8% when compared to the primary and secondary soil profiles, respectively. In this case, the ultimate displacement can be a little further from actual response, since this type of SFSI system will typically never reach the ultimate displacement of over 20 cm (7.9 in.) without causing other components in the structure to experience damage.

   As part of the comparison between Chai's model and the detailed analyses, the sensitivity of the plastic rotation variation was examined. This was accomplished by assuming the detailed methods would provide a more realistic value of plastic rotation and, therefore, the values presented in Table 3-6 for the primary and secondary soil profiles were assumed to be the correct amount of plastic rotation experienced by the system. By using plastic rotations from the detailed analyses and decreasing them by a randomly selected percentage, a new plastic displacement for Chai's model was computed, assuming no

variation in the maximum moment location. This new plastic displacement was then added to the original yield displacement found through Chai's methodology to find an ultimate displacement of the column supported on a CIDH shaft. The new ultimate displacement value was then compared to the ultimate displacement of the detailed analyses based on the assumption that these were the values expected at the top of the column for a flexural failure at the maximum moment location. The results of this sensitivity analysis are provided in Table 3-7, in which the displacement comparison shows that with minor changes in Chai's plastic rotation, the lateral displacement at the ultimate limit state is altered. This is as expected based on the fact the plastic displacement is simply the amount of rotation multiplied by the distance from the maximum moment location to column tip. An example of the plastic rotation variation is if the rotation was equivalent to that of the detailed analyses, the ultimate displacement in Chai's model would be 105% of the ultimate displacement found in the primary soil profile analysis and 93.14% of the ultimate displacement found in the secondary soil profile analysis. Overall, the trend is approximately linear and was expected based on the equation of plastic displacement.

Table 3-7: Sensitivity of Chai's (2002) plastic rotation on the ultimate displacement capacity of SS1

Error in Plastic Rotation	Percentage of Ultimate Displacement	
	Primary Soil Profile	Secondary Soil Profile
0%	105.0	93.14
2%	103.3	91.64
4%	101.7	90.14
6%	99.99	88.64
8%	98.34	87.14
10%	96.68	85.64
15%	92.54	81.89
20%	88.40	78.14
25%	84.26	74.39
30%	80.12	70.65
35%	75.98	66.90

5. Another challenge associated with Chai's model is experimental verification and determination of plastic hinge length were specified using data from testing in uniform cohesionless soils (Chai and Hutchinson, 2002). By testing in this soil type and

condition, the plastic hinge length, although recommended for use in all soil types and profiles, has effectively been under predicted in cohesive soils of uniform properties. This arises because cohesive soils are generally less stiff and, therefore, develop a larger plastic zone and plastic rotation in the foundation shaft. In addition, the model suggested by Chai (2002) was never verified in cohesive soils; therefore, most likely leading to the inaccuracies within locating the maximum moment location.

6. The final shortcoming associated with this method is the effects of temperature variation are not considered within the model development as presented in Section 3.2 nor can the model be easily extended to address this issue. This is an issue as a temperature variation as large as 60 °C (110 °F) commonly occurs across the United States, as the weather and seasons change. The changes in material properties, however, should be given consideration; since, Sritharan et al. (2007) demonstrated that the overall lateral response of the system will be significantly altered.

3.3.2 Sand

In order to demonstrate the reliability of the non-cohesive model suggested for use by Chai (2002), the four full-scale test setups in Chai and Hutchinson (2002) were examined in more detail. This was achieved by comparing the experimental force-displacement response with that of the analytical model suggested by Chai along with a detailed analysis in LPILE v 5.0 (Reese et al., 2004). Additional full-scale tests do exist in non-cohesive soils, but this was the setup used in the Suarez and Kowalsky (2007) work discussed in Section 3.4 of this report. Other full-scale test data is available (e.g., Kumar and Lalvani, 2004 and Anderson et al., 2003) and may be used for comparisons, but are not presented within this report. Therefore, the comparison presented in this section begins by defining a new moment-curvature response based on the cross-sections and material properties used in the full-scale experimentation in Chai and Hutchinson (2002).

The four column-foundation systems examined consisted of a 406 mm (15.98 in.) diameter shaft with a clear cover of 50 mm (1.96 in.) to the longitudinal reinforcement and an applied axial load of 445 kN (100 kip). Within each test pile, seven Grade A706 22.2 mm (0.874 in.) diameter bars with a well defined yield stress of 421 MPa (61.1 ksi) were used as longitudinal reinforcement. This amount of reinforcement correlates to a longitudinal reinforcement ratio, ρ_l, of 2.1%. Lateral reinforcement was MW25 [5.4 mm (0.21 in.)] or MW45 [7.3 mm (0.29 in.)]

smooth wire with an equivalent yield stress of 710 MPa (103 ksi) and 605 MPa (87.7 ksi), respectively. The MW25 reinforcement was used with test piles 1 and 2 which had an aboveground column height of 2D; whereas, the MW45 reinforcement was used with test piles 3 and 4 which had an aboveground column height of 6D. Since the piles were placed in pairs, each set had a similar concrete compressive strength. For test piles 1 and 2, a compressive strength of 41 MPa (5.95 ksi) was obtained; whereas, test piles 3 and 4 had a compressive strength of 47.5 MPa (6.89 ksi). The final dimension needed for the different analyses was that each system was embedded into the sand a depth of 13.5D or 5.48 m (~18 ft).

With the information provided in the previous paragraph, two moment-curvature analyses were obtained in VSAT (Levings, 2009) for the four different test piles. Upon completion, each analysis was idealized into an elasto-plastic response for use in the analytical model. A comparison of the different curves produced throughout this process, both actual and idealized, is provided in Figure 3-9.

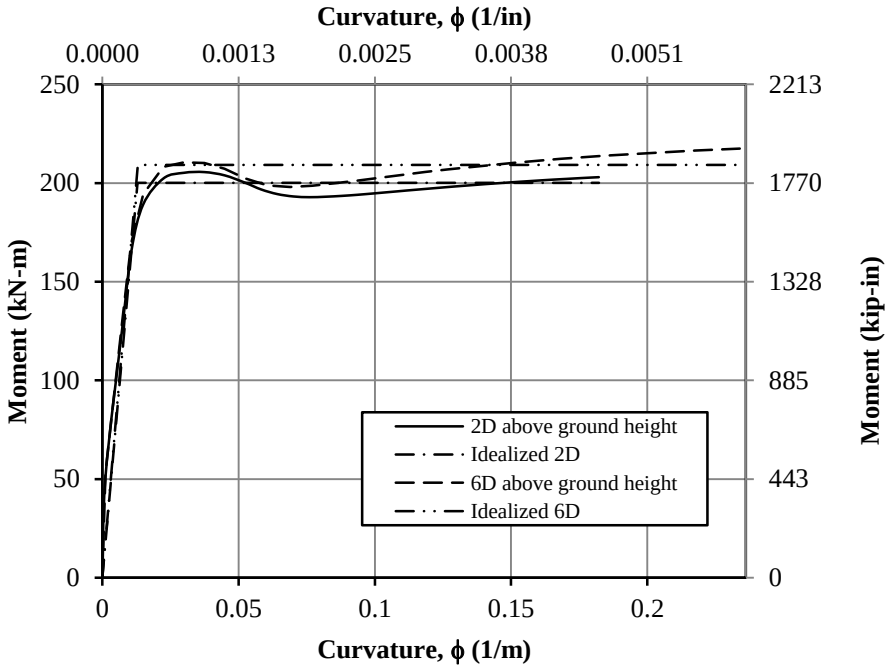

Figure 3-9: Moment-curvature comparison for non-cohesive soil example

Using the idealized and actual responses depicted in Figure 3-9, Chai's methodology (2002) in cohesionless soils and the full nonlinear analysis in LPILE were completed. The multiple analyses were undertaken following the procedures outlined in Sections 2.2.4 and 3.1 without the presence of soil confinement within the comparison. The global responses obtained from the

experiments as well as simplified analytical and detailed approaches were then compared to examine the validity of the simplified approach. Figure 3-10 shows that from a global standpoint, Chai's model can adequately capture the lateral loading response of a bridge column supported on a CIDH shaft in cohesionless soils. This is evident, especially within the 2D above ground height systems, where the analytical model proposed by Chai (2002) closely follows the experimental data. These comparisons further demonstrate a detailed analysis involving the use of soil springs along the entire length of the shaft will provide the most accurate means of determining the lateral loading behavior, since it can account for crushing and spalling of concrete and the variable nature of soil, when experiencing a nonlinear response during a design level or greater seismic event. The deviation between the experimental and methods in the 6D column systems is due to the applied axial load causing excess deformation to occur due to P-Δ effects. Chai's model does not take this phenomenon into account, but could probably be modified to handle the axial conditions, since it greatly impacts the ultimate displacement of the SFSI system.

After examining the global response, a more detailed comparison into some critical locations and values was undertaken between the experimental data and the analytical model produced by Chai. This included an examination of the maximum moment location, the secant stiffness to first yield, and the analytical plastic hinge length. The results of this comparison are provided in Table 3-8, which shows that Chai's analytical approach generally matches well with the full-scale experimental testing of Chai and Hutchinson (2002) as expected. The data provided in Table 3-8, however, suggest the analytical model proposed by Chai has some errors within the definition of the maximum moment location and the secant stiffness to the yield limit state. These errors most likely arise due to the cohesionless soil model selected when development of the maximum moment location was undertaken by Chai (2002), since this parameter greatly influences the lateral load behavior of the SFSI system.

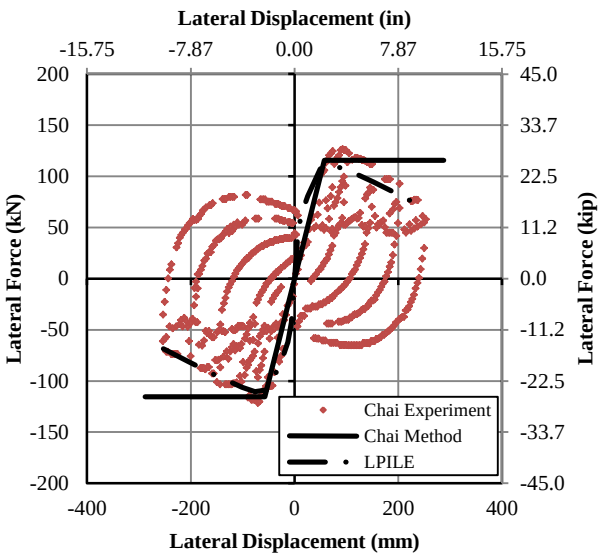

(a) Test Pile #1 – 2D Dense

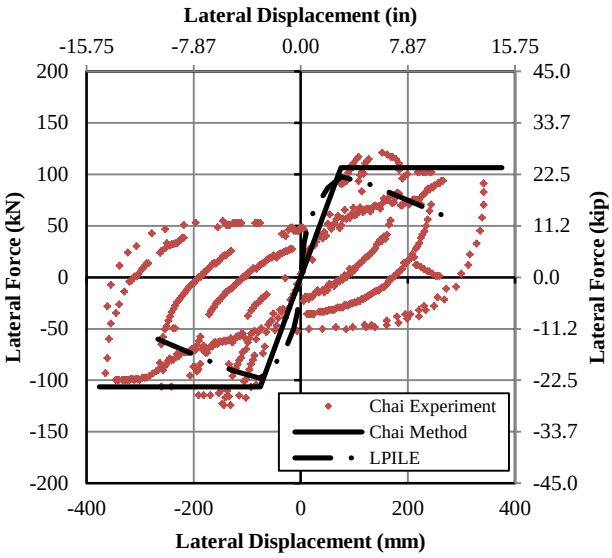

(b) Test Pile #2 – 2D Loose

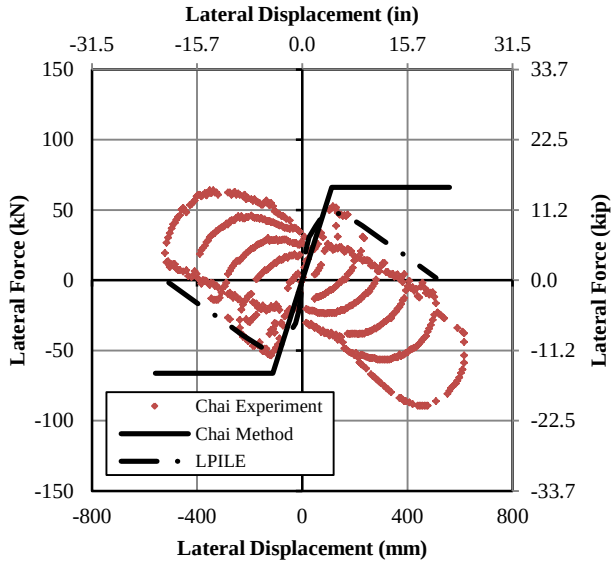

(c) Test Pile #3 – 6D Dense

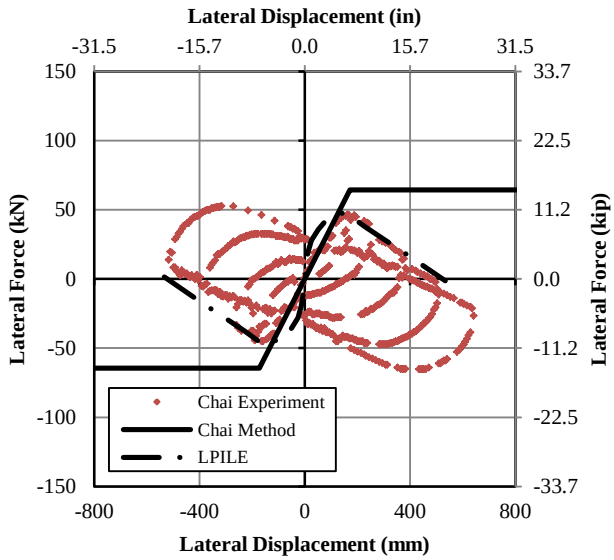

(d) Test Pile #4 – 6D Loose

Figure 3-10: Global response comparison of experimental data with other modeling approaches

Table 3-8: Detailed comparison of experimental values with Chai's analytical model

	Test Pile #1			Test Pile #2		
Value	**Exp.**	**Ana.**	**Error**	**Exp.**	**Ana.**	**Error**
L_m	2.5D	3.39D	35.6%	3.3D	3.94D	19.4%
L_p	1.11D	1.2D	-7.5%	1.2D	1.2D	0.0%
K_{sec}	1715 kN/m (9.79 kip/in)	2008 kN/m (11.47 kip/in)	17.1%	1112 kN/m (6.35 kip/in)	1417 kN/m (8.09 kip/in)	27.4%
	Test Pile #3			**Test Pile #4**		
Value	**Exp.**	**Ana.**	**Error**	**Exp.**	**Ana.**	**Error**
L_m	2.0D	2.68D	34.0%	2.31D	3.00D	29.9%
L_p	1.53D	1.6D	4.58%	1.65D	1.6D	-3.03%
K_{sec}	483.3 kN/m (2.76 kip/in)	591.7 kN/m (3.38 kip/in)	22.43%	335.3 kN/m (1.91 kip/in)	374.5 kN/m (2.14 kip/in)	11.7%

3.3.3 Seasonal Freezing Capability

Section 3.3.2 found the cohesionless soil proposed by Chai (2002) would be able to adequately capture the behavior of a SFSI column-foundation system subjected to lateral loading. Since this was the case, the report authors undertook an investigation into the capability of the method to handle the effects of seasonal freezing within the soil strata. This analysis was completed by modifying the soil parameter in Chai's model to account for freezing. The results of this method were then compared with a more detailed analysis of the SFSI system within LPILE.

In both of the aforementioned models, a modification was made to the soil profile used in test pile 2 of Chai and Hutchinson (2002) to include the effects of seasonal freezing (see Section 3.3.2). The change made to the soil profile consisted of including the presence of a 0.914 cm (36 in.) layer of frozen ground starting at the ground surface. This layer was constructed by arbitrarily increasing the strength properties of the cohesionless soil by 15%, making the soil have an effective friction angle of 42.6° and a rate of modulus increase of 5184.2 kN/m^3 (19.1 lb/in^3). This value was chosen to ensure the method could handle an increase in strength near the ground surface and still capture the lateral response. Once the soil properties were modified, the analysis was run again using a full nonlinear analysis in LPILE and then compared to the method proposed by Chai (2002). To provide a comparable soil for the method suggested by Chai, a weighted average of the soil properties were taken along the length of the foundation shaft and found to be 37.9° and 4620 kN/m^3 (17.0 lb/in^3), respectively.

Results of this comparison are provided graphically in Figure 3-11 and numerically in Table 3-9. In each instance, the data demonstrate the model would be able to adequately capture the effects of seasonal freezing on the lateral load response of a continuous column supported on a CIDH shaft. The deviation between the curves provided in Figure 3-11 is expected to increase as the displacement increases; however, the capabilities of LPILE did not allow this to be demonstrated. The differences can be accounted for based on the inclusion of P-Δ effects increasing the moment at the maximum moment location and causing a drop in the stiffness of the system at a more rapid rate.

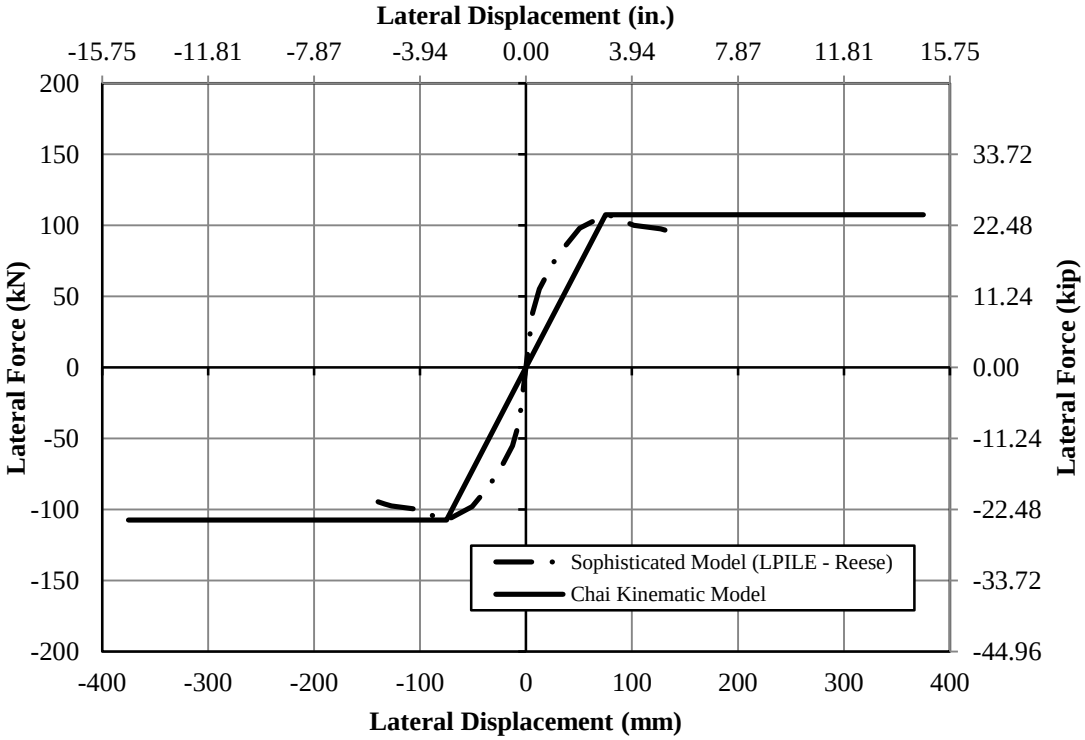

Figure 3-11: Global response comparison of seasonally frozen system in cohesionless soil

Table 3-9: Comparison of detailed analysis method with Chai's methodology (2002) in seasonally frozen ground

Value	Chai	LPILE	Error
L_{ma}	3.88D	2.96D	31.1%
L_p	1.2D	0.57D	110%
K_{sec}	1432.7 kN/m (8.18 kip/in)	2017.7 kN/m (11.52 kip/in)	-29.0%

Although the numerical results in Table 3-9 do not seem to correlate well, this is a matter of how the yield point and soil layers are defined between the two models. In the simpler approach,

the yield is actually defined as the idealized yield location of an elasto-plastic response; however, in the more detailed approach using LPILE, the yield limit state was defined at the first occurrence of yielding in the steel reinforcement. In addition to the definition of the yield limit state, the soil layering used in the two methods makes a difference. In Chai's approach, a single uniform layer of non-cohesive soil is used to estimate the lateral response of an SFSI system in a multi-layered cohesionless soil, leading to inaccuracies.

The 110% error within the analytical plastic hinge length between the two methods is most likely due to the fact that the plastic hinge length will decrease as temperature decreases, as noted in Section 2.3.1. The decrease in the plastic hinge length will directly influence the ultimate displacement of the system and brings the ending points of the two curves, provided in Figure 3-11, closer together and producing less error. The error itself arises from the fact that the analytical plastic hinge length was determined based on the experimental testing of Chai and Hutchinson (2002) performed during warm weather conditions. Even though errors occur between the two approaches, the global response and maximum moment location are captured adequately. Therefore, this method can be used when accounting for the effects of seasonal freezing.

If the ground water table was at the ground surface or not at the ground surface the increase in soil strength properties would have to take into consideration the strength gain surrounding the pile/shaft system due to formation of ice and particle interaction. The specific increases will vary depending on the amount of water present within the system, since the strength of the soil is a function of soil particle contact and quality of ice formation as discussed in Chapter 2. Additional information on how to adequately design for the frozen limit state is provided in Chapter 7 based on experimental testing.

3.4 Priestley et al. (2007)

Another common approach to handling soil-foundation-structure-interaction in cohesive soils is to use the method suggested by Priestley et al. (2007). The method is recommended for a limited range of cohesive soils; therefore, a new soil profile was needed for a basis of comparison, since the previous profile falls outside this range. The selected profile was chosen by the authors of the report to be a uniform layer of soil to a depth of 10.4 m (410 in.) below ground with an undrained shear strength of 40 kPa (5.8 psi) and an effective unit weight of 18.85 kN/m^3 (0.069 lb/in^3) because of the upper limit bound on the capabilities of this approach. Using

this new soil profile, the suggested method was compared against an LPILE analysis using a modified version of the procedure discussed in Section 3.2, which accounts for the nonlinear behavior of soil, concrete and steel.

To minimize the amount of time required to perform an LPILE analysis, the moment-curvature response from column tip to bottom of foundation was assumed constant. In addition, simplification was further included by maintaining consistent material and using a soil confinement value of 372.3 kPa (54 psi) found in the detailed analysis using the primary soil profile (see Section 3.2). This modification was done as the effects of soil confinement would not significantly alter the moment-curvature response of the column-foundation shaft using this system (see Figure 3-5). The main difference, however, was that an axial load of 400 kN (90 kips) was applied to the cross-section. The remaining soil parameters, k and ε_{50}, for Reese's stiff clay model were determined as necessary based off of recommendations by Reese et al. (2004). The results of the detailed analysis performed in LPILE are presented below in Table 3-10 and were used as the basis for comparison.

Table 3-10: Results of detailed analysis of modified SFSI system using LPILE

Global Response	
First Yielding / Ultimate Lateral Load	127 kN (28.6 kip) / 137.4 kN (30.9 kip)
First Yielding / Ultimate Column Head Displacement	12.7 cm (4.98 in.) / 112.1 cm (44.1in.)
Local Response at the Ultimate Limit State	
Maximum Moment Location from Column Tip, H_{IG}	4.54 m (178.88 in.)
Elastic Curvature at ultimate, ϕ_e	0.011 1/m (0.0002701 1/in.)
Plastic Curvature at ultimate, ϕ_p	0.114 1/m (0.002902 1/in.)
Total Plastic Rotation, θ_p	0.1938 radians
Translation at Max Moment Location, Δ_{trans}	9.1 cm (3.58 in.)
Analytical Plastic Hinge Length, L_p	169.6 cm (66.78 in.)
Actual Plastic Hinge Length, $L_{p,actual}$	4.77 m (187.94 in.)

To further establish a basis for comparison, the idealized yield and ultimate locations for the moment-curvature analysis were found through a bilinear idealization of the response. Using this method of idealization, the yield moment was found to be 747.3 kN-m (6614 kip-in) at a curvature of 0.00909 1/m (0.0002309 1/in.) and the ultimate moment was found to be 875.1 kN-m (7745 kip-in) at a curvature of 0.125 1/m (0.003172 1/in.). These values were based on the

foundation shaft response obtained with soil confinement. The actual curve produced by VSAT for the shaft is compared with the bilinear idealization in Figure 3-12.

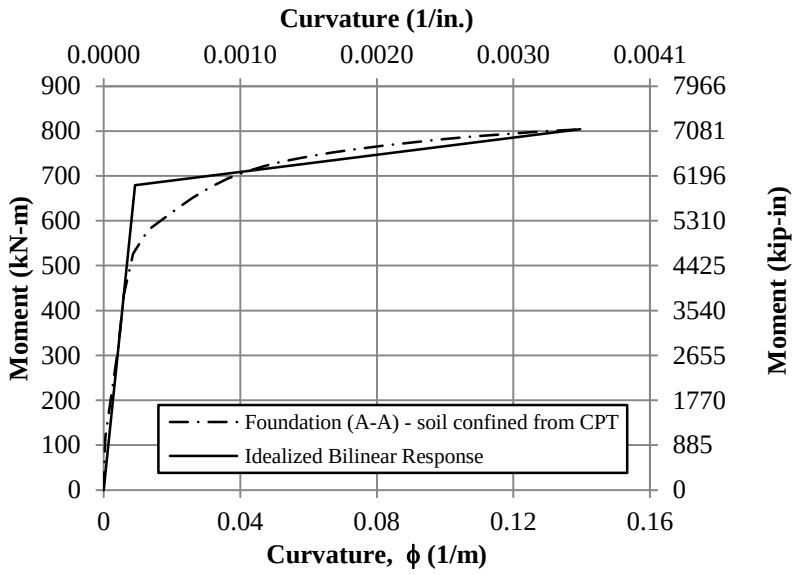

Figure 3-12: Bilinear idealized moment-curvature response

At this point, all of the information needed to perform the suggested method has been obtained and the comparison with the LPILE analysis can be conducted. Following the procedures suggested in Priestley et al. (2007) and Section 2.2.5, the lateral response of the system was determined. This included the computation of limit state strains and curvatures based on suggestions of Priestley et al. (2007), so the method was fully examined for possible limitations. The results of the proposed method are as follows:

- location of in ground hinging from column tip, H_{IG} = 4.94 m (194.3 in.);
- damage control strain limit in concrete and steel, $\varepsilon_{dc,c}$ = 0.01382 and $\varepsilon_{dc,s}$ = 0.07;
- estimated neutral axis depth, c = 13.15 cm (5.14 in.);
- concrete curvature limit state, $\phi_{ls,c}$ = 0.105/m (0.00267/in.) [Controlling limit state since this is the maximum curvature obtainable before section failure according to equations provided in Priestley et al. (2007)];
- steel curvature limit state, $\phi_{ls,s}$ = 0.166/m (0.00423/in.);
- plastic hinge length, $L_{p,IG}$ = 87.88 cm (34.6 in.);
- idealized yield curvature, ϕ_y = 0.0087/m (0.000221/in.);
- coefficient needed to account for fixity conditions, C_1 = 1.232;
- idealized yield displacement based off of in ground hinging, $\Delta_{y,IG}$ = 26.12 cm (10.28 in.);

- plastic curvature, ϕ_p = 0.0963/m (0.00245/in.) at damage control strain;
- plastic rotation, θ_p = 0.0846 rad;
- plastic displacement, $\Delta_{p,IG}$ = 41.77 cm (16.44 in.); and
- total design displacement, $\Delta_{D,IG}$ = 67.88 cm (26.73 in.).

The results of the method suggested by Priestley et al. (2007) to determine the design displacement were then compared with the results of the LPILE analysis (Table 3-10) and bilinear idealization of the moment-curvature response (Figure 3-12), since the model equations are not based on the moment-curvature limits states to find the design displacement. The global information is compared numerically in Table 3-11 while the localized information is compared in Table 3-12. In this method, the lateral loads at the yield and ultimate limit states were not computed, since this requires the use of a spectral chart to determine a period of the system based on an estimate of the viscous damping including soil effects. Additionally, an estimate using the moments associated with the appropriate limit state curvatures was not performed, since knowledge on the effective moment of inertia of the section varies greatly and the exact steel layout is typically not known during the design process.

Table 3-11: Global comparison between LPILE and Priestley models

Value	LPILE	Priestley et al. (2007)	Error
Idealized Yield Displacement	18.56 cm (7.31 in.)	26.12 cm (10.28 in.)	40.63%
Idealized Yield Lateral Load	187.3 kN (42.1 kip)	Not Computed	N/A
Ultimate Displacement	112.1 cm (44.1 in.)	67.88 cm (26.73 in.)	39.45%
Ultimate Lateral Load	137.4 kN (30.9 kip)	Not Computed	N/A

Table 3-12: Localized comparison between LPILE and Priestley models

Value	LPILE	Priestley et al.	Error
Maximum Moment Location from Column Tip, H_{IG}	4.54 m (178.88 in.)	4.94 m (194.3 in.)	8.62%
Yield Curvature, ϕ_y	0.00909/m (0.0002309/in.)	0.0087/m (0.000221/in.)	4.29%
Elastic Curvature at Ultimate, ϕ_e	0.011/m (0.0002701/in.)	0.0087/m (0.000221/in.)	18.18%
Plastic Curvature, ϕ_p	0.114/m (0.002902/in.)	0.0963/m (0.00245/in.)	15.58%
Total Plastic Rotation, θ_p	0.1938 radians	0.0846 radians	56.35%
Translation at Max. Moment Location, Δ_t	9.1 cm (3.58 in.)	N/A	N/A
Analytical Plastic Hinge Length, L_p	169.6 cm (66.78 in.)	87.88 cm (34.6 in.)	48.2%
Actual Plastic Hinge Length, $L_{p,actual}$	4.77 m (187.94 in.)	N/A	N/A

The following conclusions were drawn about the method suggested by Priestley et al. (2007) to determine the lateral response of a continuous bridge column supported by a drilled shaft foundation in cohesive soils:

1. The controlling curvature limit state in concrete was underestimated by 16% when compared to the bilinear idealization of the moment-curvature analysis. This value was based on the ultimate strain limit of the confined concrete in the plastic hinge region. This under prediction causes the plastic curvature to be lower, causing the plastic displacement to be lower than what will actually occur within the system. Although not the main contributor to the error in the plastic displacement, it will cause additional deviation from the more detailed analysis performed in LPILE.
2. The yield curvature was 4.3% lower than the idealized response and does not have a significant impact on the final design displacement or idealized yield displacement. In this case, the two displacement values would increase by half an inch which correlates to a 4% increase in the idealized yield displacement and 2% increase in the total design displacement.
3. The analytical plastic hinge length is approximately 50% less than the length determined using the more detailed methodology which employs the moment-curvature analysis in Figure 3-12. Due to this error, the plastic rotation and plastic displacement will be significantly under predicted. The issue with the plastic hinge length arises due to the fact it was determined in accordance with Chai's methodology, shown to have limitations for use in cohesive soils in Section 3.3.
4. The overall design displacement of the system was found to be 39.5% lower than that found using the detailed methodology. Most of the missing displacement is likely due to the under estimation of plastic action within the inelastic range of the lateral displacement because of a difference in the ultimate limit state curvatures and the plastic hinge length method employed in the computations.
5. A global force-displacement curve was not computed for this method, since the design spectrum, which relates the design displacement and effective damping with the period of the system, was not known. Additionally, a designer would have to estimate the effective moment of inertia of the system or the steel layout in order to determine a moment for the limit state curvatures to get a quick estimate on the lateral forces.

6. The last challenge, besides those discussed within the literature review, associated with this method is that seasonal temperature variation was once again not considered in the development of the model. This is a concern, as the lateral loading response is significantly altered in sub-freezing temperatures.

3.5 ATC 32 (1996)

In the guidelines of ATC 32 (1996), it is suggested that an alternative method, equivalent cantilever length, can be used to design a pile shaft foundation instead of the detailed method using soil springs. This approach works on the concept of defining a fixed-base cantilever system that does not include soil in the model, but is equivalent to a more detailed model which includes soil resistance. To use this method, the designer is redirected toward bridge design aids published by the California Department of Transportation (Caltrans) [Caltrans, 1990], which use an estimated depth to fixity found through a simplified or rigorous process to determine the lateral response.

The bridge design aids use one of two nomographs, based on soil type (i.e., clay or sand), to define a depth below ground to the fixity location. These graphs, however, are limited by the following parameters:

- pile diameter must fall within 1.22 m (4 ft) to 3.05 m (10 ft);
- above ground column height shall fall between 6.1 m (20ft) and 30.5 m (100 ft);
- modulus of elasticity of the concrete should be approximately 22,400 MPa (468,000 ksf); and
- the stiffness of the soil (i.e., shear strength or blow count) should be known.

The simplified design process starts by defining the structural and geotechnical parameters (e.g., shaft diameter and soil stiffness) to be used for the design. The next step in the process would be to use the nomographs to estimate the number of diameters to effective fixity based off of the soil stiffness parameter and appropriate column diameter. After defining the effective fixity location, the designer would use programs available through Caltrans to determine the appropriate loading and finalize the design of the system.

The more rigorous method of design follows the same procedures as outlined above, but determines the effective fixity location using a more detailed method. The more detailed method consists of running a program similar to LPILE, available through Caltrans, to define the top

lateral deflection of the column and rotation at the top of the column at service loads. These deflection and rotation values are then placed in equations related to the shear and moment applied to the system to determine the point of effective fixity for the system. No matter what method is used, ATC 32 further recommends that the effective cantilever length conservatively be taken to be no deeper than two pile diameters below the ground surface when determining the design shear force at column tip. If a concrete sidewalk is present, it was further stated that the shear load should be determined using a cantilever that does not penetrate into the ground.

The example problem presented in Section 3.1 does not meet the criteria specified in the above list and this method was therefore not used as a basis of comparison within this report. Instead, an elastic analysis was performed by the authors in LPILE to determine the efficiency in locating the effective point of fixity. This consisted of creating a system in LPILE with a 1.83 m (6 ft), 6.1 m (20 ft) column height, a foundation length of twenty pile diameters below ground and a uniform layer of cohesive soil with a strength of 95.76 kPa (13.89 psi) and unit weight of 18.85 kN/m^3 (0.0694 lb/in^3). The analysis consisted of pushing the top of the column to a displacement of 76.2 mm (3 in.) while maintaining a pinned head condition, so the SFSI system would remain in an elastic state.

The results concluded that the maximum moment would form at a depth of approximately 2.0 pile diameters in LPILE compared with the simplified method which predicts a fixity location at 2.4 pile diameters below the ground. This is a 20% error between the detailed analysis and simplified approach. The other challenge associated with this method is a constant shear is stipulated along the entire length of the shaft. This assumption ignores the resistance of the soil which causes a variable shear to occur along the length of the shaft once the shaft enters the ground level to act as the pile foundation. The shear and moment profile of the detailed analysis performed in LPILE (see Figure 3-13) demonstrate the shortcomings in the model.

3.6 AASHTO (2009)

In the guidelines available in AASHTO (2009), it is suggested that alternative methods to soil springs may be used to determine the lateral response of the integrated bridge column to foundation shaft. Within the guidelines, multiple alternative methods are presented [Chai (2002), Priestley et al. (2007) and AASHTO (2007) –fixity] for determining the lateral behavior of a column/foundation shaft, all of which have already been examined. Therefore, the remainder of this section focuses on the common practice approach of estimating a depth to

fixity for the system. The AASHTO (2009) guidelines state that the estimated depth to fixity may be used in lieu of a more detailed method, such as the soil spring method, and is determined by means of a simplified equation previously presented in Section 2.2.6. These equations, however, are only applicable as long as the system and all of its components follow a linear elastic behavior.

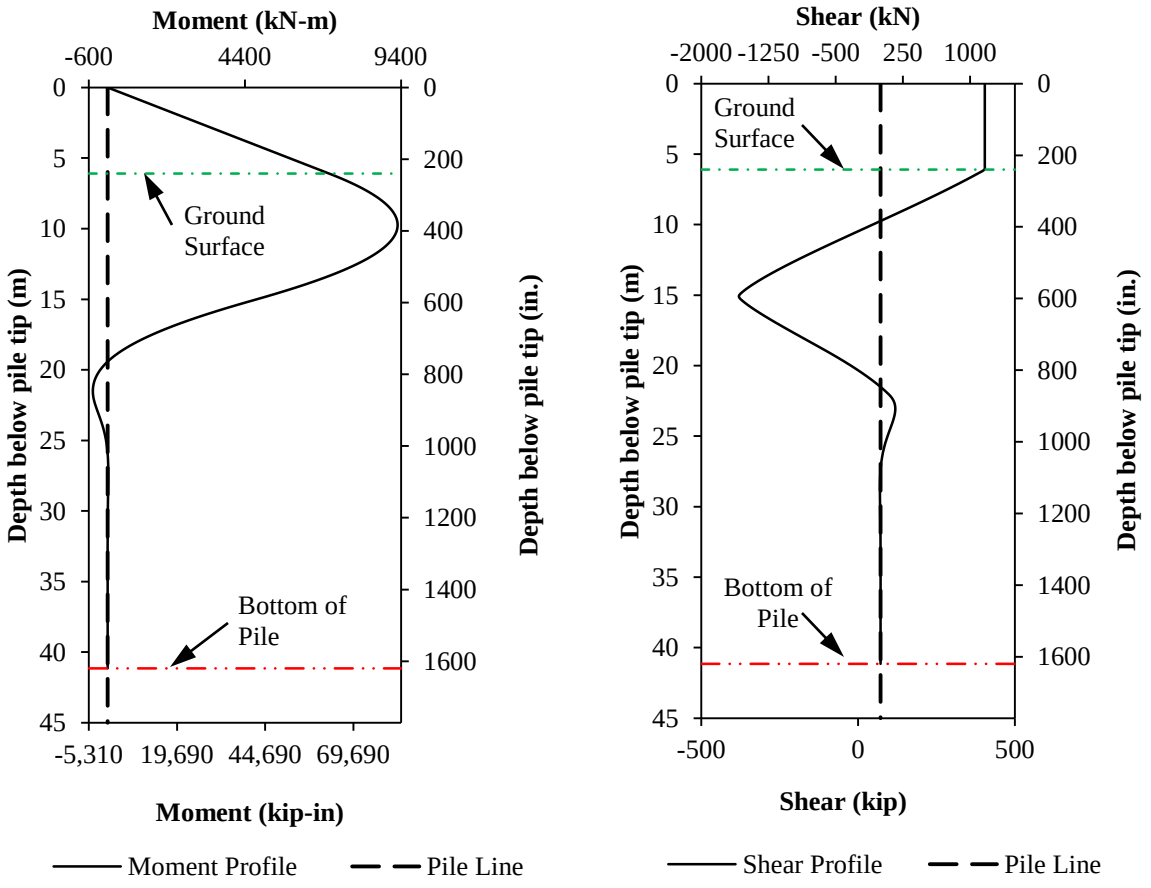

Figure 3-13: LPILE detailed analysis results (a) moment profile; (b) shear profile

For this method, the soil profile used in verifying Chai's methodology was selected, since this is an average value of the soil's undrained shear strength within the top six pile diameters and was the area where the largest influence on the lateral response would occur. Therefore, the selected soil was a cohesive low plasticity clay with c_u = 150.2 kPa (21.79 psi) and a unit weight of 21.2 kN/m^3 (0.078 lb/in^3). Using the structural parameters depicted in Figure 3-1 with elastic material properties and the equation produced by Davisson and Robinson (1965) in Section 2.2.6, the following results were obtained:

- soil modulus for clays, E_s = 10.06 MPa (1.46 ksi);
- concrete modulus of elasticity, E_c = 35.59 GPa (5161.6 ksi);
- gross moment of inertia for weak axis (circular column), I_w = 0.00678 m^4 (0.785 ft^4);
- effective depth to fixity, L_f = 3.10 m (121.97 in.); and
- effective cantilever length, L_{cant} = 5.79 m (227.97 in.).

After determining the effective cantilever length, an estimate may be obtained for the lateral load resistance and displacement capacities using structural analysis software or standard cantilever equations derived from mechanics. For this verification, the standard cantilever equations developed through mechanics were used to compute lateral resistance and displacement values. To determine these values, the model was originally defined to be fully elastic and gross section properties and the concrete modulus of elasticity could be used. To ensure the system was fully elastic, the maximum moment was assumed to occur before any yielding of the longitudinal reinforcement occurs. This meant that a moment of 435.76 kN-m (3856.8 kip-in) was attainable, according to the moment-curvature analysis presented in Section 3.2. Based off of standard cantilever equations, this correlates to a maximum lateral load of 75.26 kN (16.92 kip) at a displacement of 2.02 cm (0.80 in.).

If the designer were to assume a linear elastic behavior was attainable up to the yield point from a bilinear idealization of the moment-curvature analysis, the method suggested by Davisson and Robinson could be performed again with different results. The idealized yield moment in this situation would be 801.6 kN-m (7094.76 kip-in) and an effective moment of inertia of 0.0027 m^4 (0.240 ft^4). Using these aforementioned values, the following results were obtained for the effective point of fixity method suggested by AASHTO:

- effective depth to fixity, L_f = 2.30 m (90.67 in.);
- effective cantilever length, L_{cant} = 5.00 m (196.67 in.);
- yield lateral load, V_y = 160.47 kN (36.07 kip); and
- yield displacement, Δ_y = 9.04 cm (3.56 in.).

Although this method is very simple to use and will provide a result for design purposes, there are many shortcomings and limitations associated with its use, as summarized below:

1. A key component with this method is the model accounts for the effects of SFSI by creating a cantilever without soil in which the base is fixed against all deformation and the top is modeled based on the boundary conditions at the superstructure level. By

modeling the system in this manner, the shear along the shaft length is constant maintain the static equilibrium. This assumption, however, is not valid once the shaft is below the ground surface where shear demands will vary with depth (see Figure 3-13b). In addition to variable shear demands, the shear experienced in the foundation shaft may increase, as seen in Figure 3-13b, after the maximum moment has occurred. Should a designer ignore this increase in shear, a brittle failure from shear may occur during the formation of plastic action within the foundation shaft, which is against the principles of capacity design.

2. When the two different approaches to defining linear elastic behavior were compared with the experimental data produced by Suleiman et al. (2006), the following results were drawn:
   - lateral force at the point of first yielding was under predicted by 45.37%;
   - displacement at the point of first yielding was under predicted by 67.35%;
   - lateral force at idealized yielding was under predicted by 9.83%; and
   - displacement at idealized yielding was under predicted by 10.67%.
3. When moving from a purely elastic system in which the reinforcement does not yield to an idealized yield point, the effective point to fixity decreases by 25.7%. Although the method is used to define the equivalent stiffness of the soil column system, the maximum moment would occur at this point in a computer software package, unless the moment was specifically specified to form at a separate location not dictated in the code. Therefore, it is important to ensure this point in space is adequately defined to prevent a devastating failure in the design process due to the formation of any possible inelastic action that may occur under design level or greater earthquakes.
4. Another limitation associated with this method of relating the stiffness of the column to an equivalent cantilever is that the maximum moment location generally occurs at a point in the ground between the effective point of fixity and the ground surface. The experimental data from Suleiman et al. (2006) and the detailed analyses, completed by the authors of this report, performed using LPILE found the maximum moment location would form at approximately 1.02 m (40 in.) below the ground surface which is significantly less than either elastic method presented above. The method using the first yielding approach over predicts the location by 209.8%; whereas, the method using the

idealized yield location over predicts the location by 130.3%. As previously stated, the shaft design may violate the capacity design principles as the shaft confinement reinforcement will not be located in the correct places or designed for the correct response.

5. Another limitation of this approach is that inelastic action is not considered in determining the lateral displacement of the system. However, most of the lateral displacements for an integrated column/foundation system develop due to inelastic action that is expected with a large seismic event. By not including the effects of inelastic action, the plastic action developed due to in ground hinging at the maximum moment location is not included and the lateral response at the ultimate limit state cannot be defined.
6. This effective fixity model does not take into account the effects of seasonal temperature variations, which was expected as the current codes typically ignore the effects of cold temperatures in bridge design practice.

3.7 Summary of Examination

The examination undertaken within this chapter provided more information regarding the limitations of the existing methods for determining the lateral load response of columns supported on CIDH shafts in cohesive soils. Both simple and complex methods were presented, but each method had limitations associated with its use.

A summary of the findings within the confines of this examination are provided below:

- No matter the method selected for determining the lateral load response of a CIDH shaft subjected to a design level or greater earthquake, a designer may only be able to blindly predict the response within about 15% of the actual response. It was noted, however, that it is important to capture the point of yielding, whether idealized or first occurrence, as accurately as possible, since this is when inelastic action begins to form. Additionally, the ultimate displacement may exceed this value as these pile/shaft systems will typically not be allowed to deform to these high values in excess of 20 cm (~8 in.)
- The detailed method suggested by AASHTO (2007), although able to accurately capture the lateral load response of a column-shaft system both globally and locally, had a number of shortcomings associated with its use and are as follows:

- This method of analysis requires a significant amount of information about the structure and surrounding soil to accurately capture the response. The defining of properties for the soil surrounding the foundation shaft was found to be the area in which the most amount of information was needed. It was concluded that the lateral response of the system would experience significant differences in displacements for a given inertial loading based on the accuracy of the soil model used within the method. These differences in displacements are critical in a seismic based design where a designer must ensure other components of the structure are not damaged from excessive lateral deflection.
- Hand calculations are not easily performed for the detailed method. This means that expertise in computer programs, such as LPILE, is needed to perform the analysis.
- The design procedure using this method takes more time due to the inherent iterative process between foundation engineering and structural design. The iterations arise from the need to construct multiple models in LPILE as the structural design changes and more information is gathered on the surrounding soil.
- The effects of seasonal, wintry conditions on the lateral load response of columns supported on CIDH shafts in cohesive soils were not discussed in the specifications for bridge design. Although not discussed, Sritharan et al. (2007) demonstrated this method was capable of handling wintry conditions and the associated freezing when material properties (i.e., soil, concrete and steel) are adjusted correctly.

- The method proposed by Chai (2002) for determining the lateral load response of an integrated column/foundation system was found to have a number of challenges associated with its use in cohesive soil. These challenges are summarized below:
  - The assumption of an elasto-plastic response between the yield and ultimate conditions based on the response of SS1 in the experiment performed by Suleiman et al. (2006). This response does not compare well with experimental results because, unlike reinforced concrete members, the combined nonlinearity response of soil, steel and concrete create a secondary slope over the inelastic loading range.
  - The method was verified against a full-scale test in cohesionless soils although recommended for use in cohesive soils.

- The plastic action within the system was significantly under predicted. Most of the error in this location was found to occur within the analytical plastic hinge length that dictates the plastic rotation and plastic displacement. The plastic hinge length was found to be the largest error source, since it was defined based off of the full-scale testing of a column/foundation shaft performed by Chai and Hutchinson (2002) in a cohesionless soil. By basing the plastic hinge length on testing in cohesionless soils, it was under predicted analytically due to the differences in stiffness common between a cohesive and non-cohesive soil.
- Temperature effects were not given consideration in the development of the model, even though they will alter the lateral load response of a column supported on a CIDH shaft.

- Although the model suggested for use by Chai (2002) in cohesive soils has a number of challenges associated with its use, the model provided for cohesionless soils adequately captures the lateral loading response of a column supported by a CIDH shaft. In addition to being able to capture the desired response in the unfrozen state, it was shown that if the model is adjusted correctly the effects of seasonal freezing may be adequately determined.
- Priestley et al. (2007) suggested a method for handling the effects of SFSI in the determination of the design displacement for the lateral loading of column-pile shafts in cohesive soils. A summary of the shortcomings and limitations associated with the use of this method are presented below:
  - The model was found applicable over a limited range of geotechnical properties. This method should only be performed for cohesive soils with undrained shear strength of 20 kPa (420 psf) or 40 kPa (840 psf) based on the information provided. The range could be expanded to handle soils that fall between these bounds, but no information was provided on how to handle this situation.
  - Plastic action within the model was under predicted when determining the design displacement at the ultimate condition. This was found to be correlated with the way in which the plastic hinge length was determined for the suggested method. The authors recommended the use of the plastic hinge length developed by Chai (2002), based on cohesionless soil testing.

- Lateral forces were not computed, as an appropriate spectral graph relating the design displacement to the effective damping of the system and period was not known. A quick estimate was not provided, since the idealized yield moment and ultimate moment relating to the appropriate curvatures was unknown.
- Seasonal freezing was once again ignored in the development of the model that determines the lateral design displacement of a column-pile shaft in cohesive soils.

- The final two methods, ATC 32 and AASHTO, presented in the this chapter examine the effective point of fixity method. The shortcomings and limitations associated with the use of these models are summarized below:
  - Both methods produced a constant shear profile along the length of the column and foundation shafts. This profile, however, ignores the variable shear profile that may cause the shear demand to increase, depending on the location examined within the system. This can lead to a brittle failure of the structure when subjected to a design level or greater earthquake, thus violating the capacity design principles.
  - The maximum moment location was found to occur between the point of fixity and the ground surface, even though these models suggest it occurs at the effective point of fixity. By incorrectly defining the maximum moment location, insufficient confinement reinforcement may be provided at the actual location where the maximum moment develops and may cause a failure in the foundation shaft. This would violate the capacity design principles in which the designer wishes flexural yielding and plastic hinges to develop without failure.
  - Neither method discusses how the inelastic action expected from a design level or greater earthquake will be handled. This limits the range of the models to the elastic loading range, even though the most displacement occurs after yielding in the inelastic range.
  - The effects of seasonal freezing on the lateral response of an integrated column/foundation system were not included in the development of either method, limiting their use to warm weather conditions.
  - The ATC 32 model requires the use of computer software available at Caltrans to determine the forces used in the design of the column. In addition, this model is only

applicable over a limited range of structural parameters as described in Section 3.5 above.

- The AASHTO method is only applicable when the response of the system and materials fall within the linear elastic range. Although stated as an elastic analysis, no recommendations were made as to the range over which this occurs and the designer must ensure this will be the case when using this method. In addition, no validation of the method was provided within the specifications and guidelines provided by AASHTO.

CHAPTER 4: DEVELOPMENT OF A NEW SIMPLIFIED MODEL FOR CLAY SOILS

4.1 Objective

The current state of practice, as described in Chapters 2 and 3, are unable to satisfactorily capture the lateral load response of a bridge column supported on a drilled shaft founded in clay. The major issues associated with the existing simplified models are as follows:

- plastic action within the inelastic range of the system is generally underestimated as the analytical plastic hinge length in some models is based on experimentation in cohesionless soils;
- although recommended for use in cohesive soils, most of the current models were only verified against experimental testing performed in cohesionless soils as the engineering properties are easier to control;
- none of the current models considered the effects of seasonal temperature variation on material properties during their development;
- the maximum moment location is generally found to not coincide with that of a detailed analysis in cohesive soils; and
- localized effects (e.g., curvature and translation) at the point of the maximum moment are not accurately captured in most of the models although this is where the most damage will occur in an integrated column/foundation system subjected to design level or greater seismic events.

Due to these deficiencies within the current state of practice, a new simplified model for determining the lateral load response of drilled shafts in cohesive soils was deemed necessary. Taking the aforementioned issues into consideration, a model was created that would be able to effectively capture both the elastic and inelastic ranges of the lateral load response of bridge columns that extend into the ground as CIDH shafts. The new simplified model was also created such that effects of seasonally cold temperature conditions could be captured to address the impacts of seasonally frozen clay on the seismic design of these systems (Sritharan et al., 2007). By giving consideration to the effects of wintry conditions in the model development, the new model will be applicable for design in all seasons of the year.

4.2 Background on Model Development

This section discusses in more detail the background information used in regards to the development of the model. This includes a general description of the new model as well as an introduction to the procedures that determined the critical parameters and their values. The general description provides background as to why the selected model was chosen and brief information about the critical parameters and three springs used within the new methodology. The developmental process, on the other hand, presents a brief introduction on the procedures used to create the data necessary for determining critical parameters for use in the model.

4.2.1 Description of New Model

Model development began with the selection of the type of system to be used for determining the lateral loading response of a bridge column continued into the ground to act as a drilled shaft foundation. The premise used for the model was that it must be easy to use and generate a bilinear force displacement curve with sufficient accuracy while ensuring the model would lead to conservative outcomes from design perspectives. In addition to these two main requirements, the new model had to be easily input into a structural analysis computer program. With these constraints in mind, the model, as depicted in Figure 4-1, was conceived for further development based on the FBD of Figure 1-12(a) that locates critical regions and the reasons proposed in Section 4.1 about the missing capabilities of existing methods.

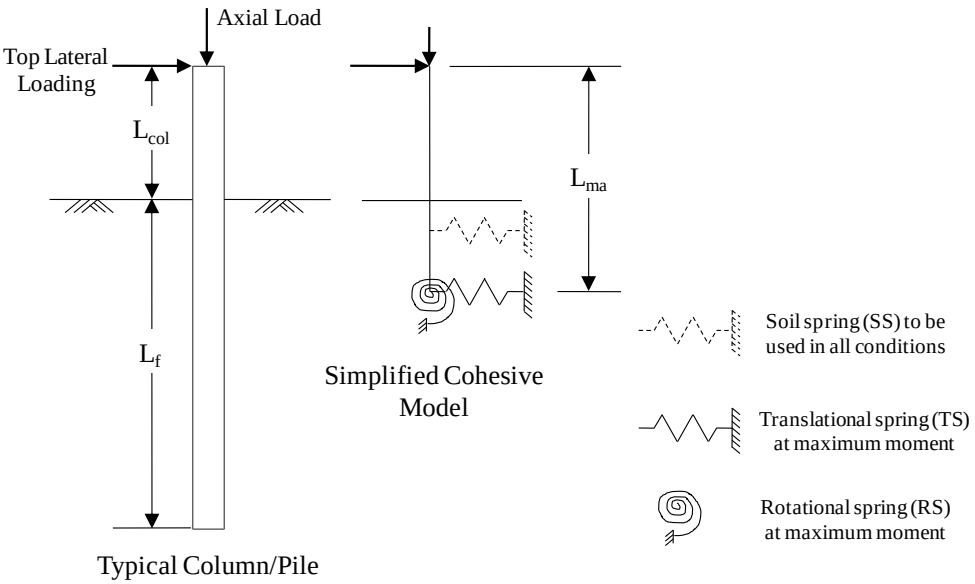

Figure 4-1: Proposed new simplified model

The model depicted in Figure 4-1 was chosen as the springs would allow the model to be easily input into a structural analysis program, while still able to locate critical locations and produce a force-displacement response as desired. The parameters used within the final model are presented in Figure 4-2 and their development is discussed further in Section 4.4. The most critical point within the model, the maximum moment location, defines the effective height of the system, but with a flexible base as opposed to a fixed base used in current practices [Chai, 2002; AASHTO, 2007; AASHTO, 2009]. This location was important since two springs, a rotational and a translational, were placed here. This point was given significant consideration, as this section in the drilled shaft is where the most damage would occur when the column-shaft system is subjected to lateral seismic loading and all plastic action is assumed to act solely in this vicinity when determining the ultimate displacement capacity. The flexible base was chosen so the translation and rotation, which occur at this point due to the CIDH shaft below this point being subjected to flexural action, could be accurately represented in the final model. The second translational spring was added to the model to represent the resistance to displacement provided by the soil above the maximum moment location as well as the variation in shear along the length of the shaft below the ground surface (see Section 1.4.1). The model was developed based on a free head condition with modifications for other boundary conditions made later.

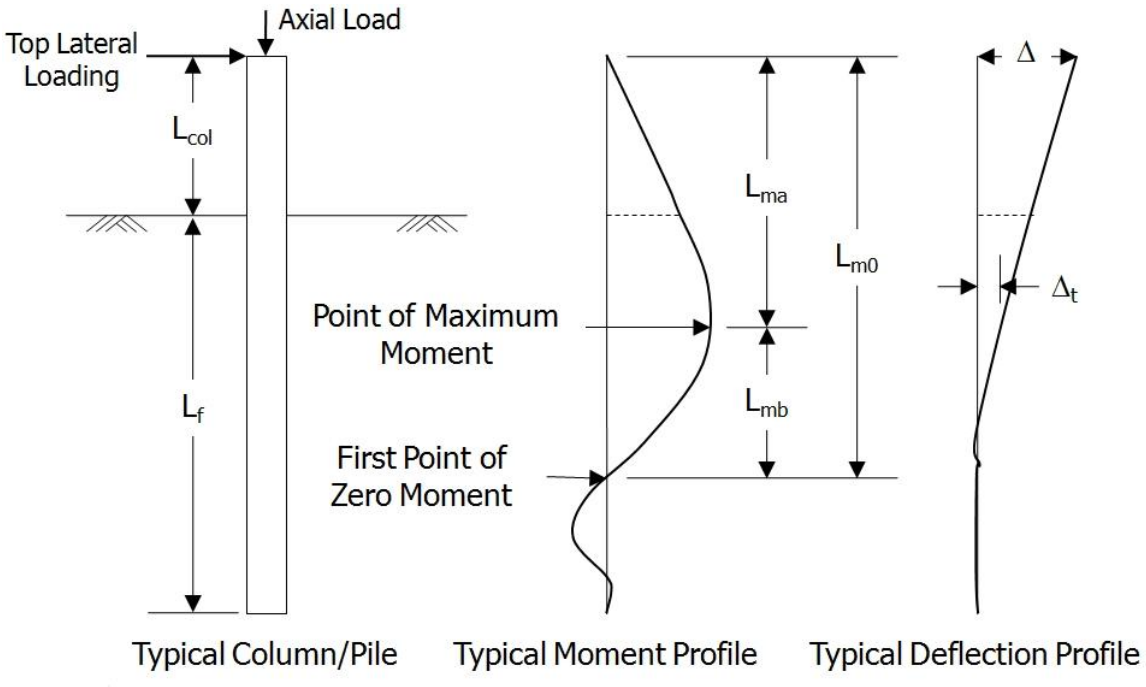

Figure 4-2: Definition of critical parameters used in the proposed simplified model

4.2.2 Process of Development

The development of critical locations and values associated with the new simplified model consisted of running a series of detailed analyses using LPILE plus 5.0 (Reese et al., 2004) and then examining the results of the different trials to rationally identify appropriate trends within the data. The first step of the examination was to determine the overall local curvatures, ϕ, experienced within the system by dividing the moment with the flexural rigidity at each node produced by the analysis along the length of the shaft. At this point, the overall curvatures developed at a given section were broken into elastic and plastic components, ϕ_e and ϕ_p, respectively, to better identify the contributions of each component to the overall lateral response of the system. To break down the curvatures into elastic and plastic components, the elastic curvature, Equation 4-1, was subtracted from the total curvature to determine the amount of plastic curvature experienced at any given section. After obtaining these components, integrations were performed along the length of the column and foundation shaft from bottom to top to determine the elastic and plastic rotation and displacement values at each node. Once this step was completed, the data sets were compiled and normalized with respect to multiple parameters (e.g., column diameter and effective height) to help examine possible trends occurring within different data sets.

$$\phi_e = \frac{M}{M'_y}\phi'_y \qquad (4\text{-}1)$$

where, M = moment at a given point along the shaft;
M'_y = moment at first yield of the concrete section; and
ϕ'_y = curvature of the concrete section at the first yield moment.

4.3 LPILE Analyses

For the numerous detailed analyses run during the development of the new methodology for determining the seismic response of drilled shafts in clay soils, certain information was needed to perform the fully inelastic analysis with a displacement convergence tolerance of 2.54E-05 cm (1E-05 in.). This section discusses the parameters varied during the model development as well as the different tools used to represent the material properties within the system.

4.3.1 Analysis Parameters

To perform the detailed analyses, a series of carefully chosen structural and geotechnical parameters were needed to provide a significant amount of data for the development of the new methodology. Selections of the parameters needed to complete these analyses were based off of commonly occurring cases in practice. The structural and geotechnical parameters were varied in the analyses as detailed below:

1. Structural Parameters
    - Axial load ratio, ALR, varied from 0% to 10% for c_u = 168.6 kPa (24.45 psi) and was equal to 5% in all other cases.
    - Top of the column was taken to experience pinned head conditions with an intention of including a procedure to deal with other boundary conditions.
    - Column diameter, D, was kept constant at 0.61 m (24 in.) as the critical parameters were nondimensionalized with respect to D.
    - Above ground column height, L_{col}, varied from 0D to 10D.
    - Length of foundation shaft, L_f, per Figure 4-2 was chosen to be long enough to ensure a portion of the shaft would not experience any lateral movement in all trials. This length was kept constant at 10.41 m (410 in.) or L_f = 17D based on results of the analyses.
    - Longitudinal reinforcement ratio, ρ_l, was maintained at 2%.
    - Horizontal reinforcement ratio, ρ_s, was constant at 0.9% based off of a 5.03 cm (1.98 in.) cover to the main longitudinal bars. This satisfies the recommendations made in ATC-32 (1996) and AASHTO (2007).
    - Expected concrete compressive strength, f'_{ce}, was kept constant at 27.6 MPa (4000 psi), since this is common practice in foundation engineering.
    - Steel reinforcement was taken as ASTM A706 Grade 60.
2. Geotechnical Parameters
    - Uniform layer of clay soil with no groundwater present.
    - Effective moist unit weight of soil, γ_m, was constant at 21.2 kN/m^3 (135 lb/ft^3), since this property does not greatly influence the soil spring properties and is an average value for cohesive soils.

- Undrained shear strength of soil, c_u, varied from 48.3 kPa to 380 kPa (7 psi to 55 psi) to represent clay soil from soft to stiff.
- Strain at fifty percent of maximum stress, ε_{50}, was selected based on the undrained shear strength of the soil as suggested by Reese et al. (2004).

4.3.2 Moment – Curvature Analyses

A key component in defining the parameters for a full inelastic analysis is to define the structural behavior of the individual elements within LPILE. To define this, a moment-curvature analysis was undertaken in VSAT (Levings, 2009) using the aforementioned structural parameters. The moments and corresponding flexural rigidities obtained from these analyses were then input into LPILE to represent the structural behavior. Within LPILE, the moment-curvature response of any section was assumed constant from column tip to bottom of the drilled shaft to reduce the number of variables modified with each analysis. The constant moment-curvature response was used for simplicity and should not greatly influence the behavior of the system outside the plastic hinge region, as this section remains elastic and the deformation is then based on the effective section properties of the concrete depending on the presence of cracking. However, these sections would not necessarily be constant along the entire length if designed to meet the appropriate bridge design standards (e.g., AASHTO, 2007). The three moment curvature responses and the corresponding input information for LPILE are provided in Figure 4-3.

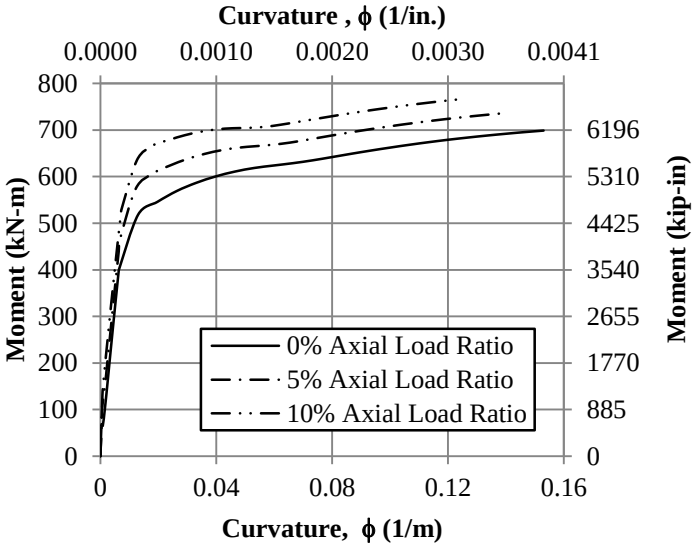

(a) Moment-curvature response of the column-foundation shaft using VSAT (Levings 2009)

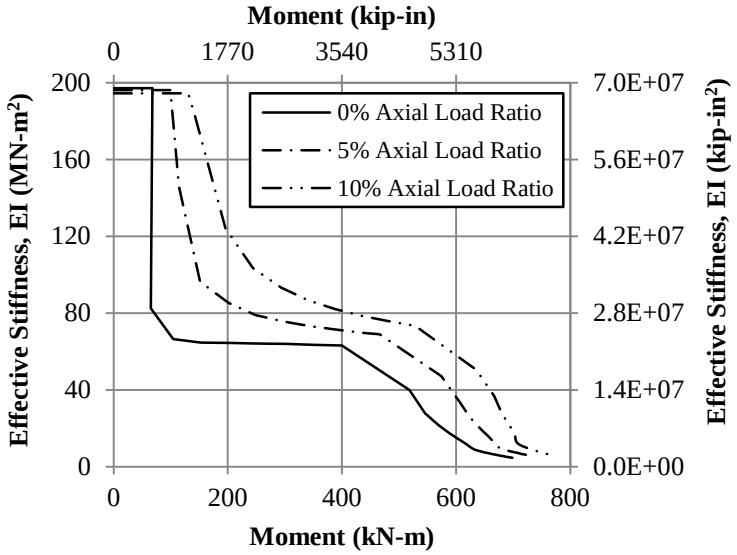

(b) Input parameters used in LPILE (Reese et al., 2004)
for the column-foundation shaft

Figure 4-3: Structural behavior of the column and foundation shafts used in model development

4.3.3 Soil Material Models

Each soil model used theoretically generated p-y curves to define the nonlinear behavior. To develop these curves, the selected soil model in LPILE was that of Reese for Stiff Clay (Reese et al., 2004) which requires input of the soil's undrained shear strength, effective unit weight and strain at fifty percent of the maximum stress with depth. Since the foundation soil was assumed to be a uniform layer, the height of the soil layer was taken to be equal to the length of the foundation below the ground surface by varying the necessary soil parameters as stated in Section 4.3.1. After specifying the parameters, LPILE internally generated the p-y curves for each node along the length of the shaft using the method suggested by Reese and Welch (1975). Although this material model is stated by Reese et al. (2004) to be for stiff clay, the original work by Reese and Welch (1975) does not specifically imply this is the only area where the soil material model is applicable. Therefore, this soil model was used for the multiple undrained shear strength parameters selected in the analyses used for trend establishment.

4.4 Simplified Model for Quantifying Lateral Response

While performing different lateral load analyses, the results were compiled in Microsoft Excel and different trends were examined to identify the suitable parameters for use in the new

methodology. Each trial was individually examined and broken into elastic and plastic components using the method described in Section 4.2.2. The remainder of this section presents the process undertaken to identify the critical locations as well as the final equations developed for use in the new model for quantifying the lateral response of drilled shafts subjected to design level or greater earthquakes.

4.4.1 Maximum Moment Location

The most critical portion of the model development was to define the effective height by locating the point of maximum moment. The process started by taking the different systems created in the detailed analyses and pushing them all to a pre-determined deflection of 24.2 cm (9.5 in.), less than the ultimate displacement and greater than the yield displacement, to locate the point of maximum moment. The displacement was selected by examining the analytical models produced by Sritharan et al. (2007) and finding a value approximately halfway between the ultimate limit state and the yield limit state. This method was chosen initially to remove the variability associated with having multiple displacement values to examine at the ultimate and yield limit states. Although this appeared to be a benefit when examining the data, no consistent trends could be developed for anything other than the maximum moment location, where data consistently varied with above ground column height as expected based on previous research. In addition, the method was not accurately predicting the maximum moment location when the pre-determined deflection was exceeded as the maximum moment location typically shifts towards the ground surface, albeit minimally, as a larger displacement is induced at the top of the pinned head column.

Due to these issues arising with the first attempt, an adjustment was made to the limit state at which the equations would be developed. The new limit state chosen was that of the ultimate condition defined by a flexural failure of the shaft when the ultimate moment capacity, M_u, and therefore ultimate curvature of the concrete cross-section, ϕ_u, were obtained anywhere along the length of the column and foundation shaft. Flexural failure was taken to be the ultimate limit state as this approach is consistent with the capacity design principles. By basing the decision on the capacity design principles, it was assumed that any other failure modes, such as a shear failure, would not occur prior to reaching the flexural failure of the system. After developing the equations at this limit state, the equations would then be verified against the yield limit state to see if the equations would still be valid for predicting the needed force-displacement point to

construct a bilinear response for the entire system. The yield limit state was defined as the first occurrence of the yield strain being reached in any one of the longitudinal tension reinforcing bars of the shaft. Since this limit state is different than the idealized yield limit state used in practice (Priestley et al., 1996), this particular state is referred to as the first yield limit state in the remainder of this report. It will be shown later that the first yield limit state was found to be more appropriate for defining the bilinear response of the column-shaft system, as the response of this system is affected by both soil nonlinearity and that of the section response. From the aforementioned first attempts at defining the system behavior, it was concluded that the axial load ratio would not significantly change the maximum moment location and that the 5% ratio provided the average effective cantilever height. This was noted as there was only a minimal variation of plus or minus 5% in the data for the different ALR examined at c_u = 168.6 kPa (24.45 psi).

Using the ultimate limit state and the 5% axial load ratio, a trend was found to be present within the data when the aboveground height, L_{col}, and the maximum moment location, L_{ma}, were normalized with respect to the diameter of the continuous column-shaft system. The diameter was chosen as the value for normalization, as this is a common approach between the different methods presented in Chapter 2 and avoids investigating the new method for different values of D. The data points for both the ultimate limit state and the first yield limit state found through this examination are shown in Figure 4-4. The trend that can be noted in this figure is that as the aboveground height of the column increases, the depth to the maximum moment location will increase in a nonlinear manner. The observed trend further demonstrates the location of the maximum moment will be a function of the undrained shear strength for the soil, as the lower this value gets at a similar above ground column height the maximum moment location will be deeper. This is expected as a less stiff soil will disperse the lateral loading over a longer shaft length, causing the maximum moment location to occur at a greater depth. The final trend depicted in Figure 4-4 is the maximum moment location does not vary significantly when examining the yield or ultimate limit state of the integrated column-foundation system.

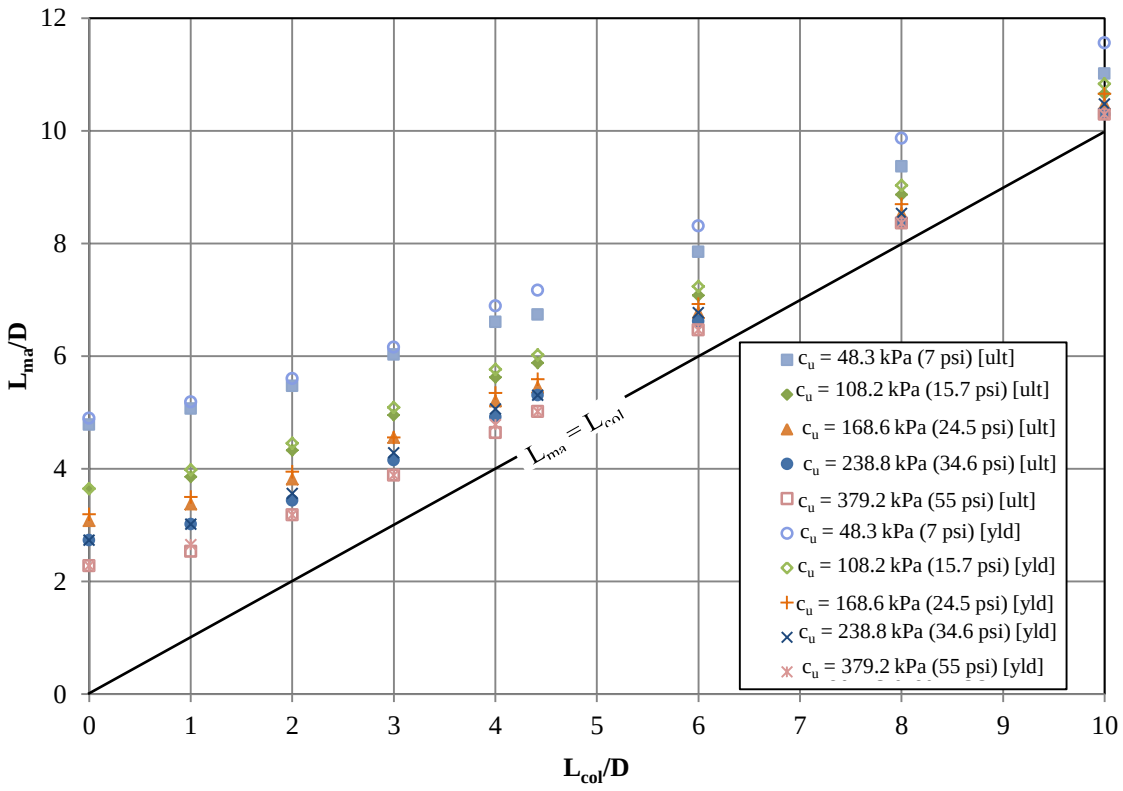

Figure 4-4: Location of the maximum moment at the first yield and ultimate limit states at 5% ALR

Based on the trends noted in Figure 4-4, equations were developed that would locate the point of maximum moment for a given design problem by creating a series of best fit lines for the different ultimate limit state data sets and then ensuring that all factors noted to influence the location were included. A linear trend was tried initially to represent the differing data sets, but was found to under predict the maximum moment location at the extremes while over predicting the moment location in soil with medium c_u values. Due to these issues, a series of second order equations were created that fit the data as shown in Figure 4-5. These equations were found to well represent the data and used to create a final equation that takes the form of $y(x) = \alpha_{ma}x^2+\beta_{ma}x+\chi_{ma}$, where x is defined as the normalized above ground height of the column, L_{col}/D; y is defined as the normalized depth to maximum moment taken from the top of the column, L_{ma}/D; and α_{ma}, β_{ma} and χ_{ma} are coefficients that account for the soil parameters based on the soils undrained shear strengths and the established trend lines.

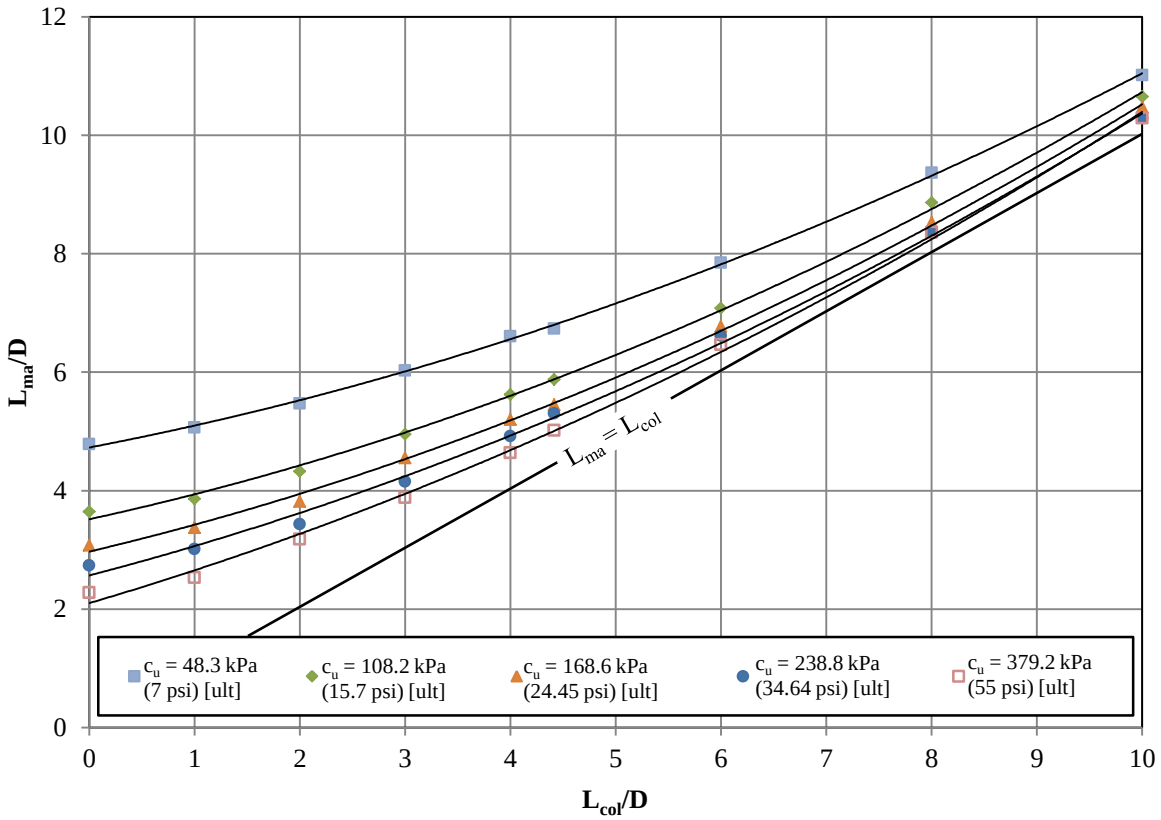

Figure 4-5: Location of the maximum moment with second order polynomial trendlines

The final step in the equation development was to define the coefficients needed to complete the second order polynomial equation. This was accomplished by taking individual coefficients for each of the lines shown in Figure 4-5 and graphing them against the undrained shear strength, so the effect of differing soil properties could be handled within a single equation. The effective unit weight and fifty percent strain values of the cohesive soil were not included as the first of these variables remained constant in all analyses, while the second variable was chosen based off of the undrained shear strength following the recommendations of Reese et al. (2004). After plotting the data, trends were then created that would allow for the coefficients (α_{ma}, β_{ma} and χ_{ma}) used to locate the maximum moment location to be computed based on the undrained shear strength of the soil. These coefficients ensure the correct polynomial line is used. The data points and the trends for the different coefficient relationships are provided in Figure 4-6. Although data suggest that a constant of $\alpha_{ma} = 0.0315$ may be appropriate, this causes the relationships to cross over one another at the higher undrained shear strengths used in the model

development. Therefore, the quadratic relationship shown is still recommended for use in the final equation.

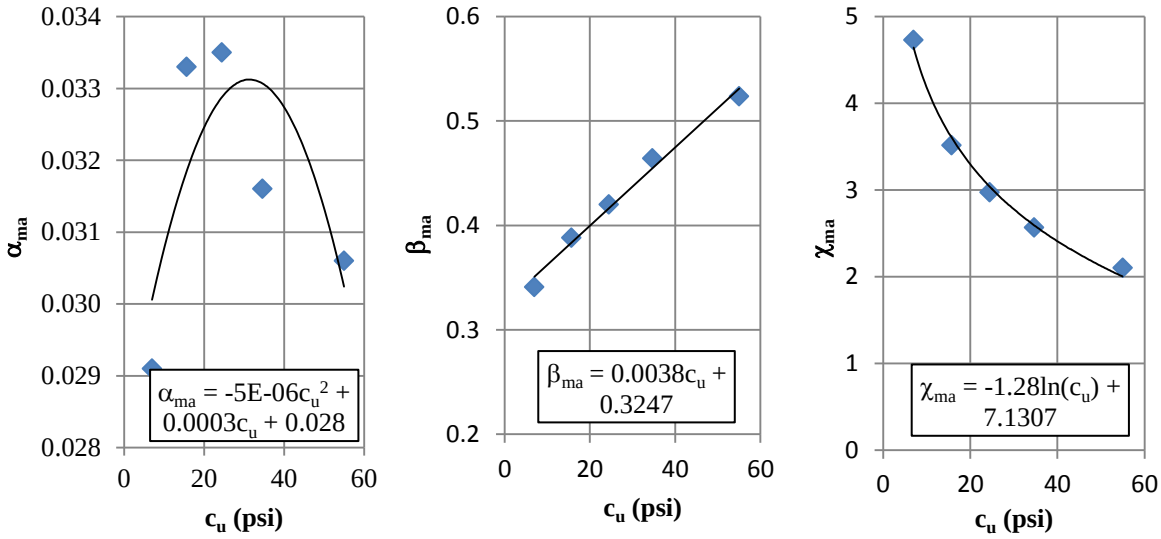

(a) α_{ma} coefficient (b) β_{ma} coefficient (c) χ_{ma} coefficient

Figure 4-6: Soil coefficient relationships used to locate the point of maximum moment (1 psi = 6.895 kPa)

At this point, the final equation for locating the point of maximum moment and, therefore, the effective height of the system was completed. The developed second order equation is provided here as Equation 4-2 with the left and right hand sides of the normalized equation multiplied by D to provide a solution with a length dimension. The final equation was then used and compared with the ultimate limit state data to ensure that the equation would accurately locate the point of maximum moment. This comparison is provided in Figure 4-7, where it can be seen that the new equation correlates well with the maximum moment locations found through the detailed analyses.

$$L_{ma} = D\left[\alpha_{ma}\left(\frac{L_{col}}{D}\right)^2 + \beta_{ma}\left(\frac{L_{col}}{D}\right) + \chi_{ma}\right] \quad (4\text{-}2)$$

where, $\alpha_{ma} = -0.000005\mathrm{a}c_u^{\,2} + 0.0003\mathrm{b}c_u + 0.028$;
$\beta_{ma} = 0.0038\mathrm{b}c_u + 0.3247$;
$\chi_{ma} = -1.28\ln[c_u(\mathrm{kPa})] + 9.6021$;
$\chi_{ma} = -1.28\ln[c_u(\mathrm{psi})] + 7.1307$;
a = 0.021 for c_u in kPa and 1.0 for c_u in psi; and
b = 0.145 for c_u in kPa and 1.0 for c_u in psi.

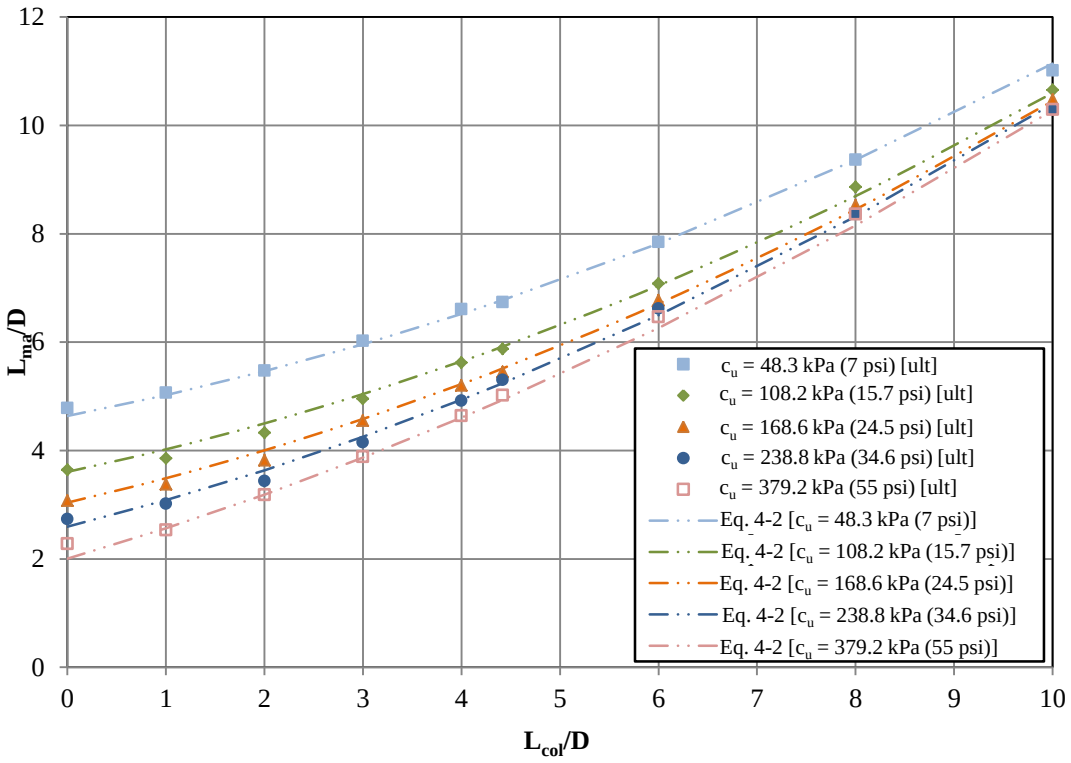

Figure 4-7: Comparison of maximum moment location using the developed equation and detailed analysis results

4.4.2 Plastic Hinge Length and Zero Moment Location

After establishing the maximum moment location, the next critical step in the development of the new model was to define the analytical plastic hinge length above and below the maximum moment location, L_{pa} and L_{pb}, respectively. This step was deemed to be the next crucial step, as this will define the amount of plastic rotation and plastic displacement experienced within the inelastic range of the system's behavior. The analytical plastic hinge length, however, should not be used to determine the area over which confinement reinforcement should be provided, since it is strictly to find an equivalent length that will estimate the plastic rotation when multiplied by the plastic curvature, ϕ_p, at the maximum moment location. The plastic hinge lengths above and below the maximum moment location were treated separately in this manner in case it was necessary to define two different trends based on the data, and the original plan was for the rotational spring to only model the system deformation below the maximum moment location.

The plastic rotation below the maximum moment location, θ_{pb}, was first obtained by performing an integration of the plastic curvatures along the length of the shaft to the maximum

moment location. Since a function is not directly obtained through the data, the integration was performed using the trapezoidal rule and averaging the plastic curvature at the point being considered with the plastic curvature at the previous point. The analytical plastic hinge length was determined by dividing the plastic rotation with the plastic curvature obtained at the ultimate limit state and the maximum moment location. This is presented algebraically in Equation 4-3, where x is the length along the shaft.

$$L_{pb} = \frac{\int_{L_f}^{Lma} \phi_p(\mathrm{x})dx}{\phi_p} = \frac{\theta_{pb}}{\phi_p} \tag{4-3}$$

After establishing the analytical plastic hinge length used for comparison purposes, trends were examined to establish an equation or graph that would easily provide a numerical value for the analytical plastic hinge length. During the iterative process, a number of comparisons were examined. The comparisons were undertaken using normalized data and trends that other researchers have previously established. The approaches, as presented in the following list, did not provide consistent trends when plotted and separated by differences in the analyses. In the following list, k_h is a horizontal subgrade modulus taken in units of force per length cubed based on Vesic's equations reproduced in Bowles (1988) and L is the total length of the system.

- L_{pb}/D versus k_hD^5/EI_e;
- L_{pb}/D versus $1000[k_hD^6/D'(EI_e)]$ (Priestley 1996);
- L_{pb}/D versus L_{col}/D (Chai 2002);
- L_{pb}/D versus (L-Lma)/D;
- L_{pb}/D versus c_uD^2/γ_m;
- L_{pb}/D versus c_u;
- $[3.7D-0.2(L-L_{ma})]/(L-L_{ma})$ versus c_u, where $3.7D-0.2(L-L_{ma})$ was a conservative lower limit on L_{pb} that does not capture the full plastic action; and
- $[3.7D-0.2(L-L_{ma})]/[D(L-L_{ma})]$ versus c_u.

At this point, a new approach was undertaken in which the analytical plastic hinge length below the maximum moment location was compared to a length within the system that might be determined through an equation-based approach. Using this method as a basis it was found that the analytical plastic hinge length ranged from 0.16 to 0.20 times the distance between the first point of zero moment, L_{m0}, after the maximum moment is obtained and this variable is defined

as, L_{mb} (see Figure 4-2). This is clarified in the bar graph shown in Figure 4-8, where the analytical plastic hinge length was divided by L_{mb} and then compared for all of the ultimate limit state trials. Recognizing the column-shaft displacement capacity will be rarely reached in seismic loading due to the influence of soil flexibility, the analytical plastic hinge length below the maximum moment location was conservatively specified at the lower limit of this ratio. The final equation developed for L_{pb} is provided below as Equation 4-4. This approach is based on the long shaft behavior of the system and occurs when $L_f \geq 1.5L_{m0}$ based on the LPILE analyses.

$$L_{pb} = 0.16L_{mb} \tag{4-4}$$

The first point of zero moment below the maximum moment location was chosen, since this is where the moment profile reverses sign and the remaining flexural action does not significantly contribute to the displacement of the column tip. This is the case, since the analyses typically demonstrate that deflections at this point are essentially negligible at about 0.25 mm (~ 0.1 in.). The minimal deformation at this point is typically less than 3% of the yield limit state column tip displacement and 1% of the ultimate limit state column tip displacement.

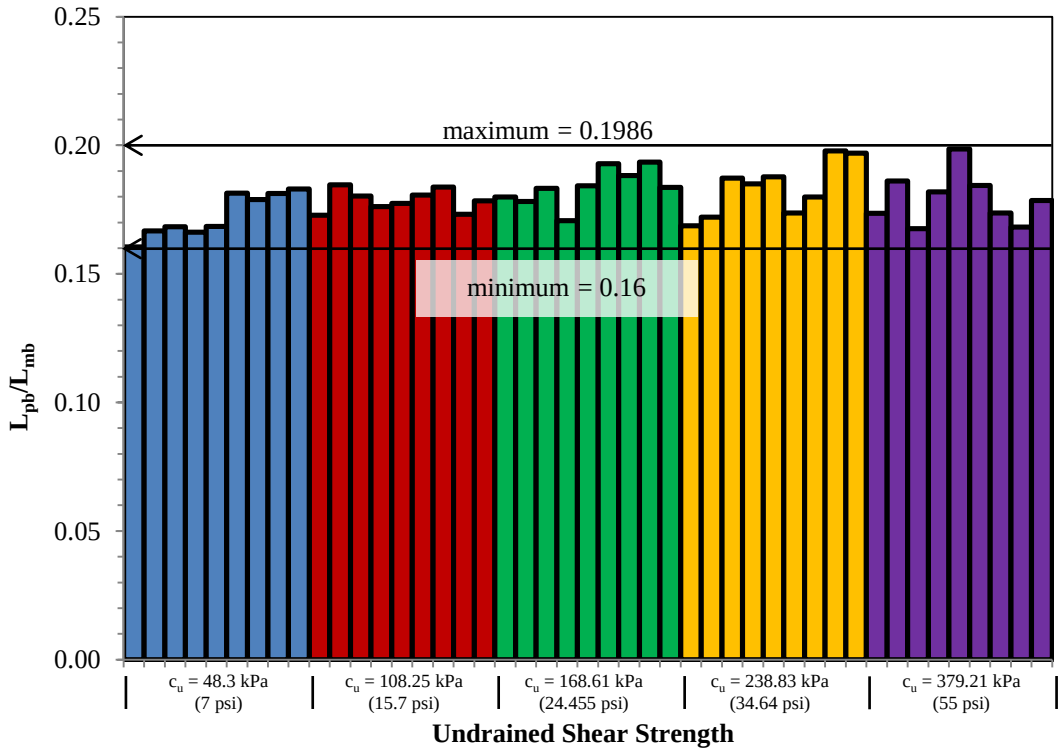

Figure 4-8: Analytical plastic hinge length in terms of L_{mb} for all aboveground column heights at the ultimate limit state as a function of c_u

Using the results from the detailed LPILE analyses at the ultimate limit state, the zero moment location was defined for each case by a linear interpolation between the positive and negative moments on either side of the zero point. The value was then normalized with respect to the shaft diameter and plotted against the normalized above ground height and the undrained shear strength of the soil. The plot against the undrained shear strength provided a better correlation when the trends were examined in detail (see Figure 4-9). The values at the first yield were included for the first two series to demonstrate that only the ultimate limit state needed to be analyzed, since data are nearly identical and this was the case with all the other series not provided in this report. Similar to the maximum moment location, the effects of the ALR were examined at an undrained shear strength of 168.6 kPa (24.455 psi). This comparison found that the ALR did not significantly alter the zero moment location and an average value for the ALR of 5% was used in the remainder of the analyses. The two main trends demonstrated in the figure are: (1) as the undrained shear strength increases the zero moment location decreases, and (2) as the normalized above ground column height increases the zero moment location increases.

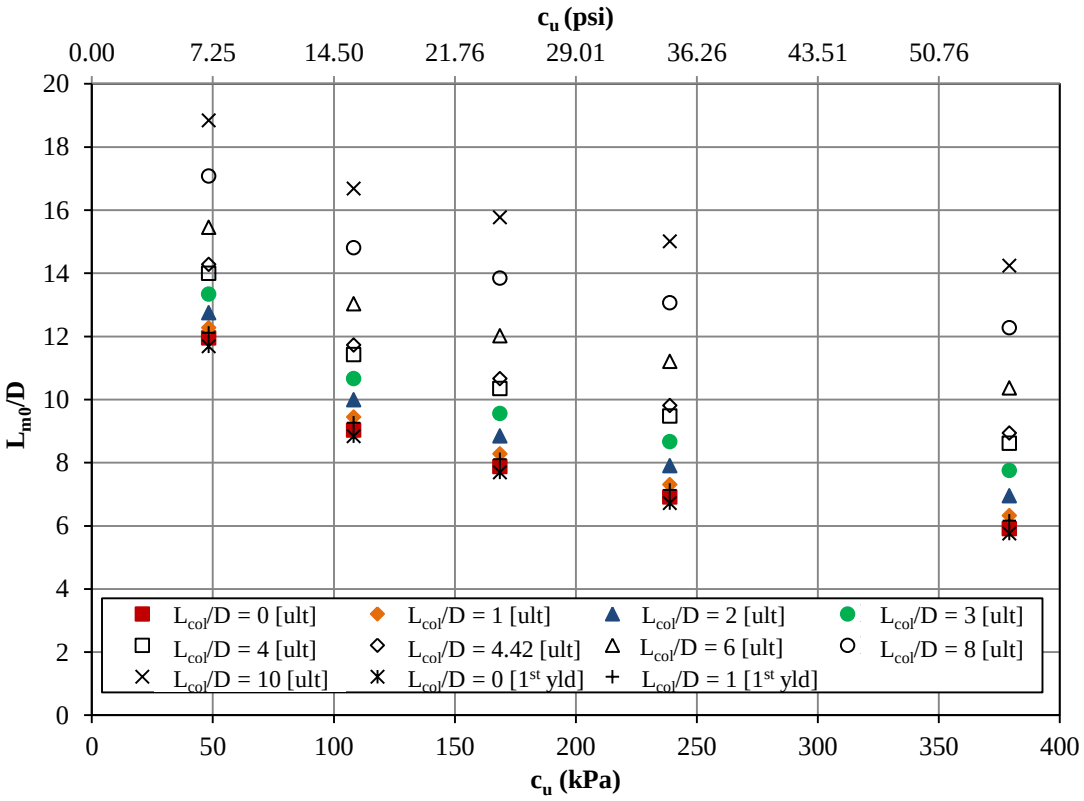

Figure 4-9: Normalized zero moment location as a function of undrained shear strength at the ultimate limit state for a column shaft system with a 5% axial load ratio

After establishing the desired plot for locating the first point of zero moment below the maximum moment, the results were examined for logical trends including functions following linear, second order polynomial and power series behaviors. During this process, it was found that a power series function would best capture the trend depicted by the data in Figure 4-10 for the ultimate limit state. This was the case, as the linear and second order polynomial functions could not accurately capture the curvilinear behavior of the data. A higher order function was not chosen to maintain simplicity and, thus, the final equation assumed the form of $y(x) = \alpha_{m0}x^{\beta m0}$, where y is the normalized length to the first zero moment location; x is the undrained shear strength of the soil; α_{m0} is a coefficient determined based on the normalized above ground height and β_{m0} is an exponent based on the normalized above ground height.

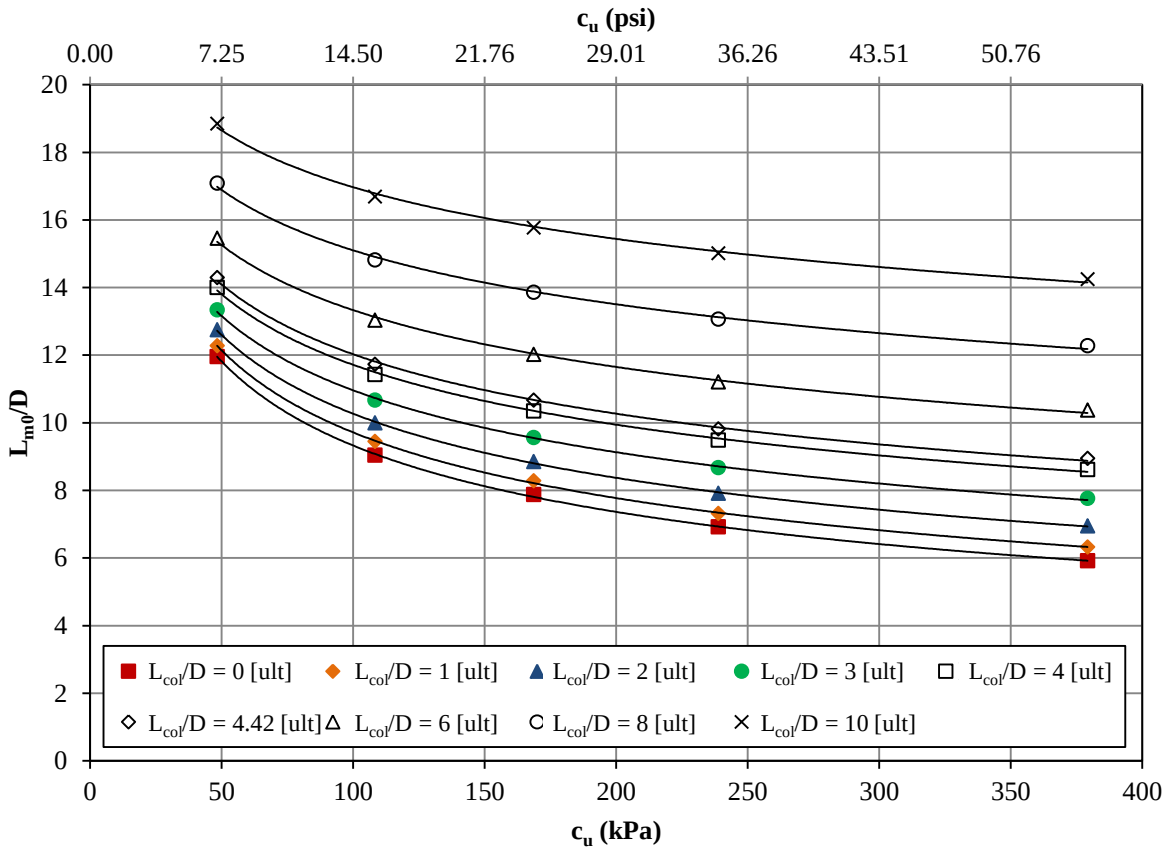

Figure 4-10: Normalized zero moment location with the established power series trend lines at the ultimate limit state

Similar to the maximum moment location, the final step in determining the first zero moment location equation was to find a means to incorporate the influence of soil and determine the coefficient value, α_{m0}, and the exponent value, β_{m0}, to be used in the proposed equation. To

define these variables, the coefficients for each trend were taken and plotted against the normalized aboveground height, as this was the main factor missing in the equation development and the soil effects are already accounted for in the overall equation. By accounting for the column height in this manner, the coefficients effectively establish the required power series in the equation for the curves shown in Figure 4-10. The data and relationships chosen for each coefficient are provided in Figure 4-11. The linear trend for the α_{m0} coefficient was selected since the data generally increase as the above ground column height increases. Although a parabolic curve as that shown by the dashed line in Figure 4-11(a) fits the data points more consistently, the equation for this approach is more complicated and does not capture the L_{m0} location as accurately as when the linear trend is used. Therefore, α_{m0} was specified to follow a linearly increasing trend that follows the equation presented in the chart.

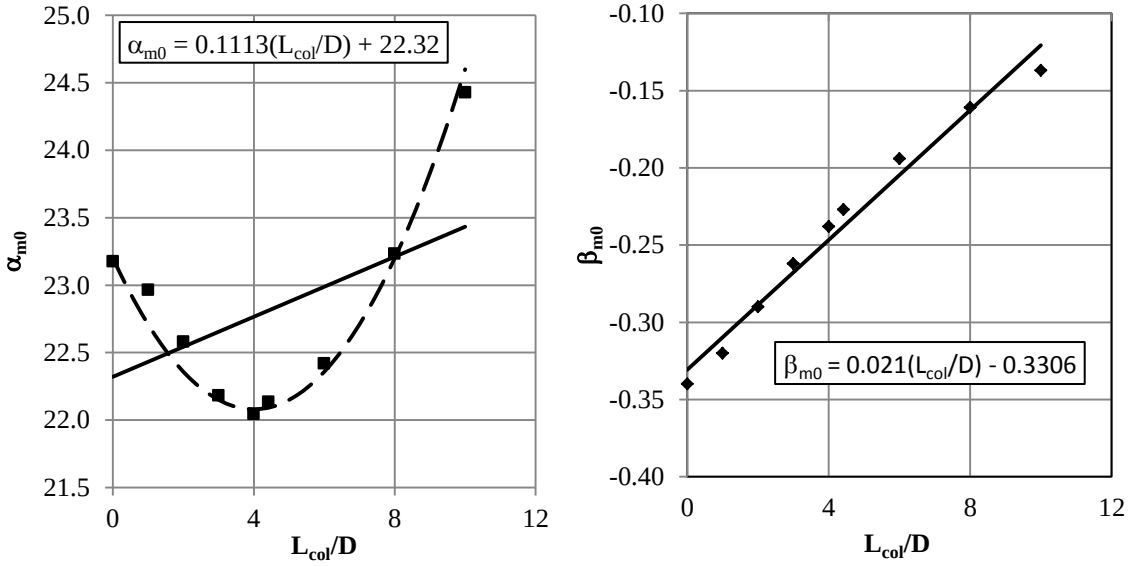

(a) α_{m0} coefficient (b) β_{m0} coefficient

Figure 4-11: Coefficient and exponent relationships used for locating the first zero moment location below the maximum moment location

Following establishment of the two relationships as included in Figure 4-11, the final equation was fully developed for defining the point at which the first occurrence of zero moment is reached below the maximum moment location. The developed equation is presented within the text as Equation 4-5 with some reorganization by moving the variable D to the right hand side of the equation and manipulation of significant figures to provide a final value that has units of length. The equation was then used to determine the zero moment location and the results

were plotted against the detailed analyses at the ultimate condition. This comparison is provided in Figure 4-12 where it can be seen that equation 4-5 correlates well with the actual data obtained from detailed LPILE analyses at the ultimate limit state. At this point, the analytical plastic hinge length below the maximum moment location was fully developed, as L_{mb} is defined as L_{m0} minus L_{ma}.

$$L_{m0} = D\alpha_{m0}[0.145c_u(\text{kPa})]^{\beta_{m0}} \text{ or} \quad (4\text{-}5)$$

$$L_{m0} = D\alpha_{m0}[c_u(\text{psi})]^{\beta_{m0}}$$

where, $\alpha_{m0} = 0.11\left(\frac{L_{col}}{D}\right) + 22.3$; and

$$\beta_{m0} = 0.021\left(\frac{L_{col}}{D}\right) - 0.33.$$

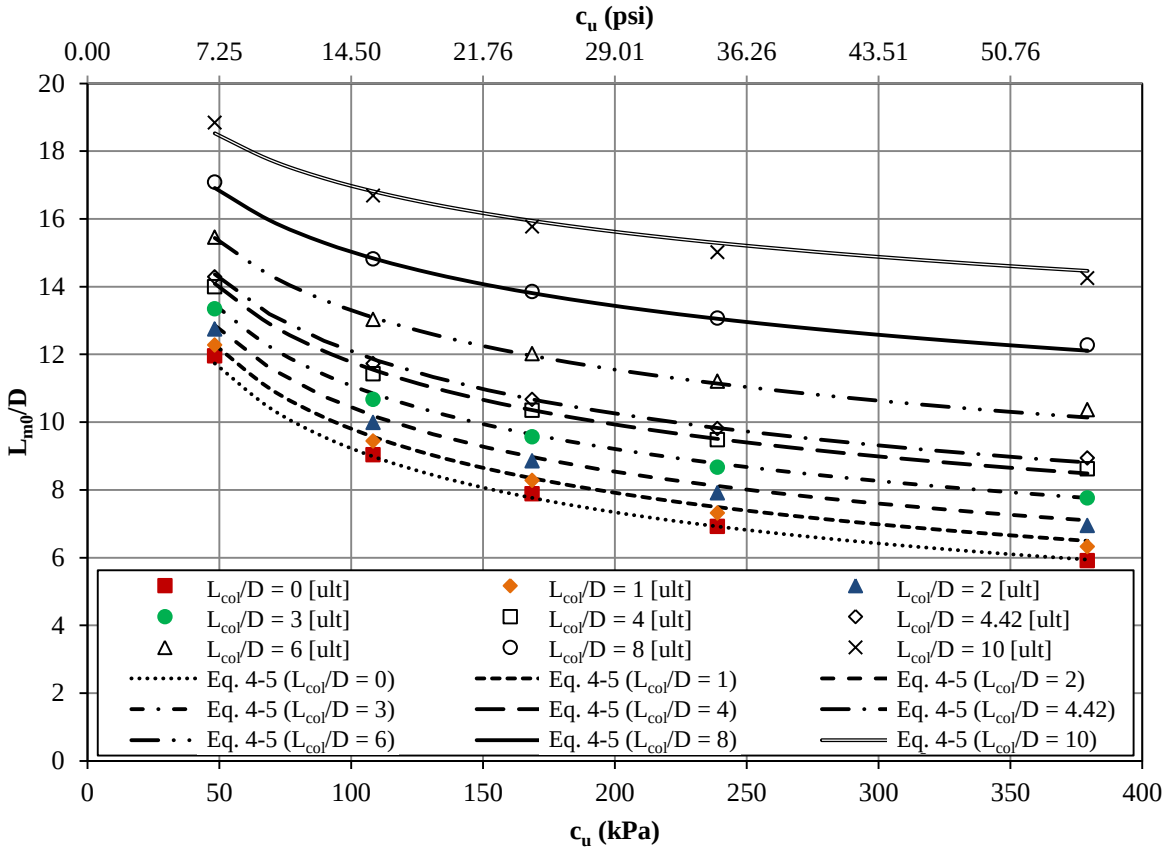

Figure 4-12: Comparison of normalized zero moment location using Equation 4-5 and detailed analyses

4.4.3 Rotational Spring at Maximum Moment Location

The next step in the development of the model was to define the spring properties at maximum moment location. This process began by establishing the bilinear rotational spring

that would be located at this point. A bilinear representation was selected for the moment-rotation response as this will provide a means to account for the strength gained due to the nonlinear behavior of soil and steel reinforcement between the first yield and ultimate limit states. The remainder of this section will discuss the development of the properties needed to define the bilinear moment-rotation behavior of the rotational spring at the maximum moment location.

The rotational spring was originally specified to model the elastic and plastic rotations occurring in the shaft below the effective height of the cantilever, but was later modified to further simplify hand calculations. This simplification was accomplished by including the effects of plastic rotation that will take place in the shaft and possibly column above the maximum moment location. This facilitates all plastic action to be concentrated solely at this point, allowing the plastic displacement, Δ_p, of the system to be determined by multiplying the effective height of the cantilever with the total plastic rotation, θ_p, as shown in Equation 4-6.

$$\Delta_p = \theta_p L_{ma} \tag{4-6}$$

To establish the plastic displacement in this manner, it was necessary to define the analytical plastic hinge length for the region above the maximum moment so that an analytical plastic hinge length for all of the plastic action could be established as $L_p = L_{pa} + L_{pb}$. The analytical plastic hinge length above the maximum moment location was found through the integration method detailed in Section 4.4.2, thus, establishing the plastic rotation to be specified as shown in Equation 4-7 with ϕ_p being determined from Equation 4-8.

$$\theta_p = L_p \phi_p \tag{4-7}$$

$$\phi_p = \phi - \phi_e \tag{4-8}$$

where, ϕ is the curvature at a given moment past the first yield point; and
ϕ_e is found using Equation 4-1.

At this point it was necessary to define the analytical plastic hinge length above the maximum moment location as a numerical value. To define the length above the maximum moment location, the results of the analytical plastic hinge lengths above and below the maximum moment location were compared using a bar graph. The bar graph used for this comparison, as presented in Figure 4-13, showed the two normalized values are approximately the same. Figure 4-13 also showed that as c_u increased L_p would decrease as expected due to the

change in stiffness of the soil and will be accounted for by the inclusion of L_{mb} in the equations. Additionally, as the aboveground column height increased, L_p increased as expected because of the longer clear distance between supporting locations. Based on this, the analytical plastic hinge length above the maximum moment location was defined as being equivalent to the analytical plastic hinge length below the maximum moment location. By defining the length in this manner, the overall analytical plastic hinge length could simply be determined by doubling the equation developed for the plastic hinge length below the maximum moment location, Equation 4-9, and thus defined the plastic displacement of the system.

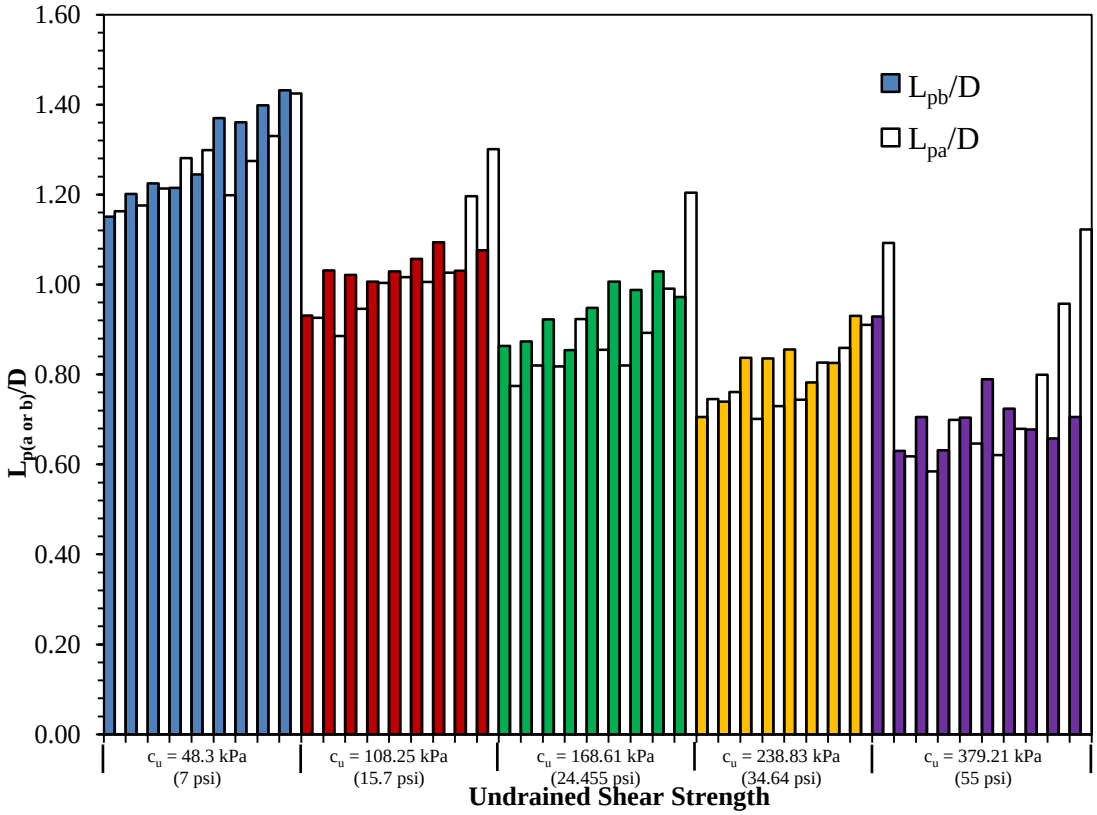

Figure 4-13: Comparison of normalized plastic hinge lengths where the solid filled bars are L_{pb}/D and the colorless bars are L_{pa}/D

$$L_p = L_{pa} + L_{pb} = 2L_{pb} = 2(0.16L_{mb}) = 0.32L_{mb} \quad (4\text{-}9)$$

The other two rotations needed for defining the rotational spring were the elastic rotations below the maximum moment location at the first yield and ultimate limit states, defined as θ_{eby} and θ_{ebu}, respectively. The elastic rotation above the maximum moment location was not included in the rotational spring, as it is subsequently accounted for when determining the elastic

displacement above the flexible base. The limit states for the rotational spring were previously defined as the first occurrence of the yield strain in the extreme tension bar and the flexural failure of the system, respectively. To determine the elastic rotation, the elastic curvature components of the detailed analyses were used to perform a first integration along the length of the pile shaft from the bottom tip to the maximum moment location. This integration was performed using the trapezoidal rule to compute the area under the curve from the bottom tip to the maximum moment location. Using these data sets, the elastic rotations were examined for trends.

The main trend examined for this process was a comparison of the elastic rotation with the normalized length, L_{mb}/D. This trend was primarily examined, since no other locations would have to be defined to determine the amount of elastic rotation below this point. The data in Figure 4-14 demonstrated two different linear trends could be developed for the first yield and ultimate limit states. The linear equations that follow the trends are provided below as Equations 4-10 and 4-11.

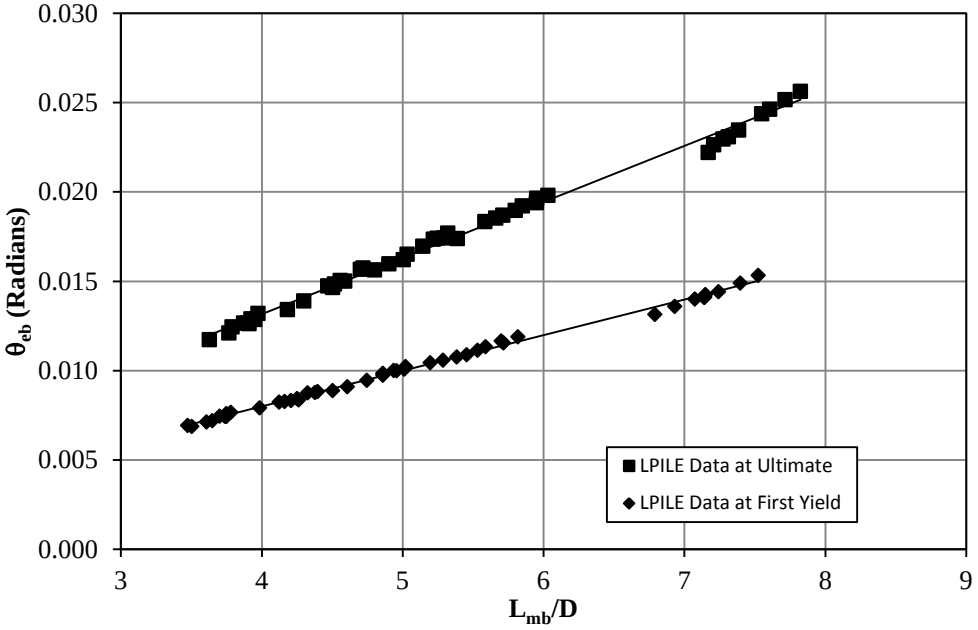

Figure 4-14: Data and trends obtained for the elastic rotation at the maximum moment location due to the elastic curvature below the maximum moment location occurring

$$\theta_{eby}(\text{rad}) = 0.002\left(\frac{L_{mb}}{D}\right) + 0.00001 \quad (4\text{-}10)$$

$$\theta_{ebu}(\text{rad}) = 0.0031\left(\frac{L_{mb}}{D}\right) + 0.0006 \quad (4\text{-}11)$$

The bilinear moment-rotation spring can now be fully defined as all of the components have been defined, with the exception of the moments which are to be taken based on a moment-curvature analysis. The three points that will define the rotational spring are the initial point, the first yielding point and the ultimate point. These points are defined graphically in Figure 4-15 and verbally as follows:

- The initial point is defined by the point of zero radians and zero moment.
- The first yielding point is defined by the yield rotation, θ_y, and the first yielding moment, M'_y, from the moment-curvature analysis. The yield rotation is defined as the elastic rotation below the maximum moment location at first yield, θ_{eby}.
- The ultimate point is defined by the ultimate rotation, θ_u, and the ultimate moment, M_u, obtained from the moment-curvature analysis. The ultimate rotation is defined as θ_{ebu} plus θ_p.

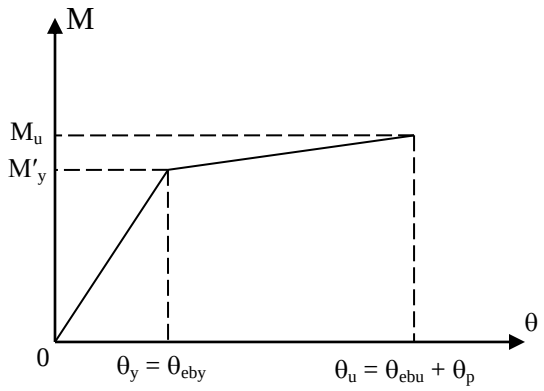

Figure 4-15: Description of bilinear moment rotation spring located at the point of maximum moment

4.4.4 Translational Spring

The translational spring above the maximum moment location used to represent the soil above the maximum moment location (see spring SS in Figure 4-1) was originally to be included in the model when dealing with the effects of seasonal freezing with the intent of capturing the necessary changes needed to relocate the point of maximum moment. However, it was quickly realized this would not be the only case in which the soil spring was needed. The need for the spring became evident when attempting to compute the top lateral force resistance using static

equilibrium of the proposed new model. Due to the large differences experienced in the top lateral force without this spring, it was specified for use in all temperature conditions that an integrated column/foundation system can be accurately modeled for design purposes.

A single spring is used to represent the resistance of the soil to lateral movement over the height of the soil, h_s, between the ground surface and the maximum moment location. Since this spring represents the average stiffness of the soil over this height, it is placed halfway between the ground surface and the maximum moment location, $h_s/2$. By locating the spring in the system in this manner, the influence of seasonal freezing on the soil properties are accounted for, and the modified behavior of the system can be captured. Even though seasonal temperature variation affects the behavior of construction material properties, their influence is relatively small on the overall response of the integrated system (Sritharan et al., 2007). However, the inclusion of construction material properties at freezing temperature is recommended; these changes are accounted for by modifying the moment-curvature response used in the analysis. If desired, the designer may replace this single spring with multiple springs to represent the soil stiffness above the maximum moment location, which can increase the accuracy of the analysis, especially when the temperature gradient is significant or expected to be irregular in this region. Each spring used would still be developed in a similar manner to that presented below, with the main difference being the length over which the passive soil pressure is activated for each spring.

The properties of the translational spring are determined following the methodology presented by Reese and Welch (1975) as discussed in Chapter 2, with modifications that create a force-displacement curve as opposed to the p-y curve presented in the research by modifying the developed curve through the multiplication of the soil subgrade reaction value, p, by the length over which the soil spring is being activated when subjected to a lateral load. For the model, this length is equal to the distance between the ground surface and the maximum moment location, h_s. When using multiple springs, the distance in the multiplication would be equal to the depth of the soil layer that each spring is supposed to represent. By performing this multiplication, a force value, V_s, for each spring can be determined at a given lateral displacement for the soil for representing the average soil resistance above the maximum moment location. Once this multiplication is completed, the force-displacement curve is fully developed for use in a computer program as provided in Figure 4-16.

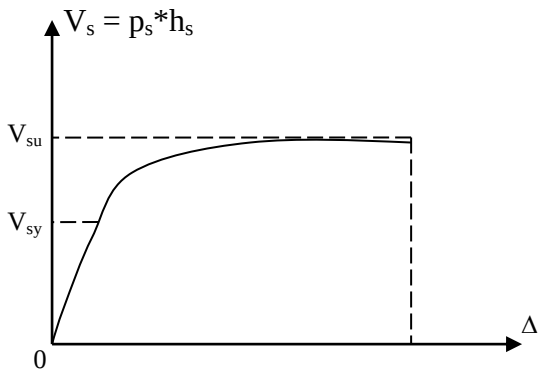

Note: Δ is computed using Equation 2-5 and designer would specify ultimate displacement

Figure 4-16: Description of soil spring located halfway between the maximum moment location and ground surface

Although the force-displacement response of the soil spring was previously defined, a simpler method for determining the soil force, V_s, was needed for the hand calculations at the ultimate and first yield limit states. For the ultimate limit state, the soil was assumed to be fully activated and, therefore, the ultimate soil subgrade reaction, p_u, found using the Reese and Welch methodology (1975) would be expected in the passive loading of the soil. With this assumption in mind, the ultimate soil shear force, V_{su}, would be equal to the ultimate soil subgrade reaction multiplied by the height of the soil above the maximum moment location as presented in Equation 4-12. In the model proposed by Reese and Welch (1975), this value is obtained and the soil proceeds to deform in a perfectly plastic manner with no ultimate displacement reached for the translational spring. A designer must make an appropriate decision on the final displacement of the soil in the region above the maximum moment location.

$$V_{su} = p_u h_s \tag{4-12}$$

where, p_u = ultimate soil subgrade reaction, smaller of Equations 2-2 and 2-3; and
h_s = height of soil between the maximum moment location and ground surface when only one SS spring is used.

To determine the resistance of the soil at the first yield condition, the ultimate soil subgrade reaction was compared with the soil reaction found at the first yield limit state, p_y, in the detailed analyses. The averages for each limit state were found by averaging the subgrade reaction at individual points along the length of the foundation shaft from the ground surface to the maximum moment location. This was considered appropriate, since the subgrade reaction was

essentially constant in this region. In order to compare the two limit states, the average value of the first yield to ultimate soil subgrade reaction was compared to the undrained shear strength of the soil. This comparison, as presented in Figure 4-17, found that as the undrained shear strength of the soil increased the ratio of the first yield to ultimate soil subgrade reaction would decrease in a logarithmic manner. Since the comparison is made based on a ratio of the first yield to ultimate limit state, a coefficient, η, could be developed that would relate the yield soil shear force, V_{sy}, to the ultimate soil shear force, as given in Equation 4-13. The value of η is then determined through Equation 4-14, which was developed based off of the best fit trend line shown in Figure 4-17.

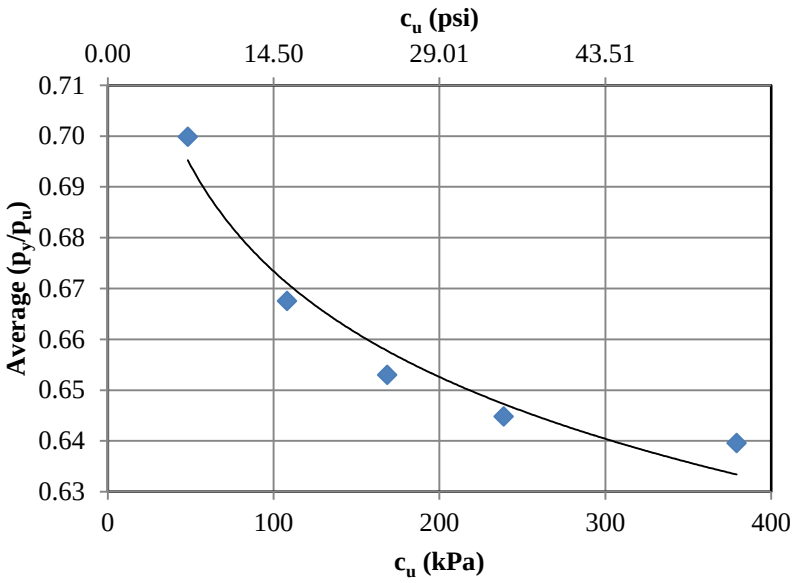

Figure 4-17: Average first yield to ultimate subgrade reaction comparison including data points and best fit trend line

$$V_{sy} = \eta V_{su} \tag{4-13}$$

$$\eta = -0.03 \ln[c_u(kPa)] + 0.8115, \text{ or} \tag{4-14}$$

$$\eta = -0.03 \ln[c_u(psi)] + 0.7536$$

4.4.5 Translational Spring Representing the SFSI Effects below Maximum Moment Location

The last major component in the development of the new model was to specify the properties of the translational spring (TS) located at the point of maximum moment. This translational spring is a bilinear representation of force and displacement that is taking place at the maximum moment location due to the behavior of the soil and foundation shaft as well as the associated

interaction below this point. The properties of this bilinear spring were specified so the changes between the first yield and ultimate limit states due to material nonlinearity, soil and structural, and the interaction effects are more realistically captured. In addition to the effects of material nonlinearity, the bilinear system was chosen since this requires definition of only three points. The remainder of this section discusses the development of the translational spring located at the point of maximum moment.

The initial development of the displacement components of the bilinear force-displacement spring were determined based off of the common moment profile for an integrated system subjected to lateral loading (see Figure 4-2). By using the moment profile in the development, the idea was to create an equation that would be solely based off of the structural parameters of the foundation shaft. For this method, the soil parameters were included in the definition of the critical locations (i.e., maximum moment and zero moment locations). To determine a displacement value in this manner, a quick integration using virtual work methods was employed over the length of shaft between the first zero moment and maximum moment location (i.e., L_{mb}). The aforementioned length was chosen as the displacement at the zero moment location is typically negligible, as found in the results of the detailed analyses, thus suggesting the lateral displacement at the maximum moment location would be mostly due to the induced moment above the zero moment location and the curvature change along L_{mb}. The integration was performed by using different geometric profiles, such as parabolic and triangular, and relating them to the typical moment profile of an integrated column/foundation system (see Figure 4-2) to determine the translational displacement. Although equations were developed using this method, they proved to be unreliable at both the first yield and ultimate limit states, when compared to the detailed analysis results.

To correct the issues associated with this method, empirical equations were developed by normalizing the translation at the maximum moment location with the foundation shaft diameter (i.e., Δ_t/D) and relating it to the normalized length between the maximum moment location and zero moment location (i.e., L_{mb}/D). The relationship was determined by plotting the normalized translation against the normalized length value for the first yield and ultimate limit states. These relationships are presented in Figure 4-18 and a linear trend for both the first yield and ultimate limit states was found to exist. The linear trend prevalent in the graph shows that as the length L_{mb} increases, the translation at the maximum moment location would also increase. This is

expected because the increase in the translation occurs with softer soil, where the length between the maximum moment location and the zero moment location will increase based on the relationships developed in Section 4.4.2. It is also noted the softer soils deviate further from the apparent linear trend than the stiffer soils, especially at the ultimate limit state.

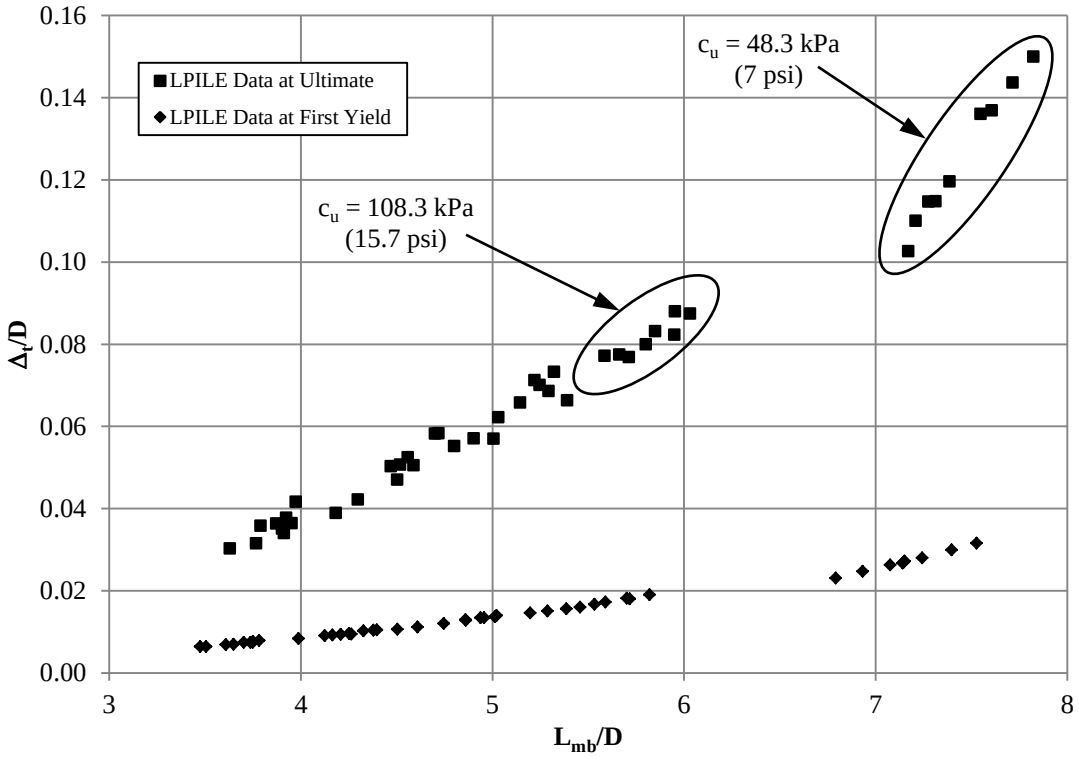

Figure 4-18: Normalized translation at first yield and ultimate limit states versus normalized length L_{mb}/D

The next step in developing the displacement components of the translational spring was to determine a set of equations that defines the translation at both the first yield and ultimate limit states. To determine equations that would represent the displacement for these limit states, best fit linear trend lines were individually created that would represent the entire data sets including the soft soil range. The trends are shown in Figure 4-19 with the developed linear equations provided herein as Equations 4-15 and 4-16, where Δ_{ty} and Δ_{tu} are the translations at the maximum moment at the first yield and ultimate limit states, respectively.

$$\Delta_{ty} = D\left[0.0058\left(\frac{L_{mb}}{D}\right) - 0.015\right] \quad (4\text{-}15)$$

$$\Delta_{tu} = D\left[0.0255\left(\frac{L_{mb}}{D}\right) - 0.0652\right] \quad (4\text{-}16)$$

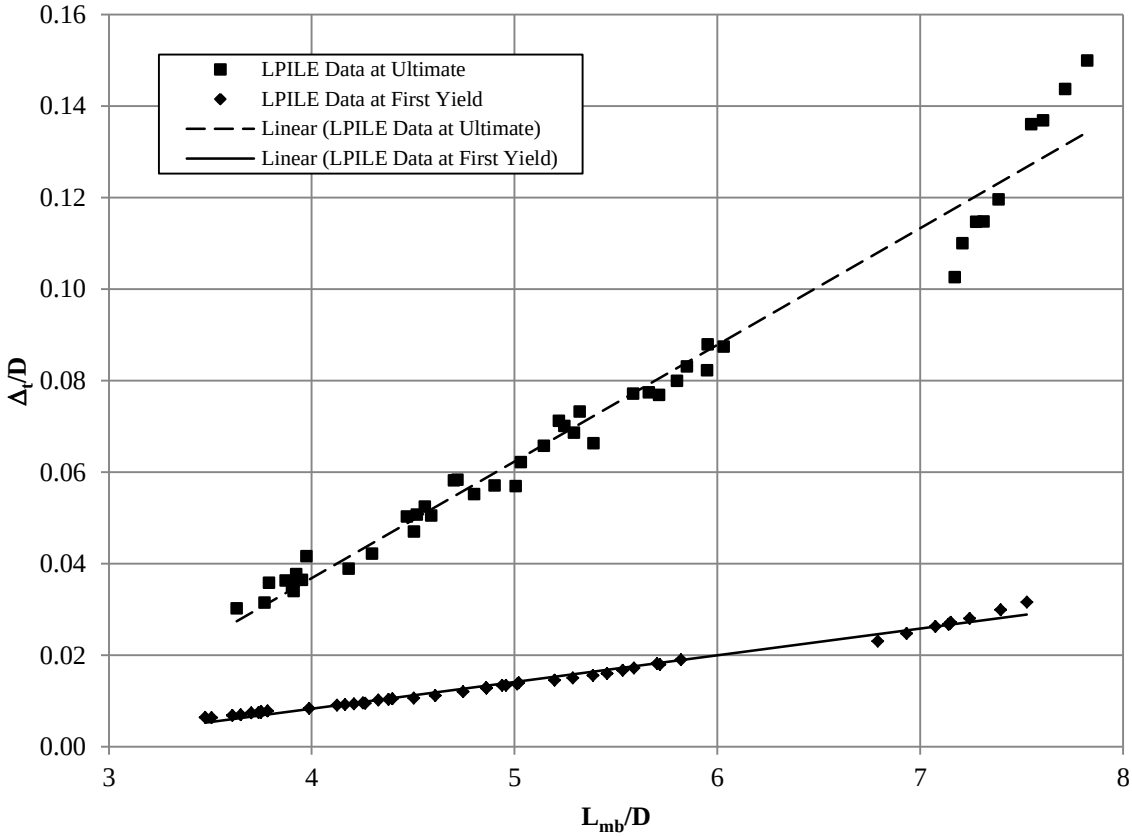

Figure 4-19: Linear trend lines associated with the yield and ultimate limit state translation at the point of maximum moment

Although two equations that represent the average displacement of the system at the point of maximum moment were found, modifications were made to better capture the effects of the soft soil and to further simplify hand calculations. The first modification undertaken was the simplification of the two equations by relating the first yield translation to the ultimate translation. By dividing Δ_{tu} with Δ_{ty}, it was found the slope would differ approximately by a factor of 4.40 and the intercept of Equation 4-15 and 4-16 would differ by a factor of 4.35. Since these values are relatively the same, they were averaged and resulted in a value of 4.372. The first yield translation in the model was, therefore, specified as the translation at the ultimate condition, as previously defined, divided by the constant 4.37, Equation 4-17.

$$\Delta_{ty} = \frac{\Delta_{tu}}{4.37} \tag{4-17}$$

Upon completion of this simplification, the modification for a soft soil was examined. The goal of the examination was to determine a coefficient, ψ, which could be included in the

ultimate translation equation so that the relationship defined in Equation 4-17 would still be valid. To do this, it was determined that the normalized length between the zero moment and the maximum moment locations should be adapted such that the coefficients already developed in Equation 4-16 for the linear trend at the ultimate limit state would remain unchanged. The new relationship would then take the form shown in Equation 4-18. The coefficient, ψ, was also specified to be used only if the soil had an undrained shear strength less than or equal to 70 kPa (10 psi) based off of the better fit of the linear trend to the detailed analyses at higher shear strengths as presented in Figure 4-19. This specific location was chosen as Figure 4-18 shows the variation does not become prevalent until after an undrained shear strength of 108.3 kPa (15.7 psi) and the value of 70 kPa (10 psi) is approximately the middle location between the data sets used in the model development and correlates with an L_{mb}/D value between 6.25 and 6.9, depending on the aboveground column height.

$$\Delta_{tu} = D\left[0.0255\psi\left(\frac{L_{mb}}{D}\right) - 0.0652\right] \quad (4\text{-}18)$$

To determine a value in this manner, the actual data points were compared to the linear trend line and the relative percentage of the normalized length was computed at each data point as demonstrated in Figure 4-20. By examining the data and possible trends presented within this figure, a secondary graph of the relative percentages of the normalized length was then plotted against the normalized above ground column height. The secondary plot, Figure 4-21, depicts a linear trend in which the relative percentage of the normalized length increases as the above ground column height increases. This response allowed the coefficient, ψ, to be determined as a linear function of the above ground height and is presented in Equation 4-19.

$$\psi = 0.0157\left(\frac{L_{col}}{D}\right) + 0.9342 \text{ for } c_u \leq 70 \text{ kPa (10 psi)} \quad (4\text{-}19)$$

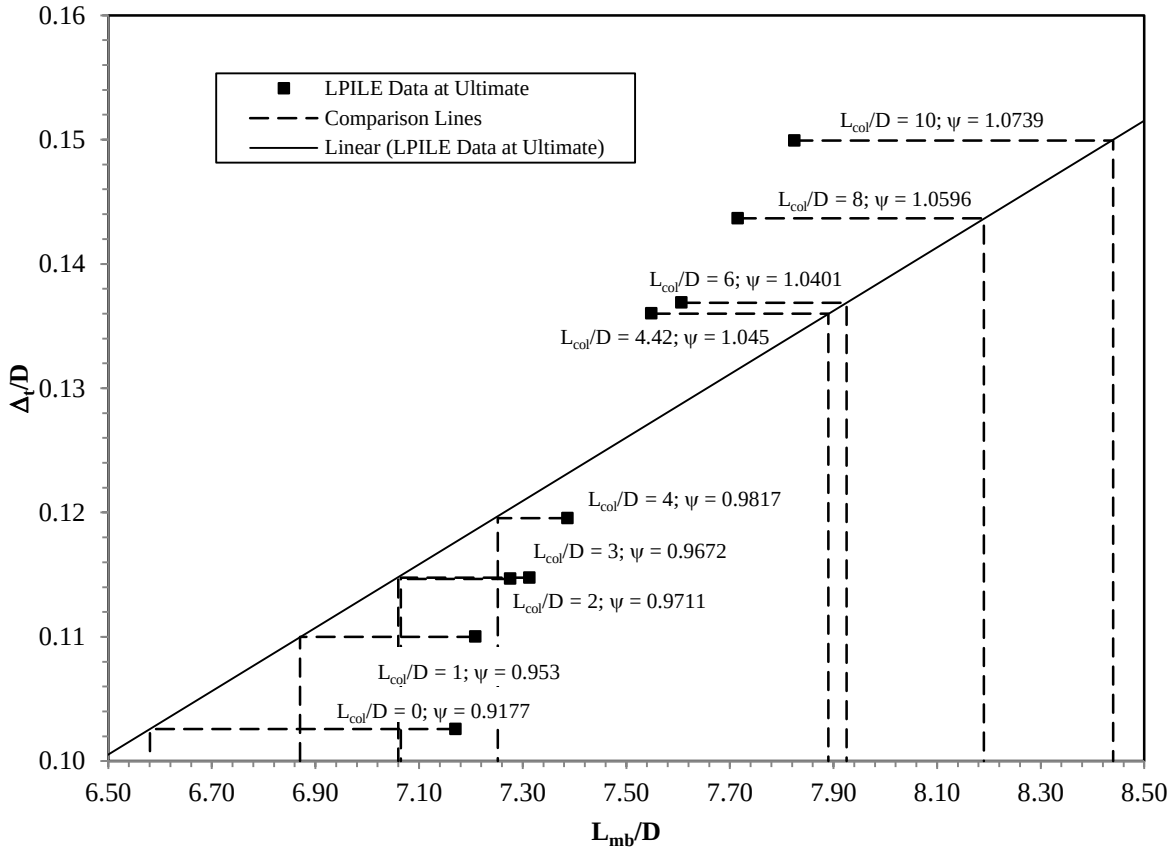

Figure 4-20: Soft soil correction information for coefficient ψ to account for deviation from the linear trend specified in Equation 4-16 (Note: ψ = Adjustment factor)

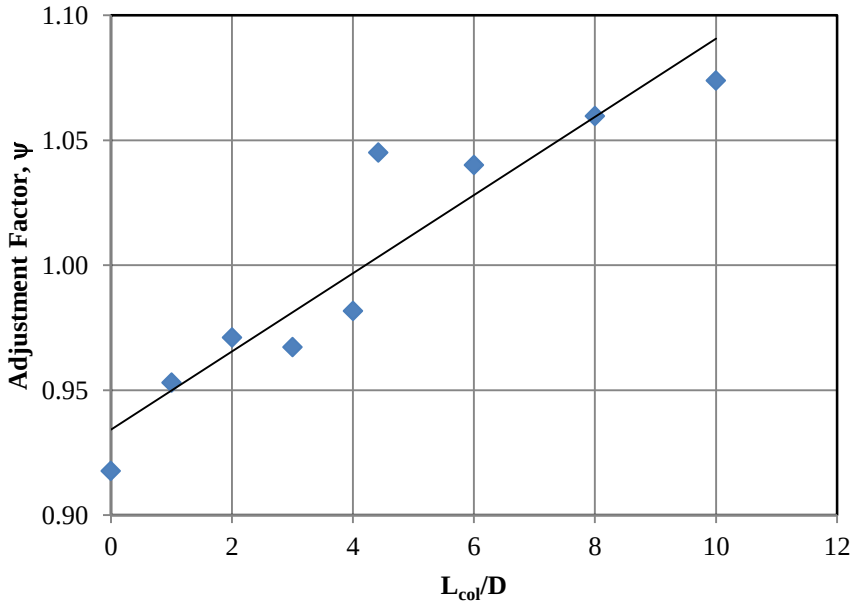

Figure 4-21: Soft soil adjustment factor data and a linear fit curve

Equations 4-18 and 4-17 were verified graphically in Figure 4-22 and mathematically in Table 4-1 to ensure that they would provide satisfactory results over the range of the soil shear strengths. A graphical and mathematical representation were both needed to ensure that the modification factor, ψ, would capture the correct data if the soil had a shear strength less than 70 kPa (10 psi). The graphical verification is only provided using ψ equal to 1.0, since this term is dependent on the aboveground column height, and the exact values of L_{mb}/D for the soft soils are only known for an undrained shear strength of 48.3 kPa (7 psi). Therefore, a mathematical verification was performed by using the normalized length L_{mb}/D obtained from the detailed analyses at an undrained shear strength of 48.3 kPa (7 psi) and determining the translation through Equations 4-18 and 4-17, depending on the limit state. This provided a direct comparison of the equations with detailed analyses and showed that an adequate value could be attained using the aforementioned equations. Although a higher percentage of error, approximately 10%, exists at the yield limit state, this is most likely due to the modifying coefficient being developed at the ultimate limit state. Both the graphical and mathematical comparisons agree well with the detailed analyses.

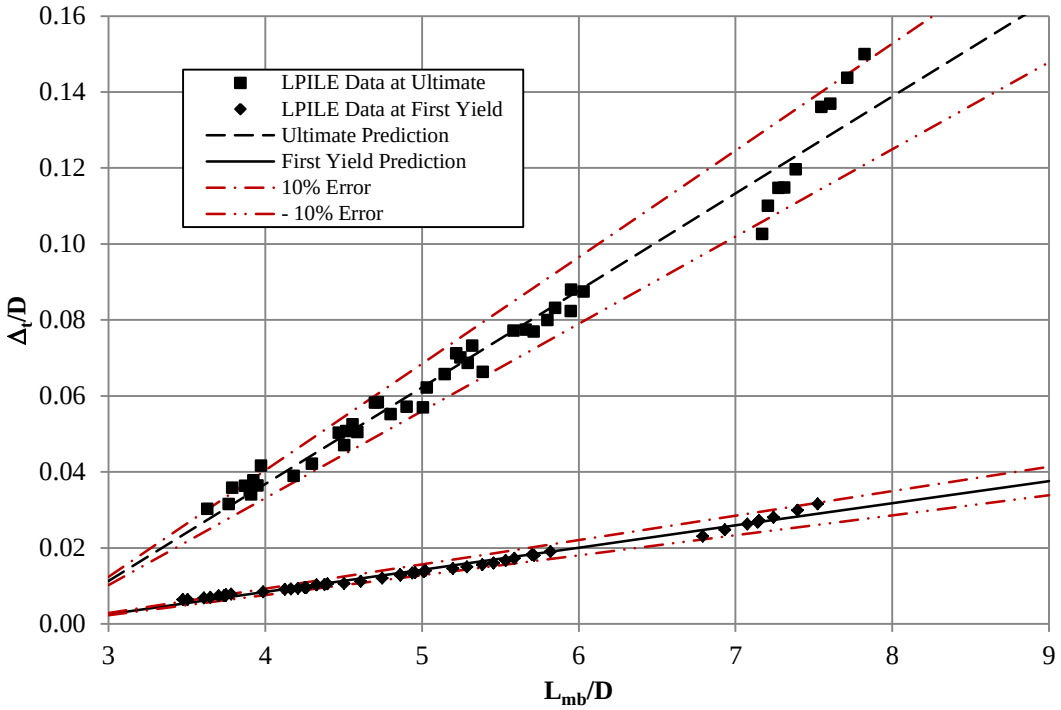

Figure 4-22: Graphical verification of proposed translation equations at the maximum moment location with ψ = 1.0

Table 4-1: Mathematical verification of the proposed translation equations at the maximum moment location for c_u = 48.3 kPa (7 psi)

			Δ_{tu}/D			Δ_{ty}/D		
L_{col}/D	L_{mb}/D	ψ	LPILE	Eqn.	Error	LPILE	Eqn.	Error
0	7.1707	0.934	0.1026	0.1056	2.96%	0.0230	0.0242	4.94%
1	7.2090	0.950	0.1100	0.10942	0.53%	0.0247	0.0250	1.30%
2	7.2763	0.966	0.1147	0.1140	0.61%	0.0263	0.0261	0.67%
3	7.3135	0.981	0.1148	0.1178	2.66%	0.0272	0.0269	0.89%
4	7.3869	0.997	0.1195	0.1226	2.56%	0.0267	0.0281	4.92%
4.42	7.5489	1.004	0.1360	0.1280	5.90%	0.0269	0.0293	9.04%
6	7.6070	1.028	0.1369	0.1343	1.89%	0.0280	0.0307	9.74%
8	7.7153	1.060	0.1437	0.1433	0.25%	0.0299	0.0327	9.74%
10	7.8246	1.091	0.1499	0.1525	1.74%	0.0316	0.0349	10.58%

The final step to define the properties for the bilinear spring is to specify the forces at which the first yield and ultimate translations will occur. These forces are specified by ensuring structural equilibrium is maintained at each limit state. Therefore, the horizontal shear forces used in specifying the bilinear spring behavior can be found by ensuring the summation of the horizontal forces are equal to zero at each respective limit state. The final definition of the translational spring is shown in Figure 4-23.

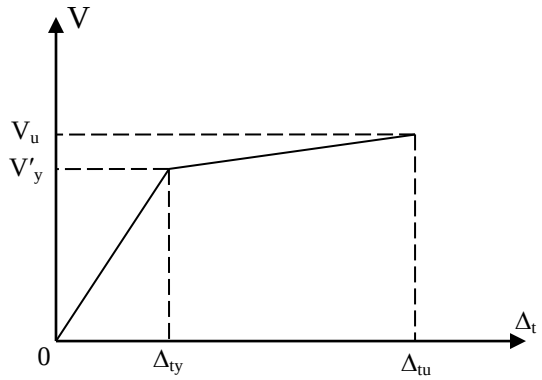

Note: $V_u = V_{tu} - V_{su}$ and $V'_y = V_{ty} - V_{sy}$

Figure 4-23: Description of the bilinear translational spring located at the point of maximum moment

4.4.6 Global Bilinear Force-Displacement Response

The necessary individual components have now been fully developed and this section establishes the global bilinear force-displacement response for a column supported by a CIDH shaft in clay. This process combines the elastic, plastic and translation components of the

displacement (i.e., Δ_e, Δ_p and $\Delta_{t,}$ respectively) to determine the total displacement, Δ, at the top of the column at the first yield and ultimate limit states (see Equation 4-20). An idealized yield location was not specified as the equations presented for the elastic rotations below the maximum moment location and the translation at the maximum moment location were specified at the first yield location. Thus, to define an idealized yield location, these components must be modified by the ratio M_{yi}/M_y prior to determining the tip lateral forces and displacements to maintain structural equilibrium within the system. This is the case, as the changes in these values do not proportionally modify the tip lateral force and displacement using the same ratio. This is primarily due to the nonlinear behavior of the soil.

$$\Delta = \Delta_e + \Delta_p + \Delta_t \tag{4-20}$$

In defining the tip lateral displacement, a minor iteration on the elastic displacement of the system is used to more accurately capture additional displacements and forces developed due to the applied axial load at the top of the column. In addition to computing the ultimate displacement of the system, the lateral load applied at the top of the column will be determined, thus finalizing the global force-displacement response of the integrated column/foundation system.

The plastic displacement shall be specified first, as this component of the total displacement requires no iterations at the first yield or ultimate limit states. When examining the first yield limit state, the system is expected to behave in a fully elastic manner which means no plastic displacement occurs at this limit state. Therefore, the plastic displacement at first yield, Δ_{py}, is equal to zero and the total displacement is just that of the elastic displacement in the system. At the ultimate limit state, the model was created such that the plastic displacement, Δ_{pu}, was simply equal to the plastic rotation multiplied by the effective height of the system as in Equation 4-21. The plastic rotation can be found using Equation 4-7 with the analytical plastic hinge length taken from Equation 4-9. The effective height of the system is the distance from the column tip to the maximum moment location as specified in Equation 4-2.

$$\Delta_{pu} = \theta_p L_{ma} \tag{4-21}$$

The second component to be specified in the final displacement equation is the translational component, Δ_t. This component is used to specify the amount of translation that takes place at the maximum moment location due to lateral movement that occurs to the shaft below this point.

Therefore, this value is simply taken as the displacement of the translational spring at the maximum moment location for the correct limit state. At the ultimate limit state, this displacement is equal to Δ_{tu} taken from Equation 4-18, thus allowing the first yield displacement, Δ_{ty}, to be determined using Equation 4-17.

The third and final component to be specified for the total displacement is the elastic displacement of the system. This component is defined as the summation of the elastic displacement occurring above the maximum moment location, Δ_{et}, and the elastic displacement caused by the elastic rotation below the maximum moment location, Δ_{eb}. The elastic component of translation at the flexible base is not included here, since it was already accounted for as Δ_{ty} in the previous paragraph. The displacement caused by the elastic rotation does not require an iterative process and is equal to the elastic rotation below the maximum moment, θ_{eb}, at the appropriate limit state multiplied by the effective height of the system as in Equation 4-22. The elastic rotation for the appropriate limit state is found through Equation 4-10 or Equation 4-11.

$$\Delta_{eb} = \theta_{eb} L_{ma} \tag{4-22}$$

where, θ_{eb} = elastic rotation at the appropriate limit state using Equation 4-10 or 4-11

To determine the component of elastic displacement above the maximum moment location, Δ_{ea}, at the ultimate limit state, an iterative process must be used due to the large displacements expected within the SFSI system. To define this deflection, the top lateral force must be approximated based on structural equilibrium including P-Δ effects. This initial estimate can be found through the use of Equation 4-23, where P is the applied axial load to the system, M_{max} is the ultimate moment capacity of the shaft at a given limit state, and V_{t1} is the uncorrected lateral load at the top of the column. Once this lateral force is obtained, an estimate on the elastic displacement may be made by using the deflection of a free end of a fixed cantilever ignoring the resisting force from the soil, Equation 4-24 (first term only), as the soil resistance typically causes a variation in the displacement of less than 10% and is therefore considered negligible by the authors. A more accurate analysis can be performed with the inclusion of this force (second term of Equation 4-24) and a fixed base cantilever, but the second term is small in comparison to the first and may be neglected when performing this step.

$$V_{t1} = \frac{M_{max} - P(\Delta_p + \Delta_{eb}) + V_s(h_s/2)}{L_{ma}} \tag{4-23}$$

$$\Delta_{ea} = \frac{V_{t1} {L_{ma}}^3}{3EI_e} - \frac{1}{8}\frac{V_s h_s}{EI_e}(L_{ma} - 0.25h_s) \quad (4\text{-}24)$$

where, EI_e is the effective flexural rigidity of the system and is taken as M'_y/ϕ'_y

Although these values are a good approximation of the global lateral load and elastic displacement above the maximum moment location, these values should be corrected again due to the large displacement of the column tip at the ultimate limit state. The correction ensures the moment caused by the P-Δ effects is adequately captured. To find a more appropriate displacement and the top lateral load, Equation 4-23 is modified to include the elastic displacement above the maximum moment location and the new lateral load input into Equation 4-24 to determine the elastic displacement above the maximum moment location, Δ_{eac}. The corrected lateral, V_t, is found through the use of Equation 4-25. By accounting for the elastic displacement in this manner, the rotation of the foundation shaft above the maximum moment location has also been accurately accounted for.

$$V_t = \frac{M_{max} - P(\Delta_p + \Delta_{eb} + \Delta_{ea}) + V_s(h_s/2)}{L_{ma}} \quad (4\text{-}25)$$

The final step in specifying the global force-displacement response of an integrated column/foundation shaft is to combine the information presented above into a graphical form. The bilinear approximation for the system uses the following three points to define the response:

- The initial point of the curve is taken as the origin of a Cartesian coordinate system. This point is used because it is assumed that at no lateral load there will be no lateral displacement and vice versa.
- The second point is defined as the first yield location. The model presented above defines this point as the location at which the extreme tension bar in the foundation shaft first experiences a yielding strain. This point would use M'_y in Equation 4-25 to determine the lateral load at the top of the column and the displacement is obtained from Equation 4-20 and does not include any plastic displacement component.
- The third and final point defines the ultimate limit state. In the model, the ultimate limit state is defined as the full development of the flexural capacity in the foundation shaft at the maximum moment location. Therefore, the point would be defined using the ultimate capacity and curvature of the foundation shaft based off of a moment-curvature analysis.

The lateral force is defined using Equation 4-25 and the lateral displacement is defined using Equation 4-20 with the inclusion of plastic action.

4.5 Model Verification

The new model established for determining the seismic response of drilled shafts in clays has been developed and the effectiveness of the approach must be verified. Therefore, verification against the detailed analyses used in developing the model as well as the experimental data reported by Suleiman et al. (2006) was performed. In each case, two different investigations were conducted to ensure both local and global responses of the system would be satisfactorily captured by the proposed model. In addition to these responses, the comparison with the experimental data will demonstrate the ability of the model to handle both the frozen and the unfrozen state, when dealing with seasonal freezing as well as its effectiveness in a real life situation. The remainder of this section will discuss in detail the results of the analytical and experimental verifications performed for the proposed methodology.

4.5.1 Experimental Verification

The first key step in performing the experimental verification was to specify an equivalent soil profile to be used in the new method based on the information provided in Section 2.3.1. This was achieved by taking the soil profile at the Spangler site on the Iowa State University campus in the frozen and unfrozen state, as illustrated in Figure 4-24, and determining an average undrained shear strength, moist unit weight and strain at fifty percent of maximum stress for the cohesive soil within the first six pile diameters below the ground surface. This depth was chosen based on the assumption that the maximum moment location occurs within the specified length and this zone has the greatest influence on the lateral load behavior. In addition to this, the height of the soil between the ground surface and the maximum moment location was not used, since this would require multiple iterations to define the response of the overall system. This length is also common within previous research (e.g., Chai, 2002 and Das, 2004) into the lateral load response of an integrated column/foundation system.

The average undrained shear strength was found by using a weighted average method based on the length of the pile between two consecutive points. The undrained shear strengths for the system were thus found to be 150.2 kPa (21.79 psi) and 440.5 kPa (63.98 psi) for the unfrozen and frozen states respectively. The fifty percent strain value was based off of recommendations

by Reese et al. (2004) and found that the corresponding values would be 0.005 and 0.004 for the unfrozen and frozen states, respectively. The last parameter, moist unit weight, was taken as 21.2 kN/m^3 (0.078 lb/in^3) based off of the laboratory testing performed by Suleiman et al. (2006) for all layers examined.

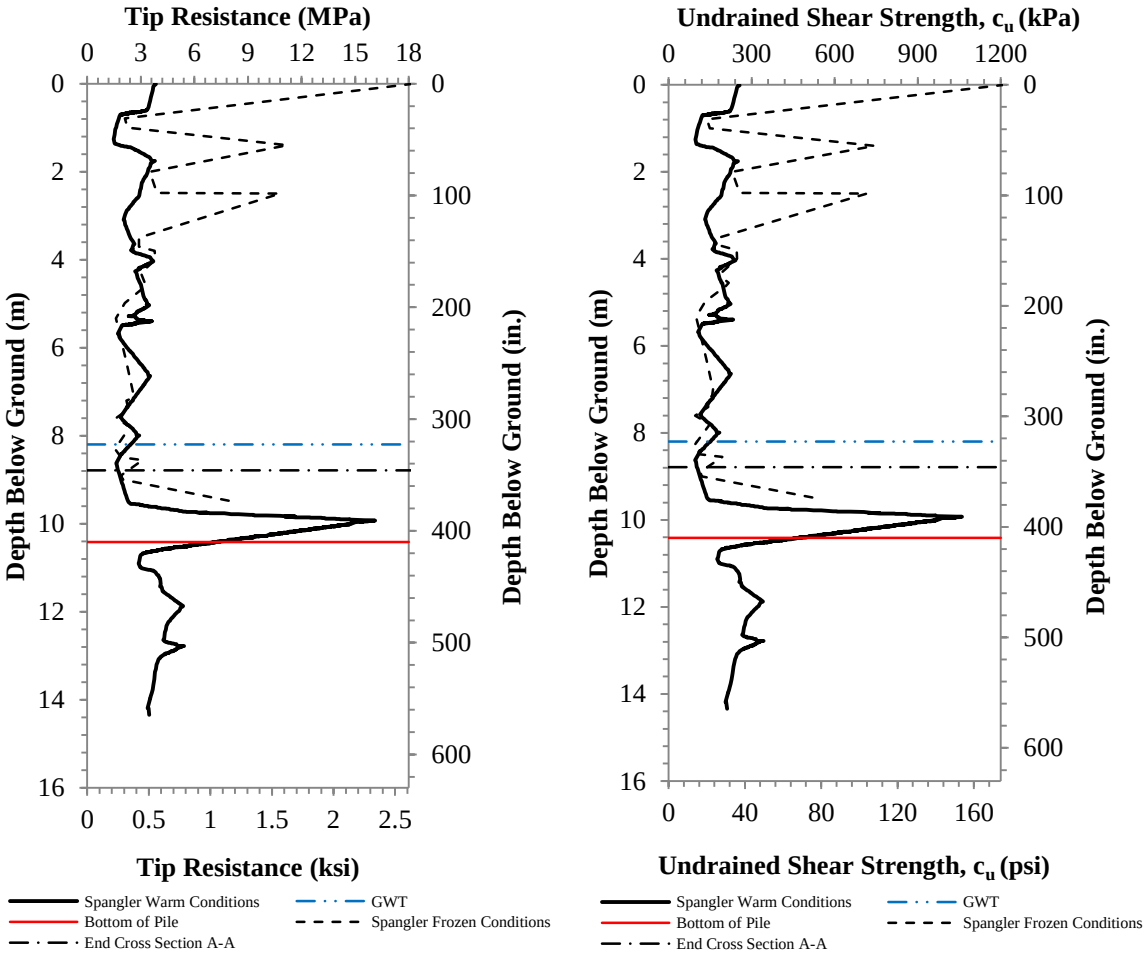

(a) CPT tip resistance (b) undrained shear strength

Figure 4-24: Spangler soil profile with depth in the unfrozen and frozen state (GWT = Ground Water Table)

The remaining information needed to perform the analysis using the simplified model is a definition of the structural response of the foundation shaft. This was performed by using VSAT (Levings, 2009) to determine the moment-curvature response of the column and shaft sections. The cross-section and material properties used within this analysis were modeled following the data presented in Sritharan et al. (2007) for the foundation shaft and then corrected based on the

information provided in Chapters 5 and 6 of this report for the effects of temperature. In addition, a soil confining pressure of 344.75 kPa (50 psi) was specified based on the work done in Chapter 3 and a water percentage by weight for the concrete was assumed to be 3% to account for the effects of frozen temperatures in VSAT. The input parameters used in VSAT were previously provided in Table 3-1 as the Foundation (A-A) cross-section. To handle the temperature effects, VSAT internally computed the modified values based on the work performed by Levings (2009) for an analysis temperature of -10 °C (14 °F) and testing temperatures of 20 °C (68 °F).

The results of the section analyses were then idealized using a bilinear representation, since this will provide enough information to use the new method. The results of the bilinear idealization are provided in Table 4-2. This is compared to the actual moment-curvature response in Figure 4-25.

Table 4-2: Bilinear idealization obtained for shafts from moment-curvature analyses

Value	SS1 at 23 °C (73.4 °F)	SS2 at -10 °C (14 °F)
First Yield Moment	435.30 kN-m (3852.72 kip-in)	451.18 kN-m (3993.24 kip-in)
First Yield Curvature	0.00591 1/m (1.50E-04 1/in.)	0.006171 1/m (1.57E-04 1/in.)
Yield Moment	678.14 kN-m (6002.01 kip-in)	705.78 kN-m (6246.70 kip-in)
Yield Curvature	0.009201 1/m (2.34E-04 1/in.)	0.009654 1/m (2.45E-04 1/in.)
Ultimate Moment	801.60 kN-m (7094.76 kip-in)	810.13 kN-m (7170.24 kip-in)
Ultimate Curvature	0.138865 1/m (3.53E-03 1/in.)	0.125594 1/m (3.19E-03 1/in.)

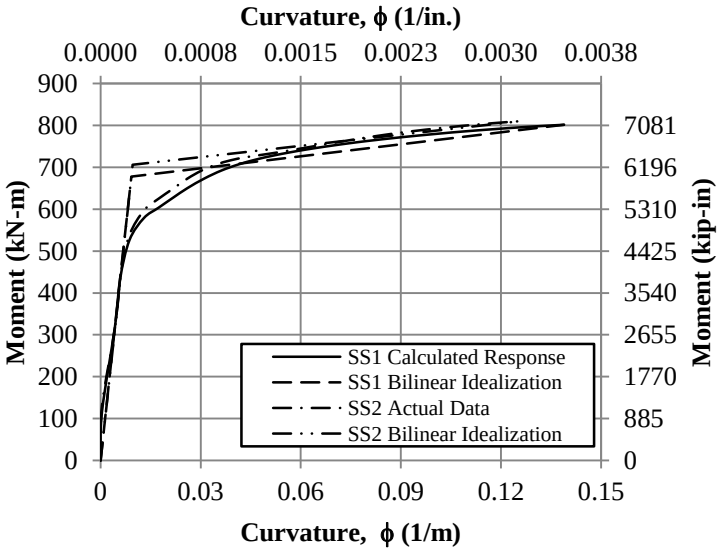

Figure 4-25: Moment-curvature section analyses of test units SS1 and SS2 of Suleiman et al. (2006) for foundation section A-A (see Figure 2-10)

Following the development of the two different models for frozen and unfrozen conditions, based on the information provided in Table 4-2, the results of the simplified model analyses were then compared to the experimental data of SS1 in Figure 4-26 and SS2 in Figure 4-27, to examine the global lateral force-displacement trend in both the warm weather and cold weather conditions. The full model development of the warm weather condition is provided in Appendix A as an example using actual numbers.

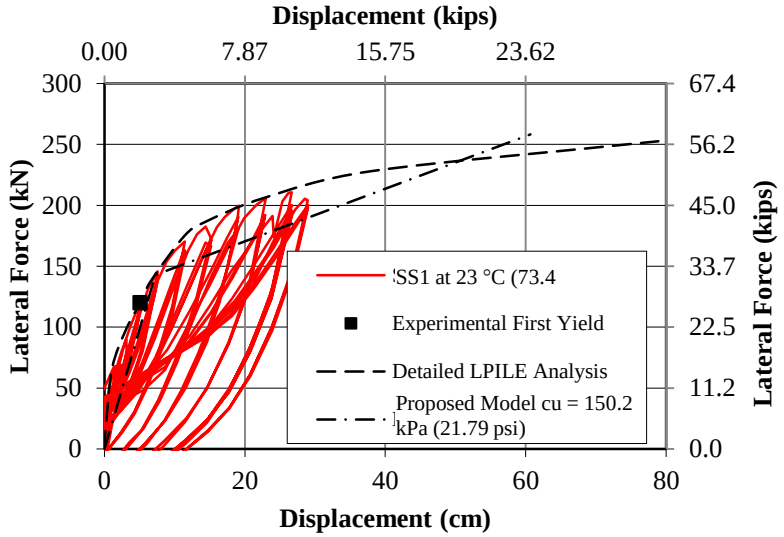

Figure 4-26: Global response comparison obtained from the new model with the experimental response and that established from a detailed LPILE analysis of SS1 at 23 °C (73.4 °F)

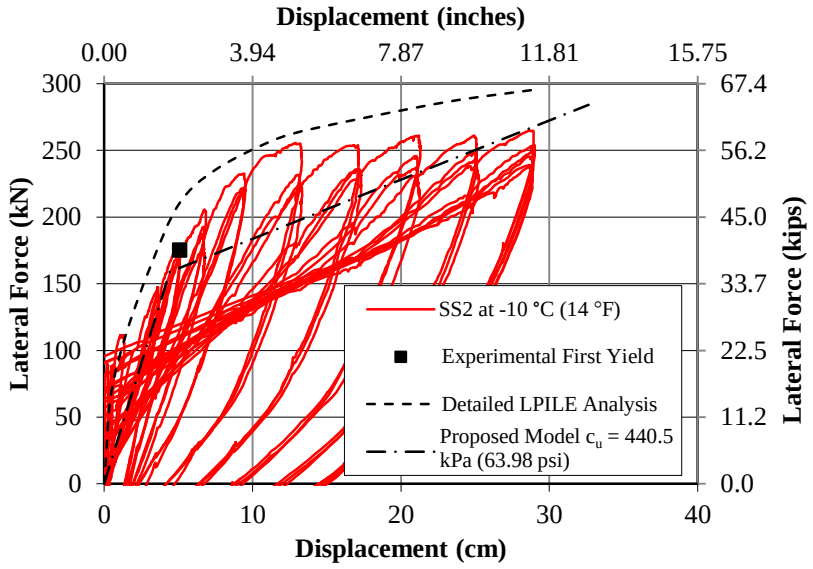

Figure 4-27: Global response comparison obtained from the new model with the experimental response and that established from a detailed LPILE analysis of SS2 at -10 °C (14 °F)

In addition, the proposed new model was compared with the detailed analyses completed for SS1 and SS2 to demonstrate the accuracy of the other parameters involved in the model development. These comparisons are provided below in Table 4-3 and Table 4-4 for SS1 and SS2, respectively.

Table 4-3: Comparison of critical parameters of SS1 at the ultimate limit state

	Detailed Analysis		Proposed New Model		
Parameter	**SI Unit**	**English Unit**	**SI Unit**	**English Unit**	**Error**
L_{ma}	3.67 m	144.5 in	3.42 m	134.7 in	-6.81%
L_{m0}	7.19 m	283.1 in	6.69 m	263.3 in	-6.95%
L_{mb}	3.52 m	138.7 in	3.27 m	128.5 in	-7.10%
p_u	249.5 kN/m	1424.9 lb/in	306.4 kN/m	1749.8 lb/in	-18.6%
V_s	243.9 kN	54.8 kip	223.6 kN	50.3 kip	-8.32%
Δ_t	6.07 cm	2.39 in	4.35 cm	1.71 in	-28.3%
θ_{eb}	0.01987 rad		0.017 rad		-14.4%
Δ_{eb}	7.29 cm	2.87 in	5.89 cm	2.32 in	-19.3%
L_{pb}	0.71 m	27.8 in	0.52 m	20.56 in	-26.8%
θ_{pb}	0.0894 rad		0.067 rad		-25.1%
θ_p	0.1739 rad		0.1337 rad		-23.1%
Δ_p	0.64 m	25.3 in	0.46 m	18.01 in	-28.1%
Δ_{ea}	5.33 cm	2.10 in	4.68 cm	1.84 in	-12.20%
V_t	252.6 kN	56.8 in	258.1 kN	58.0 kip	2.18%
Δ_u	0.79 m	31.1 in	0.61 m	23.9 in	-22.8%

Table 4-4: Comparison of critical parameters of SS2 at the ultimate limit state

	Detailed Analysis		Proposed New Model		
Parameter	**SI Unite**	**English Unit**	**SI Unit**	**English Unit**	**Error**
L_{ma}	2.80 m	110.08 in.	2.95 m	116.1 in.	5.36%
L_{m0}	4.94 m	194.39 in.	5.18 m	203.9 in.	4.86%
L_{mb}	2.14 m	84.31 in.	2.23 m	87.8 in.	4.21%
p_u	2013.7 kN/m	11498.5 lb/in	839.4 kN/m	4739.2 lb/in	-58.3%
V_s	208.6 kN	46.9 kip	215.1 kN	48.3 kip	3.12%
Δ_t	1.24 cm	0.49 in	1.71 cm	0.67 in.	37.9%
θ_{eb}	0.0105 rad		0.012 rad		14.29%
Δ_{eb}	2.95 cm	1.16 in.	3.52 cm	1.39 in.	19.32%
L_{pb}	0.31 m	12.21 in.	0.36 m	14.05 in.	16.13%
θ_{pb}	0.0355 rad		0.041 rad		15.49%
θ_p	0.0839 rad		0.0817 rad		-2.62%
Δ_p	0.23 m	9.02 in.	0.24 m	9.49 in.	4.35%
Δ_{ea}	2.84 cm	1.12 in.	3.32cm	1.31 in.	16.90%
V_t	295.8 kN	66.5 kip	284.1 kN	63.9 kip	-3.95%
Δ_u	0.29 m	11.5 in.	0.33 m	12.9 in.	13.79%

The global comparison provided in Figure 4-26 and Figure 4-27 shows the new model is able to capture the full range of elastic and inelastic action with slopes that correspond well with the experimental data produced by Suleiman et al. (2006). Therefore, the comparison is showing that the effects of nonlinearity within the system are accurately captured as desired in both seasonal temperatures. In the more direct comparison of the two methods, it may appear at first glance that the data sets do not well correlate in the inelastic range. However, this is not true based on the assumptions made within the model development. An examination of the plastic displacement and its components is the particular area within the model where the most error appears to occur. However, this was expected, since the plastic hinge length was conservatively chosen based on the information in Figure 4-8 for the entire range of data analyzed. A closer look at the experimental data in Figure 4-8 for c_u = 150.24 kPa (21.79 psi), which is close to the value of c_u = 168.61 kPa (24.45 psi) shown in the figure, would suggest a longer analytical plastic hinge length, resulting in a conservative plastic displacement. This conservatism in the displacement at the ultimate limit state was deliberately chosen, which would help to guarantee that an undesirable failure mechanism would not occur. The top lateral load, however, is not a conservative value, so the shear force is adequately captured and allows for the horizontal shear reinforcement to be correctly included. By maintaining conservatism in this manner, the proposed model better adheres to the capacity design principles by allowing flexural action to occur while preventing an undesirable failure mechanism. The more detailed method also demonstrates that the critical locations within the integrated column foundation system are accurately captured with an error of less than 10%. In addition to the critical parameters, the effects of seasonal freezing were effectively captured during the modeling of SS2 even though c_u = 441.1 kPa (63.98 psi) exceeds the range [i.e., c_u = 48.3 kPa (7 psi) – 379.2 kPa (55 psi)] used for the detailed LPILE analyses in the model development. Therefore, it can be said that the new method is effectively capturing the lateral loading behavior of an integrated column/foundation system during the different seasons of the year.

4.5.2 LPILE Analytical Verification of Concrete Drilled Shafts

To further expand on the verification process, the simplified model was also compared against more detailed analyses used to create the model in the first place. This verification is provided here as the two models above only provide information in the mid and upper ranges [c_u = 150.2 kPa (21.79 psi) to 441.1 kPa (63.98 psi)] of the soil undrained shear strengths for which

the model was developed. Although numerous comparisons were made (see Appendix A), this section discusses a model on the lower end of the proposed model [c_u = 48.3 kPa (7 psi)], since the experimental verification establishes validity for the mid and upper range of c_u. The remainder of this section presents the model verification for a column continued into the ground as a drilled shaft foundation with the same cross-sectional dimensions and reinforcement as SS1, but with no column shaft above ground. The drilled shaft was assumed to have a five percent axial load ratio and is to be constructed in a soft cohesive soil of uniform strength with c_u = 48.3 kPa (7 psi).

Similar to the previous section, a global comparison and a more direct comparison of the simplified model with the detailed LPILE analysis was performed to examine the accuracy of the new model. The global comparison is provided using force-displacement responses obtained from a detailed LPILE analysis (Reese et al., 2004) and that from the simplified method in Figure 4-28. The direct comparison at the ultimate limit state, presented in Table 4-5, examines the critical locations and values of the detailed LPILE analysis and the simplified model to further validate the model.

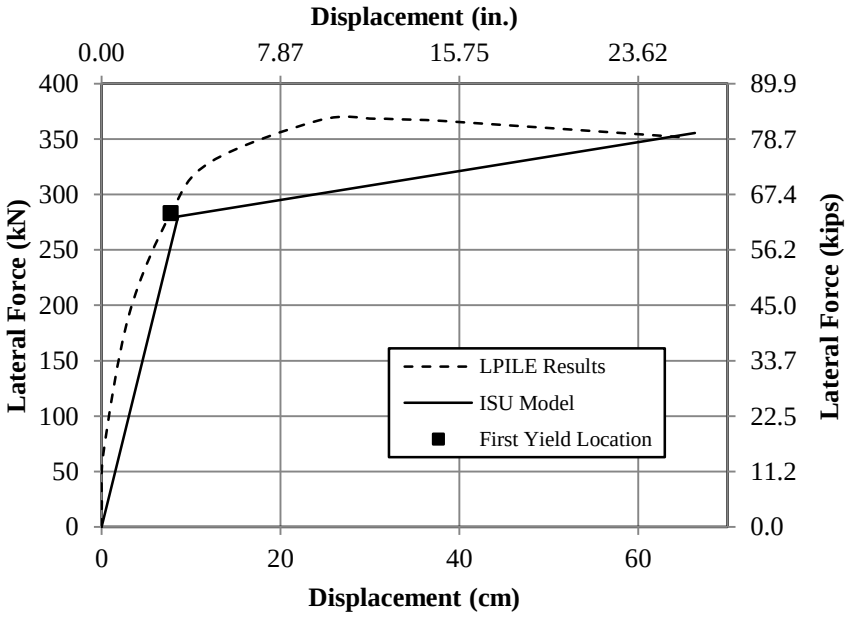

Figure 4-28: Global response comparison obtained from the new model with that established from a detailed LPILE analysis at c_u = 48.3 kPa (7 psi) and L_{col}/D = 0

Table 4-5: Comparison of critical parameters at the ultimate limit state obtained from the new model with that established from a detailed LPILE analysis at c_u = 48.3 kPa (7 psi) and L_{col}/D = 0

	Detailed Analysis		Proposed New Model		
Parameter	**SI Unit**	**English Unit**	**SI Unit**	**English Unit**	**Error**
L_{ma}	2.92 m	114.8 in.	2.83 m	111.4 in.	-3.08%
L_{m0}	7.29 m	286.9 in.	7.15 m	281.6 in.	-1.92%
L_{mb}	4.37 m	172.1 in.	4.32 m	170.2 in.	-1.16%
p_u	137.1 kN/m	782.6 lb/in	127.7 kN/m	729.3 lb/in	-6.86%
V_s	399.6 kN	89.8 kip	361.3 kN	81.2 kip	-9.58%
Δ_t	6.25 cm	2.46 in.	6.33 cm	2.49 in.	1.28%
θ_{eb}	0.0222 rad		0.023 rad		3.60%
Δ_{eb}	6.47 cm	2.55 in.	6.39 cm	2.52 in.	-1.24%
L_{pb}	0.70 m	27.61 in.	0.69 m	27.24 in.	-1.43%
θ_{pb}	0.0891 rad		0.088 rad		-1.23%
θ_p	0.179 rad		0.176 rad		-1.68%
Δ_p	0.52 m	20.59 in.	0.50 m	19.58 in.	-3.85%
Δ_{ea}	3.68 cm	1.45 in.	3.89 cm	1.53 in.	-5.52%
V_t	351.8 kN	79.1 kips	355.5 kN	79.9 kips	1.06%
Δ_u	0.65 m	25.53 in.	0.66 m	26.12 in.	1.54%

The two comparisons provided within this section further validate the accuracy of the simplified model when determining the lateral response of a drilled shaft in clay soils as the results of the direct comparison are typically within 10% between the simplified model and the detailed LPILE analysis. The graphical comparison shows the yield and ultimate limit locations closely match the detailed analysis results produced using LPILE. This is seen as the first yield limit state point is almost exactly on the line obtained for the detailed analysis. In addition to this, the representation shows that the ultimate limit state is captured accurately and the effects of nonlinearity between the yield and ultimate limit states occur. For this case, conservatism in the ultimate displacement has disappeared because this is the trial in Figure 4-8, for which the minimum value in the analytical plastic hinge length, L_{mb}, was obtained, producing the most accurate estimate for the plastic displacement.

The additional verification information provided in Appendix A further demonstrates the validity of the model. Each case presented in this section provides a detailed comparison of the simplified model with a detailed LPILE analysis at the ultimate limit state and a global lateral force-displacement response comparison. For all cases in the additional comparisons provided in

Appendix A, the first yield limit state was typically captured within 5% of the expected force and 10% of the expected displacement based on the detailed analyses in LPILE. At the ultimate limit state, the displacements obtained through the proposed simplified model are a conservative estimate and are justifiable, since an integrated column/foundation system should not be permitted to experience lateral displacements as high as 100 cm (39.4 in.) when subjected to a design level or greater seismic event. The top lateral load, on the other hand, was not a conservative value and typically overestimated the top lateral load at the ultimate condition. Obtaining an overestimation in this manner is more appropriate in the capacity design principles to prevent any undesirable failure mode developing when the system is pushed past the point of first yielding in a seismic event.

CHAPTER 5: CONCRETE BEHAVIOR AT FROZEN TEMPERATURES

5.1 Introduction

A critical component of seismic design is being able to effectively define material properties for all possible loading conditions. This is especially true when defining the behavior of confined concrete within the plastic hinge region of column or foundation shaft. Defining the behavior of confined and unconfined concrete requires a definition of the stress-strain behavior of the specimens. A typical idealized representation of the stress-strain behavior of concrete is shown in Figure 5-1.

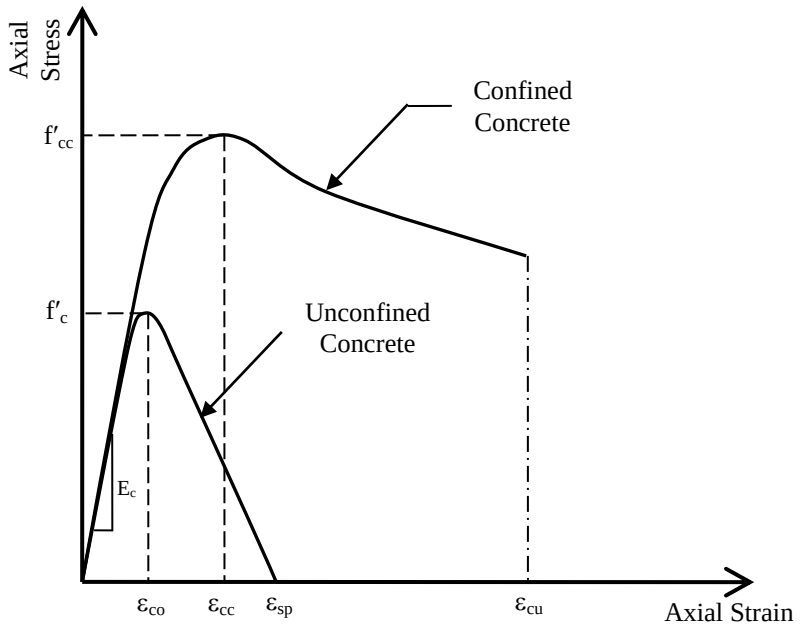

Terminology:
f'_c = peak unconfined compressive stress; E_c = concrete modulus of elasticity; ε_{co} = strain at peak unconfined concrete stress; ε_{co} = peak unconfined compressive strain; f'_{cc} = peak confined compressive stress; ε_{cc} = strain at peak confined concrete stress; ε_{cu} = ultimate confined compressive strain;

Figure 5-1: Idealized stress-strain behavior of confined and unconfined concrete subjected to an axial loading

To better understand the effects of seasonally frozen temperatures on confined and unconfined concrete, an experimental study was undertaken as part of this project. Testing was needed as it was found that no research has ever really been performed on the effects of confined concrete when it is subjected to frozen conditions. This chapter discusses in detail the investigation completed at ISU that examined multiple concrete strengths, multiple horizontal

reinforcement ratios and multiple temperatures in an attempt to define changes in the concrete's compressive behavior, ultimate strength, elastic modulus and Poisson's ratio as a function of temperature.

5.2 Test Matrix

Before any testing could be performed on concrete, it was important to define horizontal reinforcement ratios, concrete strengths and temperatures experienced in the State of Alaska and other seismic regions so that representative samples could be constructed. To complete this task, reinforcement ratios and concrete strengths typical of design in columns and foundations for Alaska were examined along with expected seasonal temperatures (see Section 5.2.1). After defining the type of concrete and testing temperatures to be used in the experimental investigation, a test plan was created to capture the desired results (see Section 5.2.2) so the appropriate amount of samples would be constructed.

5.2.1 Concrete Selection

Throughout Alaska and the United States, it was determined that typical concrete compressive strengths should be in the range between 27.6 MPa (4 ksi) and 55.2 MPa (8 ksi), horizontal reinforcement ratios should vary between 0.006 and 0.012, confinement reinforcement should include horizontal spirals and steel shell external reinforcement, and a minimum temperature of -40 °C (-40 °F) would be appropriate, as they encompass the full variation of seasonal temperatures

The concrete strengths and reinforcement ratios were selected as these are common in high seismic regions, including Alaska and many parts of the United States. The minimum temperature for testing purposes was determined based on discussions with the personnel of the ADOT&PF and AUTC organizations. During these discussions, it was also concluded that the mix designs to be used for the concrete could be representative of the local batch plant, as this would adequately represent the mix available in Alaska. Since it was known that the specimens would be too small to handle deformed bar reinforcement, the horizontal reinforcement would be designed such that the reinforcement ratio would provide an equivalent confining stress to the selected ratio when Grade 60 reinforcing bar was used in the specimens. With these values in mind, Table 5-1 was created to define the ratios and concrete strengths needed for experimental testing.

Table 5-1: Concrete strength, reinforcement type and horizontal reinforcement ratios of cylindrical test specimens

Reinforcement Type	Reinforcement Yield Stress	Grade 60 Reinforcement Ratios	Concrete Strengths
(material)	**MPa (ksi)**	**(ρ_s)**	**MPa (ksi)**
None	None	Unconfined	27.6 (4), 41.4 (6), 55.2 (8)
1/8 inch wire	344.7 (50)	0.006, 0.009, 0.012	27.6 (4)
1/8 inch wire	344.7 (50)	0.009	41.4 (6)
1/8 inch wire	344.7 (50)	0.009	55.2 (8)
Steel Shell	248.2 (36)	0.013	27.6 (4), 41.4 (6), 55.2 (8)

5.2.2 Testing Plan

The next step in the process was to effectively decide upon a testing plan so that all of the required samples could be constructed and tested as needed. By using the information in Table 5-1, a testing sequence was setup such that a significant amount of data on material properties for use in the design of CIDH shafts would be obtained. The concrete samples were tested at four temperature levels, 20 °C (68 F), -1 °C (30.2 °F), -20 °C (-4 °F), and -40 °C (-40 °F), to represent the changes in ground and ambient air temperatures experienced in cold weather conditions. Using the above information and the confined concrete properties in Table 5-1, the test matrix provided in Table 5-2 was established to allow sample construction.

The information provided in Table 5-2 shows that the tests specified will be conducted under a monotonic loading at a table displacement of 1.27 mm/min (0.05 in/min) or an approximate strain rate of 0.5%/min. The main loading rate specified for testing was selected based on ASTM C 39/C 39M (2003), where the test apparatus head should travel at a rate of approximately 1 mm/min (0.05 in/min). The other key component demonstrated in the test plan is the largest amount of testing will be performed on 27.6 MPa (4 ksi) concrete, since this mix represents the most commonly specified concrete strength used in foundation design throughout the United States including Alaska.

Table 5-2: Test Matrix used for Cylindrical Concrete Specimens

Concrete Strength	Cyclic or Monotonic	Reinforcement Ratio	Number of Samples	Temperature °C	Loading Rate
27.6 MPa (4 ksi)	Monotonic	Unconfined	12	20, -1, -20, -40	LR1
		0.006	12	20, -1, -20, -40	LR1
		0.009	12	20, -1, -20, -40	LR1
		0.012	12	20, -1, -20, -40	LR1
		Steel Shell	12	20, -1, -20, -40	LR1
41.4 MPa (6 ksi)	Monotonic	Unconfined	6	-1, -20	LR1
		0.009	6	-1, -20	LR1
		Steel Shell	6	-1, -20	LR1
55.2 MPa (8 ksi)	Monotonic	Unconfined	6	-1, -20	LR1
		0.009	6	-1, -20	LR1
		Steel Shell	6	-1, -20	LR1
		Total	96		

The majority of the testing was performed under monotonic loading because a previous study at ISU demonstrated the peak values on the cyclic stress-strain curve adequately agreed with the monotonic stress-strain curve as shown in Figure 5-2 (Thiemann, 2009). This allowed the experimental study to be performed at a quicker rate instead of having to account for the degradation of the samples to be considered through loading to a given strain point three times before moving to the next strain limit.

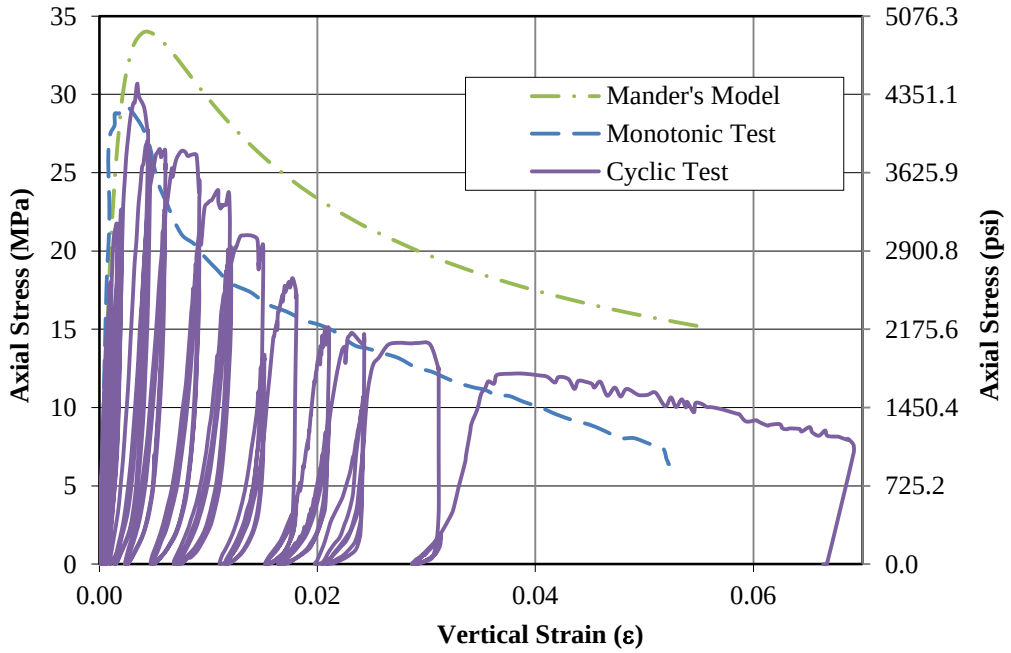

Figure 5-2: Experimental testing of a confined concrete specimen with ρ_s = 0.7% subjected to monotonic and cyclic loading (after Thiemann 2009)

5.3 Testing Procedures

Prior to performing any tests, a number of steps were followed to prepare the samples and available test space. These steps included creating the samples, modifying the load frame setup to maintain a controlled environment, installing the appropriate instrumentation and defining the loading protocols used during the testing. The processes undertaken to complete this portion of the experiment are provided within the following sections.

5.3.1 Specimen Construction

Using the information in Table 5-1 and Table 5-2, the confined and unconfined concrete samples were constructed to create the desired testing specimen as provided in Figure 5-3. This process began by creating the necessary amount of forms needed during the placement of the concrete mixes. For the spirally reinforced and unreinforced concrete specimens, the forms were made of plastic cylinder molds of 101.6 mm by 203.2 mm (4 in. by 8 in.) for the 27.6 MPa (4 ksi) and 41.4 MPa (6 ksi) concrete mixes. In addition, 76.2 mm by 152.4 mm (3 in. by 6 in.) cylinder molds were used for the 55.2 MPa (8 ksi) unconfined and spirally reinforced concrete samples. Each mold then had spiral reinforcement, formed by wrapping the reinforcement wire around a steel pipe, as specified in the aforementioned tables placed inside. The spacing of the reinforcement was determined such that the amount of horizontal reinforcement ratio would be the equivalent of a concrete cylinder confined by Grade 60 deformed reinforcing bar. After placement of the spiral reinforcement, two horizontal bars were placed through the mold so that gauges could be placed for measuring vertical strain over the middle third of the specimen to capture the stress-strain behavior. These bars were wrapped in tape to create an unbonded state within the cylinder except for a single nut placed at the center of the bar to prevent its rotation by creating localized anchoring to the concrete. Additionally, a thermocouple was placed within the center of each specimen to ensure the entire sample was at the desired testing temperature. A picture of the samples prior to placement of the concrete is provided in Figure 5-4.

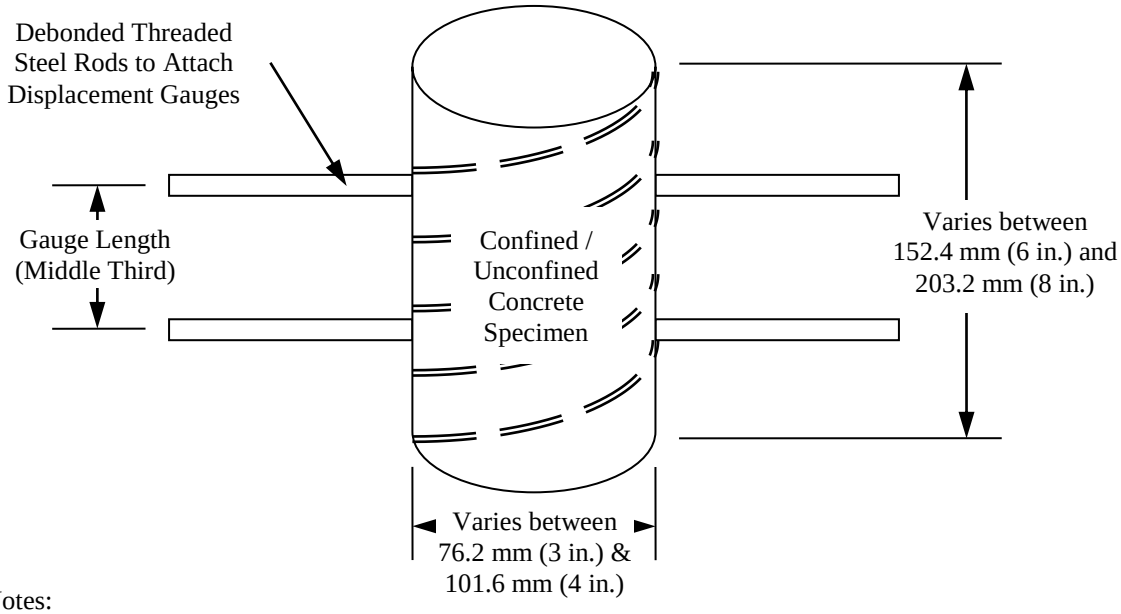

Notes:
- Spiral reinforcement shown as the dashed line was not present in all specimens.
- High strength sulfur caps were used to ensure cylinder levelness on top and bottom.
- Instrumentation is not depicted within the figure.

Figure 5-3: Details of specimens used for testing of confined and unconfined concrete

Figure 5-4: Constructed concrete cylinder molds prior to placement of concrete

In addition to the plastic molds, a number of steel shell cylinder molds were constructed for testing purposes. This was performed by machinists on the ISU campus by creating cylinders with dimensions of 74.2 mm by 146 mm (2.92 in. by 5.75 in.) and 99.6 mm by 196.8 mm (3.92 in. by 7.75 in.) using 0.38 mm (0.015 in.) steel shim stock with holes on the side for the horizontal rods. To ensure the shell would act as lateral confinement only, the shell height was

intentionally cut 6.3 mm (0.25 in.) short in total to allow for compression of the concrete cylinder without applying direct load to the steel shell. The diameter was fabricated smaller by 2 mm (0.08 in.), so the expansion of the metal due to welding would permit the outside of the specimen to fit exactly within a typical plastic cylinder mold. The cylinders were made to the correct size by first cutting an appropriate sized rectangle for the desired cylinder size. This was then wrapped around a milled circular template and the ends were welded together along the entire height of the specimen. The next step was to create the remainder of the mold by removing the top and bottom of a plastic cylinder and attaching them to the shell such that the appropriate height of concrete was obtained for testing. The final step in the process was to insert the horizontal rods and thermocouples needed for measurements during testing.

Upon completion of the mold construction, the specimens were taken as necessary to local concrete batch plants, where materials were donated to the project by the owning organizations. Each mix was tested in accordance with ACI field testing procedures to determine temperature, air content, slump and strength. The results of this testing are provided herein as Table 5-3.

Table 5-3: A summary of concrete batch testing results

Mix ID	*Man AB*	*Man C*	*IF*
Specified 28-Day Strength	27.6 MPa (4 ksi)	41.4 MPa (6 ksi)	55.2 MPa (8 ksi)
Mix Temperature	21.1 °C (69.9 °F)	20.7 °C (69.3 °F)	21.7 °C (71 °F)
Slump	3.8 cm (1.5 in.)	17.8 cm (7 in.)	20.3 cm (8 in.)
Air Content	3.50%	1.60%	4.40%
Measured 28-Day Strength	37.1 MPa (5.38 ksi)	46.6 MPa (6.76 ksi)	54.5 MPa (7.91 ksi)
w/c ratio	0.26	0.33	0.31

After testing the concrete mixes, they were placed within the molds using three lifts per mold and consolidation through rodding and tapping procedures dictated in the appropriate field testing guidelines. The specimens were then covered and allowed to cure for one day prior to transporting the specimens back to the structures laboratory at ISU. Once at the lab, the specimens were field cured by leaving them in the molds for 28 days and covering them with a thin layer of water and plastic wrap to lock in the moisture at the top of the concrete specimens. After the full cure time of 28 days had elapsed, the specimens were removed from the molds and stored in the lab until testing.

5.3.2 Load Frame Setup and Instrumentation

Once the specimens were cured and stripped of the plastic molds, they were taken to the testing apparatus at the time of testing. If they were cold temperature samples, they were pre-frozen in a separate freezer chamber to decrease testing time. After removal from the freezer in the next room or the plastic molds, the specimens were instrumented and placed within the test apparatus as quickly as possible. The loading frame consisted of an MTS uniaxial testing frame as depicted in Figure 5-5. Within the confines of the frame, an environmental chamber was centered so the specimens would be kept at the desired temperature throughout the duration of the test. The environmental chamber, purchased through MTS, uses pressurized liquid nitrogen to cool the interior of the chamber to the testing temperature specified for the cylinder. To test a specimen within this chamber, two extensions were designed and milled at ISU to extend from the wedge grips into the center of the chamber and safely obtain the maximum compressive capacity of the loading frame of 489.3 kN (110 kips).

The final component of the loading system was the compression platens located at the ends of the extension rods. These platens consisted of a fixed head at the bottom of the specimen and a rotating head at the top of the specimen. The rotating head was used to ensure that the compression forces were evenly distributed across the contact surface of the specimen. Although this method works fairly well for unconfined concrete, this movable head caused unequal loading in confined concrete. This was noted early in the experimental program when a specimen was noted to experience bending instead of pure compression as shown in Figure 5-6. The authors believe the additional rotation of the movable head came from the failure process of confined concrete in which one side of the specimen experiences damage before another, causing a non-uniform pressure which the head adjusted by rotating to apply even pressure.

To correct this problem, a simple clamping system was devised as shown in Figure 5-7. This system allows the rotating head to be used initially so the desired testing position can be obtained through a small initial pressure [e.g., ~0.14 MPa (20 psi)] and then locked into place, preventing additional rotation. Therefore, a uniaxial compressive force was obtained during the testing of the remaining confined and unconfined cylinders.

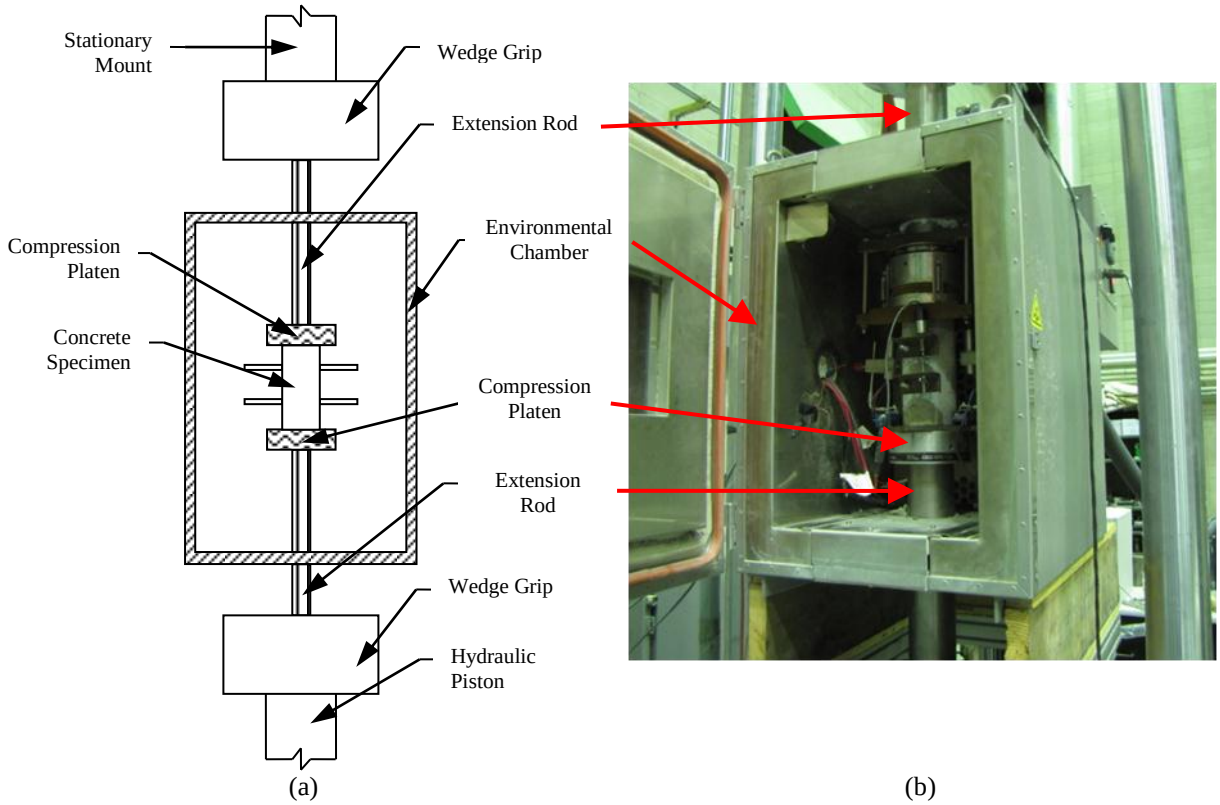

Figure 5-5: Loading frame setup for testing of cylindrical concrete specimens: (a) front schematic view; (b) actual view of testing apparatus

Figure 5-6: Axial and bending failure of confined concrete cylinder when upper head rotated after damage to the confined specimen

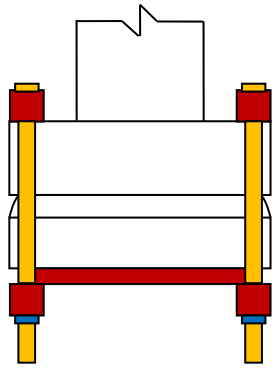

(a) Front View

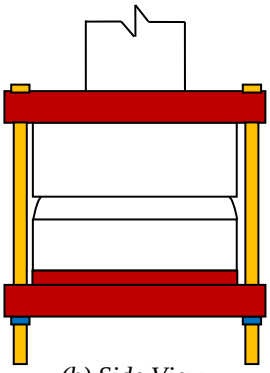

(b) Side View

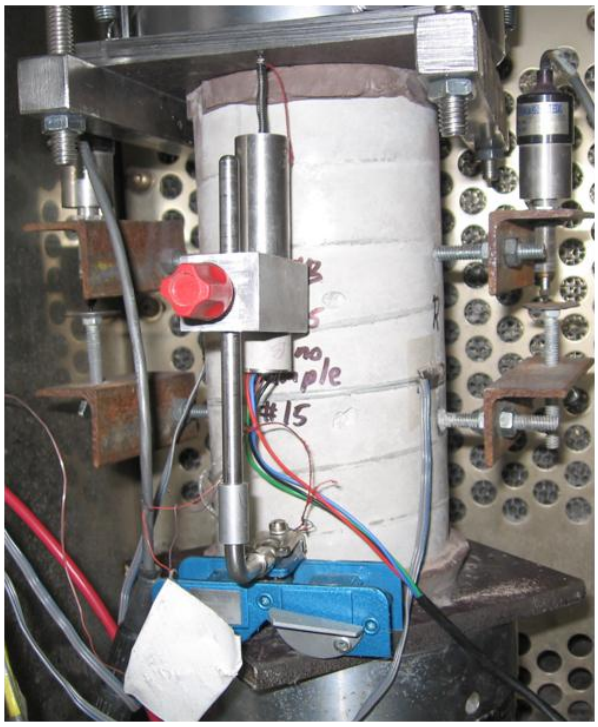

(c) Actual Clamp at the Top of Picture

Figure 5-7: Clamping system for concrete cylinder tests

The remaining component needed for testing purposes was the instrumentation setup for each cylinder as shown in Figure 5-8(a). This originally consisted of a displacement gauge on either side of the cylinder, attached to the top bar of horizontal thread rods, to measure the change in length experienced in the center of the specimen due to compression loading, determining a vertical strain for the concrete specimen to go along with the frames load cell measuring the applied compressive force. A thermocouple was placed at the center of the specimen prior to placement of the concrete to provide confidence that the entire specimen had reached the desired testing temperature. The laterally confined specimens using spiral reinforcement or external steel shells had two strain gauges placed on opposite sides of the cylinder to measure the hoop strain developed from the steel resisting the dilation of the concrete. Additionally, these gauges were placed where they could be used to make a comparison between the concrete dilation and vertical strain being applied to the system. This instrumentation was modified, Figure 5-8(b), to include two additional displacement gauges placed along the plane perpendicular to that of the thread rods. These gauges were used to measure vertical strain over the entire height of the

specimen as it was noted during testing that the original rods would rotate significantly in the softening region and not adequately capturing the full stress-strain behavior.

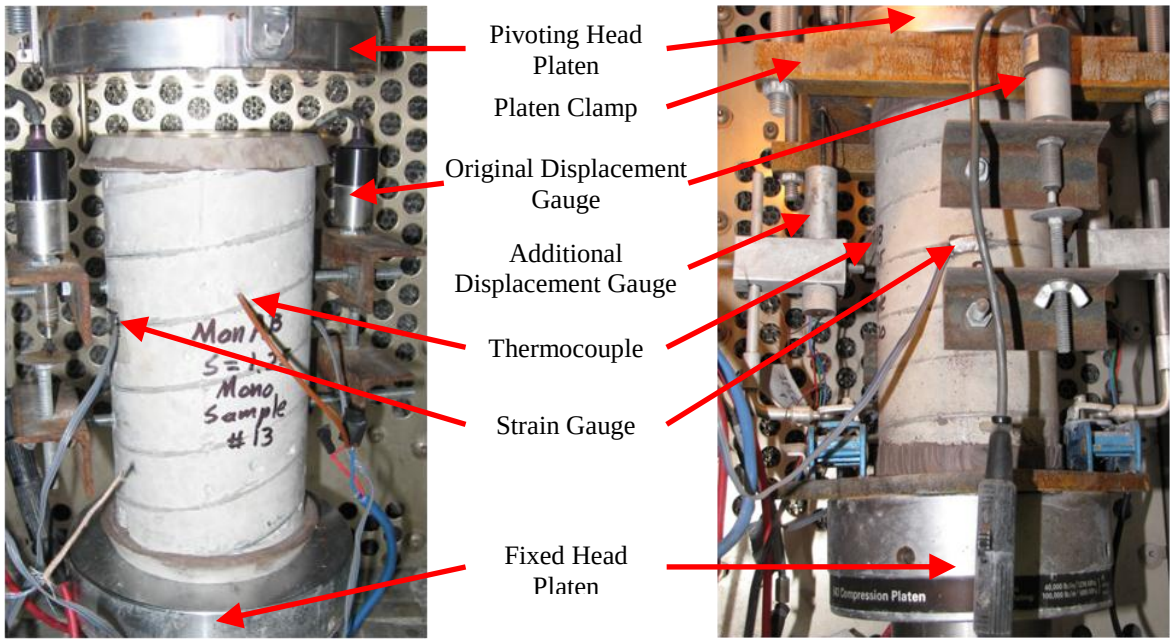

Figure 5-8: Concrete experimental instrumentation setup: (a) original; (b) modified

5.3.3 Loading Protocols

The last step prior to any testing of the specimens was to establish the loading protocols needed for the monotonic testing. This was a crucial step to make sure that all of the specimens were tested in the exact same way to eliminate as much error as possible due to variable loading. To accomplish this task, the testing software provided with the loading frame was used to define a program that would perform the same loading tasks each time it was started.

Monotonic testing

Monotonic testing started by loading to an initial force value of 1.3 kN (0.3 kip) to ensure the specimen was seated correctly within the testing apparatus. After this stage, the machine automatically applied compressive force to the specimen with a table rate of movement equal to 0.5 mm/min (0.02 in./min). This rate was followed until the table had displaced approximately 0.63 mm (0.025 in.), so that a better seating would take place as the multiple components of the testing apparatus became fully seated. Once this limit was reached, the computer increased the rate of table movement to 1.27 mm/min (0.05 in/min) in accordance with Table 5-2. This rate was then used until the end of the test, defined as the ultimate capacity of the testing apparatus

[490 kN (110 kip)], complete failure of the unconfined specimen, failure of the lateral reinforcement or an additional head displacement of 12.7 mm (0.5 in.) was reached without failure. The last value was selected, as this would correspond to an approximate strain of 0.06 which exceeds strains typically used in the design process. In addition, the axial stress being maintained at this level is typically below 40% of the maximum stress experienced by the specimen at the peak load. At this point, the specimen was unloaded and removed from the environmental chamber so that another specimen could be instrumented and tested.

5.4 Results

After completing the experimental testing program described in Sections 5.1 through 5.3, the data obtained from the tests were analyzed and examined for trends and comparisons with previous research. The trends noted within the testing were examined first for the unconfined concrete specimens, since this could be compared against other research [i.e., Sehnal et al. (1983) and Lee et al. (1988 a & b)]. Then the trends in the confined concrete specimens were examined so the differentiation in the responses could be better defined. The following sections will provide the results obtained from the examination of the data obtained from the experimental testing performed on confined and unconfined concrete subjected to varying temperatures

5.4.1 Monotonic Testing of Unconfined Concrete

The following section presents the results found from the testing of the unconfined concrete cylinders subjected to monotonic loading. This includes results regarding the ultimate concrete compressive stress (f'_c), concrete modulus (E_c) and strain at the ultimate concrete compressive stress (ε_{co}) of the cylinder.

Ultimate Concrete Compressive Strength, f'_c

The examination of the ultimate concrete compressive strength of cylinders began by establishing a normalized strength gain factor (SGF) so the multiple concrete mixes could be easily compared. This was done by normalizing the ultimate concrete compressive strength at the desired temperature, $f'_{c,exp}$, against the average ultimate concrete compressive strength at 20 °C (68 °F), $f'_{c,avg20}$. The SGF is arithmetically described in Equation 5-1.

$$SGF = \frac{f'_{c,\exp}}{f'_{c,avg20}} \tag{5-1}$$

After defining the normalized value to be used in comparing the three different specified concrete strengths, individual figures were plotted to examine the trends that formed within the data sets and to compare the information with past studies. An example of this is provided in Figure 5-9 with the remainder of the individual graphs provided in Appendix B.

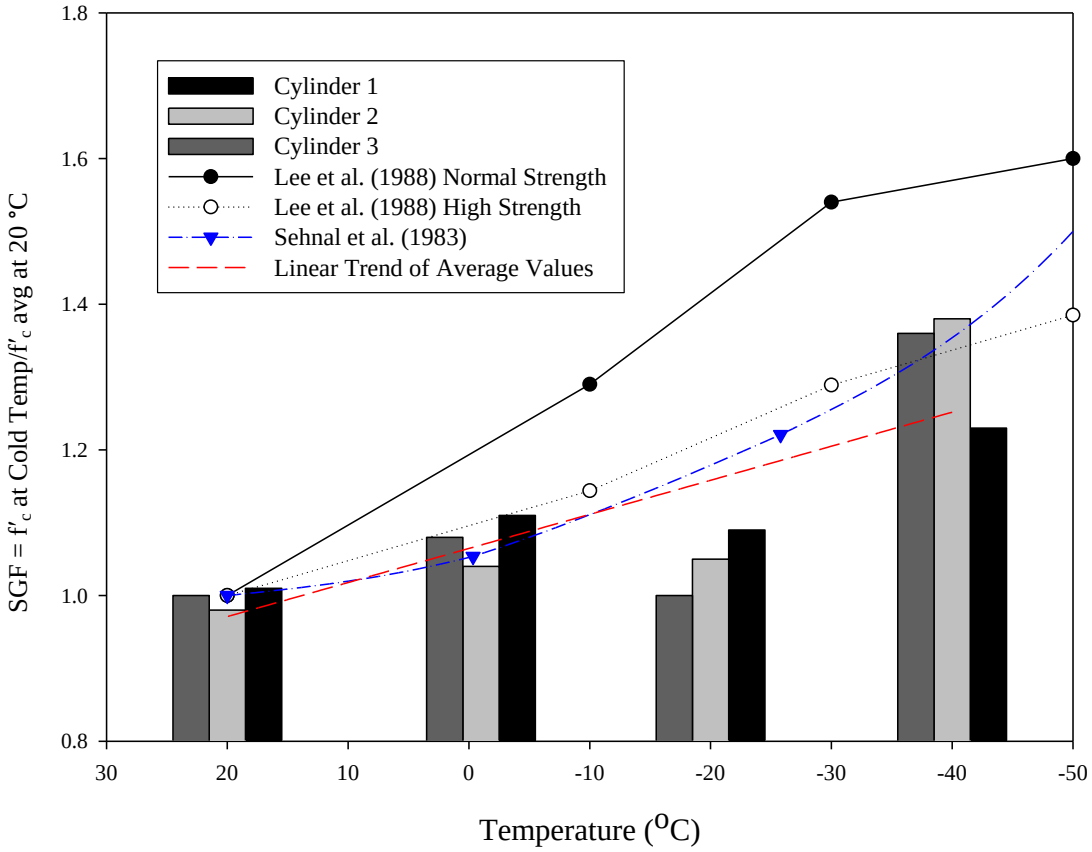

Figure 5-9: Comparison of SGF obtained from experimental testing for Man AB concrete mix, a linear best fit curve and trendlines established in past studies

In all figures, the data obtained experimentally are shown as a series of bars centered on the temperature at which the specimens were tested for that concrete mix. In addition, the graphs provide information from past studies as a series of lines with data points at the testing temperatures performed by previous research groups. In the case of the Man AB and IF mixes, the experimental values correlate well with the past studies of Lee et al. (1988b) and Sehnal et al. (1983) thus providing additional validation to the experimental study. The third mix tested, Man C, did not follow the expected trend from previous research and the trends noted within the other concrete mixes. This mix, in particular, experienced a decreasing trend in the SGF from a value

of 1.0 at 20 °C (68 °F) to approximately 0.9 at -20 °C (-4 °F). It is not known why the material behaved in this manner, since the concrete strengths and w/c ratios were similar to past research and test specimens used within this study. Further testing on the peak unconfined compressive strength would be needed to determine the direct cause of the decreasing trend. Therefore, the data obtained from this data series were omitted when establishing trends for the change in the ultimate unconfined concrete compressive stress when subjected to temperatures varying from 20 °C (68 °F) to -40 °C (-40 °F).

After establishing individual comparisons for the different concrete mixes, the data were combined into a single figure that included the Man AB and IF mixes along with previous research data of Lee et al. (1988b) and Sehnal et al. (1983), Figure 5-10. The low strength mix data from Lee et al. (1988a) was not included, since these values were approximately 20% higher than those of the other data sets that had a similar starting unconfined compressive strength.

Figure 5-10 demonstrates the water to cement ratio (w/c) does not appear to affect the overall strength increase when unconfined concrete is subjected to freezing temperatures. Also, the data set of Lee et al. (1988b) seems to closely match the experimental data and will therefore be included as a third data set during the establishment of the strength trend of unconfined concrete. Although the curvilinear data of Sehnal et al. (1983) adequately captures the upper bound of the increase in concrete strength as temperature decreases, a linear trend is also apparent within the temperature range focused herein and will be easier to use in design practice.

Using the information presented in Figure 5-10, a secondary graph of average values, Figure 5-11, was created and a linear trend was established. The linear trend, as presented in Equation 5-2, was found using a best fit line of the data and then modified to ensure that at 20 °C (68 °F) the SGF would be equivalent to a value of one. The line shown in the graph demonstrates the equations will adequately capture the strength increase of concrete as temperature decreases from 20 °C (68 °F) to -40 °C (-40 °F). Therefore, the equations are recommended for use in accounting for variations in concrete strength when subjected to seasonal freezing.

$$SGF = \frac{f'_c}{f'_{c,20}} = -0.0047[T(°C)] + 1.094 \quad (5\text{-}2a)$$

$$SGF = \frac{f'_c}{f'_{c,68}} = -0.0026[T(°F)] + 1.177 \quad (5\text{-}2b)$$

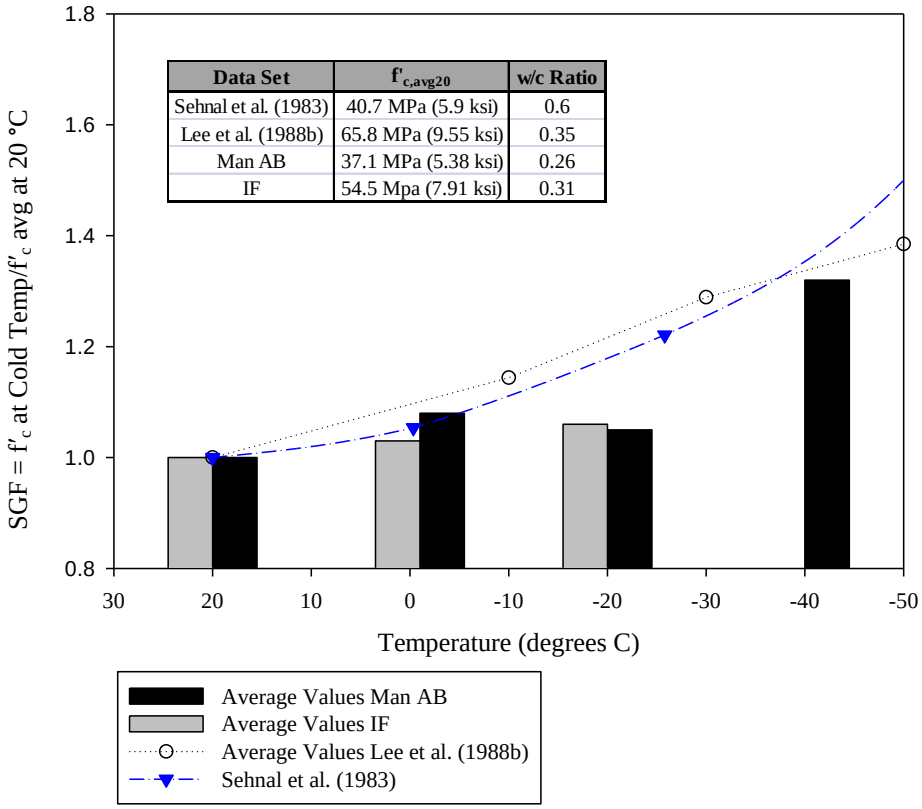

Figure 5-10: Average value comparison of experimental concrete study and past research

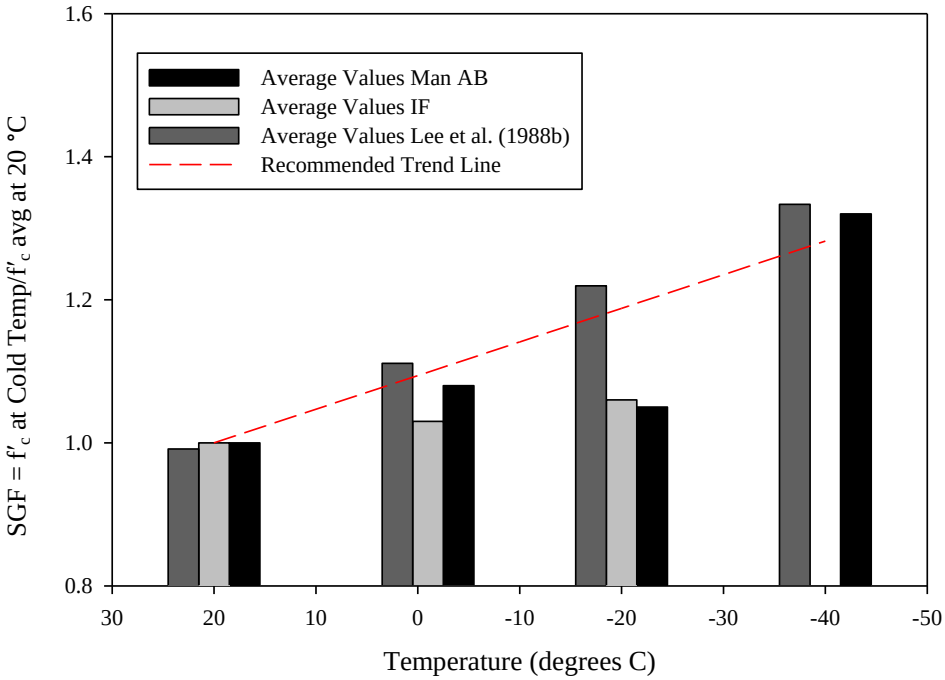

Figure 5-11: Recommended strength increase curve for unconfined concrete with average test data

Strain at Peak Compressive Stress, ε_{co}

The next critical step to define the changes of unconfined concrete subjected to decreasing temperature is to define the strain at the peak of the concrete stress-strain curve. The establishment of this strain value with decreasing temperature was performed by examining the actual strain values attained at the peak of the stress-strain curves for the Man AB mix and plotting them as a series of bars centered on the testing temperature, Figure 5-12. The Man AB mix was used to establish trends based on the testing matrix specifications and the remaining mixes were used to verify the trends previously defined. In addition, if a given data point drifted by more than 20% from the median value at the testing temperature, it was removed from the data set. This was not performed at the testing temperature of -40 °C (-40 °F), since the data points were approximately equidistant from the median value and provided a more accurate behavior in the establishment of a trend. Additionally, no published information was found for ε_{co}.

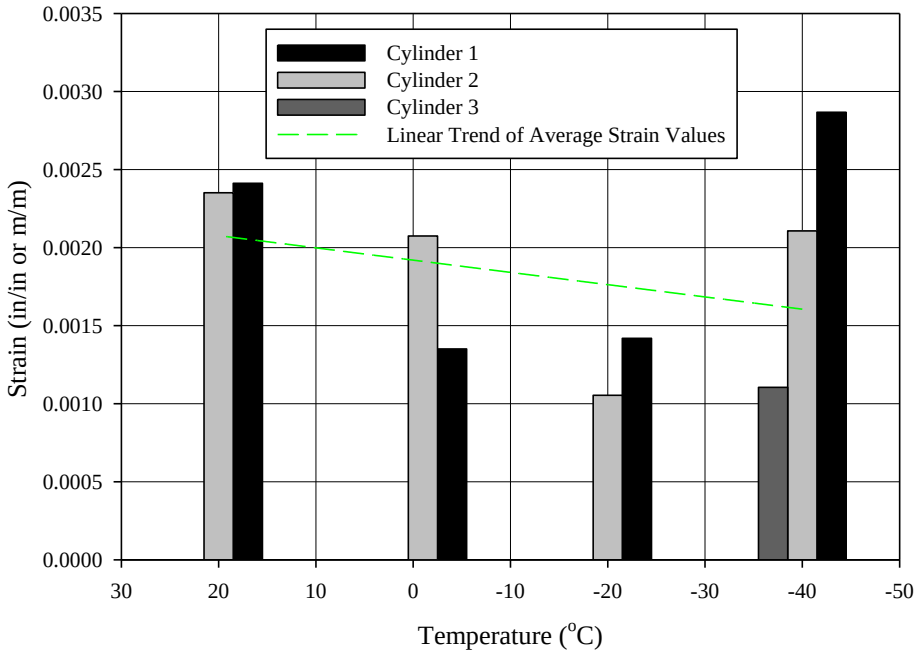

Figure 5-12: Change in ε_{co} of Man AB mix as temperature decreases

The data provided in Figure 5-12 suggest an approximate decrease of 23% in the strain of unreinforced concrete at peak compressive stress is expected as temperature falls from 20 °C (68 °F) to -40 °C (-40 °F). This suggests the unconfined concrete becomes more brittle as the strength of the concrete increases while the strain at the peak stress decreases. This suggests that

additional confinement may be required in the seismic design of structures at freezing temperatures to ensure adequate ductility of the system is obtained; however, further testing should be conducted to verify the decreasing strain at peak compressive stress. Another key point found in Figure 5-12 is the assumed strain of 0.002, used commonly in practice (e.g., Priestley et al., 1996), correlates well with the linear trendline established from the experimental testing. Based on this, the value of 0.002 is recommended for use at 20 °C (68 °F) and, therefore, was used in the establishment of the strain relationship at the peak compressive strength as temperature decreases.

Using the information provided in Figure 5-12, a relationship was established for the strain of concrete at peak compressive strength. The arithmetic relationship provided in Equation 5-3 was found by connecting the recommended strain value of 0.002 at 20 °C (68 °F) with a linear curve to the strain value of 0.00159 found at -40 °C (-40 °F) using the linear trendline presented in Figure 5-12. The relationship was then graphed over the experimental data, Figure 5-13, and found to adequately capture the decrease in strain as temperature varies from 20 °C (68 °F) to -40 C (-40 °F).

$$\varepsilon_{co,20} = 6.9\text{E} - 06[T(°C)] + 1.86\text{E} - 03 \quad \text{(5-3a)}$$

$$\varepsilon_{co,68} = 3.8\text{E} - 06[T(°F)] + 1.74\text{E} - 03 \quad \text{(5-3b)}$$

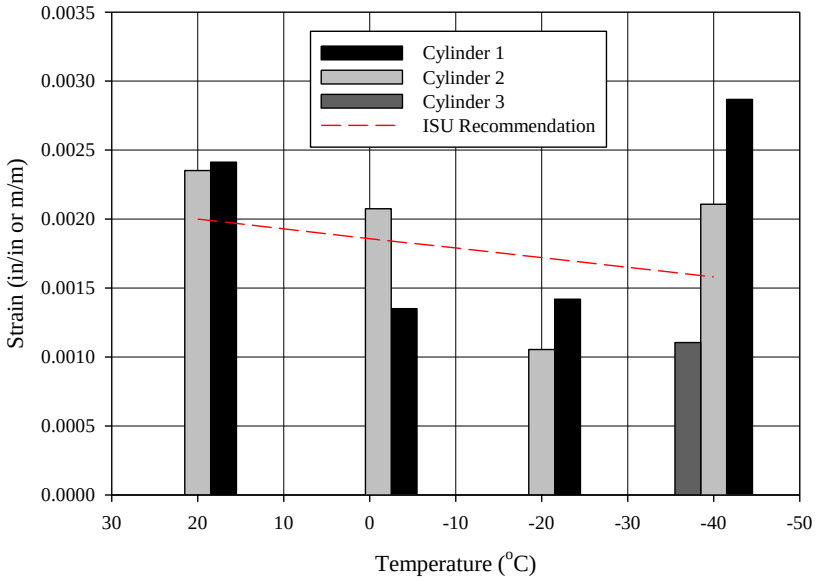

Figure 5-13: Comparison of recommended ε_{co} and experimental results of Man AB mix

After establishing the relationship for the variation in strain at the peak unconfined compressive stress with temperature for the Man AB mix, the curve was compared to the data obtained for the two remaining mixes. This was performed by plotting the recommended line over the experimental results and provided in Figure 5-14. Similar to the Man AB mix, data were removed if a drift from the median value by more than 20% existed. The ISU relationship was once again found to adequately capture the experimental data and is recommended for defining the strain at the unconfined compressive strength as temperature decreases.

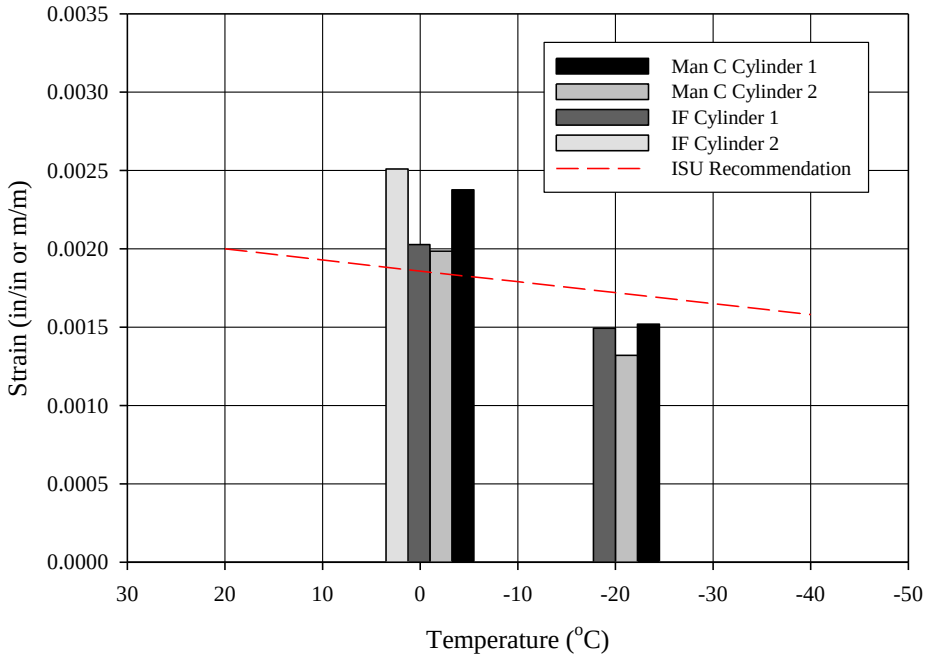

Figure 5-14: Comparison of the recommended curve with experimental results for strain at peak compressive stress of the Man C and IF concrete mixes

Modulus of Elasticity

The final parameter of the unconfined concrete examined was the modulus of elasticity of concrete, E_c. This examination started by comparing the previous research results of Lee et al. (1988 a&b) and Sehnal et al. (1983) with experimental data for the ISU tests. To perform this comparison, the experimental moduli, $E_{c,exp}$, were all normalized against the average value of the moduli obtained at 20 °C (68 °C), $E_{c,avg20}$, for a given concrete mix, establishing a Reference Value (RV), Equation 5-4, appropriate for comparison between different strength concrete. The experimental moduli were found using a chord method to a second point on the data set that started from the point suggested in ACI 318-05 (ACI, 2005). The origin could not be used in all

cases as the initialization of the stress-strain curve was curvilinear and caused the slope formed by the modulus value to not be parallel with the elastic range of the data set. Although Sehnal et al. (1983) did not provide any information on the cold temperature effects on modulus, it was assumed for comparison purposes in this study that the RV for the modulus would be proportional to the square root of the ratio of compressive strength at a given temperature to the compressive strength at 20 °C (68 °F). This relationship is provided in Equation 5-5 and was deemed appropriate, since industry (e.g., ACI 318) assumes that the modulus is a function of the square root of the unconfined compressive strength of the concrete. After compiling the data sets and removing experimental data that drifted from the median value by more than 20%, the remaining information was plotted for further examination, as shown in Figure 5-15.

$$RV = \frac{E_{c,exp}}{E_{c,avg20}} \tag{5-4}$$

$$RV_{Sehnal} = 1.0\sqrt{\frac{f'_c}{f'_{c,20}}} \tag{5-5}$$

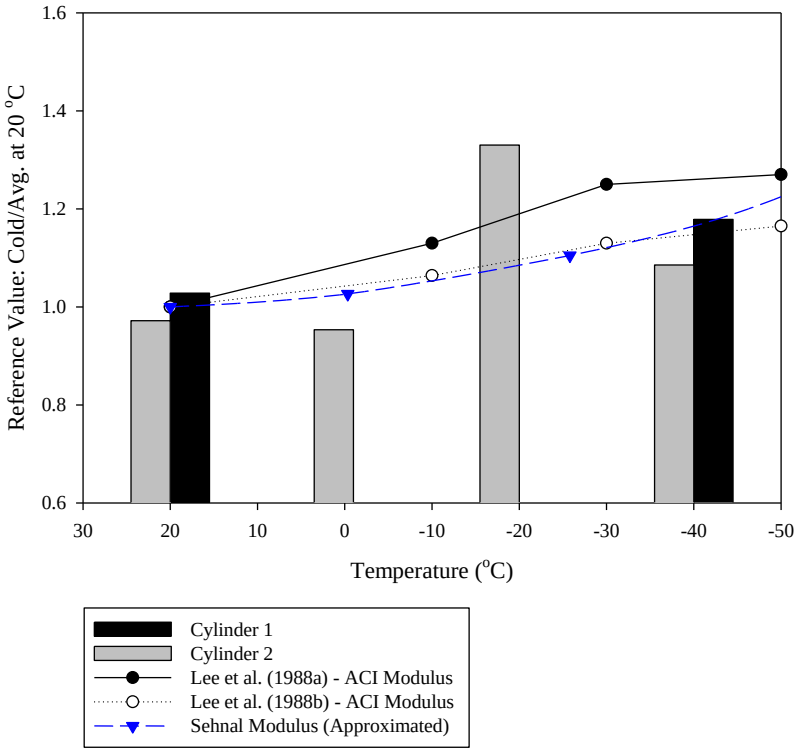

Figure 5-15: Comparison of experimental modulus of Man AB mix with trends established from previous unconfined concrete research

The experimental data for the elastic modulus of the Man AB concrete mix shown in Figure 5-15 generally follows a linear increasing trend as temperature decreases. Also, the increase in elastic modulus is in agreement with previous studies by Lee et al. (1988b) and Sehnal et al. (1983) as they appear to provide a good upper bound location for the increase in modulus as temperatures decrease, except at -20 °C (-4 °F). Although, Lee et al. (1988a) supports the idea that as temperature decreases the modulus will increase, these data do not correlate well with the experimental research or other studies that have similar increases; suggesting that this data set should not be used in any trend establishment. The final factor to note was although the data have large scatter between -1 °C (30.2 °F) and -20 °C (-4 °F), the linear trendline for the data will fall directly between these two locations. That is, the upper and lower values are approximately equidistant from the median range. Thus, the data will help to more accurately predict the increase of modulus expected as temperature decreases.

Using the data presented in Figure 5-15, an arithmetic means of capturing the increase in modulus was determined. This was achieved by relating the unconfined concrete compressive strength to the modulus of elasticity in a similar manner to that of Equation 5-5. By relating the modulus in this manner, no additional equations would need definition for the unconfined concrete data set, since this ratio was established in Equation 5-2. Therefore, the relationship established for the RV for the modulus of elasticity is that shown in Equations 5-6. The equations were then plotted against the experimental data set of the Man AB mix, Figure 5-16, to examine the validity of the approach.

$$RV_{Modulus} = \frac{E_c}{E_{c,20}} = \sqrt{SGF} = \sqrt{-0.0047[T(°C)] + 1.094} \quad (5\text{-}6a)$$

$$RV_{Modulus} = \frac{E_c}{E_{c,68}} = \sqrt{SGF} = \sqrt{-0.0026[T(°F)] + 1.177} \quad (5\text{-}6b)$$

The linear curve shown in this figure correlates well with the experimental data included in the figure. In addition to the Man AB mix, the information obtained from IF mix testing was used as a basis of comparison for the relationships established for the modulus of elasticity. In this comparison, the IF mix moduli at the different temperatures were established using the equation-based recommendations of ACI 318-05 (ACI, 2005), as these test specimens only had two instruments on the concrete specimens, in which the modulus is equivalent to 57,000 times the square root of the unconfined compressive stress of the concrete in pounds per square inch.

Using this method, the RV obtained at -1 °C (30.2 °F) and -20 °C (-4 °F) were 1.01 and 1.02, respectively. These values match well with the equation values of 1.05 and 1.09 which are within 10% of one another. The Man C values were not examined, since the data in the experiment does not adequately reflect the behavior of concrete subjected to freezing conditions. Therefore, Equation 5-6 is suggested for use in estimating the effects of freezing on the modulus of elasticity in unconfined concrete.

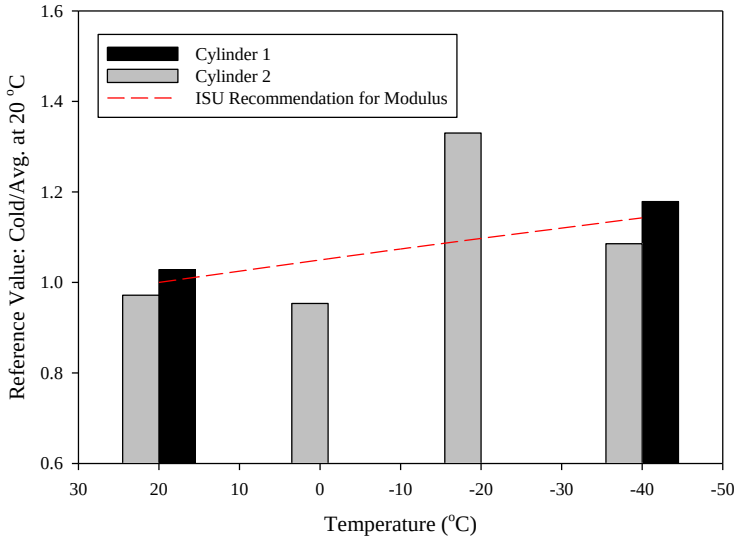

Figure 5-16: Comparison of RV for experimental modulus of Man AB concrete mix to recommended equations

5.4.2 Monotonic Testing of Confined Concrete

In seismic design, confinement is used to increase the strain capacity and overall strength of unreinforced concrete, so that plastic hinges can be formed with sufficient ductility allowing a structure to sustain large lateral deformation but not fail when subjected to high intensity ground motions. To accomplish a satisfactory performance-based design, the designer must ultimately know the seismic behavior of the system at all times of the year. A key component in understanding this behavior is to know the changes occurring to the confined concrete stress-strain curve, since this will dictate the moment-curvature response of the section and its deformation and moment capacities. In all seasons of the year, the confinement, provided typically by transverse reinforcement, causes an increase in the compressive strength and ductility of the system as demonstrated in Figure 5-1. However, these increases are highly dependent on the strength, size and spacing of the reinforcement as well as the initial unconfined compressive strength of the concrete. Although the effects of these parameters are adequately

known in the unfrozen condition, minimal research exists on the effects of confinement on concrete when subjected to temperatures at or below the freezing limit. The following sections present the results of the experimental study that investigated the behavior of confined concrete subjected to monotonic loading at temperatures ranging from 20 °C (68 °F) to -40 °C (-40 °F) based on the test matrix of Table 5-2.

Ultimate Confined Concrete Compressive Strength, f'_{cc}

The confined concrete compressive strength at the peak of the stress-strain curve was the first parameter examined during the analysis of test data. This was performed through the use of the Man AB mix data and then later compared to the remaining concrete mixes to determine the effectiveness of the established relationship for other concrete strengths. The examination into the effects of temperature on f'_{cc} began by normalizing the maximum concrete stress obtained for each confined cylinder against the average value of f'_c obtained experimentally at 20 °C (68 °F). By normalizing the data set in this manner, a direct comparison was possible between the unconfined and confined concrete specimens. If the effects of confinement are assumed to remain unchanged with temperature, a constant increase in strength that follows the slope of the linear relationship previously established for unconfined concrete (see Equation 5-2 and Figure 5-11) should be maintained as temperature decreases. In order to determine whether or not this was the case, the normalized data were plotted in Figure 5-17 along with the unconfined relationship established in Section 5.4.1. In addition, the model proposed by Mander et al. (1988) was included in the plot by modifying material properties for temperature effects through the relationships defined in Section 5.4.1 for unconfined concrete and Chapter 6 for A706 reinforcing steel.

The multiple graphs provided in Figure 5-17 allow numerous observations on the effects of cold temperature on the behavior of confined concrete. The first noticeable effect is that as temperature decreases from 20 °C (68 °F) to -40 °C (-40 °F), the strength of confined concrete increases but not as significantly as it was observed for unconfined concrete. In other words, strength gains due to the presence of confinement diminish as temperature reduces. This is demonstrated by the dash-dot-dot average trend line curves of the experimental data sets in Figure 5-17b and Figure 5-17c and the dashed line of the recommended unconfined concrete strength increase in which a larger separation between the two curves exists at the warmer temperatures than at the colder temperatures. For example, Figure 5-17c demonstrates an

approximate 20% separation exists between the unconfined curve and average experimental trend line curve at 20 °C (68 °F) compared to the 3% difference at -40 °C (-40 °F). Figure 5-17a does not demonstrate this trend; however, it is believed this was most likely due to the large spacing of the horizontal reinforcing wire used on the cylinders to obtain the desired volumetric reinforcement ratio. Thus, the behavior of these specimens was closer to the unconfined concrete than confined concrete specimens as reflected by the concrete strength gain. The same trend is also expected to occur in Figure 5-17d, but no conclusions could be drawn due to the load capacity of the testing apparatus being reached before test completion at -20 °C (-4 °F) and -40 °C (-40 °F).

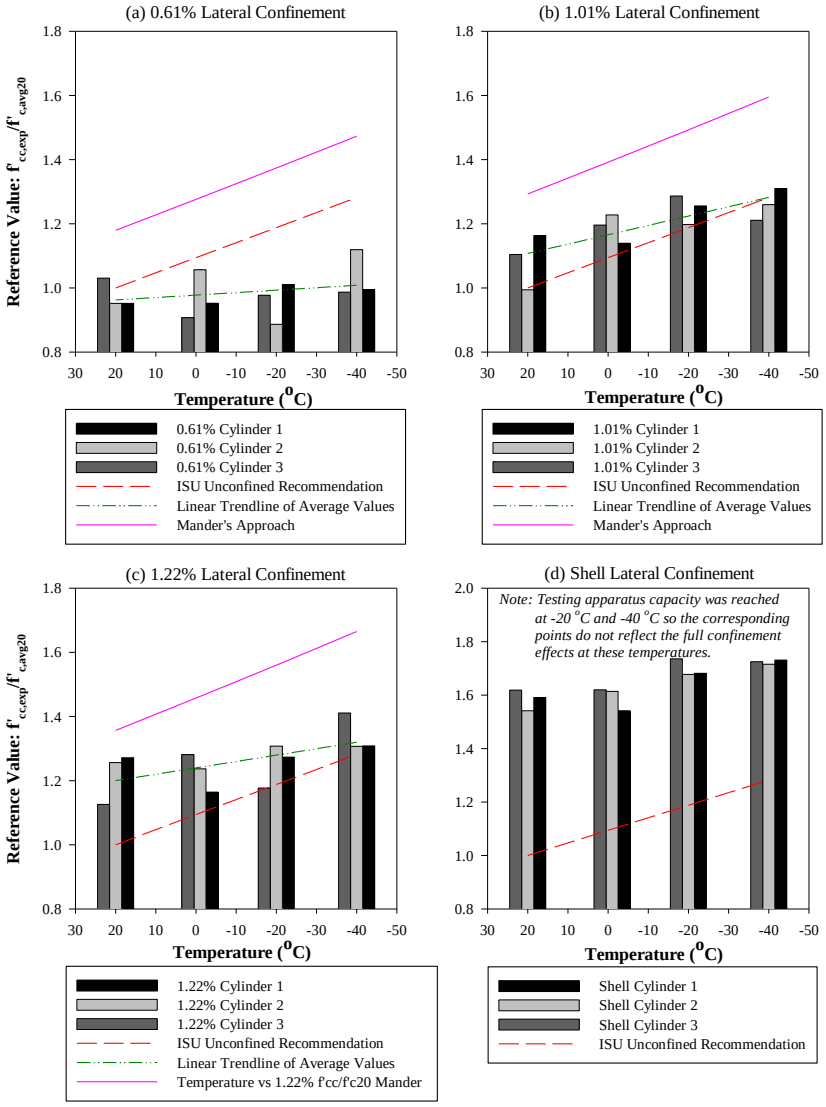

Figure 5-17: Comparison of strength RV of Man AB confined cylinders with the ISU unconfined recommendation and Mander et al. (1988)

The decrease in the confinement effects with cold temperatures is believed to be due to the increase of Poisson's ratio as temperature decreases shown in Figure 5-18, based on data reported by Lee et al. (1988 a&b). When Poisson's ratio increases, the concrete begins to dilate faster causing the horizontal reinforcement to expand quicker, thus reducing its efficiency. As a result, the steel confinement reinforcement is unable to provide the resistance needed to gain the same amount of additional strength experienced at 20 °C (68 °F). However, to understand the true impact of the reduced confinement effects at cold temperatures, the entire system should be analyzed at the lower temperatures, as the demands and capacities of the concrete foundation and column section can significantly change as discussed in Section 2.3.1. The expected changes, typically associated with an increase in force demand and decrease in displacement capacity, suggest the amount of horizontal reinforcement in the system may need to be altered so the required performance of the system is met.

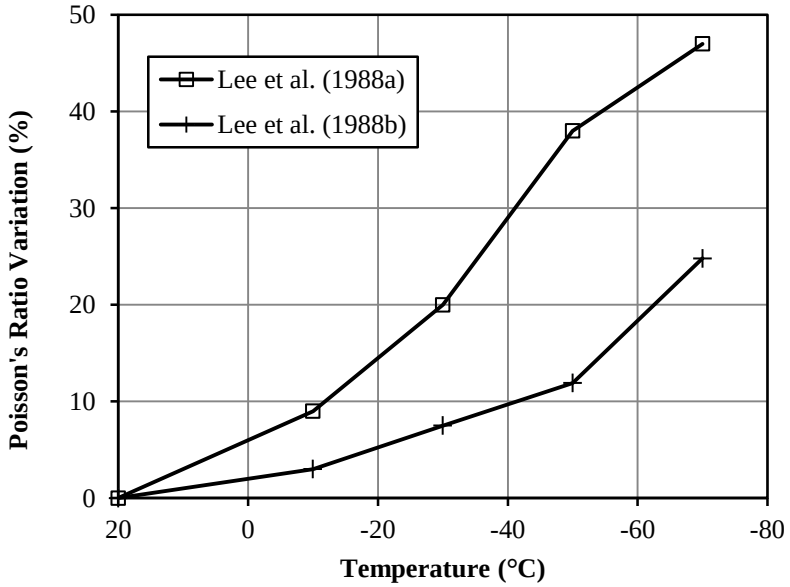

Figure 5-18: Effect of cold temperature on Poisson's ratio of concrete [reproduced from Lee et al. (1988b)]

Another observation noted in Figure 5-17 is the model suggested by Mander et al. (1988) for use in the establishment of the confined concrete strength consistently produced higher values than those found from the experimental tests. This observation is consistent with the data presented above with regards to the change in Poisson's ratio. To further examine this trend, a graph was created to compare the effects of confinement at 20 °C (68 °F) with the ratio of

$f'_{cc}/f'_{c,avg20}$ obtained through experimental means and the theoretical curve of Mander et al. (1988). This graph is provided in Figure 5-19.

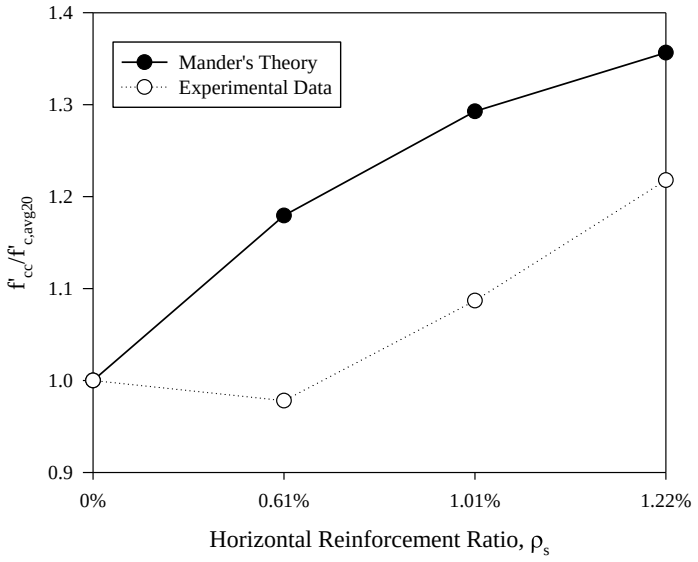

Figure 5-19: Comparison of Mander et al. (1988) and experimental $f'_{cc}/f'_{c,avg20}$ data at 20 °C (68 °F) for the ManAB concrete mix

As expected, the experimental data provided in Figure 5-19 demonstrate that as the amount of lateral reinforcement increases the effect on the overall confined strength of the cylinder also increases. This concurs with the theoretical model suggested by Mander et al. (1988a). Although the effect of confinement is not apparent for 0.61% for the reason discussed above, the increase in confined compressive strength with a decrease in temperature exists and was left in the data sets when determining a relationship for the confined concrete strength. To ensure the data from the multiple reinforcement ratios increased as expected at all temperatures, Figure 5-20 was created to compare the different confinement ratios with the ratio of $f'_{cc}/f'_{cc,avg20}$ for the Man AB concrete mix and the remaining temperatures not examined in Figure 5-19. The data provided in the figure concur with the theory, except again for the 0.61% ρ_s data, which means that as lateral reinforcement increases the confined strength of the cylinder increases similar to the warm weather comparison in Figure 5-19.

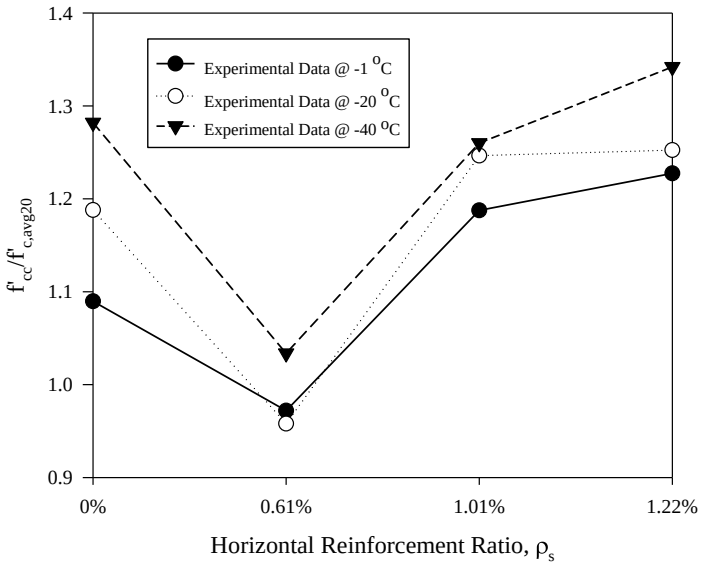

Figure 5-20: Effect of reinforcement ratio on $f'_{cc}/f'_{cc,avg20}$

Even though the experimental data increase as expected in Figure 5-19, the resulting increase is lower than the theoretical Mander et al. curve (1988a) by a minimum of 11% at ρ_s of 1.22% and a maximum of 20.5% at ρ_s of 0.61%. The difference noted between the two curves may be due to the fact the experimental testing performed at ISU did not include longitudinal bars in the specimen, although the testing performed by Mander et al. (1988b) used varying amounts of longitudinal reinforcement. These vertical bars increase the efficiency of the confinement. Although not included in the comparison model constructed using Mander et al. (1988) in comparing to the confined concrete strengths, the efficiency factor could still be significantly different than predicted by the model. A second difference in the experimental testing and theoretical model verification of Mander et al. (1988b) is that 500 mm (~20 in) diameter specimens were used which are nearly full-scale models compared to the small specimens tested at ISU. Although these are important differences in the experiments, the variation in strength suggests the designer of the system should first establish an appropriate means for determining the confined concrete strength at the warm weather condition prior to establishing any effects that take place due to variation in temperature from 20 °C (68 °F) to a lower freezing temperature.

At this point, a method for establishing the effects of temperature on the confined strength of concrete was established. Since it was previously concluded that the experimental data and theoretical model would not satisfactorily agree, a new method for determining the confined

compressive strength of concrete as a function of temperature was established similar to the approach used for the unconfined concrete. This was completed by first normalizing the confined concrete strength of the cylinders, f'_{cc}, with the average value of the confined concrete strength for the corresponding horizontal reinforcement ratio obtained at 20 °C (68 °F), $f'_{cc,avg20}$. After normalization, the data were examined and linear trends appropriate for capturing temperature effects were determined for the average normalized data sets of the different horizontal reinforcement ratios. The linear trend lines were then plotted, Figure 5-21, and it was noticed that the increase in the $f'_{cc}/f'_{cc,avg20}$ ratio, RV_{conf}, did not follow the expected pattern of the lower reinforcement ratios being below the higher reinforcement ratios. This is noted by the fact that as ρ_s increases the 1.01% curve is higher than the remaining horizontal curves.

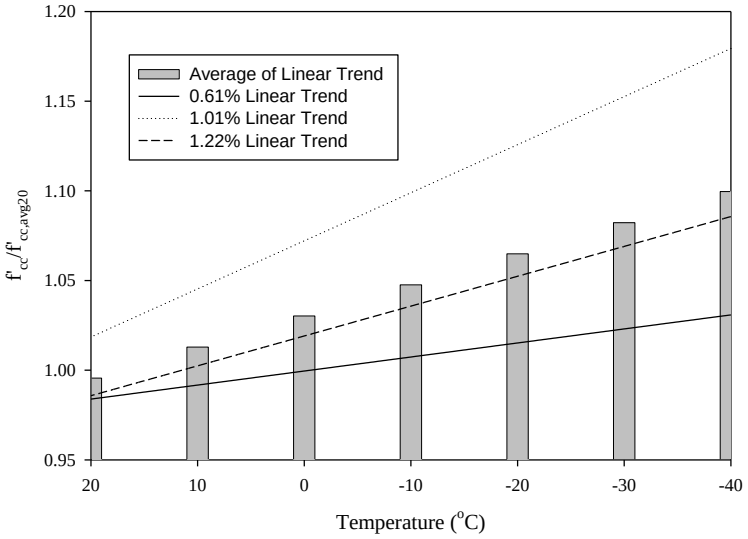

Figure 5-21: Confined concrete strength ratio deviation with temperature

Once it was determined that the amount of horizontal reinforcement did not directly influence the strength gain of the confined concrete samples due to temperature, the data sets were averaged together. The average values as provided within Figure 5-21 were within 10% of the maximum and minimum points obtained using the linear trend data at any given temperature. In addition, an approximate value of 1.0 occurred at 20 °C (68 °F). Therefore, the average data set was used to establish the ISU recommendation for the increase in the RV_{conf} term. To accomplish this task, the slope of the linear curve was established first by using the average value obtained at -40 °C (-40 °F) and a value of 1.0 at 20 °C (68 °F) based on the appearance of

the average data set. The intercept of the line could then be determined using either data point to complete the linear curve. This relationship is provided arithmetically in Equation 5-7.

$$RV_{conf} = \frac{f'_{cc}}{f'_{cc,20}} = -0.00166[T(°C)] + 1.0332 \quad (5\text{-}7a)$$

$$RV_{conf} = \frac{f'_{cc}}{f'_{cc,68}} = -0.00092[T(°F)] + 1.0627 \quad (5\text{-}7b)$$

After defining the trend for the average data set shown in Figure 5-21, a verification of the RV_{conf} term was performed by graphing the proposed curve of Equation 5-7 with the experimental data obtained from the confined cylinder specimens of the Man AB concrete mix. The multiple charts provided in Figure 5-22 demonstrate the proposed curves adequately capture the behavior of the confined concrete strength as temperature varies from 20 °C (68 °F) to -40 °C (-40 °F) in the spirally reinforced specimens. In addition, the steel shell experimental data appear to initially follow this trend between 20 °C (68 °F) and -1 °C (30.2 °F) as provided in Figure 5-22d, suggesting the proposed curve may be used for this type of reinforcement. The experimental data for the steel shell specimens at -20 °C (-4 °F) and -40 °C (-40 °F) were not included in this figure, since the testing apparatus capacity was reached and the maximum compressive strength of the specimens were not attained during testing. Since the proposed curves adequately capture the behavior of the confined strength, they are recommended for use when establishing the peak point of the confined concrete stress-strain curve for seasonal temperature variations between summer and winter months.

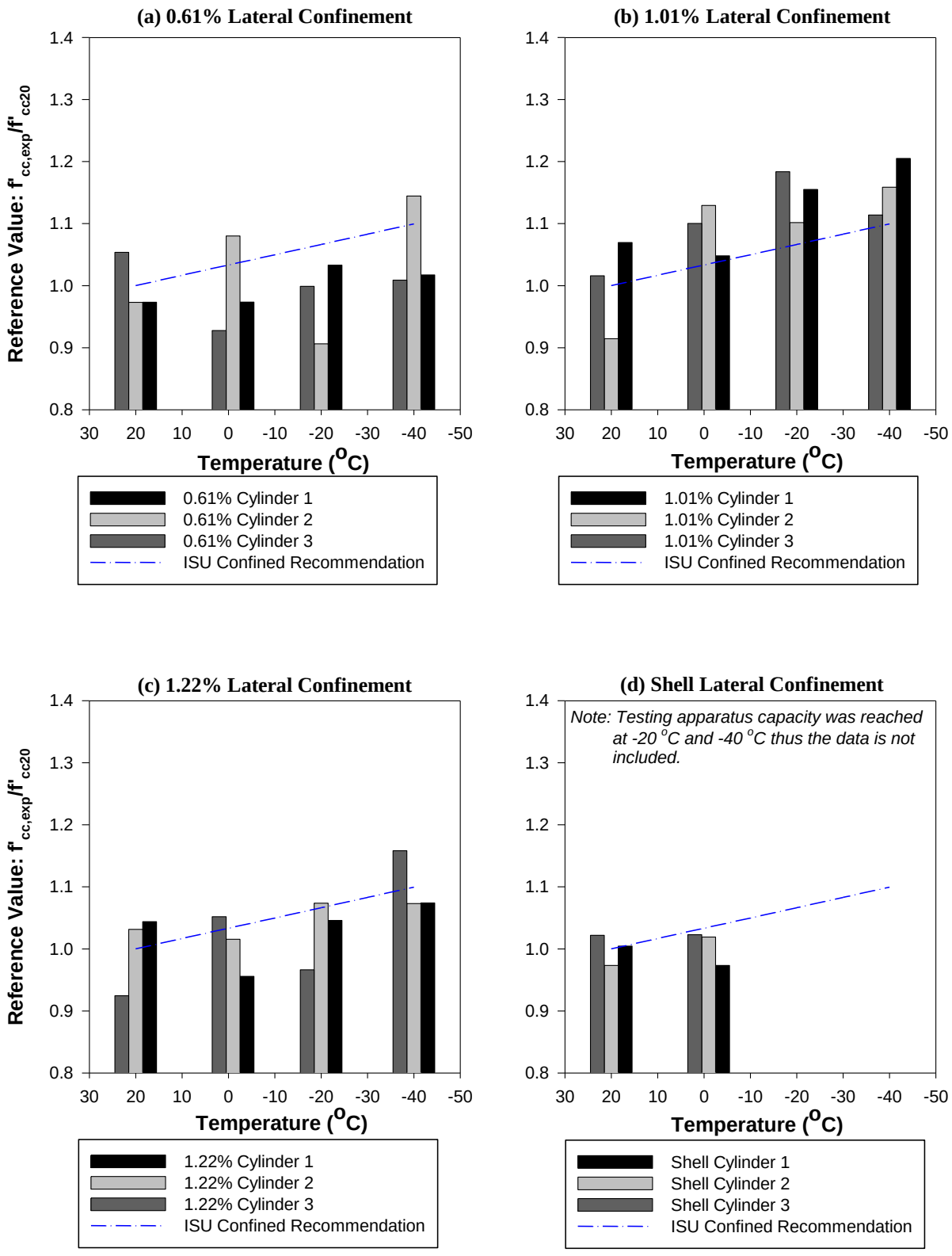

Figure 5-22: Comparison of the proposed equation for the increase in confined compressive strength against the test data for the Man AB confined concrete specimens

Confined Concrete Strain at Peak Compressive Strength, ε_{cc}

The strain at the peak of the confined concrete stress-strain curve is another key component to be defined. This strain defines the point at which the transition occurs from strengthening and softening compressive behavior of confined concrete. To establish this point, an examination of the actual strain values obtained at f'_{cc} for the confined cylinder specimens of the Man AB concrete mix was undertaken by plotting them as a series of vertical bars centered on the testing temperature, Figure 5-23. In addition to the experimental data, a linear trend of the average data for each confinement ratio and a theoretical trend predicted by Mander et al. (1988a) were included. The theoretical model of Mander et al. (1988a) was constructed by modifying the concrete material properties based on the experimental testing (i.e., E_c, f'_c and ε_{co}) and the steel material properties based on the information provided in Chapter 6 (i.e., f_y). Erroneous data were removed from the multiple sets if a given data point drifted from the median value by more than 20% or if the peak stress was not attained due to the maximum capacity of the testing apparatus being reached.

The linear trends depicted in Figure 5-23 have an overall increase in ε_{cc} between 0% to 40% as temperature decreases from 20 °C (68 °F) to -40 °C (-40 °F). The overall increase in strain contrasts with the theoretical curve of Mander et al. (1988a), which shows a decrease in ε_{cc} is expected as temperature decreases. This major variation in the experimental testing and theoretical model demonstrates the confinement model commonly used in practice cannot be adjusted to adequately capture the experimental results.

To define changes in ε_{cc} as a function of temperature, the process began by creating a curve that would capture the response of the strain at the peak confined concrete stress. In order to establish this curve, the average experimental strain at -40 °C (-40 °F) was divided by the average experimental strain at 20 °C (68 °F) for the three confinement ratios of spiral reinforcement provided in Figure 5-23. These ratios were found to be 1.237, 0.983 and 1.396 for the horizontal reinforcement ratios of 0.61%, 1.01% and 1.22% respectively. Since a distinct order of increasing or decreasing with reinforcement ratio existed and the values were within plus or minus 20% of the median value, an average number of 1.205 was computed for the increase in the ratio of $\varepsilon_{cc}/\varepsilon_{cc,20}$ at -40 °C (-40 °F). Thus, a single curve could be established by

assuming the increase of the aforementioned ratio would be equal to a value of 1.0 at 20 °C (68 °F). The curve produced using this method is provided arithmetically in Equation 5-8.

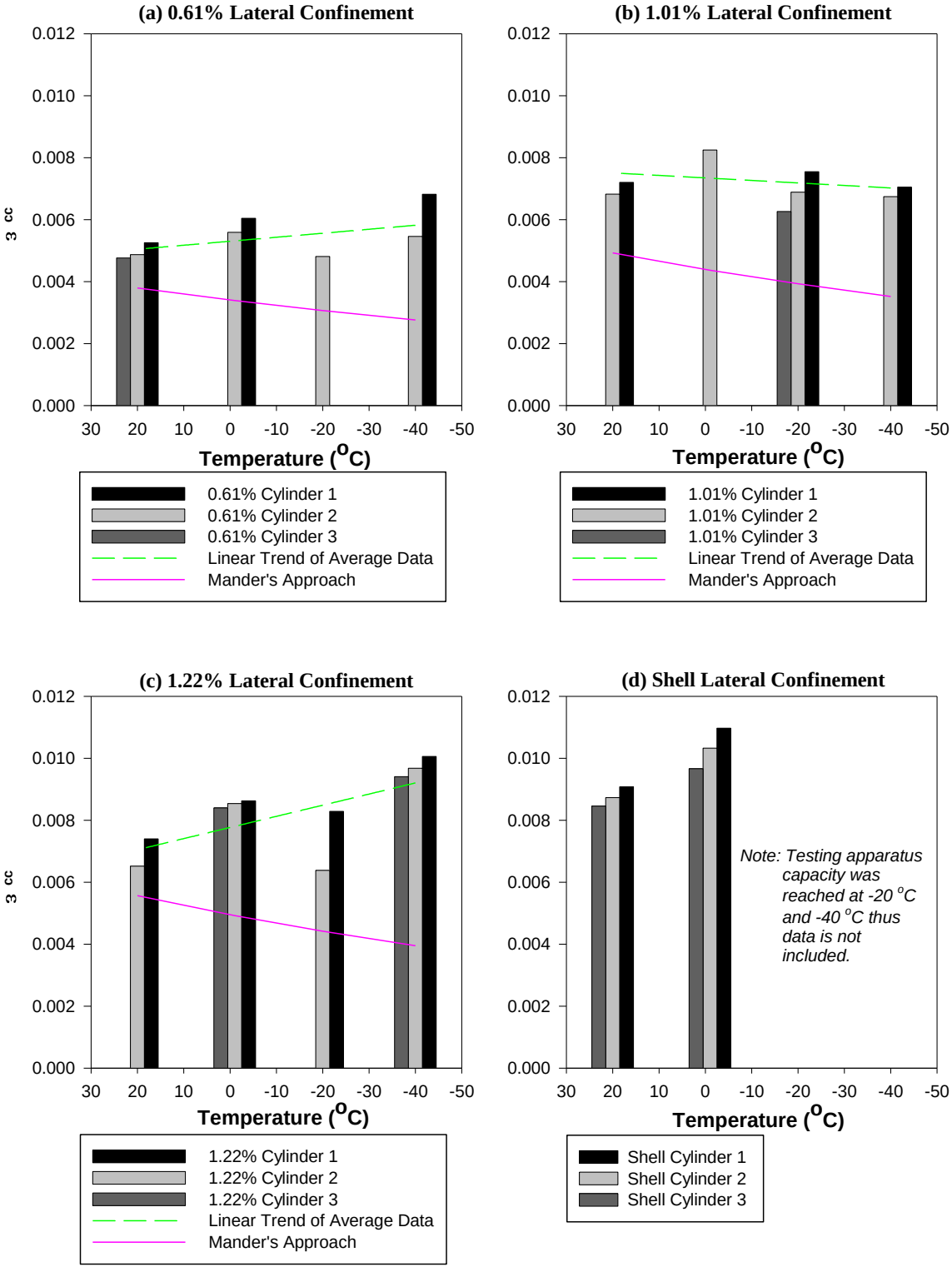

Figure 5-23: ε_{cc} values obtained from experimental testing of Man AB confined specimens

$$RV_{\varepsilon cc} = \frac{\varepsilon_{cc}}{\varepsilon_{cc,20}} = -0.0034[T(°C)] + 1.068 \quad \text{(5-8a)}$$

$$RV_{\varepsilon cc} = \frac{\varepsilon_{cc}}{\varepsilon_{cc,68}} = -0.0019[T(°F)] + 1.128 \quad \text{(5-8b)}$$

The final component in the strain at peak confined compressive strength is to define the initial strain value to be used within the design process. The authors first started this process by taking a closer look at the average experimental and theoretical ε_{cc} strain values obtained at 20 °C (68 °F). This examination is provided in Figure 5-24, where the two data sets are plotted as a function of the confinement reinforcement ratio. As expected, both data sets depict an increasing trend as the amount of lateral confinement rises from 0% to 1.22% with the difference between the theoretical and experimental curves ranging from 19% at no reinforcement to 42% at approximately one percent reinforcement. The differences in the theoretical and experimental data may be due to the lack of vertical bars in the specimen as well as the possibility of the small specimen size tested at ISU, but further investigation is required for this matter.

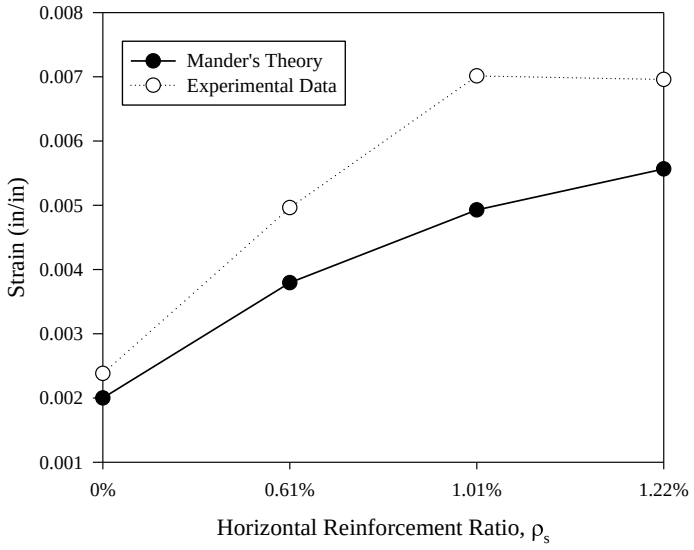

Figure 5-24: Comparison of theoretical ε_{cc} from Mander's et al. (1988a) with average experimental results at 20 °C (68 °F) for the Man AB concrete mix

In addition to the comparison of the theoretical and experimental curves provided in Figure 5-24, an additional graph was created to examine the effects of confinement at cold temperatures. The experimental strain data at the remaining three testing temperatures were plotted against the horizontal reinforcement ratio in Figure 5-25. Each curve provided in the figure follows an increasing trend in strain at the peak of the confined concrete stress-strain curve as the horizontal

reinforcement varies from 0% to 1.22%. Thus, at frozen temperatures, the more spiral reinforcement present within the system will increase the effectiveness of the confinement. This concurs with the theory of confined concrete during warm weather conditions.

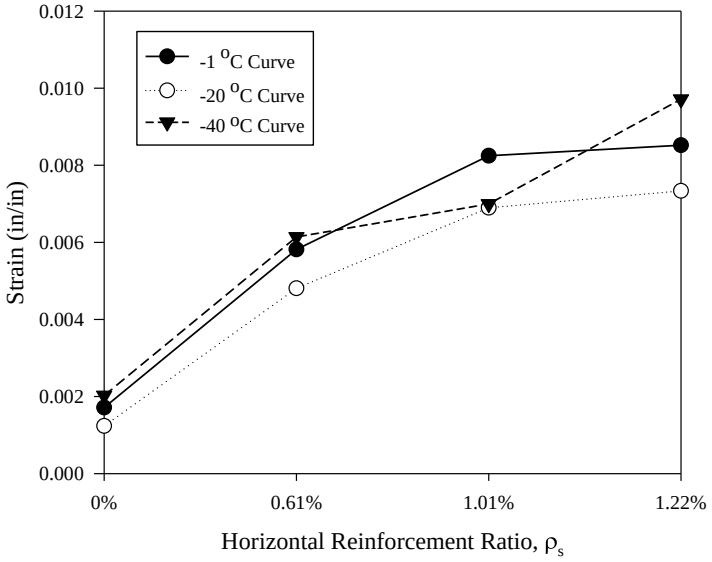

Figure 5-25: Experimental results of ε_{cc} plotted against ρ_s at freezing temperatures

The experimental strain values are consistently higher than the theoretical values suggested by Mander et al. (1988a) as depicted in Figure 5-24; therefore, the theoretical model was considered conservative by the authors as the lower strain values at the peak will lead to a lower strength gain and, therefore, moment behavior in the confined region of a concrete column or foundation. Due to the conservatism in the method, the designer should select an appropriate starting point for defining the strain at peak confined stress. For the purposes of verifying Equation 5-8, the approach suggested by Mander et al. (1988a) was deemed adequate for defining the initial strain value at 20 °C (68 °F). After establishing the starting point for each horizontal reinforcement ratio, the reference values were computed and graphed in Figure 5-26 against the experimental data to examine the efficiency of the approach.

The information provided within the aforementioned figure demonstrates that Equation 5-8 is able to adequately capture the increase in ε_{cc} as temperature decreases from 20 °C (68 °F) to -40 °C (-40 °F). Although the data are consistently lower than the experimental values, the overall trend is well captured. This provides a conservative estimate on the strain at peak confining stress. The conservatism suggests that a higher ductility of the system will be attained during a

seismic event during all seasons of the year. Additional verification information on the confined concrete peak strain can be found in Appendix B of the IF and Man C concrete mixes.

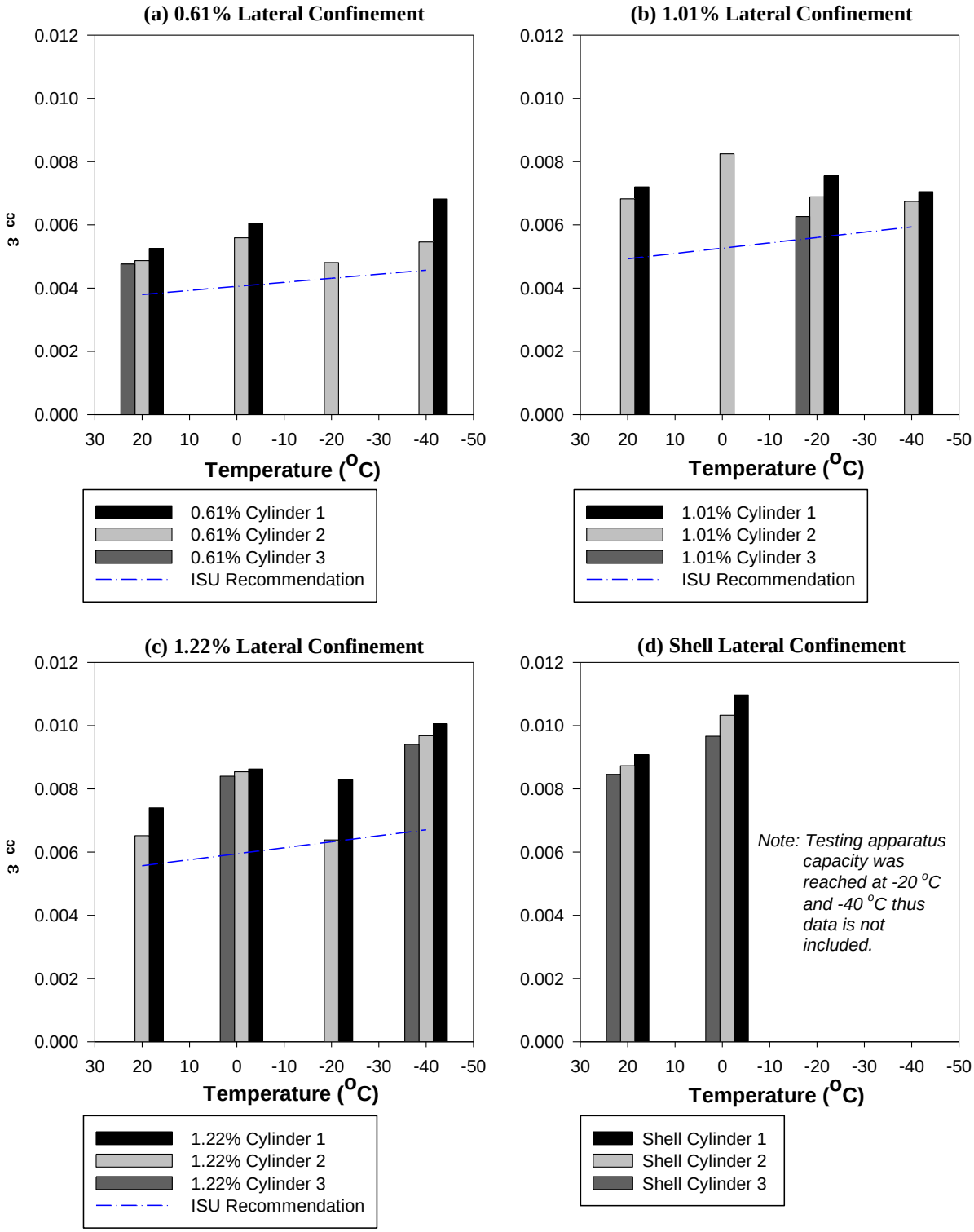

Figure 5-26: Verification of equations for strain at peak confined concrete stress

Ultimate Confined Compressive Strain, ε_{cu}

Another major factor in the definition of the confined concrete stress-strain curve is the establishment of the ultimate confined compressive strain. This strain is a major component in any design, as this defines the ultimate displacement that a section can attain when subjected to any form of loading. This arises as the concrete strain establishes one of the ultimate limit state curvatures that would be used in any model to effectively define the plastic behavior of the specific cross-section used in any design. Therefore, the ultimate confined compressive strain was plotted as a function of temperature in Figure 5-27 to determine if any trends existed in the results of the test specimens. The data presented show the ultimate strain capacity is not affected by decreasing temperature. Thus, it is recommended that the ultimate strain be taken the same as a designer defines in the warm weather condition.

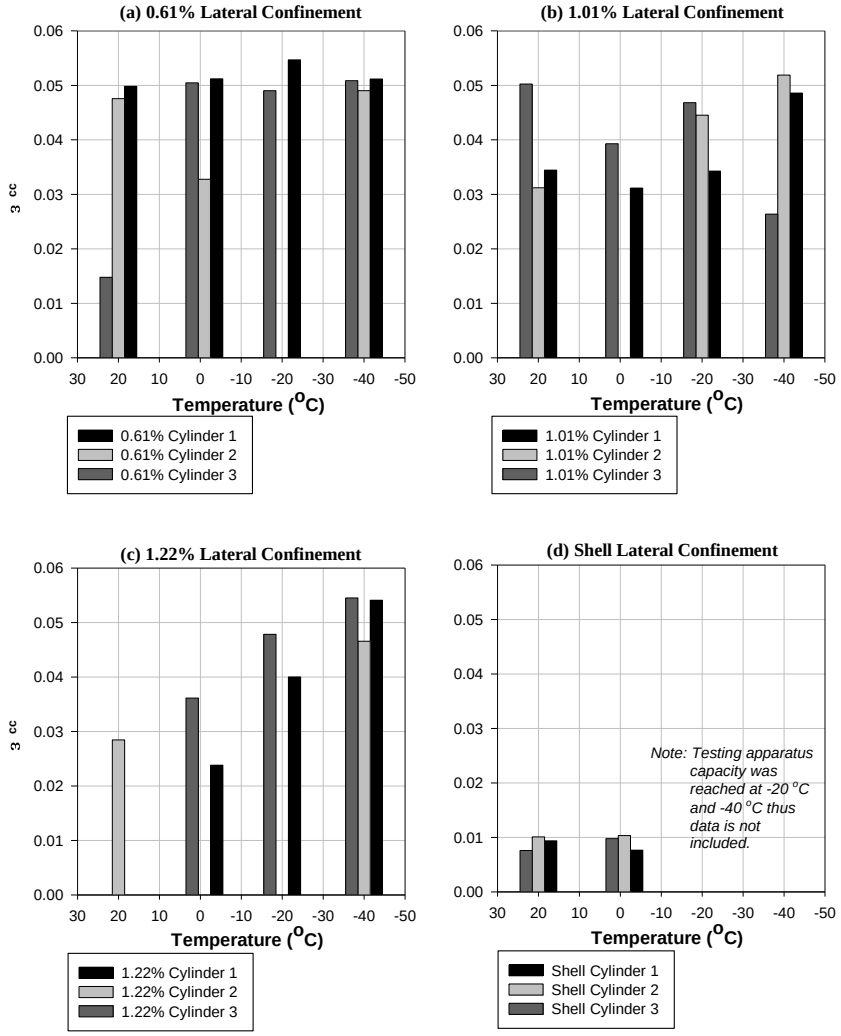

Figure 5-27: Ultimate confined strain capacity of the Man AB mix test specimens

Confined Concrete Modulus of Elasticity, E_{cc}

The last key component in adjustments made to the stress-strain curve of confined concrete at frozen temperatures is to establish an appropriate modulus of elasticity of the concrete specimens. This process was undertaken by using a secant chord on the linear portion of the experimental stress-strain curves for the multiple Man AB specimens tested between 20 °C (68 °F) and -40 °C (-40 °F). The experimental results, after removing invalid data points, of these chord values are provided graphically in Figure 5-28. Experimental data points were removed if they were an order of magnitude greater than the expected response based on other results. In addition, data points were removed if a given value at a specific temperature and horizontal confinement ratio exceeded the median value by more than 20%.

At each temperature, the graphs provided in Figure 5-28 show that the unconfined specimens consistently maintained a higher modulus of elasticity than the confined concrete specimens tested between 20 °C (68 °F) and -40 °C (-40 °F). This is in contrast with the idea of confined concrete in which the modulus of elasticity remains constant between the unconfined state and the confined state. Although these differences are prevalent within the data sets, the confined modulus of elasticity is still believed to remain the same as the unconfined concrete specimens. The authors believe this is the case, upon further inspection of the actual concrete stress-strain curves attained from the experimental testing. This comparison, provided herein as Figure 5-29, shows the slope of the elastic portion of the curves are nearly identical, even though the values of the unreinforced concrete modulus of elasticity were consistently 25% to 80% higher than the confined concrete values. The discrepancy between the experimental results is most likely due to the selection of data points when determining E_c or E_{cc}. This is shown in the inset portion of Figure 5-29, where the instantaneous values for the modulus of elasticity of the unreinforced concrete sample vary based on the stress level selected for the computation.

Since the remaining temperatures tested for the confined concrete samples experienced similar trends upon closer inspection of the data sets, it is recommended that the confined modulus of elasticity remain the same as the unconfined modulus of elasticity. This is consistent with current methods for the establishment of confined concrete stress-strain curves. Therefore, E_{cc} is equal to E_c and is affected by temperature in accordance with Equation 5-6.

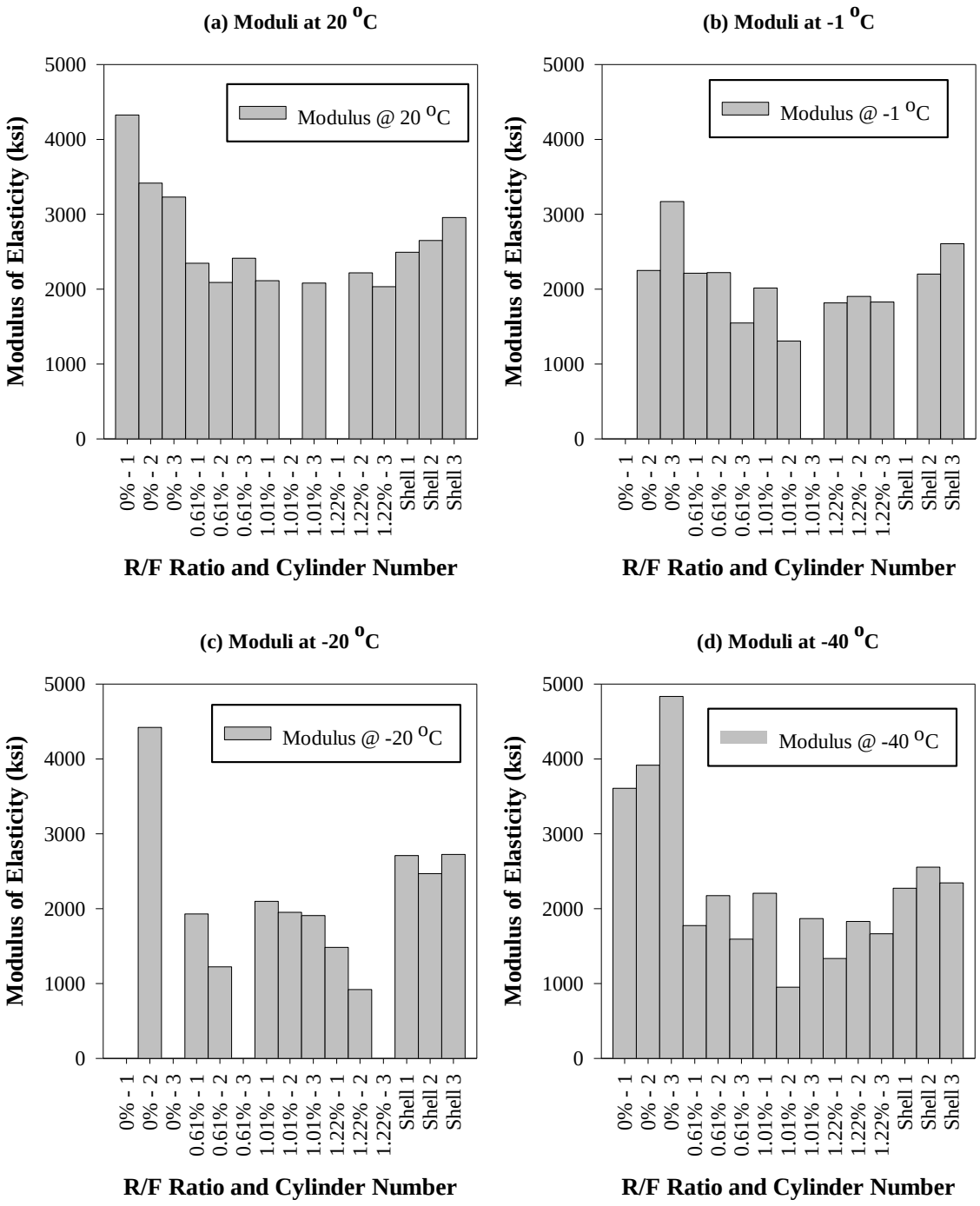

Figure 5-28: Modulus of elasticity experimental data points for confined and unconfined concrete at the four testing temperatures

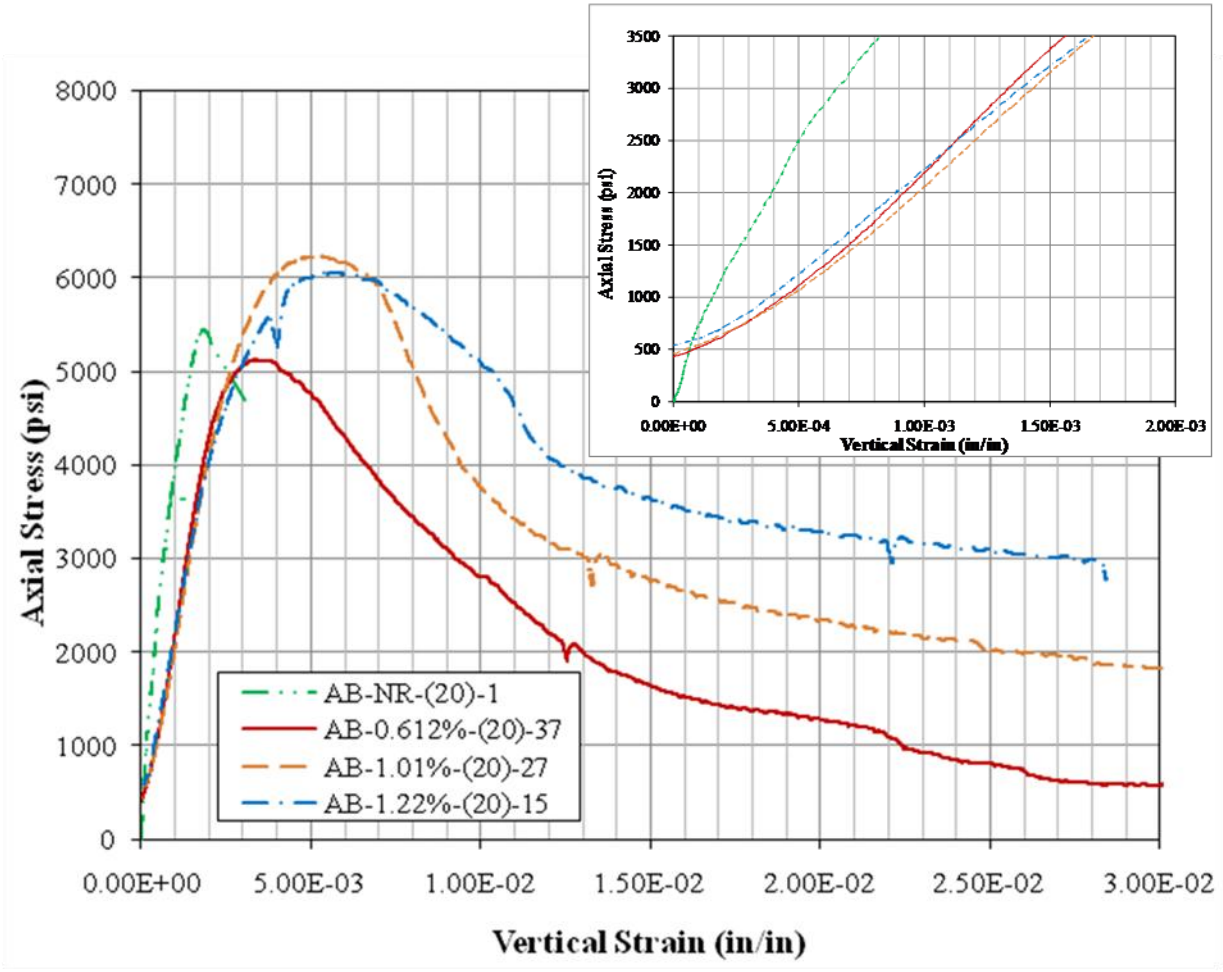

Figure 5-29: Experimental concrete stress-strain curves of the Man AB concrete mix tested at 20 °C (68 °F)

5.5 Conclusions

The preceding chapter undertook an investigation of the effects of seasonal freezing on the behavior of confined and unconfined concrete through an experimental testing program on small scale specimens. The testing program provided the necessary data for making modifications to a confined or unconfined concrete stress-strain curve subjected to seasonal freezing. These modifications were determined through the establishment of trends related to temperature and a property specific to concrete such as compressive stress, strain at peak compressive stress and modulus of elasticity. Below is a list summarizing the results presented within this chapter, along with recommendations for future research on concrete materials testing at cold temperatures.

- The unconfined concrete compressive stress (f'_c) of concrete increased an average of 28% when temperature decreased from 20 °C (68 °F) to -40 °C (-40 °F). The recommended equation for defining the linear increase is presented as Equation 5-2.
- The concrete strain at the peak of the unconfined concrete curve (ε_{co}) was found to be approximately 0.002 at 20 °C (68 °F). This value will decrease in a linear manner by approximately 23% as the temperature decreases to -40 °C (-40 °F). The equations for defining the concrete strain at peak compressive stress for a given temperature is presented in Equation 5-3.
- The modulus of elasticity for unconfined concrete (E_c) was found to increase by 13% as temperature decreased to -40 C (-40 F) from 20 C (68 F). The increase in E_c was found to follow a power series trend related to the unconfined compressive strength of the concrete and an exponent of 0.5. This relationship correlates well with current practice in which the modulus of elasticity is related to the square root of the unconfined compressive strength of the concrete. The equation for defining the increase is presented in Equation 5-6.
- Similar to the unconfined compressive stress, the confined concrete compressive stress (f'_{cc}) was found to increase as temperature decreased from 20 C (68 F) to -40 C (-40 F). This meant the confinement behaves differently than at warm weather conditions and separate recommendations were made for the increase in confined concrete compressive stress. The recommended equation for the increase is presented as Equation 5-7.
- The rate of increase in f'_{cc} was determined to be affected by the increase in Poisson's ratio of the concrete specimen as temperature decreases. The changing Poisson's ratio decreased the effectiveness of the confinement thus reducing the overall strength gain possible. However, additional steel added to the specimen will increase the ductility of the confined region as it does during a warm weather condition.
- In contrast to the unconfined concrete, the strain at the peak confined compressive stress (ε_{cc}) increased between 0% and 40%, depending on the amount of horizontal reinforcement present in the specimen, as temperature went from 20 °C (68 °F) to -40 °C (-40 °F). The increase, however, was able to be setup as a single trend with a variable

starting location based on the amount of horizontal reinforcement. The recommended equation is presented in Equation 5-8.

- The modification of material properties alone in Mander's model will not adequately capture the behavior of confined concrete subjected to seasonal freezing as shown in Figure 5-23.
- The ultimate confined compressive strain (ε_{cu}) was found to not be affected by decreasing temperature. Therefore, it is recommended the value be equal to that which a designer establishes in the warm weather condition.
- The unconfined concrete modulus was consistently higher than the confined concrete modulus; however, this was most likely due to a localized value being selected for determining the modulus of elasticity. Therefore, it is recommended that the modulus for confined concrete be equal to the value attained for unconfined concrete. The recommended equation is presented in Equation 5-6.
- Additional specimens should be constructed and tested so that a larger data set can be obtained to further verify the equations presented within this chapter.
- Larger specimens should be constructed and tested with the inclusion of longitudinal reinforcement to verify the approach with this reinforcement. This will also calibrate the equations for any possible size effect issues.

CHAPTER 6: STEEL BEHAVIOR AT FROZEN TEMPERATURES

6.1 Introduction

ASTM A706 Grade 60 reinforcing steel is being increasingly used in seismic applications, but a systematic study on the behavioral changes of this reinforcement at low temperatures does not exist. To fulfill this need, a study to determine the cold temperature effects on the stress-strain behavior of A706 reinforcement was undertaken. Several reinforcement samples were tested in a controlled environment utilizing monotonic quasi-static loading and varying temperatures between 20°C (68°F) to -40°C (-40°F).

Based on the measured data, this chapter presents the effects of cold temperature on the yield strength, yield strain, modulus of elasticity, strain at the onset of strain hardening, ultimate tensile strength, and ultimate tensile strain of ASTM A706 Grade 60 mild steel reinforcement. Two bar sizes tested at five different temperatures, three different strain rates at two temperatures, and utilizing a cyclic loading path were also examined in this study. This chapter presents a historical background of ASTM A706 reinforcing steel as well as relevant past research, laboratory testing, experimental findings, and material modeling recommendations.

6.1.1 Background

The most commonly used reinforcing steel in the US is ASTM A615, originally standardized in 1968 but included no specific regard for seismic or welding applications (ASTM Standard A615, 2009). The first version of ASTM A706 was published by ASTM International in 1974. This reinforcement standard was created in response to the engineering requirements for deformed reinforcing bars to a) have a controlled tensile strength for improving earthquake-resistant design of structures, b) enable weldability of reinforcement(Gustafson, 2007), and c) increased elongation for improved plastic deformation capacity. In 1990, the Concrete Reinforcing Steel Institute (CRSI) published Report No. 34, "ASTM A706 Reinforcing Bars-Technical Information with Commentary on Usage and Availability" to respond to questions regarding A706 mild steel reinforcement from engineers, architects, and contractors(Concrete Reinforcing Steel Institute, 1990).

It was the California Department of Transportation (Caltrans) that first required the use of A706 reinforcement in virtually all concrete bridge structures(Gustafson, 2007). From 1995 to the present time, several Departments of Transportation (DOT's) have followed in the footsteps

of Caltrans in utilizing A706 as the standard reinforcement type. These DOT's, which are also active seismic states in the US, include: the Alaska DOT & Public Facilities, Illinois DOT, and Washington DOT. Today, Section 21.1.5.2 of the ACI 318-08 code states that all "Deformed reinforcement resisting earthquake-induced flexural and axial forces…shall comply with ASTM A706" (American Concrete Institute (ACI), 2008), making A706 steel required for all buildings designed in seismic regions.

6.1.2 Previous Research

Previous studies reported by Bruneau et al. (1997), Filiatrault and Holleran (2001, 2002), and Sloan (2005) examined the effects of low temperature on various steel types under monotonic loading. Although most of these studies were not performed on A706 reinforcing steel, they are discussed herein as they offered insight into possible strength increases that could be expected for A706 steel at low temperatures. The previous information was used to create a test matrix and define specimen preparation methods in the present study. The material properties of ASTM A706 reinforcing steel will be compared to the observations of the previous research in a subsequent section.

Bruneau et al. (1997) summarized the results of cold temperature testing conducted by the Bethlehem Steel Corporation on ASTM A572 Grade 50 steel. The yield and ultimate strengths of A572 were found to increase in a polynomial fashion by 9 percent and 5 percent, respectively, when the specimen temperature was decreased from 20°C (68°F) to -40°C (-40°F). It was also reported that the modulus and ultimate strain were unaffected by cold temperatures. No information regarding the sample shape, size, test temperatures and temperature control method was available in this reference.

The studies by Filiatrault and Holleran (2001, 2002) examined the effects of cold temperature on CSA G30.16 reinforcing steel with a nominal yield strength of 400 MPa (58 ksi) at 20°C (68°F), -20°C (-4°F), and -40°C (-40°F) and the following loading strain rates: (80×10^{-6}) /s, 0.005 /s, 0.02 /s, and 0.1 /s. The stress-strain response of the milled 15 mm (0.591 in.) diameter deformed bar samples were all from a single bar. A temperature chamber was installed around the samples to maintain a constant temperature during each test. The researchers concluded that the elastic modulus and the ultimate tensile strain of CSA G30.16 reinforcing appeared to be unaffected by cold temperature. In contrast, the yield strength and ultimate tensile strength increased linearly by 20 percent and 10 percent, respectively, when

temperatures were decreased from 20°C (68°F) to -40°C (-40°F). Their data suggests that the yield strength and ultimate tensile strength changes associated with altering the strain rate are affected by temperature. Increasing the strain rate caused higher increases for cold specimens than warm specimens.

Sloan (2005) conducted testing on A706 mild steel reinforcement at temperatures of approximately 22°C (71.6°F) and -20°C (-4°F). This cold temperature was achieved by placing the specimens in an insulated box with dry ice. When the samples were ready to test, they were reported to have been quickly removed, placed into the grips of the Materials Testing Systems (MTS) fatigue machine and tested. The data presented in Figure 6-1 was compiled from the information reported by Sloan (2005).

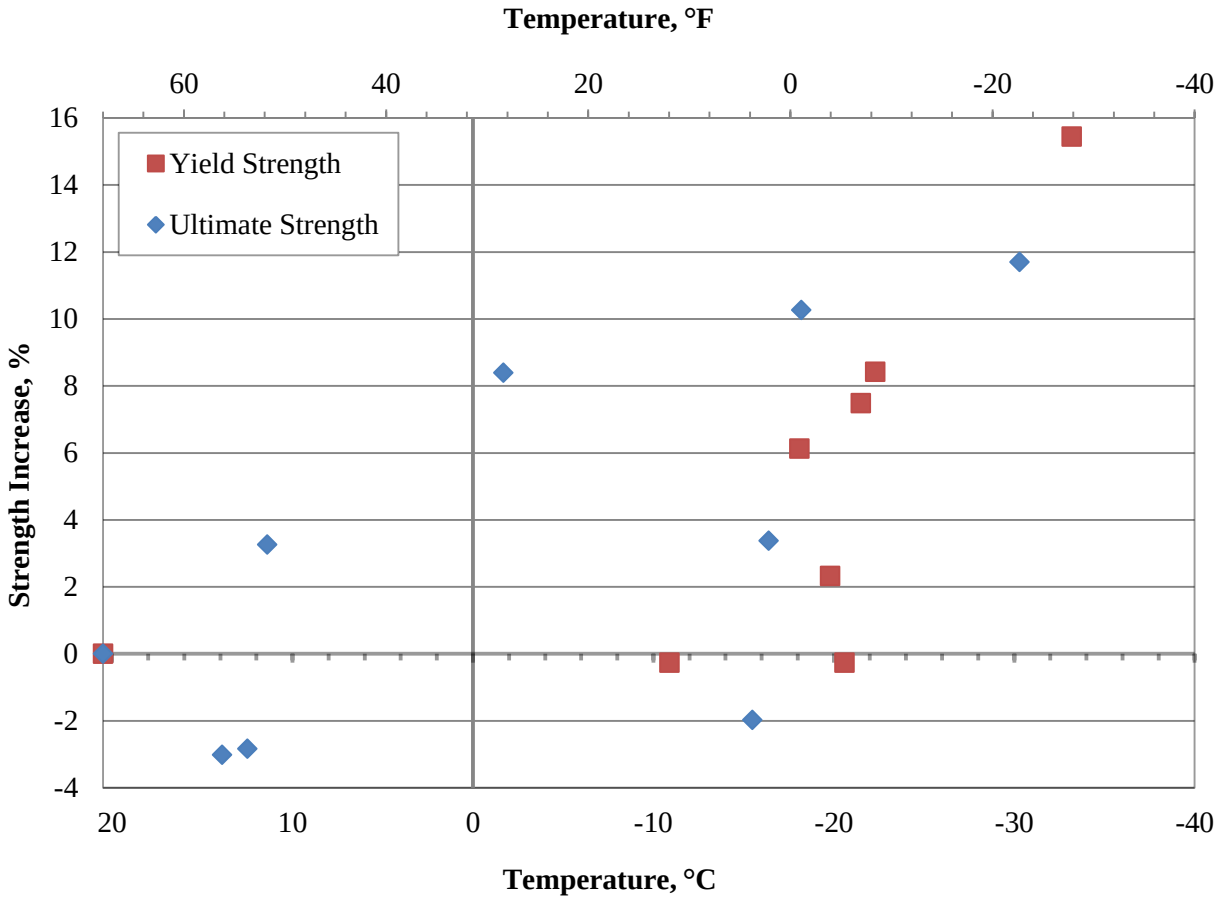

Figure 6-1: Yield and ultimate tensile strength increases reported for A706 steel by Sloan (2005)

The data collected by Sloan (2005) demonstrated an increase of approximately 8 percent in yield strength and 10 percent in ultimate tensile strength when temperatures decreased from 20°C (68°F) to -20°C (-4°F). As noted by Sloan (2005), some concerns arose due to using dry ice to cool the test samples rather than placing a controlled environment. The first concern was that a thermocouple was attached to the exterior of each sample during cooling with the sample being tested upon reaching the desired temperature. It was suspected that the test method may have caused the temperature inside the specimen to be different than the target value. The second concern was related to maintaining the target temperature of the specimen after removing it from the dry ice for testing. A similar approach was explored in the study reported herein, but it was found that the samples had increased by 10 to 20°C before testing could be completed. Sloan (2005) stated that the warming of the samples made it difficult to correctly quantify the cold temperature stresses. The final concern was that specimen failure occurred near the grips due to rapid warming(Sloan, 2005). This may be attributed to heat transfer between the specimen and testing apparatus. Milled samples were utilized in an attempt to resolve this concern.

From this previous research, the experimental study presented in this chapter was modified to include additional, yet beneficial, data. The effects of temperature on strain hardening were included in this study as it has not been previously examined for A706 reinforcement. A smaller incremental temperature difference was used in order to capture the effects around 0°C (32°F) and to allow for a dependable data curve fit to be established. Furthermore, a reliable cooling method was utilized to determine if the previous research provided is applicable to the ASTM A706 Grade 60 reinforcing steel used in the U.S.

6.2 Experimental Study

Details of the experimental study undertaken to quantify the stress-strain response of A706 reinforcing steel at low temperatures are presented in this section. The testing performed followed ASTM E8 guidelines as much as possible (ASTM Standard E8, 2004 (2006)). Like the previous research, some challenges were encountered during this study. They were successfully overcome as discussed below.

6.2.1 Sample Preparation

Monotonic

Deformed bars provided from a national steel manufacturing company with a nominal diameter of 19 mm (0.750 in.) and 25 mm (1.0 in.) were used in this study to ensure that the material composition and performance be reflective of that used in the field. Specimens were cut from these bars into roughly 0.9144 m (3 ft) lengths. These long specimen lengths were necessary to accommodate the environmental chamber that was positioned between the grips of the MTS machine as the grips could not fit inside the chamber. Each bar was separated, labeled, and tested at each predetermined temperature to avoid introducing the influence of other variables into the data. Comparisons between temperature variations would then only be made between samples of the same manufacturer's heat number. All specimens were milled to a cylindrical cross-section at their center for a specified gauge. This approach enabled the exact cross-sectional area of the specimen, utilized in calculating stress, to be accurately determined. This also forced the failure to occur within the monitored milled region and away from the grips.

It was found that deformed reinforcing bars cannot be gripped directly due to the bar deformations (ribs) on the bar. Gripping directly to the reinforcing bars was initially utilized but led to the failure of the testing apparatus grips during early stages of testing. This problem was resolved by using one of two methods. In the first method, four aluminum half-pipe sleeves, as shown in Figure 6-2a, were placed on the ends of the bar at the point of gripping. Upon gripping, the sleeves formed to the outer surface of the bar (see Figure 6-2b), which allowed for a constant transverse stress distribution to be attained around the bar during each test. For the second method, the ends of each bar were milled to a cylindrical cross-section to avoid any stress concentration. The first of these methods were used for testing the 19 mm (0.75 in.) bars while the latter for the 25 mm (1.0 in.) bars due to the size constraints of the MTS apparatus.

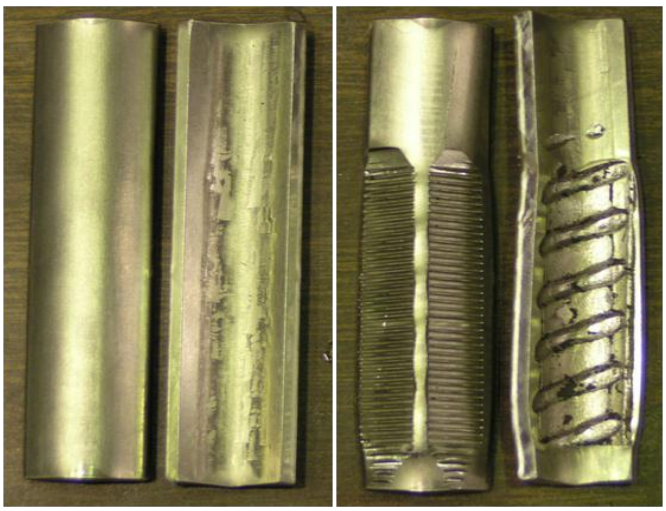

(a) Before Testing (b) After Testing

Figure 6-2: Aluminum sleeves used to ensure uniform grip at bar ends

Cylcic

Deformed bars with a nominal diameter of 36 mm (1.41 in.) were used instead of 25 mm (1.0 in.) bars for this portion of the study. Similar to the monotonic testing, specimens were cut into roughly 0.9144 m (3 ft) lengths with each specimen reduced at its center to the size of a milled 25 mm (1.0 in.) bar. In addition, as shown in Figure 6-3, the ends of each specimen were milled down to fit the size constraints of the MTS machine while maintaining a cross-sectional area 15 percent larger than the 25 mm (1.0 in.) diameter milling. This specimen configuration was necessary for accurate data collection and preventing failure of the specimens outside the monitored region while maintaining the expected force resistance of a 25 mm (1.0 in.) deformed bar.

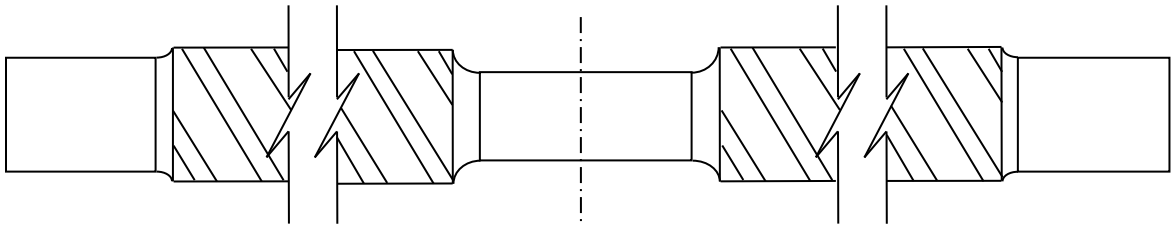

Figure 6-3: Milled specimen for cyclic loading

6.2.2 Test Setup

All specimens were tested in an environmental chamber that was designed to fit a 489 kN (110 kip) capacity uniaxial MTS fatigue machine as shown in Figure 6-4. The environmental

chamber ensured that the specimens would be subjected to the intended temperatures during testing via electronic temperature readouts. To confirm that each specimen had reached the desired temperature, a "dummy" bar housing a thermocouple within a hole drilled at its centerline was inserted from the side of the chamber as shown in Figure 6-4. Another thermocouple was placed in the chamber to verify that the environmental temperature readout was accurate during testing.

When conducting a trial test, it was found that it could take an excess of 2-3 hours for the sample to cool to the desired testing temperature. To lessen this time burden, the chamber was initially set at a temperature 10-15°C colder than desired. This reduced the time necessary for a sample to reach the target temperature to about 30 minutes. Upon reaching the desired stable temperature, the testing of each specimen was initiated. During each test, the temperature was monitored to ensure no significant change, ± 0.1°C, in temperature occurred that would compromise the rest results.

A low-temperature rated extensometer was used to record the elongations and thus the strains induced in the specimens. The extensometer was placed on the milled section of the specimen by direct contact to capture strains for the milled area instead of the nominal bar area (See Figure 6-4). The tensile stresses induced on the specimen were determined by a load cell that measured the applied axial load. These values were then divided by the reduced cross-sectional area of the specimen. Data recorded from each test was used to develop a stress-strain curve as a function of temperature similar to that found in Figure 6-5. Data for each test was gathered at least 300 times a minute to better define the stress-strain curve.

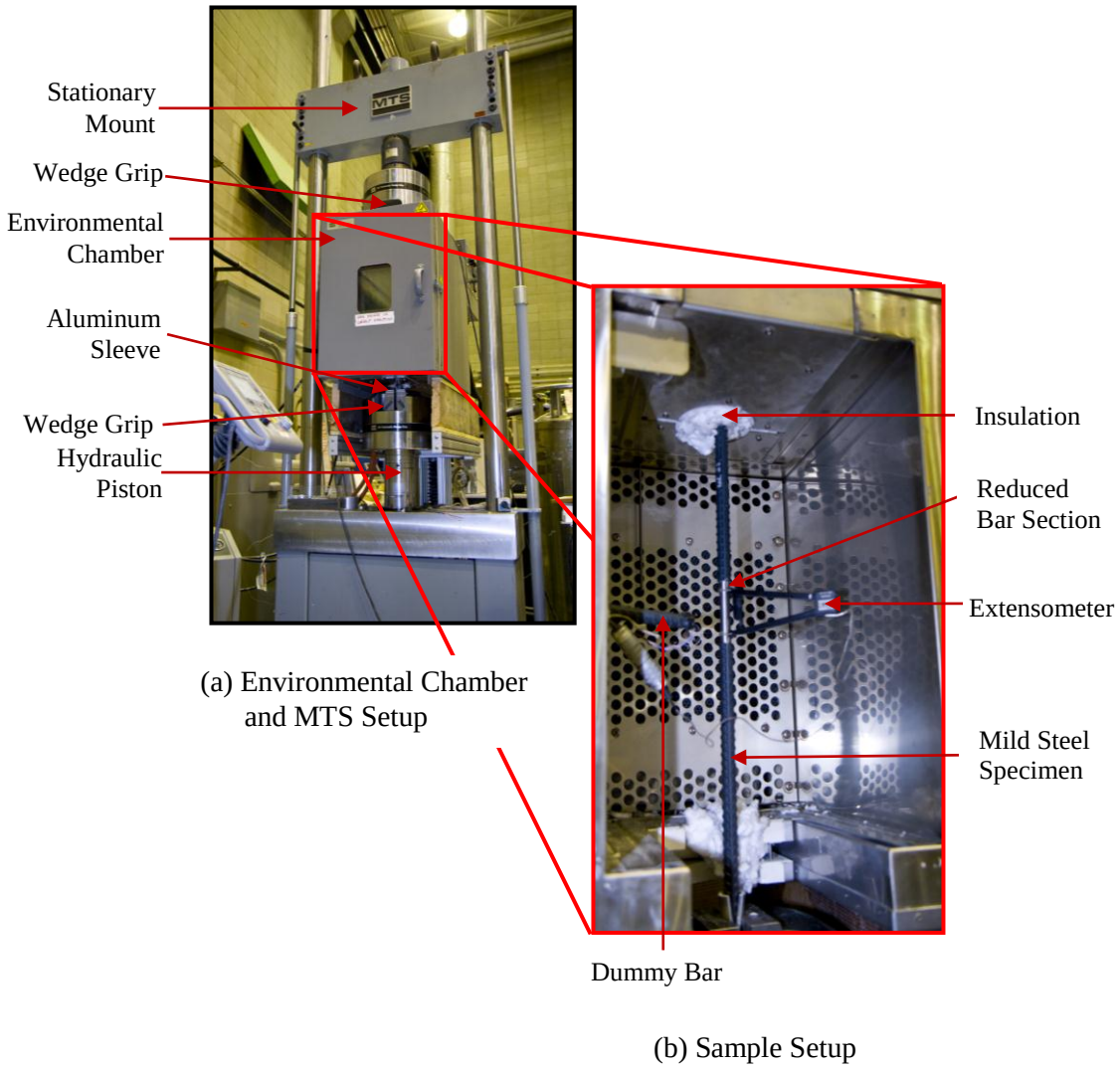

Figure 6-4: Setup used for testing A706 specimens within an environmental chamber

6.2.3 Loading Protocol

Monotonic

The monotonic testing, with the setup shown in Figure 6-4, utilized two different constant strain rates per test. Both strain rates corresponded to the mid ranges of the acceptable values specified by ASTM E8. The first strain rate of 0.001896 /min., which determined the yield strength of the sample, was used up to a strain of 1 percent. This strain approximately corresponded to the onset of the strain hardening region of the stress-strain curve. Upon reaching 1 percent strain, a faster rate of 0.275 /min. was used until the test was terminated at 18 percent strain, by which point the ultimate strength of the specimen had been recorded.

Additional testing was conducted at constant strain rates of 0.003, 0.03, and 0.3 /min., gathering data 300 times a minute, at two temperatures to determine if strain rate would affect the stress-strain behavior of the material.

Cyclic

The cyclic testing, with the same setup as shown in Figure 6-4, utilized a constant strain rate of 0.03 /min. per test which was determined from the completed monotonic tests. The cyclic loading path chosen for the tests, consisting of increasing tension and compression strains, can be found in Table 6-1. The specimens were to be loaded to the targeted tension strain and then unloaded to the targeted compressive strain. At each strain set, a minimum of three cycles were planned before continuing onto the next set of targeted strains. All compressive strains shown in Table 6-1 are 1/3 of the tensile strains for each strain set in order to achieve a compressive strain between 0.02 and 0.03 during the final cycle set.

Table 6-1: Cyclic test target strains for A706 mild steel reinforcement

Cycle Set	Target Tensile Strains	Target Compressive Strains
1	-0.00060	0.00020
2	-0.00119	0.00040
3	-0.00179	0.00060
4	-0.00238	0.00079
5	-0.00500	0.00167
6	-0.01000	0.00333
7	-0.01500	0.00500
8	-0.02000	0.00667
9	-0.04000	0.01333
10	-0.06000	0.01667
11	-0.08000	0.02667

6.2.4 Test Matrix

A summary of all the tests performed on ASTM A706 Grade 60 is presented in Table 6-2. As seen in Table 6-2, the first portion of the study utilized two different size bars subjected to monotonic testing at five temperatures: 20°C (68°F), 5°C (41°F), -1°C (30.2°F), -20°C (-4°F), and -40°C (-40°F). These bar sizes were chosen because their expected ultimate load capacity was below that of the MTS fatigue test machine. Eight tests, with three samples per test yielding

a total of 24 samples, were used to determine the combined effects of low temperatures and the effects of bar size.

The second portion of the study consisted of testing 25 mm (1.0 in.) diameter bars, tested at two temperatures: -1°C (30.2°F) and -20°C (-4°F). Six tests, with a minimum of two samples per test yielding a total of 12 samples, were used to examine the effects of strain rate on the stress-strain behavior of A706 reinforcing steel.

Table 6-2: Monotonic test matrix used to study the effects of temperature, bar size and strain rate on A706 mild steel reinforcement

Purpose	Temperature in °C (°F)	Nominal Bar Diameter mm (in.)	Loading Rates Strain/min	Number of Test Samples
Determine the Effects of Temperature	-40 (-40.0)	25 (1.0)	0.001896/0.2750	3
	-20 (-4.0)	25 (1.0)	0.001896/0.2750	3
	-1 (30.2)	25 (1.0)	0.001896/0.2750	3
	5 (41.0)	25 (1.0)	0.001896/0.2750	3
	20 (68.0)	25 (1.0)	0.001896/0.2750	3
Determine the Effects of Temperature and Bar Diameter	-40 (-40.0)	19 (0.75)	0.001896/0.2750	3
	-20 (-4.0)	19 (0.75)	0.001896/0.2750	3
	-1 (30.2)	19 (0.75)	0.001896/0.2750	3
	5 (41.0)	19 (0.75)	0.001896/0.2750	3
	20 (68.0)	19 (0.75)	0.001896/0.2750	3
Determine the Effects of Strain Rate	-20 (-4.0)	25 (1.0)	0.003	2
	-1 (30.2)	25 (1.0)	0.003	2
	-20 (-4.0)	25 (1.0)	0.03	2
	-1 (30.2)	25 (1.0)	0.03	2
	-20 (-4.0)	25 (1.0)	0.3	2
	-1 (30.2)	25 (1.0)	0.3	2

The final portion of the study, as depicted in Table 6-3, consisted of testing milled 36 mm (1.41 in.) diameter bars at two temperatures: -1°C (30.2°F) and -20°C (-4°F). Two tests, with a minimum of two samples per test yielding a total of 4 samples, were used to examine the behavioral differences between monotonic and cyclic loading. Monotonic test matrix used to study the effects of temperature, bar size, and strain rate on A706 mild steel reinforcement.

Table 6-3: Cyclic test matrix used to study the effects of temperature on A706 mild steel reinforcement

Purpose	Temperature in °C (°F)	Milled Bar Diameter mm (in.)	Loading Rate strain/min	Number of Test Samples
Determine the Effects of Cyclic Loading	-20 (-4.0)	25 (1.000)	0.03	2
	-1 (30.2)	25 (1.000)	0.03	2

6.3 Results and Discussion of Study

This section is devoted to the key experimental results. Although all stress calculations were based on the measured cross-sectional bar area, it is believed that all data is applicable to the behavior of deformed bars as well. A summary of the temperature effects on the modulus of elasticity, E_s; yield strength, f_y; yield strain, ε_y; strain at the onset of hardening, ε_{sh}; ultimate tensile strength, f_{su}; and ultimate tensile strain corresponding to f_{su}, ε_{su}, of A706 mild steel is discussed first, followed by a discussion on the effects of strain rate and bar size. Figure 6-5 provides an idealized stress-strain graph for mild steel reinforcement with these critical parameters.

6.3.1 Temperature Effects

Elastic Modulus

The modulus of elasticity, E_s, was found using the best fit slope between (0, 0) and (ε_y, f_y). From the moduli established at different temperatures, it was observed that varying the temperature between 20°C (68°F) to -40°C (-40°F) caused no significant change in the elastic modulus of the material. This observation is consistent with the observations made in past research.

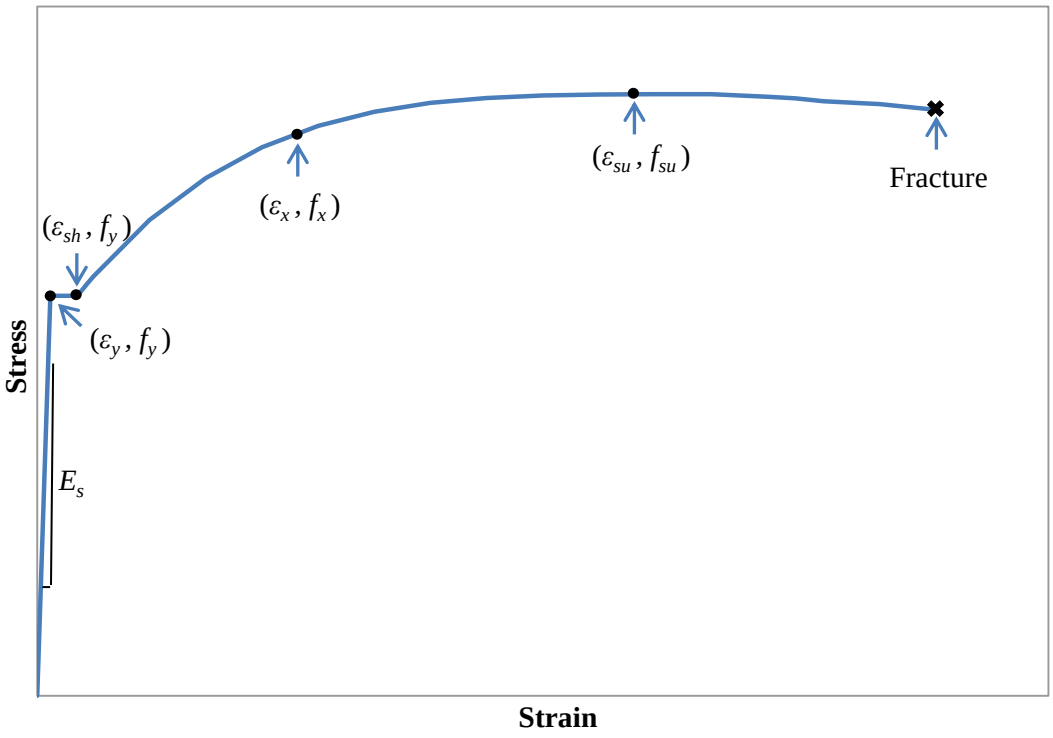

Figure 6-5: Idealized stress-strain curve for A706 mild steel reinforcement

Yield Strength

The yield strength, f_y, was attained by applying a best fit horizontal line to a minimum of 500 data points within the yield plateau region of the recorded stress-strain curve. The value of f_y varied in a quadratic fashion with temperature, as depicted in Figure 6-6. Also included in this figure is Eq. (6-1), which corresponds to the best fit trendline established for the increase in the yield strength based on the test data. A standard deviation equation, ±σ, has been provided in Eq. (6-2).

$$\Delta f_y(\%) = 0.0009(T)^2 - 0.0674(T) + 0.9880 \quad \text{(6-1a)}$$

where, T is in °C

$$\pm\sigma(\Delta f_y, \%) = \pm[0.0191(T) - 0.3820] \quad \text{(6-2a)}$$

$$\Delta f_y(\%) = 0.00028(T)^2 - 0.0552(T) + 2.4707 \quad \text{(6-1b)}$$

where, T is in °F

$$\pm\sigma(\Delta f_y, \%) = \pm[0.0106(T) - 0.7216] \quad \text{(6-2b)}$$

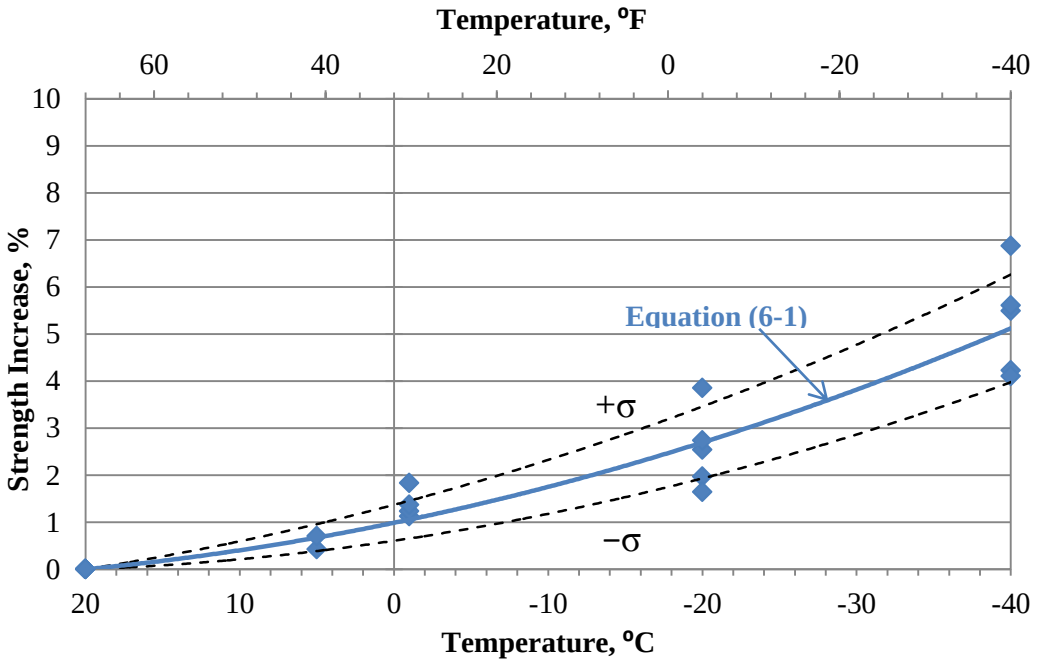

Figure 6-6: Effects of cold temperature on the yield strength of A706 mild steel reinforcement established from monotonic testing

As shown in Figure 6-6, the test specimens experienced a 5.1 percent increase in yield strength as the temperature decreased from 20°C (68°F) to -40°C (-40°F) with strength increases apparent before reaching 0°C (32°F). This polynomial data variation is similar in trend to A572 reported by Bruneau et al. (1997), but does not support the linear variation reported for CSA G30.16 steel by Filiatrault and Holleran (2001, 2002). In addition, the magnitude by which the yield strength of A706 is affected for the temperature range examined is less than that observed for both A572 and CSA G30.16 steel reinforcement. The yield strength increase experienced at -20°C (-4°F) is about 3 percent, which is considerably less than that indicated by the data produced by Sloan (2005). The scatter of the data is also considerably less than that reported by Sloan, confirming the higher quality of data resulting from testing the steel coupons in a well-controlled environmental chamber.

Yield Strain and Onset of Strain Hardening

The yield strain, $\varepsilon_{y,}$ was calculated by dividing the yield strength by the elastic modulus for each specimen (i.e., $\varepsilon_y = f_y / E_s$) because the modulus remained constant between tests. Consequently, the calculated yield strain increased proportionally to the yield strength. The onset of strain hardening, ε_{sh}, was defined as the strain at which the specimen began to steadily

increase in strength after yielding (see Figure 6-5). The yield plateau length was then be defined as the difference between the onset of strain hardening and the calculated yield strain (i.e., $\varepsilon_{sh} - \varepsilon_y$). It was observed that no considerable change occurred in the yield plateau length when varying the temperature from 20°C (68°F) to -40°C (-40°F).

Ultimate Tensile Strength

The ultimate tensile strength, f_{su}, was defined as the maximum stress recorded during a test (see Figure 6-5). The test data showed a polynomial trend, as depicted in Figure 6-7. Also included in this figure is Eq. (6-3), which corresponds to the best fit trendline established for the increase in strength on the test data. A standard deviation equation, ±σ, has been provided in Eq. (6-4).

$$\Delta f_{su}(\%) = 0.0007(T)^2 - 0.0912(T) + 1.5440 \quad \text{(6-3a)}$$

where, T is in °C

$$\pm\sigma(\Delta f_{su}, \%) = \pm[0.0200(T) - 0.4000] \quad \text{(6-4a)}$$

$$\Delta f_{su}(\%) = 0.00022(T)^2 - 0.0645(T) + 3.3866 \quad \text{(6-3b)}$$

where, T is in °F

$$\pm\sigma(\Delta f_{su}, \%) = \pm[0.0111(T) - 0.7556] \quad \text{(6-4b)}$$

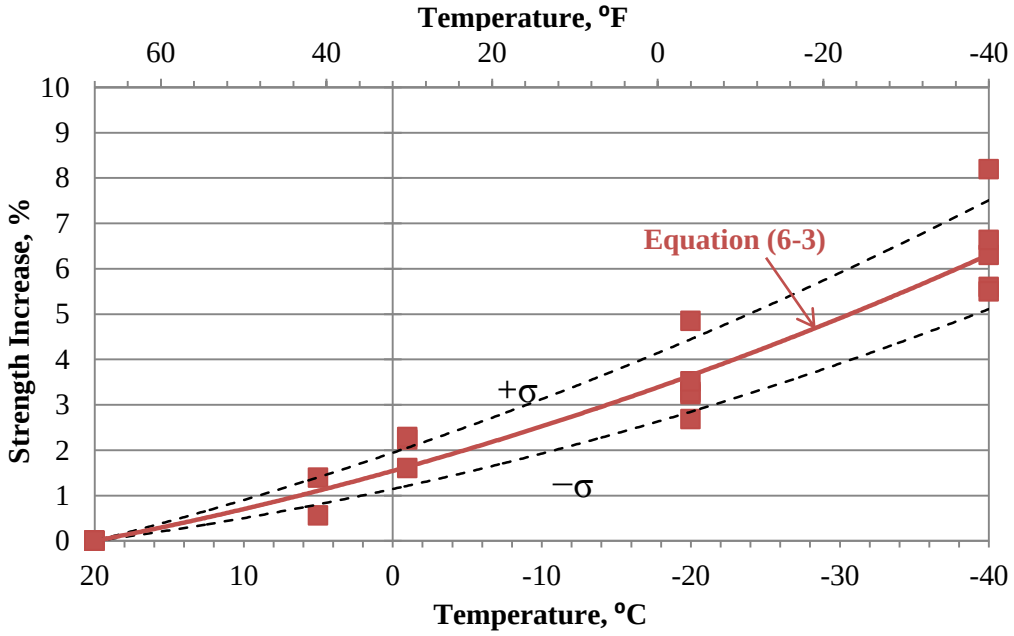

Figure 6-7: Effects of cold temperature on the ultimate tensile strength of A706 mild steel reinforcement established from monotonic testing

As shown in Figure 6-7, the A706 steel specimens experienced a 6.3 percent increase in ultimate tensile strength as the temperature decreased from 20°C (68°F) to -40°C (-40°F) with strength increases apparent before reaching 0°C (32°F). This polynomial data variation is similar in trend to A572 reported by Bruneau et al. (1997), but again does not support the linear variation reported for CSA G30.16 steel by Filiatrault and Holleran (2001, 2002). In addition, the magnitude by which the ultimate tensile strength of A706 is affected for the temperature range examined is more than that observed for A572, but less than that reported for CSA G30.16 steel reinforcement. Lastly, the ultimate tensile strength increase experienced at -20°C (-4°F) is about 3.5 percent, which is considerably less than that indicated by Sloan (2005). Similar to the yield strength, the data scatter was considerably less than reported by Sloan (2005).

Ultimate Tensile Strain

The ultimate tensile strain, ε_{su}, was defined as the strain corresponding to the ultimate strength, f_{su}, as shown in Figure 6-5. The average value of ε_u obtained from data at all temperatures was 0.116. For the temperature range of 20°C (68°F) to -40°C (-40°F), the scatter of the data revealed no considerable change to the ultimate tensile strain as the temperature decreased. The observation of cold temperatures having no impact on the ultimate tensile strain was also observed by the data presented by Bruneau (1997) and Filiatrault and Holleran (2001, 2002) on A572 and CSA G30.16, respectively.

6.3.2 Effects of Bar Size

The increases in yield and ultimate strength presented in the previous section ignored the effects of bar size and included the data from both 19 mm (0.750 in.) and 25 mm (1.0 in.) diameter milled bars. Figure 6-8 provides a comparison between the yield and ultimate strength increases associated with lowering the temperature from 20°C (68°F) to -40°C (-40°F).

The data in the figure shows that, in general, the temperature-induced strength increases for the 25 mm (1.0 in) diameter bar are higher than the 19 mm (0.75 in.) diameter bar as indicated by the best fit trendlines. From the presented data, it appears that the increases in yield and ultimate tensile strengths are somewhat affected by specimen size, but there is insufficient data to fully establish this hypothesis at this stage.

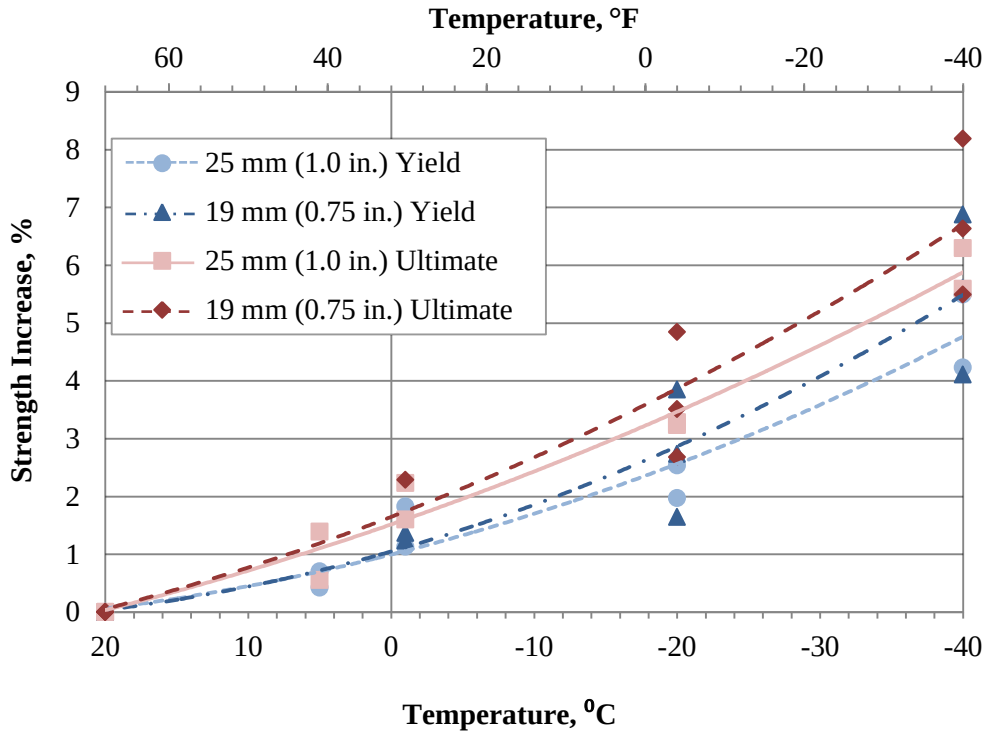

Figure 6-8: Comparison between yield and ultimate tensile strength increases obtained for tow bar sizes subjected to monotonic loading

6.3.3 Strain Rate Effects

Elastic Modulus

From the testing performed on 25mm (1.0 in.) reinforcing bars, it was observed that varying the strain rate from 0.003 to 0.3 /min. caused no significant change in the modulus at both -1°C (30.2°F) and -20°C (-4°F). This is apparent in the graphical representation of data presented in a logarithmic scale in Figure 6-9, where the scatter is relatively small and without an apparent trend due to strain rate. This finding is consistent with the observations of Filiatrault and Holleran (2001, 2002) for CSA G30.16 steel.

Yield Strength

As depicted in Figure 6-10, increasing the strain rate from 0.003 to 0.3 /min. caused an increase of about 3 percent (13.79 MPa or 2 ksi) in the yield strength of the milled 25 mm (1.0 in.) rebar specimens at temperatures of -1°C (30.2°F) and -20°C (-4°F) with minimal scatter. The best fit trendlines corresponding to the yield strength increases of this data set are logarithmic functions and are included in the figure for the two tested temperatures.

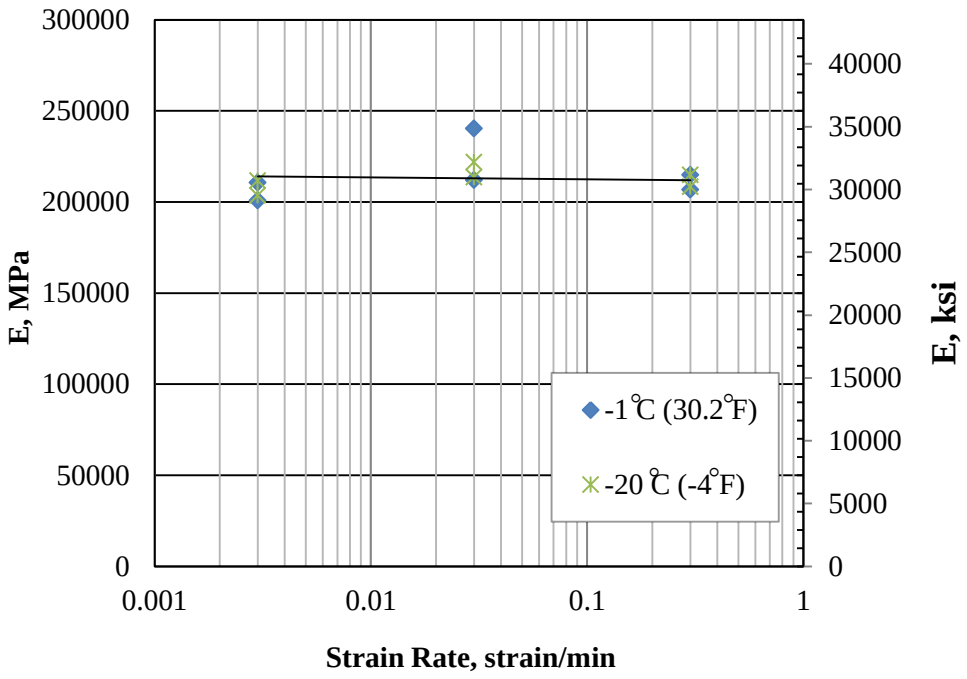

Figure 6-9: Modulus of elasticity vs. strain rate at -1°C (30.2°F) and -20°C (-4°F)

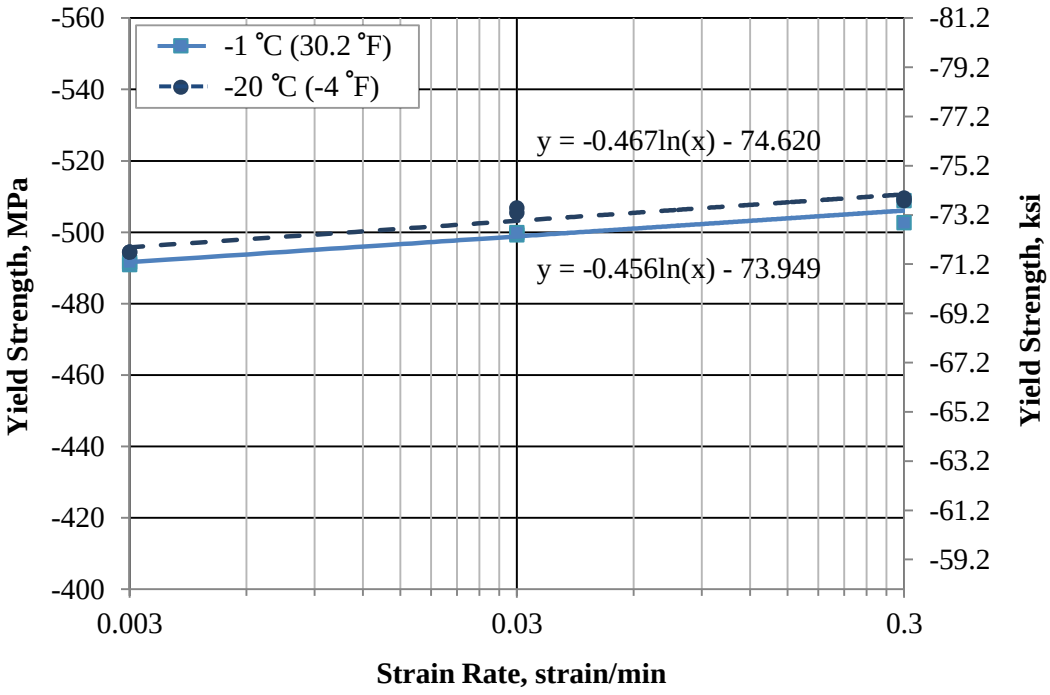

Figure 6-10: Effects of strain rate on the yield strength of A706 mild steel reinforcement at -1°C (30.2°F) and -20°C (-4°F)

From the presented data, it appears that the yield strength increases are a function of strain rate and temperature as shown by the slight variation in trendline slope, a 2.5% increase from -1°C (30.2°F) to -20°C (-4°F). This observation is consistent with that of Filiatrault and Holleran (2001, 2002) for CSA G30.16 steel where a larger range of temperature was examined.

Onset of Strain Hardening

The effects of strain rate upon the onset of strain hardening were also examined and are expressed in Figure 6-11. Under the strain rate and temperature conditions previously mentioned, the yield plateau length (as previously defined) dissipated at an average of 0.00084 strain (or by 34.7 percent) as the strain rate was increased from 0.003 to 0.3 /min at both -1°C (30.2°F) and -20°C (-4°F). The scatter for this portion of the study was relatively high due to the high yield plateau length dissipation (see Figure 6-12), making the yield plateau length parameter harder to quantify.

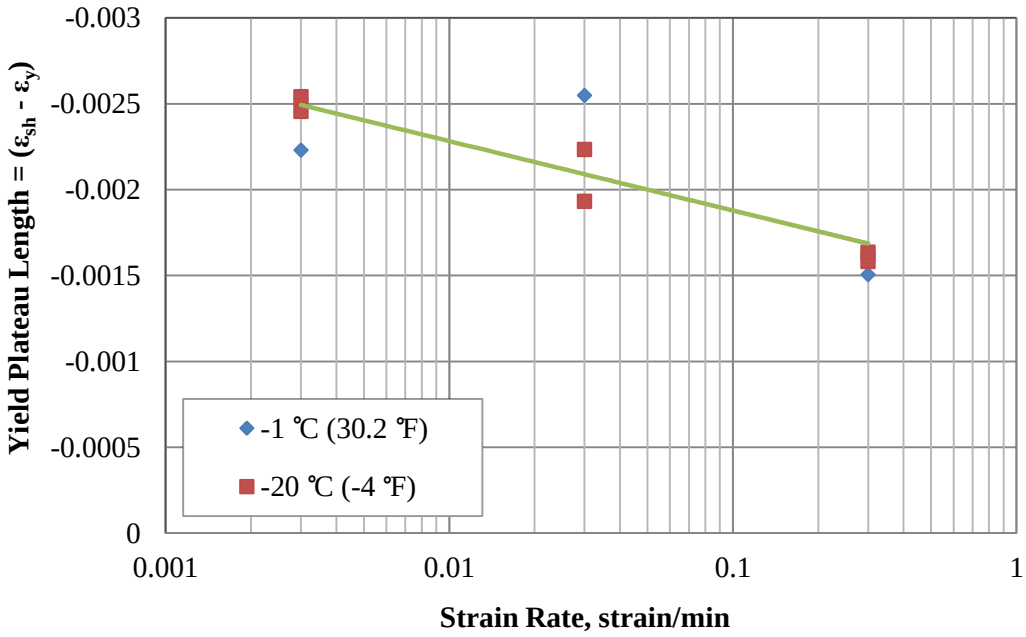

Figure 6-11: Effects of strain rate on the yield plateau length of A706 mild steel reinforcement at -1°C (30.2°F) and -20°C (-4°F)

At the highest strain rate of 0.3 /min., it was necessary to define ε_{sh} as the minimum stress following the first peak above 500 MPa (72.5 ksi). In this case, the yield plateau length appears to be completely dissipated.

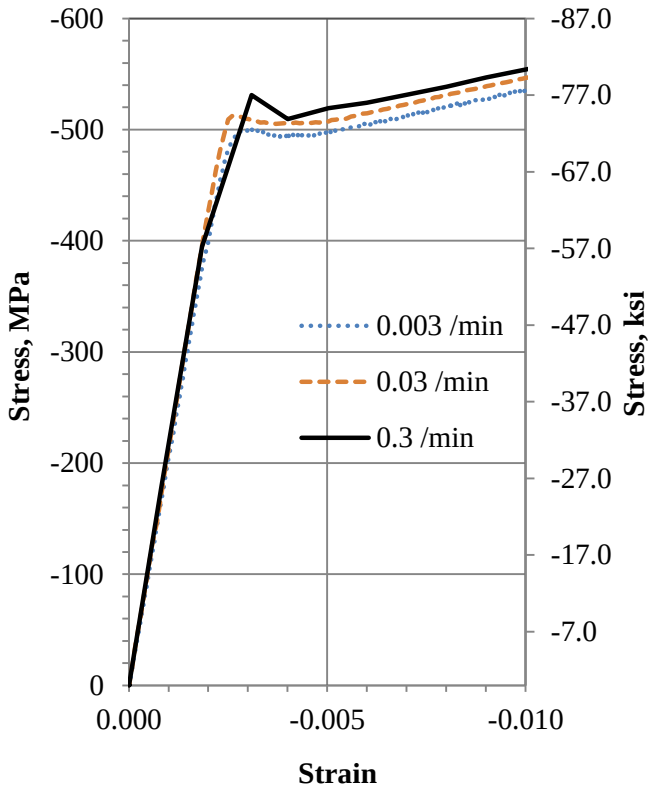

Figure 6-12: Dissipation of yield plateau length due to strain rate of a milled #8 A706 mild steel reinforcing bar at -20°C (-4°F)

Ultimate Tensile Strength

As depicted in Figure 6-13, increasing the strain rate from 0.003 to 0.3 /min. caused an increase of around 1.67 percent (13.79 MPa or 2 ksi) in the ultimate tensile strength of the milled 25 mm (1.0 in.) rebar specimens at temperatures of -1°C (30.2°F) and -20°C (-4°F) with minimal scatter. The best fit trendlines corresponding to the ultimate tensile strength increases of this data set were logarithmic as indicated in the figure for the two tested temperatures.

From the presented data, it appears that the ultimate tensile strength increases with increasing strain rate and temperature as shown by the variation in trendline slope, a 17% increase from -1°C (30.2°F) to -20°C (-4°F). This observation is consistent with CSA G30.16 steel where a larger temperature range was examined (Filiatrault and Holleran 2001, 2002).

Ultimate Tensile Strain

Varying the strain rate caused no significant change in the ultimate strain when varying the strain rate from 0.003 to 0.3 /min. at -1°C (30.2°F) and -20°C (-4°F). For all practical purposes,

the ultimate strain may be considered independent of cold temperature and strain rate within the limits of this study.

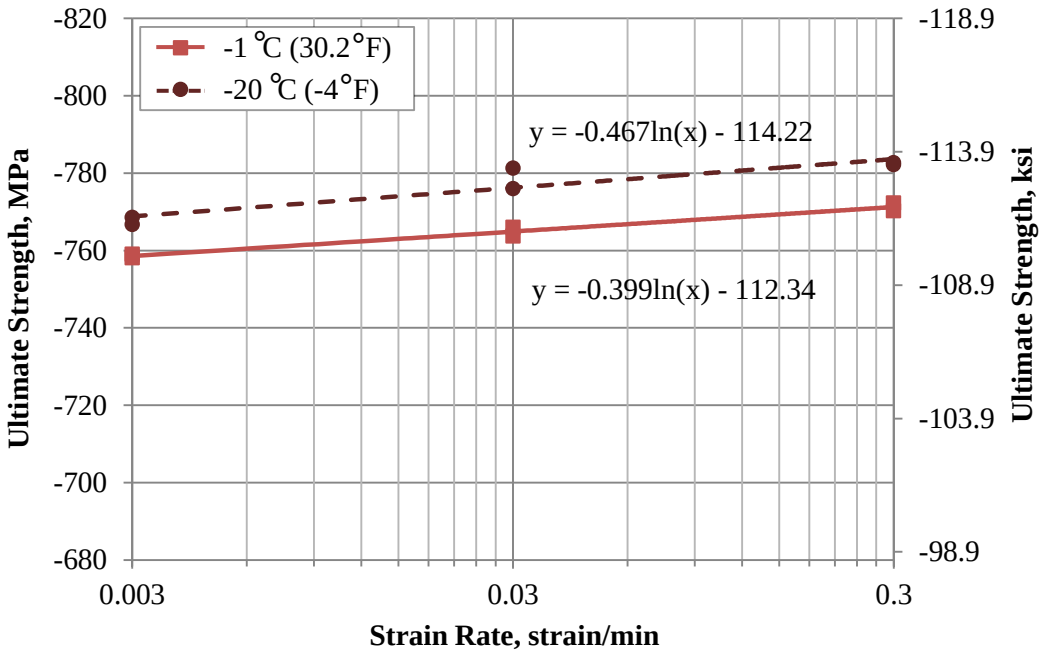

Figure 6-13: Effects of strain rate on the ultimate strength of A706 mild steel reinforcement at -1°C (30.2°F) and -20°C (-4°F)

6.3.4 Comparison with Previous Recommendations

Figure 6-14 illustrates the mean yield and ultimate tensile strength increases established for A706 mild steel as a function of cold temperature in the current study with the previously recommended trends. Although Sloan (2005) presented no trendlines, Montejo et al. (2008) at North Carolina State University (NCSU) presented a recommendation for yield and ultimate tensile strength variations using the data of both Filiatrault and Holleran (2001, 2002) and Sloan (2005), which is included in this comparison.

As previously stated and as shown in the Figure 6-14, when the temperature was reduced, both the yield and ultimate strengths were found to increase in a polynomial fashion for the A706 mild steel specimens in this study. This is similar to the trends reported for A572 steel by Bruneau et al. (1997), but dissimilar from the linear trends observed for CSA G30.16 steel by Filiatrault and Holleran (2001, 2002) and the recommendation by Montejo et al. (2008).

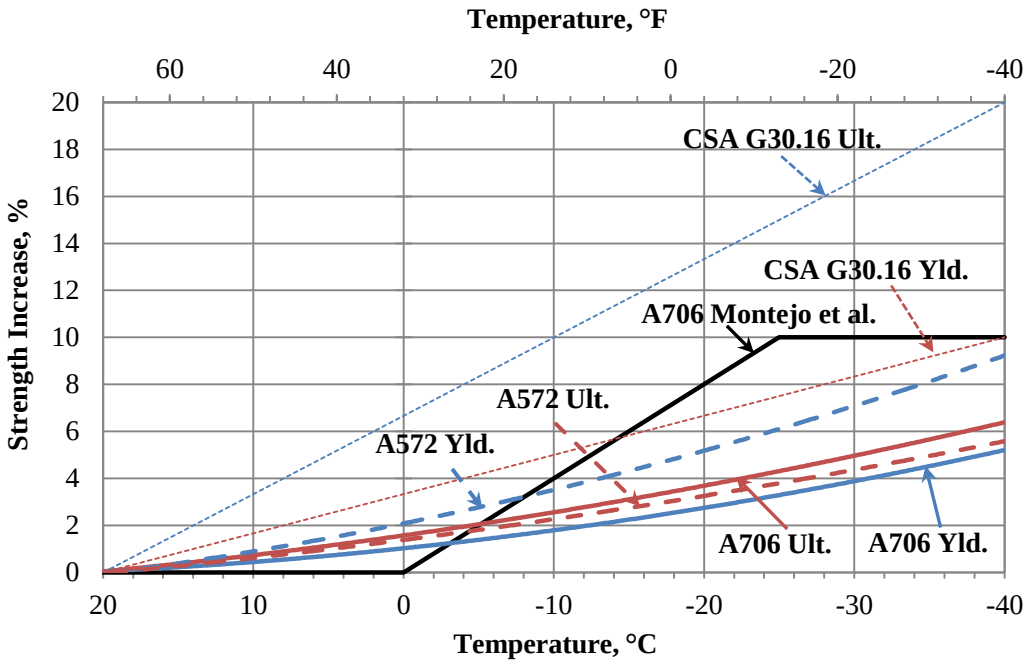

Figure 6-14: Comparison of proposed A706 temperature effects to those found in the literature for A572, CSA G30.16, and A706

The increase in magnitude of the yield and ultimate tensile strengths due to decreasing temperature observed for this study are generally less than previous recommendations with the exception of the ultimate strength that was reported for A572 steel by Bruneau et al. (1997). The impact of lowering the temperature from 20°C (68°F) to -40°C (-40°F) had a greater impact on the ultimate strength of A706 mild steel than the yield strength. This is opposite to the trend reported by Bruneau et al. (1997), Filiatrault and Holleran (2001, 2002), Sloan (2005) and Montejo et al. (2008). Finally, an increase in the yield and ultimate tensile strength for A706 was observed before reaching 0°C (32°F). This observation is consistent with previous research except that recommended by Montejo et al. (2008).

6.3.5 Effects of Cyclic Loading

The initial cyclic tests, coinciding with the path previously provided in Table 6-1, experienced two challenges that needed to be addressed. First, a "noise" phenomenon occurred in the extensometer causing recorded strains to oscillate. Changing the parameters of the extensometer that controlled the data accuracy and the rate of data collection alleviated this challenge. Second, global buckling occurred before reaching the target compressive strains of

around 2 percent. In an attempt to avoid this problem, all target compressive strains were modified to 0 percent strain. As shown in Figure 6-15, global buckling still occurred at a compressive stress of around 398.5 MPa (57.8 ksi). The buckling observed was likely due to the length, 0.9144 m (3 ft), and diameter to length ratio, 1/36, that was required for each specimen to be tested with the MTS grips positioned outside of the environmental chamber (see Figure 6-4).

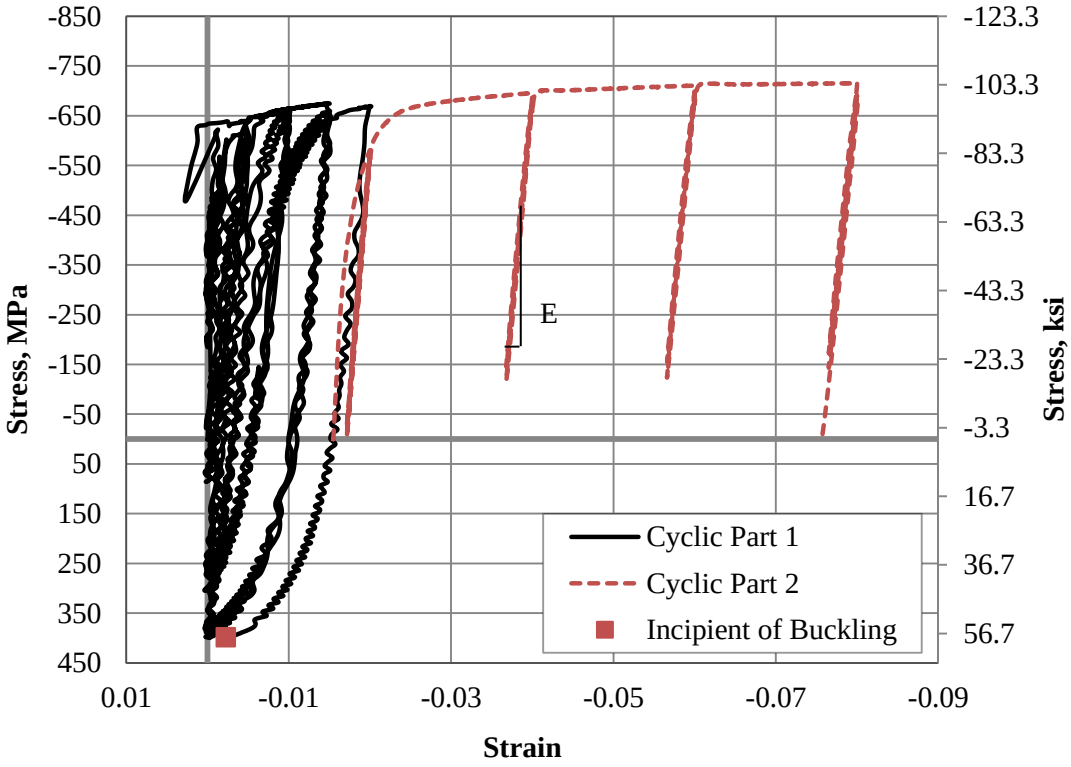

Figure 6-15: Initial cyclic buckling problem for A706 mild steel reinforcement

Because the specimens could not be loaded to 0 percent strain, it was decided to unload the specimens from the target tensile strains to low compressive stresses. To aid in determining the strains corresponding to these low compressive stresses, the buckled sample was straightened and further tested as shown in Figure 6-15. The modulus was estimated from the unloading portion of each test cycle via a best fit trendline in order to extrapolate the strains that would attain a 0 MPa (0 ksi) compressive stress. The modified loading path is compared with the planned loading path in Figure 6-16.

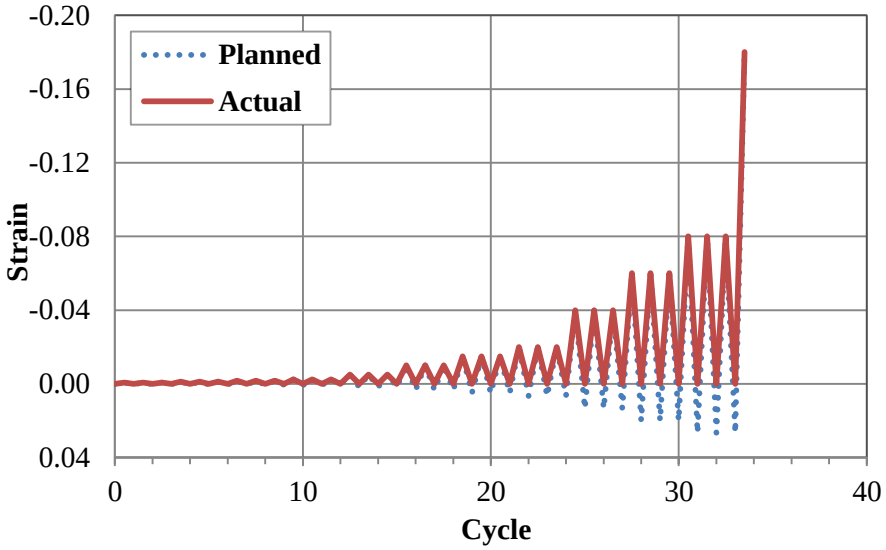

Figure 6-16: Comparison of planned and actual loading path used for cyclic testing

Figure 6-17 and Figure 6-18 show that the possible cyclic loading path, given the MTS and specimen length constraints, resulted in similar findings to monotonic testing for both -1^{0}C (30.2^{0}F) and -20^{0}C (-4^{0}F). For any given strain, similar stresses were attained except within the yield plateau region. No clearly defined onset of strain hardening was observed for the steel coupons subjected to cyclic loading. Furthermore, the ultimate tensile strain was unaffected by the performed cyclic loading when compared to the monotonic specimens.

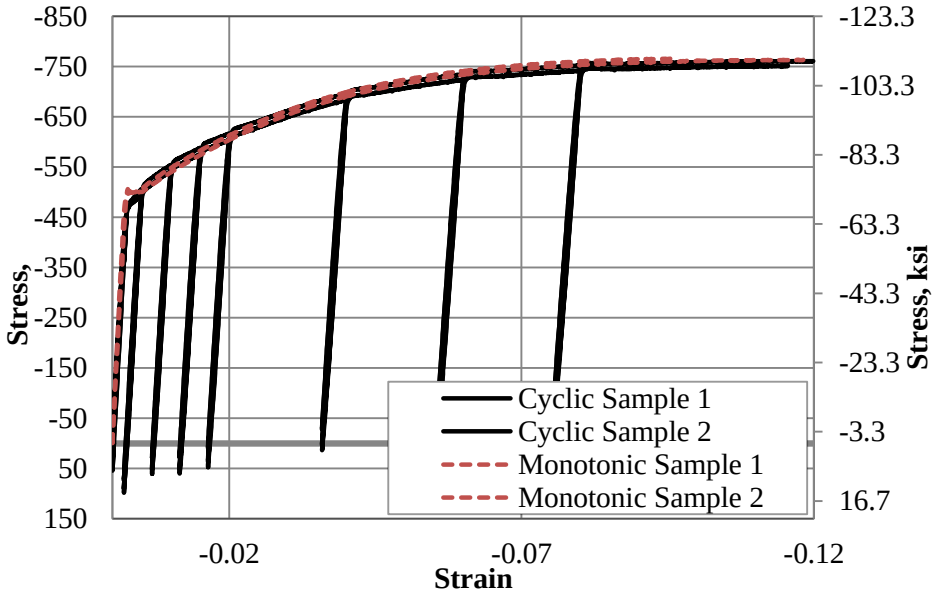

Figure 6-17: Effects of cyclic loading on stress-strain behavior of A706 mild steel reinforcement at -1°C (30.2°F) and at 0.03 /min.

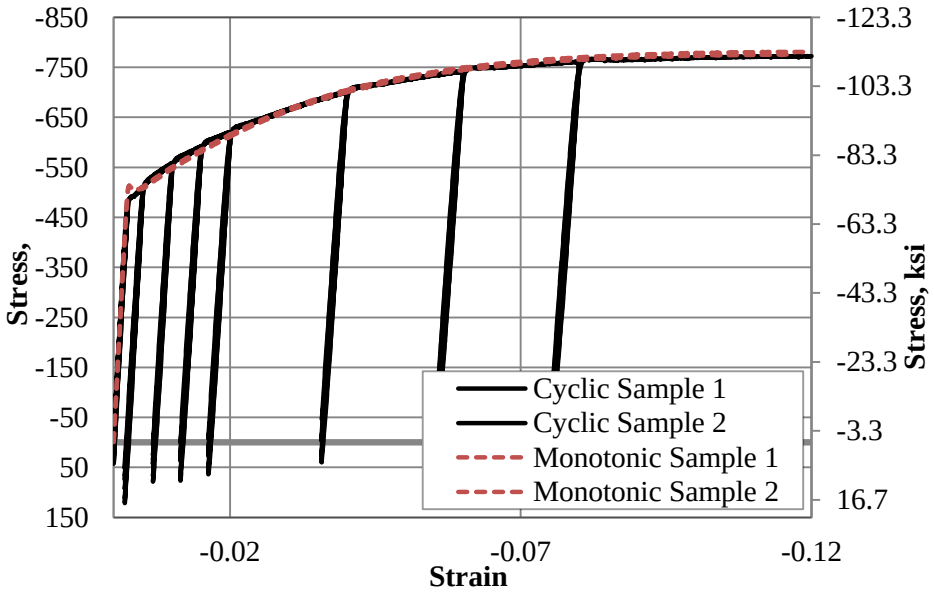

Figure 6-18: Effects of cyclic loading on stress-strain behavior of A706 mild steel reinforcement at -20°C (-4°F) and at 0.03 /min.

6.3.6 Analysis Model

Dodd and Restrepo-Posada (1995) have presented a typical model for adequately defining the stress-strain curve of mild steel, which includes an elastic, perfectly plastic, and strain-hardening behavior of the material as in Figure 6-5. To correctly define the strain-hardening region for a given cold temperature, a representative point along the strain hardening curve, (f_x, ε_x), is required in addition to Eqs. (6-1) and (6-3). The intermediate strain chosen for A706 mild steel was 3 percent. For simplicity, a linear combination of the yield and ultimate strength increase equations (i.e., Eq. (6-1) and Eq. (6-3) were used in conjunction with the Dodd and Restrepo-Posada model (1995) to create the following equation:

$$\Delta f_{0.03}(\%) = \left[3 * \Delta f_y(\%) + \Delta f_{su}(\%)\right]/4 \qquad (6\text{-}5)$$

Eq. (6-5) represents the best linear combination of Eq. (6-1) and Eq. (6-3) for the recorded data and is valid between the tested temperature range of 20°C (68°F) to -40°C (-40°F). The comparison of the theoretical and measured stress-strain curve is presented in Figure 6-19, where the proposed yield, 0.03 strain, and ultimate strength increase equations were used. It is seen that the proposed equations make the Dodd and Restrepo-Posada material model correlate well with the measured data obtained for the 19 mm (0.750 in.) milled samples. A more detailed

comparison between the theoretical and measured stress-strain curves for each temperature observed in this study can be found in the appendix.

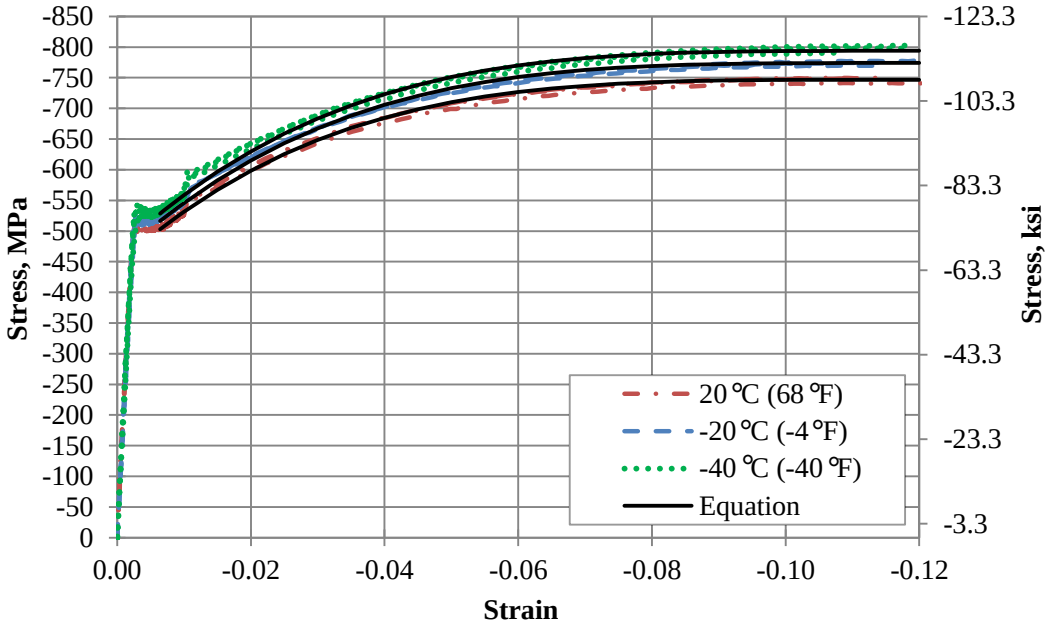

Figure 6-19: Validation of proposed temperature effect strength increase equations for A706 mild steel reinforcement

In lieu of test data, Table 6-4 may be used to assist in identifying the stress-strain behavior of A706 Grade 60 mild steel reinforcement at warm temperatures. This table was created from the previously mentioned monotonic testing of this section by scaling all stresses proportionally to achieve a yield stress of 60ksi (i.e., f_y = 60ksi).

Table 6-4: Adjusted parameters to define the stress-strain behavior of A706 mild steel reinforcement at warm temperatures

Parameter	Value
f_y [MPa (ksi)]	413.69 (60.00)
E_s [MPa (ksi)]	205,905 (29,864)
ε_{sh}	0.007115
$f_{0.03}$ [MPa (ksi)]	535.41 (77.65)
f_{su} [MPa (ksi)]	621.81 (90.19)
ε_{su}	0.12

6.4 Recommendations and Conclusions

This chapter has presented an investigation on the effects of cold temperature, bar size, strain rate, and cyclic loading on the behavioral changes of ASTM A706 Grade 60 mild steel

reinforcement for the purposes of improving the design of structures that experience seasonal freezing. The conclusions drawn from this study and some recommendations are presented below:

- A706 mild steel experienced an increase in yield and ultimate tensile strengths of 5.1 and 6.3 percent, respectively, when the temperature was reduced from 20°C (68°F) to -40°C (-40°F). These increases varied in a non-linear manner. The recommended equations for defining these increases are presented in Eqs. (6-1) and (6-3).
- The magnitude of temperature increases for the yield and ultimate tensile strengths of A706 mild steel are generally lower than that suggested by previous research on other types of steel. They are also lower than the maximum increases observed in Sloan's research (2005) for A706 steel.
- The impact of temperature on the ultimate tensile strength is greater than that of the yield strength, which is opposite to the trends of the previous research presented in this paper on other steels.
- Material behavior is altered even at temperatures higher than 0°C (32°F). An increase of around 1.0 and 1.6 percent for the yield and ultimate tensile strengths were observed between 20°C (68°F) and 5°C (41°F).
- The impact of changing the strain rate from 0.003 to 0.03 /min showed a 3 percent increase in the yield strength and 1.67 percent increase in the ultimate tensile strength at both -1°C (30.2°F) and -20°C (-4°F).
- The yield plateau generally shortened as the strain rate increased and completely disappeared upon reaching a strain rate of 0.3 /min. A total dissipation of 0.00084 strain (34.7 percent) was experienced in the yield plateau length when varying the strain rate from 0.003 /min. to 0.3 /min. This reduction appeared to be dependent upon temperature, but should be further researched for validation.
- The modulus of elasticity and ultimate tensile strain of A706 were not significantly affected by temperature and strain rate.
- Although a complete conclusion on the effects of bar size could not be made due to the use of two bar sizes, it appeared that bar size may affect the magnitudes of the yield and ultimate tensile strength increases with larger changes occurring in the smaller bar size.

- Although a complete conclusion on the combined effects of strain rate and temperature could not be made due to the scope limits of this study, strength increases associated with strain rate changes may be dependent upon the testing temperature used. It appeared that a slightly greater strength increase occurred for specimens at a lower temperature when varying the strain rate from 0.003 /min to 0.3 /min.
- The cyclic loading, consisting mainly of inelastic tensile strains and zero compressive strains, led to no change in the cold temperature effects of parameters from that established from the monotonic testing except for the exclusion of the onset of strain hardening. It is recommended that the initially proposed cyclic loading path, involving both inelastic compression and tensile strains, be performed on a higher diameter/length ratio so that buckling does not occur and more useful data can be collected.

CHAPTER 7: SOIL BEHAVIOR AT FROZEN TEMPERATURES

7.1 Introduction

During the design process of columns supported on CIDH shafts, defining the properties of soil surrounding the foundation shaft is of extreme importance. The response of the soil becomes even more important in the frozen state as it will alter the lateral response of the system significantly. This is due to the frozen state causing a significant increase in the stiffness of the soil thus potentially making the structural components of the system to resist additional load while displacing less (see Section 2.3). In order to better understand the changes in soil stiffness, an experimental study was conducted on five types of soil common to the State of Alaska to examine the effects of frozen temperatures. The following sections present details of the experimental testing completed at Mueser Rutledge Consulting Engineers (MRCE) in New York and the obtained key test results.

7.2 Testing Matrix

Prior to any experimental testing being performed on soil, the types of soil to be tested were defined and representative samples were obtained from within the State of Alaska. The completion of this task, required an examination of the types of soil common to the state and the soil properties that they may have in the in-situ condition (see Section 7.2.1). After defining the five most common types of soil present within the state at bridge sites, a testing matrix was constructed so that the effects of multiple variables could be examined (see Section 7.2.2) and an appropriate amount of soil samples for testing were obtained.

7.2.1 Soil Selection

For the purposes of the study, five soil types were selected by examining population and bridge distributions within the state. Population trends revealed that approximately sixty percent of Alaskan residents live within the south-central portion of the state, around Anchorage (State of Alaska 2006). An additional twenty percent of the population resides near or in the city of Fairbanks and the city of Juneau (State of Alaska 2006). Comparing bridge and population distributions led to the conclusion that a majority of the critical bridges were located within the aforementioned areas (i.e., Anchorage, Fairbanks and Juneau). The five main soils selected for the project were obtained from the areas where population and bridge distributions coincided.

By examining the Major Land Resource Areas (MLRA) as determined by the United States Department of Agriculture (USDA) in conjunction with the Natural Resources Conservation Service (NRCS), the soils, annual temperature range and moisture range were determined using the Agriculture Handbook No. 296 (USDA, NRCS 2006). Furthermore, the temperature ranges were expanded using information available from the ENSR group at the University of Alaska at Fairbanks (2002) to identify the full range of temperatures that the soils experience seasonally. Upon discussing the initial soil selections with the Chief Engineering Geologist for the State of Alaska, the soil selections were modified using the paper entitled *"Physiographic Divisions of Alaska"* (Wahrhaftig, 1965) and the technical knowledge of the geologist. Although this study provides information regarding the saturated moisture content of the soils, it is noted that not all samples may be saturated depending on the location and time of year sampled. An average range of the different soil dry densities was provided to better improve the soil description prior to sampling. The final results of the soil selection, expected seasonal temperature range, saturated moisture content and dry soil density are shown in Table 7-1.

Table 7-1: Five main soils types and expected temperature and moisture content ranges

Soil Type	Soil Description	Temperature in °C (°F)	Saturated Moisture Content	Dry Soil Density in kN/m^3 (lb/ft^3)
Alluvial Deposits	Well graded to well sorted, fine to coarse-grained (fan deposit or flood plain deposit)	35 to -30 (95 to -22)	10% - 50%	10 to 30 (63.7 to 191.0)
Glacial Till / Ice Contact Deposits	Well graded; very dense	35 to -30 (95 to -22)	10% - 50%	10 to 30 (63.7 to 191.0)
Estuarine / Lacustrine	silty/clayey/organic(?) ; soft/loose	35 to -30 (95 to -22)	15% - 30% / 90% - 150% (Silty,Clayey/Organic)	8 to 20 (50.9 to 127.3)
Glacial Outwash	coarse-grained; loose to dense	35 to -30 (95 to -22)	10% - 50%	10 to 30 (63.7 to 191.0)
Loess	Silty	35 to -30 (95 to -22)	15% - 30%	10 to 17 (63.7 to 108.2)

7.2.2 Testing Plan

Using the information provided in Table 7-1 it was decided that a set of soil samples from Alaska should be tested at the following four different soil temperatures to understand the impact of temperature on soils: 20°C, -1°C, -10°C, -20°C. Frozen soil tests were performed using an

apparatus specifically designed for this purpose to determine initial, secant and unload/reload moduli, shear strength, and Poisson's ratio. To determine these properties, twenty tests with three samples per test (i.e., a total of sixty samples) were completed. In addition to the testing for material properties with variable temperature, additional testing was performed at 20°C and -1°C under repeated loading and unloading with three different loading rates. The additional testing used a minimum of six tests with two samples per test (i.e., a total of twelve samples) to examine strain rate effects and cyclic loading on frozen soil. Table 7-2 summarizes the soils testing performed as part of this investigation.

Table 7-2: Summary of Completed Soil Tests

Soil Type	Samples Tested	Temperature in °C (°F)	Moisture Content, %	Moist Unit Weight in kN/m^3 (lb/ft^3)	Loading Rate
I: Alluvial Deposits – well graded to well sorted, fine to coarse-grained (fan deposit or flood plain deposit)	3	-22.8 (-9)	30	20 (127.3)	LR1
	3	-10 (14)	30	20 (127.3)	LR1
	3	-1 (30.2)	30	20 (127.3)	LR1
	3	20 (68)	30	20 (127.3)	LR1
	3	-20 (-4)	30	10 (63.7)	LR1
	3	-20 (-4)	30	30 (191.0)	LR1
	3	-20 (-4)	15	20 (127.3)	LR1
	3	-20 (-4)	45	20 (127.3)	LR1
II: Glacial Till/Ice Contact Deposits – well graded, very dense	3	-20 (-4)	30	20 (127.3)	LR1
	3	-1 (30.2)	30	20 (127.3)	LR1
	3	20 (68)	30	20 (127.3)	LR1
III: Estuarine/Lacustrine – silty/clayey/organic(?), soft/loose	3	-20 (-4)	22	14 (89.1)	LR1
	3	-1 (30.2)	22	14 (89.1)	LR1
	3	20 (68)	22	14 (89.1)	LR1
IV: Glacial Outwash – coarse-grained – loose to dense	3	-20 (-4)	30	20 (127.3)	LR1
	3	-1 (30.2)	30	20 (127.3)	LR1
	3	20 (68)	30	20 (127.3)	LR1
V: Loess - silty	3	-20 (-4)	25	14 (89.1)	LR1
	3	-1 (30.2)	25	14 (89.1)	LR1
	3	20 (68)	25	14 (89.1)	LR1
Total Tests	60				
Additional Testing – Repeated Loading and Unloading under Variable Loading Rates					
I: Alluvial Deposits	2	-1 (30.2)	30	20 (127.3)	LR2
	2	-20 (-4)	30	20 (127.3)	LR2
	2	-20 (-4)	30	20 (127.3)	LR3
	2	-1 (30.2)	30	20 (127.3)	LS1
	2	-20 (-4)	30	20 (127.3)	LS1
	2	-20 (-4)	30	20 (127.3)	LS2
Total Tests	12				

LR1 = 1% per min LR2 = 0.1% per min LR3 = 10% per min LS1 and LS2 = Cyclic loading

Table 7-2 demonstrates that most of the testing was performed in a monotonic manner at a rate of 1% strain per minute. As can be seen, the test matrix included a plan to examine the effects of density as well as moisture content on the behavior of frozen soil. In addition to being able to account for these variables, the effect of loading rate was taken into consideration within the additional testing section by performing monotonic testing at 0.1% strain per minute and 10% strain per minute. This information allowed for a better prediction of the soil strength during different types of loading in the frozen state. The final portion of the test matrix showed that cyclic loading of the specimens was used to determine an unloading/reloading secant modulus for comparison with the initial modulus found for the soil.

The cyclic loading process was performed at two different loading rates, 1% and 10% strain per minute, to examine the effects of loading rate. The overall testing pattern of the cyclic test consisted of loading to the set target strain and then fully unloading the specimen prior to proceeding to the next target strain. Once a strain of 1% was reached for the first time in the loading pattern, the effects of reloading to a certain strain level were examined by reloading to that strain point three times prior to proceeding to the next target strain. The pattern selected for the cyclic testing was based on observations made of the stress-strain curves obtained from the monotonic triaxial testing on the alluvial soil specified in Table 7-2. The final pattern selected for the testing is provided in as Table 7-3.

Table 7-3: Target strains for cyclic loading of Type I: Alluvial Soil at strain rates of 1% per minute and 10% per minute

Target Strain (%)	Loading Cycles (#)
0.25	1
0.5	1
0.75	1
1.0	3
1.5	3
2.0	3
3.0	3
4.0	3
6.0	3
8.0	3
10.0	3
12.5	3
15.0	3

7.3 Testing Procedures

Using the information provided in Table 7-1 and Table 7-2, a number of samples were collected both disturbed and undisturbed from the State of Alaska courtesy of the AUTC and the ADOT&PF. These samples were then shipped to New York for testing purposes at MRCE where the appropriate test setup was already in place for handling frozen soils. Although ASTM D7300 – 06 states that the soils should not be artificially prepared in a laboratory setting due to the variation in ice content and strength (ASTM Standard D7300, 2006), this was not possible to perform for our testing. The disturbed sampling, however, was not expected to be an issue with the laboratory results as the authors believe this process would be more representative of multiple freeze thaw cycles changing the soil structure. In addition, this approach made it easier for samples to be collected from actual bridge sites since the collecting organizations typically perform construction in summer months when the ground is in an unfrozen state. The following sections describe in detail the process used for preparing the specimens, the testing apparatus setup and the loading protocols used in monotonic and cyclic testing.

7.3.1 Specimen Preparation

Once the disturbed samples arrived at MRCE, the soils were separated into the main groupings proposed in Table 7-1 and then kept in plastic containers to maintain consistent moisture contents until samples for testing purposes were made. The next step in preparing the multiple samples was to create the specimen that would be placed into a modified triaxial chamber as presented in Section 7.3.2. These specimens were cylindrical in nature and were created by loosely placing the soil which passed a #4 sieve into a mold supported on a hard surface and a consistent effort was used to compact the soil (see Figure 7-1). The effort consisted of striking a metal plunger on top of the soil a set number of times with a hammer as shown in Figure 7-1b. For each specimen, the process of compaction was done in three lifts with the same amount of blows per lift to ensure that the soil shaft would have a constant density over the length of the shaft. Upon completion the specimens and molds were placed inside a freezer to immediately begin the freezing process if needed. Unfrozen test specimens were tested immediately as no freezing was required and final preparations prior to testing were done in a similar fashion to the frozen specimens as described in the next paragraph.

Figure 7-1: Sample compaction process: (a) loosely placing soil in mold; (b) using a plunger to compact soil; (c) placing compacted soil and molds in storage freezer

Immediately prior to placing the specimen in the triaxial chamber, the sample was removed from the storage freezer for final preparation. These final preparations took place inside the testing room that was maintained at subzero temperatures to help keep the sample from warming prior to testing. The process began by extruding the frozen sample from the mold using standard practices, Figure 7-2a. After extrusion, the sample was reduced to the correct diameter of 50.8 mm (2 in.) using a split ring mold and trimmed with a saw as needed to get a consistent specimen with level ends. A 50.8 mm (2 in.) diameter specimen was needed so that the testing apparatus could typically reach an axial stress level of 27.6 MPa (4,000 psi). Once all trimming was completed, the specimen was measured and placed between the upper and lower loading plates and then covered with a neoprene membrane to protect the sample from contamination inside the testing chamber. At this point, the sample is ready for testing, Figure 7-2b, and the testing apparatus may be constructed around the specimen.

7.3.2 Specimen Setup in Chamber

In order to capture the changes in soil properties at subzero temperatures, a specially designed triaxial chamber was used. The chamber allowed for a liquid capable of maintaining frozen temperatures (i.e., antifreeze or salt water) to be circulated around the soil specimen thus creating an ideal temperature controlled environment for testing. This section discusses the testing apparatus shown in Figure 7-3 that was designed and used for testing of frozen soils at MRCE in New York City.

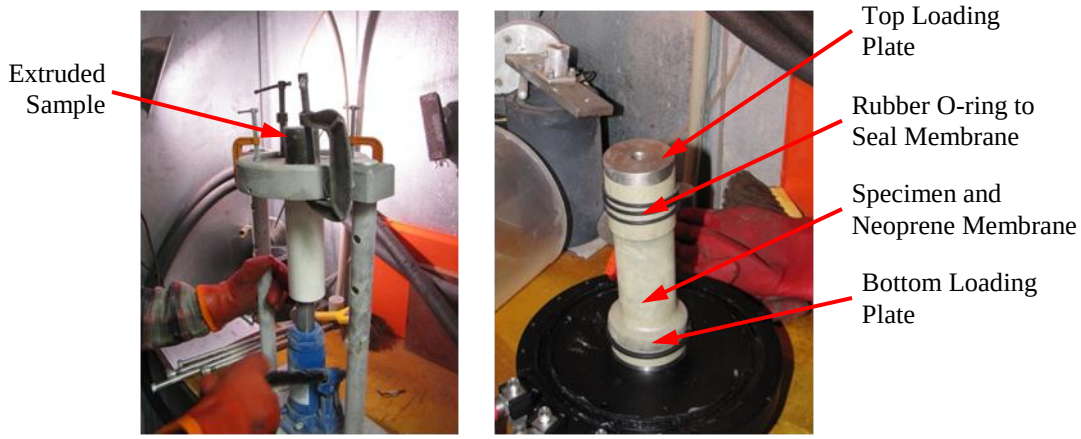

Figure 7-2: Final soil sample preparation: (a) extrusion of sample from mold; (b) fully prepped sample ready to be tested

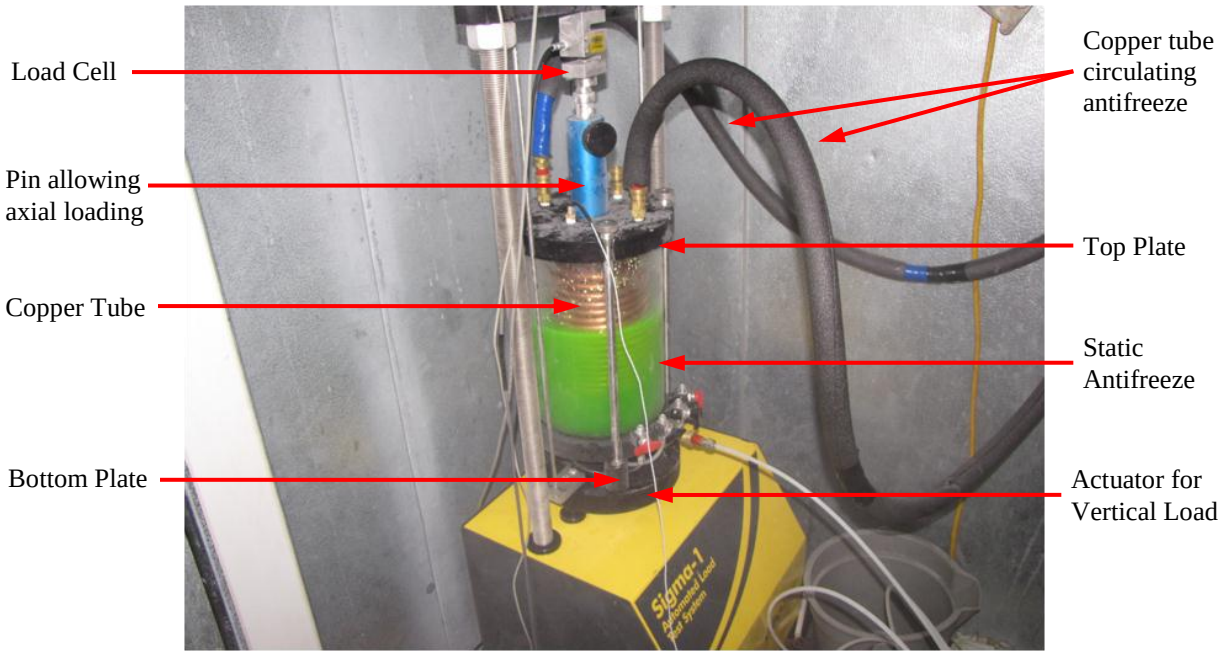

Figure 7-3: Modified triaxial chamber setup for testing of frozen soils at MRCE

The chamber, placed within a walk-in freezer, consists of a top and a bottom plate separated by a large diameter clear tube capable of sustaining a horizontal pressure. All interfaces were sealed using o-rings and vacuum seal grease such that any fluid within the chamber would be unable to leak out of the chamber when pressurized. The bottom plate was a rigid plate that created a surface for supporting the specimen as well as ports to put the static antifreeze into the

chamber. The top plate, on the other hand was designed such that an axial load could be applied to the specimen by lifting the entire chamber upwards without compressing the clear tube. In addition, the top plate was further modified to allow copper coils to be placed around the specimen that would constantly circulate cold antifreeze with a pump to maintain the temperature. The overall loading frame was a Sigma-1 automated load test machine capable of applying a 44.5 kN (10 kip) axial load to the sample.

7.3.3 Testing Process

After placing the specimen within the chamber depicted in Figure 7-3, sufficient time was permitted for the specimen to stabilize at the testing temperature within the chamber. The temperature of the specimen was monitored using a steel probe thermocouple that was placed directly in the center of the chamber and connected to a data acquisition system to continuously monitor the temperature. Upon reaching the desired temperature, the test system was activated through an external computer that would apply a consistent loading rate to the soil sample as specified in Table 7-2 and Table 7-3. Throughout testing the sample was in an unconsolidated, undrained state. During testing, the data acquisition system recorded the applied force and deformation to the sample. These values were then used to create a stress-strain curve similar to that shown in Figure 7-4 so that the critical parameters could be determined.

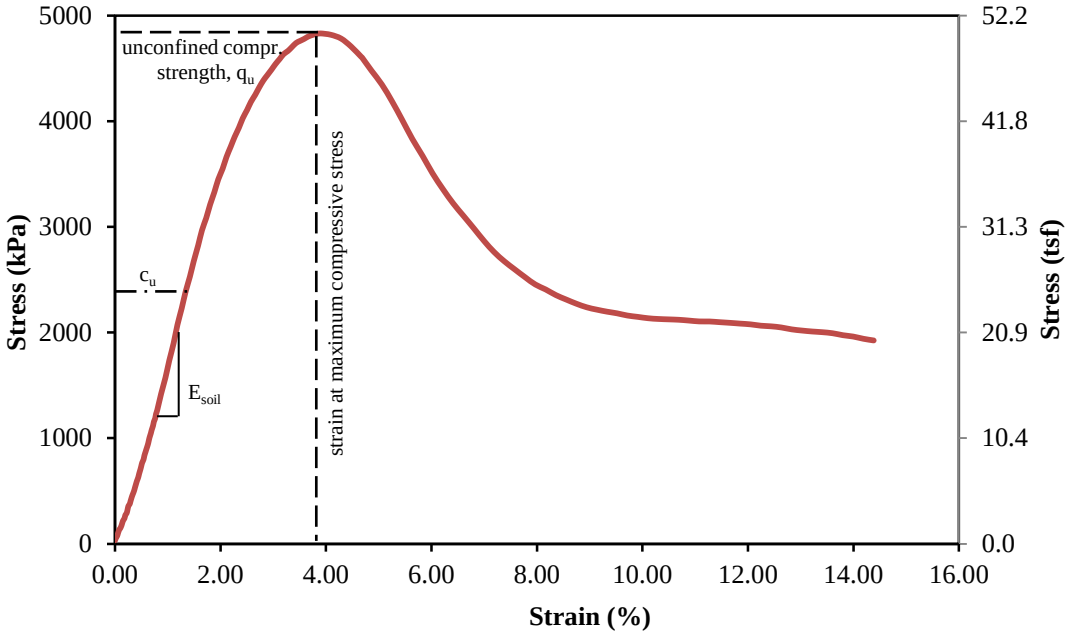

Figure 7-4: Experimental stress-strain curve for a Type I soil at -20 C (-4 F) and a 15% moisture content

7.4 Results

Upon completion of the experimental testing, the data was analyzed to examine trends within the data. The trends examined were on both a localized value to the different soil types as well as a side by side comparison of the different soil types in some instances for a better definition of the soil properties. The results of the different comparisons are provided in the following sections and are separated between the monotonic testing and cyclic testing.

7.4.1 Typical Results of Experimental Testing

Monotonic Testing

Figure 7-5 shows the typical stress-strain response of the Type I soil specified in Table 7-2 when subjected to a monotonic loading rate of 1% strain per minute and temperatures ranging from 20 °C (68 °F) to -22.8 °C (-9 °F). The results demonstrate that between the extreme testing temperatures the elastic modulus of the soil increased by a factor of 300, the ultimate compressive strength increased by a factor of 80 and the ultimate strain capacity decreased by 5%. The secant modulus to the undrained shear strength, the ultimate compressive strength and the ultimate strain capacity of the data in Figure 7-5 is listed in Table 7-4 to provide a numerical evaluation of the effects of temperature on the behavior of a Type I soil. Although the information provided in this section is for a Type I soil, these results are typical of the other soil types examined in this investigation. Additional information on the other data sets is provided in the following sections and Appendix D.

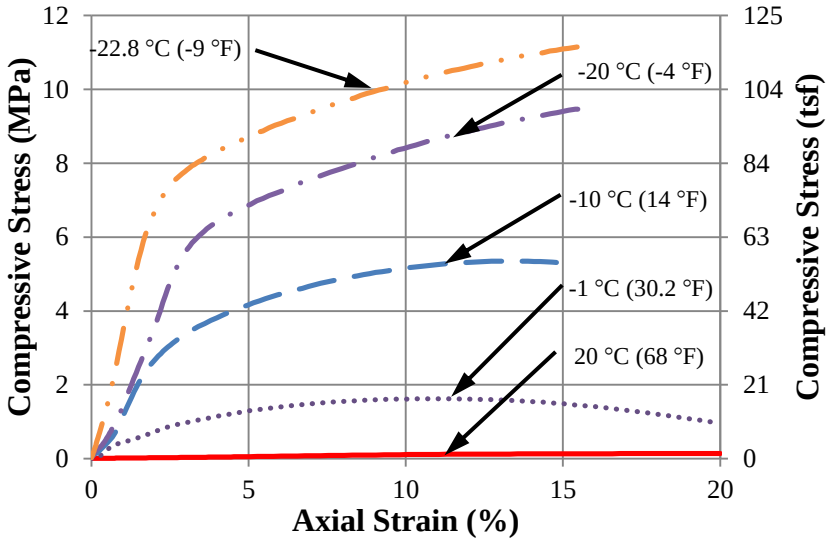

Figure 7-5: Stress-strain response of a Type I soil subjected to monotonic loading and temperatures between 20 °C (68 °F) and -22.8 °C (-9 °F)

Table 7-4: Numerical results of the Type I soil stress-strain curves depicted in Figure 7-5

Testing Temperature °C (°F)	E_{soil} MPa (tsf)	q_u MPa (tsf)	Strain at c_u %	Strain at q_u %	Strain at End of Test %
20 (68)	1.13 (11.82)	0.14 (1.47)	6.29	19.83	20.01
-1 (30.2)	36.01 (376.0)	1.63 (16.97)	2.24	10.82	20.01
-10 (14)	133.8 (1397.5)	5.35 (55.89)	1.97	13.11	14.79
-20 (-4)	190.1 (1985.6)	9.46 (98.83)	2.51	15.49	15.49
-22.8 (-9)	357.4 (3731.9)	11.15 (116.5)	1.58	15.49	15.49

Cyclic Testing

Figure 7-6 shows the typical response of the Type I soil tested under cyclic loading according to the sequence presented in Table 7-3 at a strain rate of 1% per minute in and temperatures of -1 C (30.2 F) and -20 C (-4 F). The results, similar to the monotonic testing, demonstrate that the modulus of elasticity increased by a factor of 8 and soil strength increase by more than a factor of 10 as the testing temperature decreased from -1 °C (30.2 °F) to -20 °C (-4 °F). Additionally, Figure 7-6 indicates that the unloading and reloading moduli were approximately the same as the initial loading modulus. The -1 °C (30.2 °F) test specimens, therefore, had a residual strain equivalent to 93% of the maximum strain reached during a given cycle, and the -20 °C (-4 °F) cyclic tests had a residual strain of 84% of the maximum. The results demonstrate an 80% degradation in compression strength upon repeated loading to a given strain level.

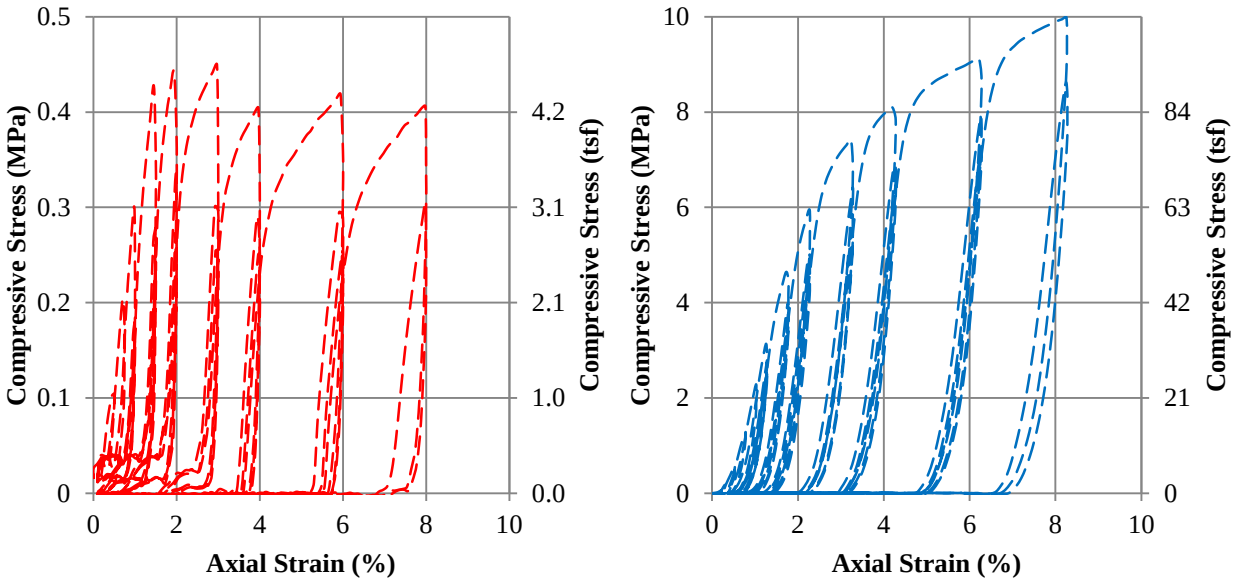

(a) -1 °C (30.2 °F) (b) -20° C (-9 °F)

Figure 7-6: Experimental cyclcic stress-strain response of a Type I soil

7.4.2 Summary of Monotonic Testing

Ultimate Compressive Strength

As a baseline of comparison, the ultimate compressive strength of the different soil specimens at the warm condition [i.e., 20 °C (68 °F)] was established first by taking the peak point of the typical stress-strain curves depicted in Figure 7-4 and averaging the results. These values are provided below in Figure 7-7, where it can be seen that the data varies depending on the type of soil being examined. The ultimate compressive strengths in the soils range from 14.25 kPa (0.15 tsf) to 145.5 kPa (1.52 tsf) with average density and moisture content as stated in Table 7-1.

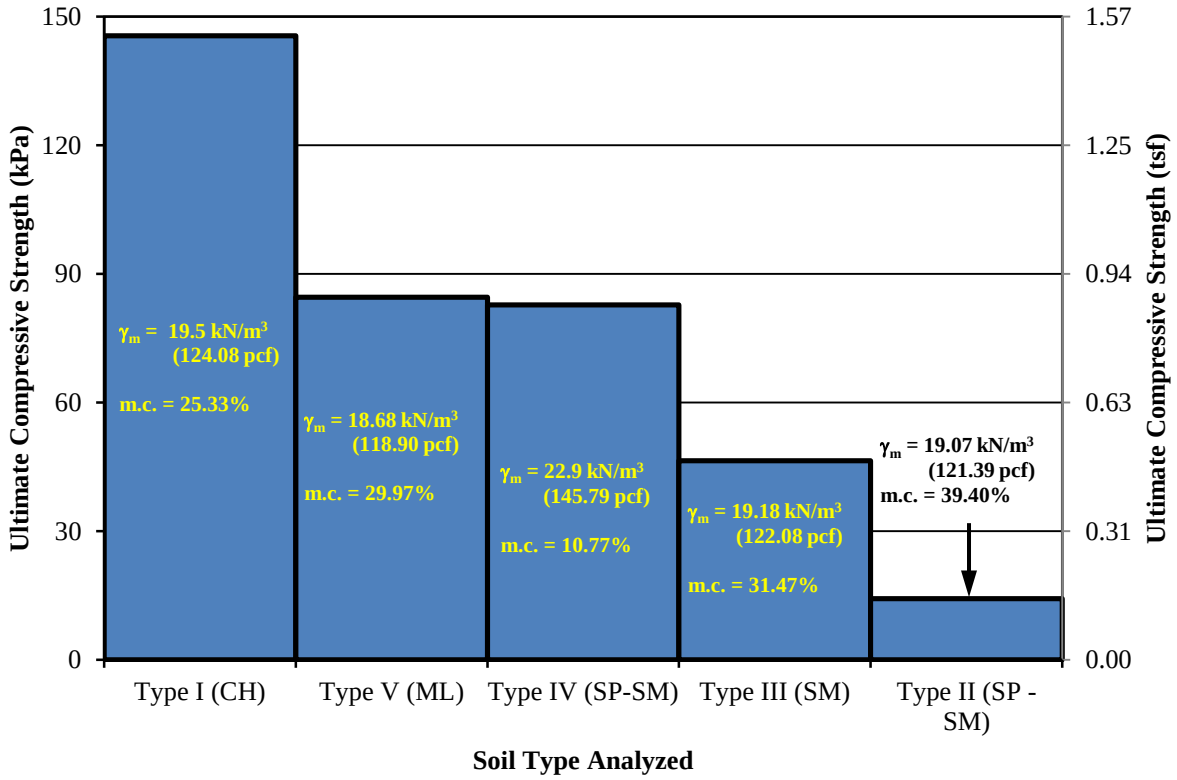

Figure 7-7: Failure strengths of analyzed soils at 20 °C (68 °F) [Note: 1 tsf = 95.8 kPa; 1 pcf = 0.157 kN/m^3]

Once the baseline values were established at the warm weather condition, a series of comparisons were made to examine the effects of cold temperatures on the ultimate compressive strength of the soil as this is an indirect measure of the undrained shear strength. The comparison was performed by defining a reference value based on the average ultimate compressive strength established at a cold temperature divided by the average ultimate

compressive strength at the warm temperature tests of 20 °C (68 °F). Using this reference value a series of charts were produced to examine the overall trends present within each type of soil. Figure 7-8 provided below shows the individual chart produced for the alluvial soil specified as Type I in the testing matrix. The other individual charts are provided in Appendix D of this report.

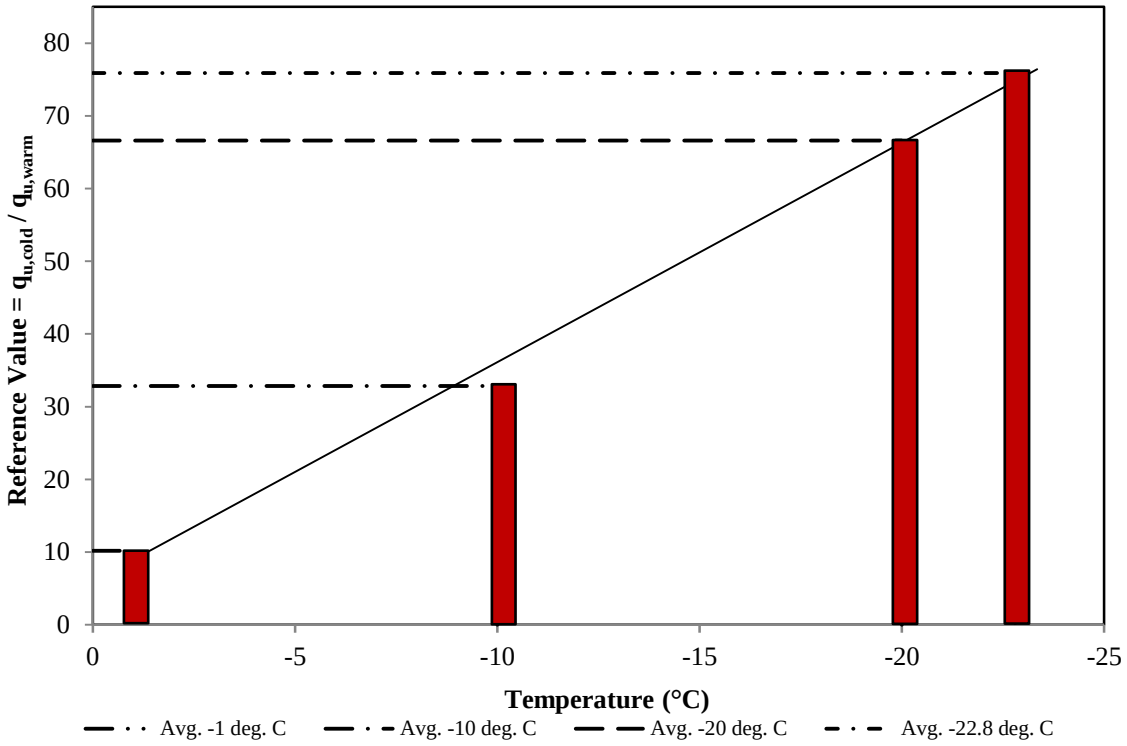

Figure 7-8: Increase in the ultimate compressive strength of a Type I soil with respect to warm temperature at 20 °C (68 °F)

Figure 7-8 demonstrates that as temperature decreases, the strength of the soil is going to increase in a linear manner in which the rate and magnitude of increase for each soil type varied depending on the type of soil examined. The importance of the temperature effects, however, stems from the fact that as the soil strength and stiffness increases (see Figure 7-5) the foundation and column shafts must begin to resist more of the lateral load being applied to the system. Also, the increased stiffness will cause an upward shift of the maximum moment location while decreasing the overall ductility of the SFSI system.

In addition to the individual graphs two additional figures were created for a side by side comparison of the data. These charts were done at -1 °C (30.2 °F) and -20 °C (-4 °F) for the multiple soil types since this is where the majority of the testing was performed. These charts

are provided here as Figure 7-9 and Figure 7-10. In Figure 7-9 the ultimate compressive strength of the Type IV soil was not provided as only a limited amount of material was obtained for this soil type.

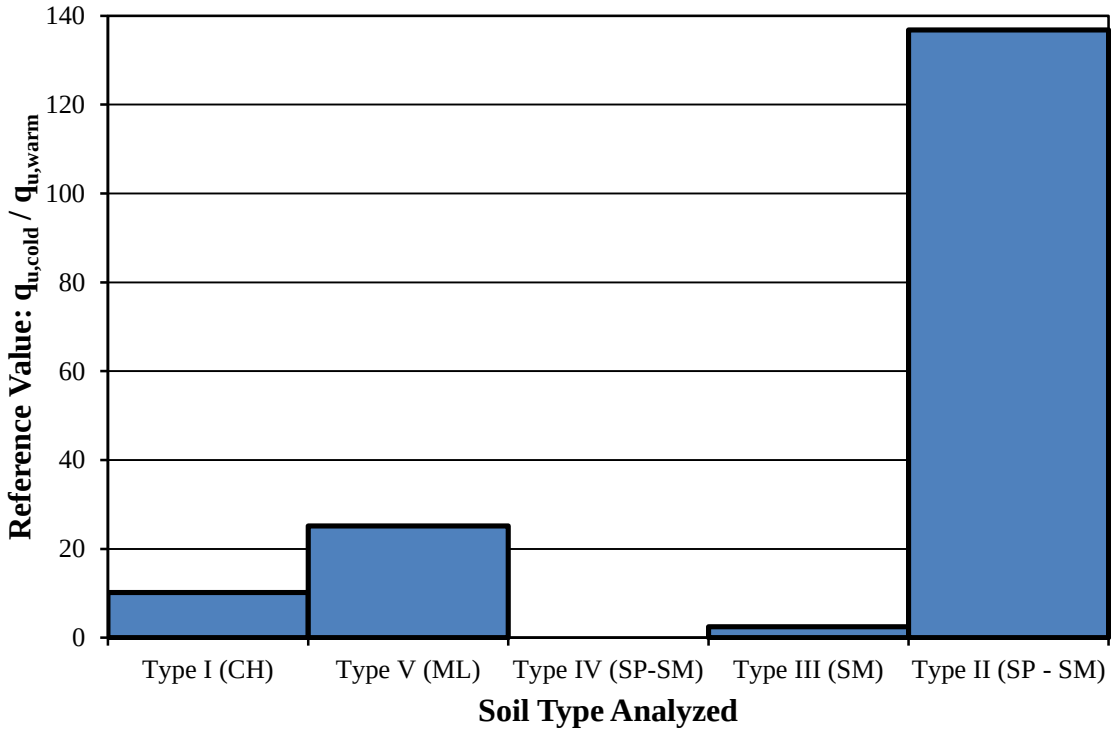

Figure 7-9: Increase in ultimate compressive strength of the five soil types specified in Table 7-2 tested at -1 °C (30.2 °F) with respect to the ultimate compressive strength at 20 °C (68 °F)

The data provided in the figures suggest that even a temperature near the freezing point of water significantly alters the ultimate compressive strength of the soil and continues to increase as temperature decreases. Although it appears that the relative increase in strength varies greatly between soil types, a closer examination of the data reveals that the ultimate compressive strength of the soils has a consistent increase as a function of temperature. That is to say, the magnitudes of strength in the frozen states are very similar to one another and can most likely be attributed to the presence of ice crystals forming in the soil voids and their influence on strength. However, the main conclusion that can be drawn is that the increase in soil strength must be accounted for in the design of foundation shafts subjected to seasonally frozen conditions.

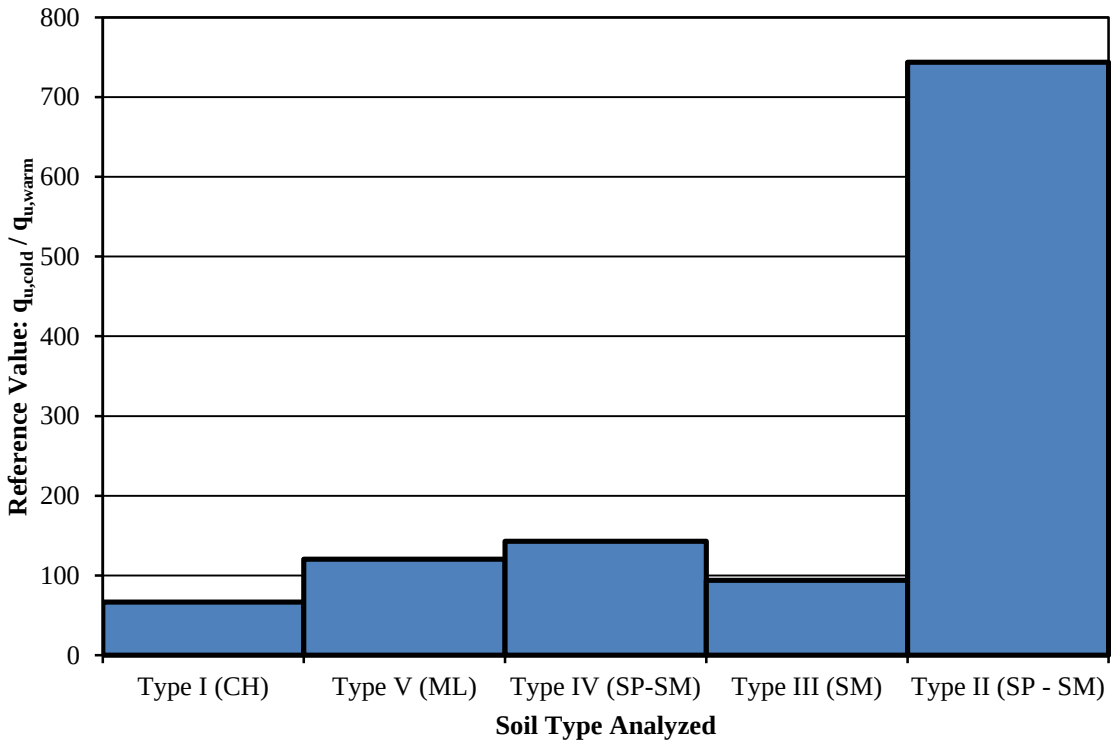

Figure 7-10: Increase in ultimate compressive strength of the five soil types specified in Table 7-2 tested at -20 °C (-4 °F) with respect to the ultimate compressive strength at 20 °C (68 °F)

Strain at Ultimate Compressive Strength

After comparing the strength at failure, the strain achieved at the ultimate compressive strength was also examined. Although multiple data sets were examined, no definitive conclusions were drawn about the effects of freezing temperature on the strain at the peak stress of the soil specimens as the data did not have any consistent trends. This is evident in Figure 7-11 where the data corresponding to the CH alluvial deposit is shown. Although a clear trend is not seen in this figure, the indication is that strain at failure decreases with reducing temperature. This is expected based on the soil stress-strain curves presented in Figure 7-4. Therefore, it is believed that the ultimate compressive strain of the soil decreases with freezing conditions but no trend can adequately be established. Additional charts representing this conclusion are provided in Appendix D.

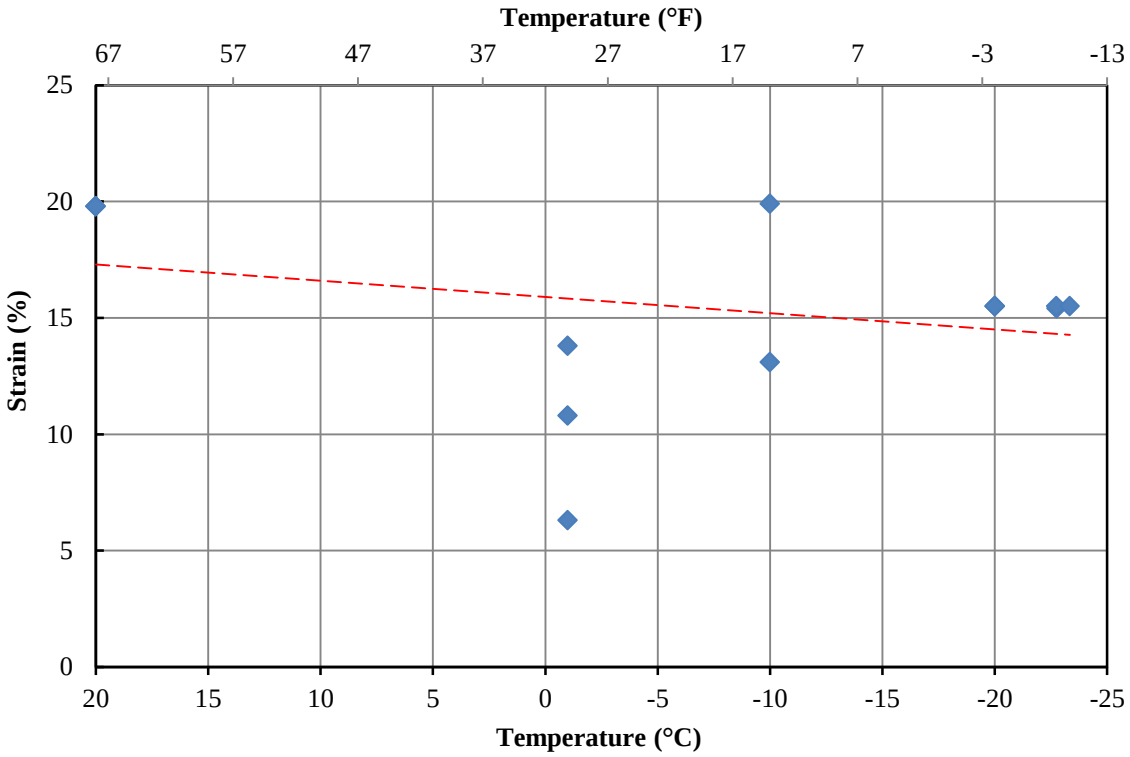

Figure 7-11: Effects of temperature on the strain at the ultimate compressive strength of a Type I: Alluvial soil

Modulus of Elasticity

The effect of temperature on the soil modulus of elasticity was the next soil property investigated. The examination consisted of computing the secant modulus of elasticity from the point of $q_u/2$ to the origin and then dividing the cold temperature value with the average soil modulus of elasticity at 20 °C (68 °F). Figure 7-12 shows the results of this process for the five soil types that were tested. The figure shows that as the temperature decreases, the soil modulus of elasticity increases in a curvilinear manner as a function of soil type. This relationship follows an exponential or second order polynomial as shown by the equations within the figure. The results being a function of soil type is depicted in the figure by the fact that the more cohesive soils tested (e.g., Type I) increase at a slower rate than the non-cohesive soils (e.g., Type II). Although trends exist, an adequate approach for accounting for the increase cannot be established due to the large scatter in the data points and variability in soil types. It is noted however that the modulus of elasticity is significantly altered as temperature decreases as evidenced by the large reference equal to 1400 for the Type II soil.

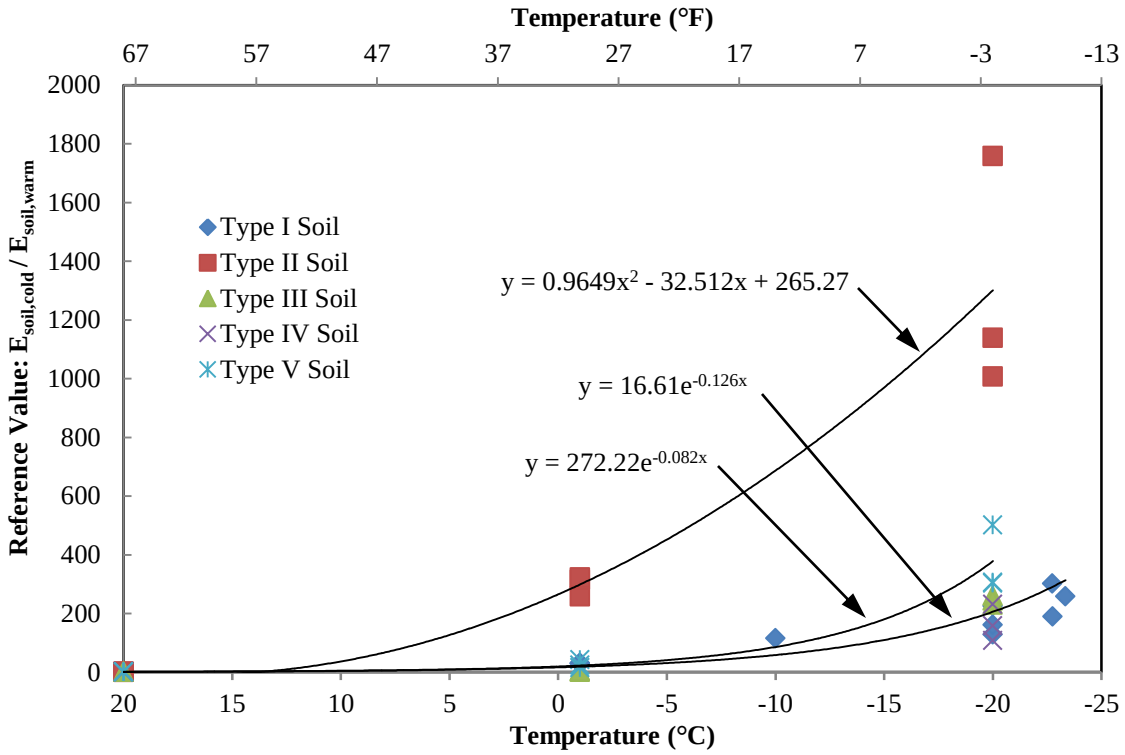

Figure 7-12: Effects of temperature on the soil modulus of elasticity under monotonic loading

Density Effects

The process of examining the effects of moist soil density on the undrained shear strength of the soil at a subzero temperature was undertaken for the Type I: Alluvial soil that was classified using the USCS classification system as a CH soil. This variable was tested by varying the compaction of the soil in the samples while maintaining consistent moisture content in the multiple specimens. At each set of densities, three samples were produced and tested at -20 °C (-4 °F) to examine the effects of the frozen state on the undrained shear strength. The results of the strength testing are provided in Figure 7-13. As seen in this figure, when the density of the specimen was increased, there appears to be a linear increase in the undrained shear strength of the soil. This is similar to the behavior of soil in a warm condition where the compacting causes the internal soil matrix to become closer together thus increasing the amount of friction between the soil particles and in turn the undrained shear strength of the soil.

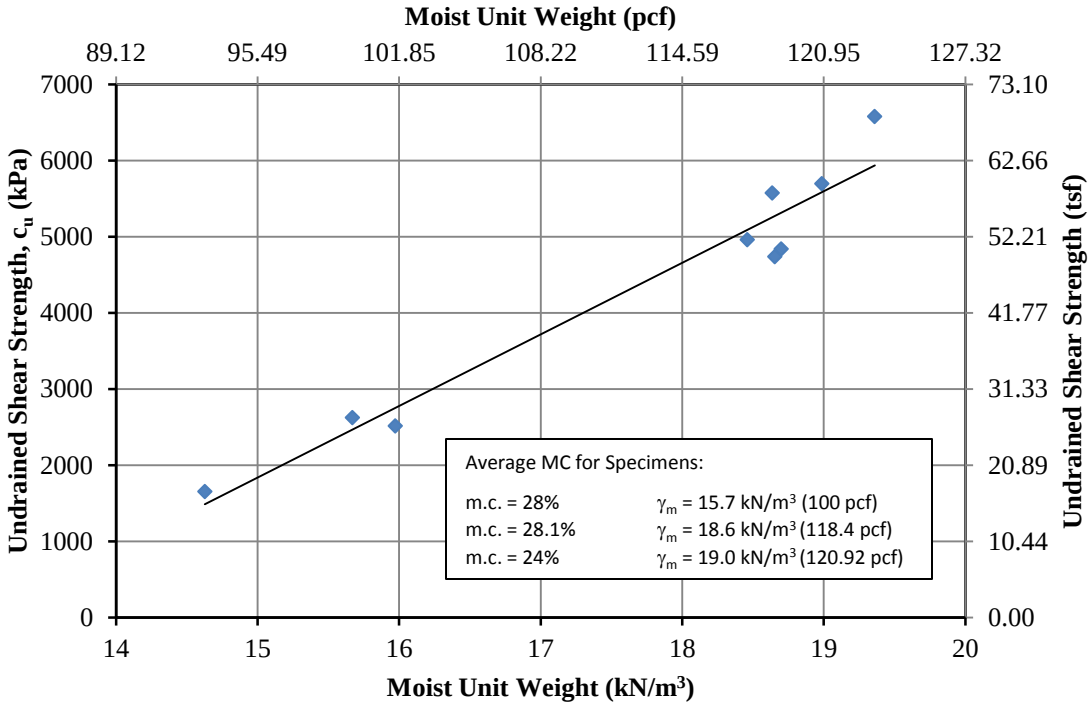

Figure 7-13: Effects of density on undrained shear strength of a CH soil at -20 °C (-4 °F)

Moisture Content Effects

The next variable that was examined was the presence of different amounts of moisture content within the soil. This was once again examined in the alluvial soil classified as a CH according to USCS. In order to complete this testing sequence, the samples were constructed such that a uniform density would be maintained as much as possible while varying the moisture content. The samples were then tested at -20 °C (-4 °F) and the effects of moisture content on the undrained shear strength of the soil were examined as shown in Figure 7-14.

In Figure 7-14 it can be seen that originally the variation in moisture content caused an increase in the density of the soil even though a standard compaction effort was used in all specimens. This is believed to have occurred due to the parabolic curve that typically appears when a standard proctor test is performed. This was the case as the laboratory process used for determining the proctor curve is similar to the process used in the experiment. Despite this anomaly, the data was corrected as noted by the square data point based on the results of the density effects chart previously presented. The data taken from the linear trend was found to have an undrained shear strength of 3514 kPa (36.7 tsf) at a moisture content of 28.1% and an

approximate density of 17.0 kN/m^3 (108 pcf). When this point is included into the data set, it can be seen that a linear increase in the undrained shear strength is generally seen with an increase in the moisture content at a comparable density. This was once again expected due to the fact that an increase in moisture content will cause an increase in the amount of ice formation, thus enhancing the overall strength of the sample.

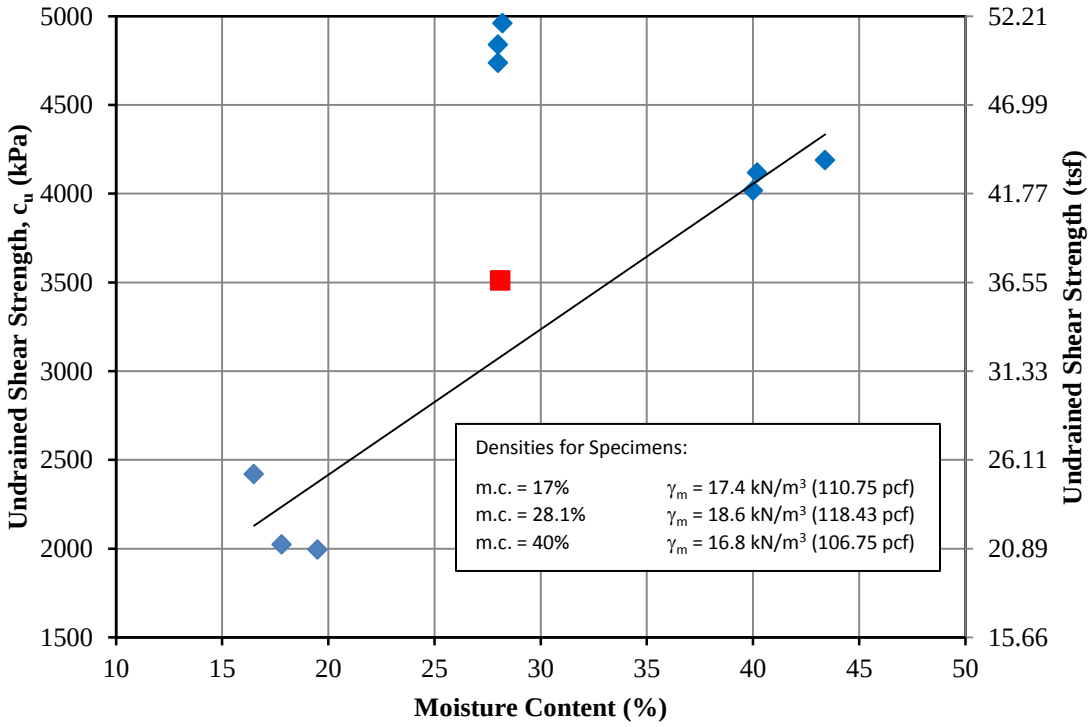

Figure 7-14: Effects of moisture content on the undrained shear strength of a CH soil at -20 °C (-4 °F)

Effect of Strain Rate

As part of the experimental investigation at MRCE, a number of samples were prepared at a similar moisture content and density for testing under variable loading rates as shown in Table 7-2. These tests were used to examine the effects of different rates of loading on the ultimate compressive strength of the soil, the strain at the ultimate compressive strength and the secant modulus of elasticity to the undrained shear strength of the soil at a temperature of -20 °C (-4 °F). The strain rate effects were only examined for the CH soil listed as Type I in the five main soil types of Alaska.

The first variable examined for strain rate effects was the ultimate compressive strength of the Type I soil by comparing the applied loading rate with the ultimate compressive strength of

the soil as shown in Figure 7-15. The figure shows that as the loading rate increases for a 0.1% strain per minute to 10% strain per minute a linear increase of 33% in the ultimate compressive strength of the soil occurred. The results were expected as the rapid loading does not allow the soil to respond as quickly thus decreasing the deformation at a given point while increasing the ultimate compressive strength. This result concurs with the previous study of Zhu and Carbee (1984) as depicted in Figure 2-26 where the strength of the remolded silt depended on the rate of loading applied to the test specimens.

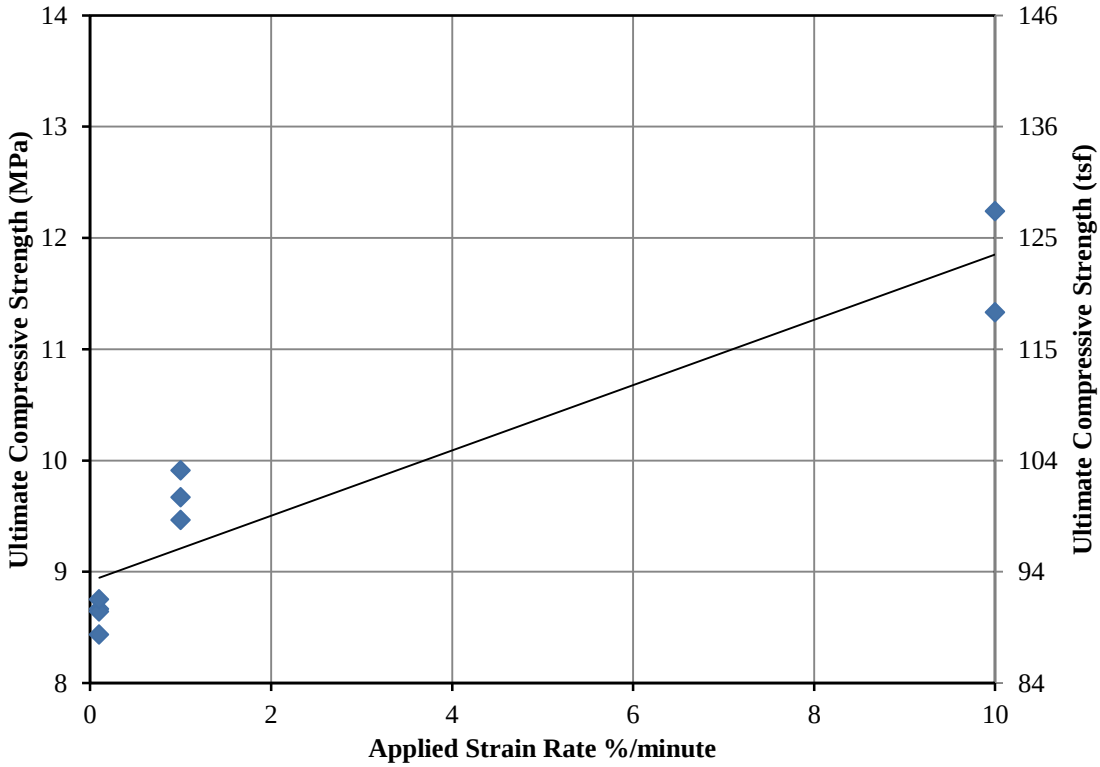

Figure 7-15: Effect of strain rate on the ultimate compressive strength of a Type I soil tested at -20 °C (-4 °F)

The strain at the ultimate compressive strength of the soil was the next parameter studied for the effects of strain rate. This was performed by plotting the strain attained at qu with the applied strain rate to the specimen as shown in Figure 7-16. Similar to the ultimate compressive strength, the strain increased linearly by approximately 25% as the rate of loading increased from 0.1% strain per minute to 10% strain per minute. The increase in strain at the peak stress was expected based on the previous studies of Zhu and Carbee (1984) presented in Figure 2-26 where it can be seen that the strain at the peak is shifting to the right as rates of applied strain increased.

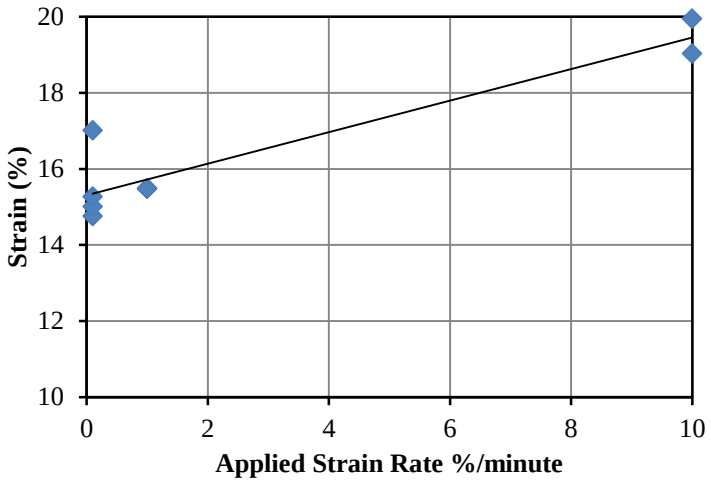

Figure 7-16: Effect of strain rate on the strain at the ultimate compressive strength of a Type I soil tested at -20 °C (-4 °F)

The final parameter investigated for the effects of strain rate was the secant modulus of elasticity to the undrained shear strength point of the Type I soil as presented in Figure 7-17. The data sets presented in this figure show a large scatter in the secant modulus of elasticity at each applied strain rate making a definitive trend hard to establish. Although a clear trend is not seen in this figure, the data indicates that as the applied rate of loading increased an increase of 25% in the secant modulus of elasticity occurred. This increase, however, is essentially negligible as the secant moduli of materials are known to vary by as much as 20%. Therefore, the authors of this report concluded that the secant modulus of elasticity was unaffected by the strain rate applied to the specimen.

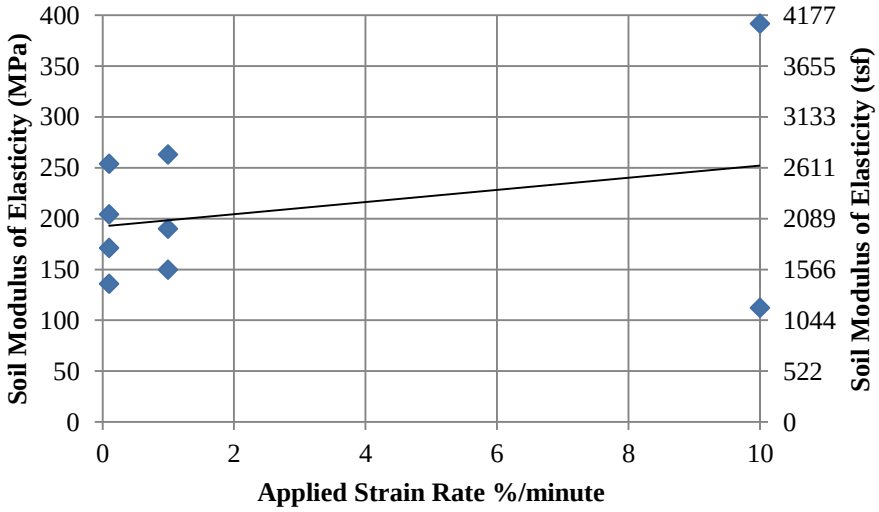

Figure 7-17: Effect of strain rate on the secant modulus of elasticity to the undrained shear strength of a Type I soil tested at -20 °C (-4 °F)

7.4.3 Cyclic Testing

Cyclic testing was performed on the Type I soil specified in Table 7-1 to examine the effects of temperature on the behavior of soil subjected to cyclic loading. The results of this experimentation is provided here as Figure 7-18. In this figure, it can be seen that as the temperature decreased from -1 °C (30.2 F°) to -20 °C (-4 °F) the ultimate compressive strength of the soil increased by 22 times the warmer temperature tested. This concurs with the monotonic testing where an increase in the ultimate compressive strength of the Type I soil was a function of temperature as noted in Sections 7.4.1 and 7.4.2. Additionally, the data presented in the figure shows that the modulus of elasticity increased as temperature decreased which is in accordance with the monotonic testing. The figure further demonstrates that the unloading and reloading moduli were approximately equal to the initial soil modulus of elasticity found for the temperature at which the samples were tested.

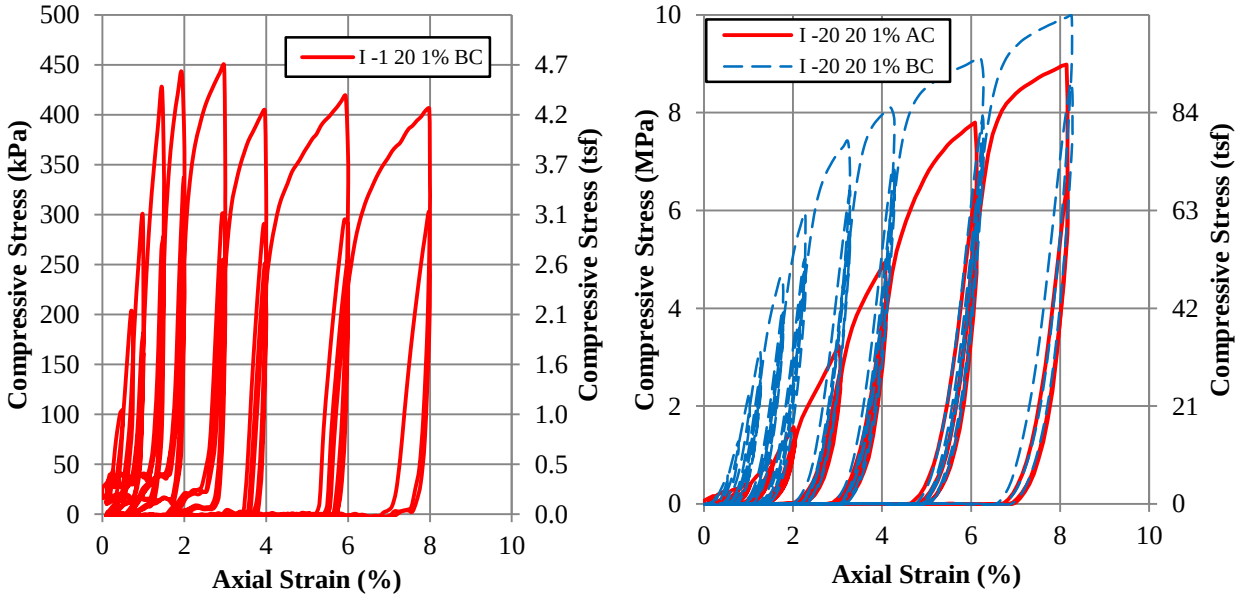

(a) -1 C (30.2 F) (b) -20 C (-4 F)

Figure 7-18: Experimental cyclic stress-strain results of a Type I soil subjected to subzero temperatures and a loading rate of 1% strain per minute

A prevalent trend in the cyclic testing depicted in Figure 7-18 is that residual deformation of the soil specimens occurred after each loading cycle. This residual deformation was found to be a function of temperature and the peak strain applied during a given cycle as the amount of residual displacement was 93% of the peak strain at -1 °C (30.2 °F) and 84% of the peak strain at

-20 °C (-4 °F). The variation in residual strain was not surprising as the stiffening of the soil caused the samples to behave in an elastic manner for higher strain values as seen in Figure 7-5. Additionally, the second and third cycles of loading demonstrated an 80% drop in the peak stress attained during the first loading cycle at a given strain limit.

Effect of Strain Rate

In order to better understand the cyclic behavior of soil at subzero temperatures, Type I soil specimens were subjected to the cyclic load pattern of Table 7-3 at -20 °C (-4 °F) and an applied loading rate of 10% strain per minute as this is comparable to an actual seismic event. The results of the variable loading rate testing performed at MRCE are provided in Figure 7-19. The data was split into the "A" and "B" samples for each cyclic pattern for ease of comparison in the figures. In each instance the solid line represents the applied loading rate of 1% strain per minute while the dashed line represents the applied loading of 10% strain per minute.

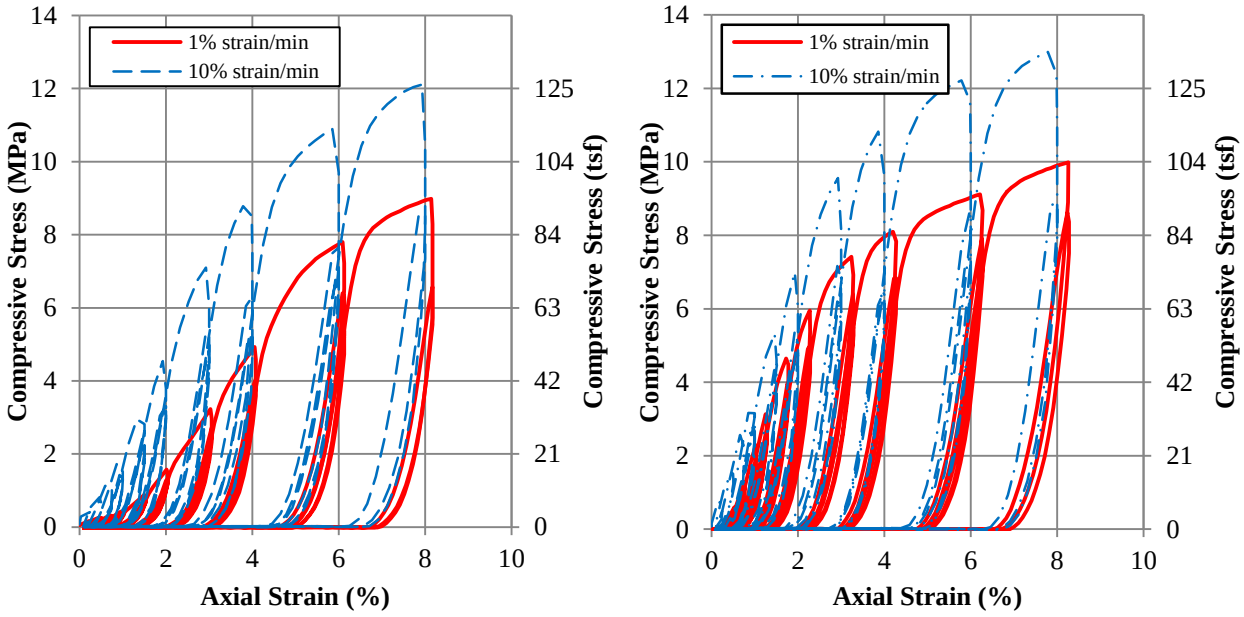

(a) "A" Samples (b) "B" Samples

Figure 7-19: Experimental strain rate effects on the cyclic stress-strain response of a Type I soil tested at -20 °C (-4 °F)

As the applied rate of loading increased, Figure 7-19 shows that the compressive strength of the soil increased by 30% which is comparable to the effects of strain rate noted for the monotonic loading of the soil specimens. This figure further demonstrates that the secant modulus of elasticity was unaffected by a variable loading rate as described in Section 7.4.2 of

this report (especially prevalent in Figure 7-19b). Additionally, the unloading/reloading moduli and the residual deformation of the soil specimens were unaffected by the change in the rate of applied loading. This was demonstrated by the fact that the unloading and reloading cycles to a given strain limit at the 10% strain per minute closely follows the path established by the curves established for a 1% strain per minute loading. The strain at the ultimate compressive strength was not examined for the cyclic testing since the test was performed using a specified strain limit.

7.5 Conclusions

This chapter of the report has presented the results of an investigation conducted at MRCE into the effects of seasonal freezing on the response of soil through an examination of the failure strength, density effects and moisture content effects of the five soil types (see Table 7-1) tested from the State of Alaska. The following section provides the conclusions drawn in regards to the response of soil subjected to seasonal freezing conditions.

- The failure strength of the five soil types significantly increased when subjected to freezing temperatures. At -1 °C (30.2 °F), the increase was typically by a magnitude of ten whereas at -20 °C (-4 °F) the soil samples typically experienced a magnitude of one hundred increase. It is suggested that the relative increase in strength of magnitude 10 and 100 be used to account for seasonal freezing at -1 °C (30.2 °F) and -20 °C (-4 °F) if actual testing of specimens in the frozen state is not possible. These relationships are shown in the equations below.

$$(\sigma)_{-1} = 10(\sigma)_{20} \quad (7\text{-}1)$$

$$(\sigma)_{-20} = 100(\sigma)_{20} \quad (7\text{-}2)$$

- To more accurately define the p-y curves additional testing is needed on sandy soils to examine the effect of cold temperatures on the effective friction angle. This data would be used to define the modulus of horizontal subgrade reaction. It is believed that the friction angle increases at temperatures decreases and an estimate on the friction angle. Therefore, the designer can estimate a friction angle such the ultimate strengths of the p-y curves agree with the relationships in Equations (7-1) and (7-2).

- Although a correlation for the strain at the ultimate compressive stress of the soil could not be established, the data suggests that a decrease in strain is experienced as temperatures decrease from 20 °C (68 °F) to -23 °C (-9.4 °F).
- The modulus of elasticity increased according to a polynomial or exponential curve as temperature of the tested soil specimens decreased from 20 °C (68 °F) to -23 °C (-9.4 °F). A direct correlation was not established due to the scatter in the test data because of the multiple soil types tested in this investigation. The cold temperature modulus of elasticity increased by 200 times for the Type I soil and 1400 times for the Type II soil.
- As the density of the specimen increased the undrained shear strength of an alluvial deposit of CH soil increased in a linear manner in a frozen state when the moisture content was held constant. The increase in undrained shear strength experienced at -20 °C (-4 °F) was a factor of 2.75 from a density of 15.7 kN/m^3 (100 pcf) to 19.0 kN/m^3 (121 pcf)
- The effects of moisture content on the undrained shear strength of an alluvial deposit of CH soil at -20 °C (-4 °F) was found to increase in a linear manner when the density of the specimens were maintained at a constant level. The increase in strength was a factor of 2 from a moisture content of 17% to a moisture content of 40%.
- The effects of strain rate on the monotonic testing of soils was found to agree with previous studies and have an impact on the stress-strain behavior of a Type I (CH) soil tested at -20 °C (-4 °F). The ultimate compressive strength of the soil was found to increase linearly increase by 33% between an applied loading rate of 0.1% and 10% strain per minute. The strain at the ultimate compressive strength of the soil was found to linearly increase by 26% between an applied loading rate of 0.1% and 10% strain per minute. Although slight increase in the secant modulus of elasticity was noted, the difference was found to be negligible thus suggesting that modulus of elasticity was unaffected by a change in the applied rate of loading during testing.
- The effects of temperature on cyclic testing on a Type I soil produced similar results to the monotonic testing. The strength of the specimens tested at -20 °C (-4 °F) increased by 22 times the strength of the specimens tested at -1 °C (30.2 °F). The modulus of elasticity was also noted to increase as the temperature decreased.

- The cyclic testing found that the unloading and reloading moduli of the soil at the frozen state were equivalent to the initial modulus of loading (see Figure 7-18).
- Residual strains of 93% and 84% of the peak strain during a given cycle were present during the cyclic testing of a Type I soil at -1 °C (30.2 °F) and -20 °C (-4 °F). Additionally, the second and third cycles at a given strain experienced an 80% drop in strength from the first loading cycle applied to the soil specimens.
- The effects of strain rate on the cyclic testing were found to agree with the results found for the monotonic testing. The compressive strength increased and the modulus of elasticity remained unchanged. Also, the unload and reload moduli were not affected by the variable loading rates of 1% strain per minute and 10% strain per minute.
- It is recommended that future testing should be performed to provide a larger data set of results so that the effects of density and moisture content can be better examined for all soil types.
- More testing should also be performed on all soil types in order to provide a more statistically sound equation for determining the increase of failure strength with a decrease in temperature.

CHAPTER 8: SUMMARY, CONCLUSIONS AND RECOMMENDATIONS

8.1 Introduction

The research on the seismic design of drilled shaft foundations in clay soils was motivated on the basis of the challenges associated with models in practice today and the experimental testing performed by Suleiman et al. (2006) especially in high seismic regions such as Alaska where seasonal freezing is a major concern. Therefore, the objective of this research was to develop a simplified method for use in the seismic design of drilled shafts in clay that would provide a good representation of the critical locations and lateral loading response of an integrated column/foundation system. The proposed model had to capture the lateral loading response in all seasons of the year without the use of a detailed approach as this has not been handled in current approaches even though numerous models exist in practice today. The sections presented below provide a summary of the completed work, conclusions drawn from the project and recommendations developed throughout the process.

8.2 Summary

The research presented in the report started with a brief historical background on bridges and their evolvement with time. Seismic engineering practices were then examined with specific details about seismic loading, the design philosophy used in practice and concerns associated with seasonal temperature variation. Multiple foundation types were then presented along with the seismic design approaches used for each foundation. Specific emphasis was given to deep foundations, specifically drilled shafts, based on the topic of the project. The effects of soil-foundation-structure-interaction on drilled shafts were then described prior to defining the scope of research.

An extensive literature review was completed with the goal of obtaining knowledge on the lateral response of drilled shafts when subjected to design level or greater earthquakes in all seasonal conditions. Several analytical methods for determining the lateral response in design and analysis were investigated based off of current code and guideline recommendations. A seasonal freezing investigation that included analytical and experimental case studies was provided along with a broad impact study on infrastructure within the United States and Japan. During this investigation it was noted that seasonal freezing would significantly alter the lateral load response of an integrated column/foundation system by:

- Increasing the effective elastic stiffness of the system;
- Increasing the shear demand experienced by the column and foundation shafts;
- Shifting the maximum moment location toward the ground surface;
- Reducing the lateral displacement capacity when compared to the warm weather condition; and
- Reducing the plastic hinge length.

In addition to the lateral response, it was found that material properties are effected during times of seasonal freezing with the typical trend being an increase in overall strength, thus causing a larger zone of elastic behavior. Finally, the capabilities of the sectional analysis tool to be used within the research were discussed.

An examination of the existing methods was completed, identifying the associated challenges. This process involved comparisons between detailed analyses and the common simplified methods presented within the literature review. Thus providing justification as to why a new method of determining the lateral response of integrated column/foundation systems in clay soils was needed.

A simplified method for determining the lateral response of drilled shafts in clay soils was developed for the pinned head condition. The new method was modeled as a cantilever with an effective height from the top of the bridge column to the point of maximum moment within the foundation shaft. Properties of the flexible base and spring representing soil resistance were established thus defining critical locations for an integrated column/foundation system including the maximum moment location and point of first zero moment after the maximum moment. A bilinear force-displacement curve representing the lateral load response of the system using the origin of a Cartesian coordinate system, the first yield limit state and the ultimate limit state was constructed based off of the information presented in Section 4.4. The accuracy of the method was then verified against experimental data from Suleiman et al. (2006) and detailed analyses performed in LPILE in Section 4.5. To adjust for different boundary conditions at the tip of the column, it is expected that the model can be adjusted similarly to a column supported on a spread footing by adjusting the effective height of the cantilever to the inflection point and computing deflections from this location while the force will not change at the column tip. This is currently under investigation by the researchers.

8.3 Conclusions

Based on the completed study presented within this report, the following conclusions were drawn:

- Approximately two-thirds of about 600,000 bridges in the United States are effected by seasonal freezing alone. In addition, it was found that half of the approximately 70,000 bridges located in high seismic regions would be affected by seasonal freezing, which includes areas such as the north eastern part of California, the eastern half of Washington, Alaska and Missouri. It was also concluded that freezing and high seismicity would occur in the northern regions of Japan, especially on Hokkaido Island. Although all these bridges are effected across the world, it appears that the effects of seasonal freezing are not routinely addressed in current seismic design practice around the world.
- The detailed method used to determine the lateral load response suggested by AASHTO (2007), although accurate if correctly modeled, requires a significant amount of information about the structure and surrounding soil in order to complete the analysis.
- The method suggested for the lateral design of drilled shafts by Chai (2002) has challenges associated with its use that include the following based off of the information examined in Chapter 3:
    - Although the model was created for cohesive and cohesionless soils, it was only verified experimentally against cohesionless soils thus invalidating its use in cohesive soils;
    - The maximum moment location was found to be improperly located by 12.5% to 27.7% when compared to the detailed analyses performed in LPILE which was shown in Chapter 2 to be able to capture the behavior of the system accurately;
    - The analytical plastic hinge length was specified based off of experimental testing in cohesionless soils and is therefore not applicable to cohesive soils. This was demonstrated in Chapter 3 when it was shown that the analytical plastic hinge length was off by 27.6% and 35.9% when compared to the detailed LPILE analyses for the primary and secondary soil profiles, respectively;
    - Seasonal freezing was not included in the development of the model and therefore should only be used in warm weather conditions; and

- The method also uses an idealized elastic perfectly-plastic force-displacement response between the yield and ultimate conditions which is not capturing the nonlinear effects of the material properties (soil, steel and concrete). This idealization also significantly over predicts the behavior of the integrated column/foundation system tested by Suleiman et al. (2006) in both frozen and unfrozen conditions.

- The use of the method suggested by Priestley et al. (2007) had its own challenges and the conclusions drawn from this are as follows:
  - Although the method was developed for both cohesive and cohesionless soils, it was once again only verified against experimental data performed in cohesionless soils thus providing no validation for the cohesive soil model;
  - The model is only applicable for a limited range of soft cohesive soils and should technically only be used for the two undrained shear strengths of 20 kPa (420 psf) and 40 kPa (840 psf);
  - Lateral forces were not computed as an appropriate spectral graph relating the design displacement to the effective damping of the system and period was not known. A quick estimate was not provided since the idealized yield moment and ultimate moment relating to the appropriate curvatures was unknown;
  - The analytical plastic hinge length used in the model is based off of the suggestions made by Chai (2002) which was previously shown to be invalid for use in cohesive soils. This challenge along with the underestimation of the controlling limit state curvature by 16% led to the underestimation of the final design displacement by 40%; and
  - The method was not created with the thought of seasonal freezing effects in mind thus limiting the model to use in warm conditions only.

- Simplified methods suggested by ATC 32 (1996) and AASHTO (2009) were also found to have the following challenges associated with their use:
  - The equivalent fixed based cantilever method is only applicable within the elastic range of loading and will not capture the inelastic action where the most significant displacement will occur in the system;
  - When compared to a detailed analysis in LPILE based on the discussion in Chapter 2, the effective fixity location where the maximum moment would occur was found to

be over predicted by approximately 100%. This is a major concern as this point is where the most damage to the system will occur when subjected to a design level or greater earthquake;

- The shear is assumed to be constant along the length of the shaft, which is incorrect once the soil begins to resist the lateral movement. This is a concern as an increase in shear typically occurs in the shaft below the ground surface; and
- No consideration was given to the effects of seasonal freezing in the development of the model thus limiting it use to warm weather conditions.

- A new method was developed for the lateral loading response of drilled shafts that can capture both the elastic and inelastic range during all seasons of the year. The new model can be run using a structural analysis program or through the use of hand calculations as desired. In addition, the model is applicable in clay soils that range from soft to very stiff.
- The new method is able to effectively provide a bilinear force-displacement curve for the lateral load response of an integrated column/foundation system. The new method does this through the location of the first onset of yield strains and ultimate flexural capacity using minimal input parameters about the shaft and surrounding soil;
- Verification using the experimental data by Suleiman et al. (2006) demonstrated that the model is able to effectively capture the critical locations within the system (e.g., the maximum moment location), the global-force displacement response and localized effects in the system (e.g., translation and rotation at the maximum moment location). The following conclusion were drawn from the verification:
  - the ultimate lateral force in both warm and freezing conditions was within 10% of a detailed analysis;
  - the ultimate displacement for the SS1 was found to be 23% less than the experimental data by Sritharan et al. (2007) which is a conservative estimate due to the assumption purposely made for the analytical plastic hinge length;
  - The maximum moment and zero moment location were located accurately with less than 8% error when compared to the experimental findings from the test in warm conditions. When compared to the test in cold conditions, these locations were located accurately with less than 6% error;

- The proposed model predicts the secant stiffness to the first yield location within 5% of the experimental value;
- The second slope in the warm test comparison under predicts the lateral shear force for an equivalent displacement between yield and ultimate by an average of 10%; and
- The effects of seasonal freezing were effectively handled by varying material properties for the soil, steel and concrete as seen in the SS2 global comparison.

- The analytical verification of the proposed new model provided the following conclusions:
  - The secant stiffness to the first yield location is within 10% of the detailed analysis performed in LPILE;
  - The yield and ultimate shear forces at the top of the column were predicted within an error of approximately 1%;
  - The yield displacement was found within approximately 10% and the ultimate displacement was within 2.3% of the LPILE analysis; and
  - The second slope under predicts the lateral shear force by an average of 13%.
- Within the material testing of confined and unconfined concrete a number of conclusions were drawn about the behavior when subjected to seasonal freezing conditions. Based on the information presented in Chapter 5, these conclusions are provided below:
  - The unconfined concrete compressive stress of concrete increased an average of 28% when temperature decreased from 20 °C (68 °F) to -40 °C (-40 °F). The recommended equation for defining the linear increase is presented as Equation 5-2.
  - The concrete strain of unconfined concrete at peak compressive strength was found to be approximately 0.002 at 20 °C (68 °F). This value will decrease in a linear manner by approximately 23% as the temperature decreases to -40 °C (-40 °F). The equation for defining the strain at peak compressive strength for a given temperature is presented in Equation 5-3.
  - The modulus of elasticity for unconfined concrete was found to increase by 13% as temperature decreased to -40 C (-40 F) from 20 C (68 F). The increase in E_c was found to follow a power series trend related to the unconfined compressive strength of the concrete and an exponent of 0.5. This relationship correlates well with current practice in which the modulus of elasticity is related to the square root of the

unconfined compressive strength of the concrete. The equation for defining the increase is presented in Equation 5-6.

- Similar to the unconfined compressive stress, the confined concrete compressive stress (f'_{cc}) was found to increase as temperature decreased from 20 °C (68 °F) to -40 °C (-40 °F). This meant that the confinement behaves differently than at warm weather conditions and separate recommendations were made for the increase in confined concrete compressive stress. The recommended equation for the increase is presented as Equation 5-7.
- The rate of increase in f'_{cc} was determined to be affected by the increase in Poisson's ratio of the concrete specimen as temperature decreases. The changing Poisson's ratio decreased the effectiveness of the confinement thus reducing the overall strength gain possible. However, additional steel added to the specimen will increase the ductility of the confined region as it does during a warm weather condition.
- In contrast to the unconfined concrete, the strain at the peak confined compressive stress (ε_{cc}) increased between 0% and 40%, depending on the amount of horizontal reinforcement present in the specimen, as temperature went from 20 °C (68 °F) to -40 °C (-40 °F). The increase, however, was able to be setup as a single trend with a varying starting location based on the amount of horizontal reinforcement. The recommended equation is presented in Equation 5-8.
- The modification of material properties alone in the Mander's model will not adequately capture the behavior of confined concrete subjected to seasonal freezing as shown in Figure 5-23. However, it is noted that the change in f'_{cc} does not greatly impact the overall moment-curvature response of the system.
- The ultimate confined compressive strain (ε_{cu}) was found to not be affected by decreasing temperature. Therefore, it is recommended that the value be equal to that which a designer establishes in the warm weather condition.
- The unconfined concrete modulus was consistently higher than the confined concrete modulus; however, this was most likely due to a localized value being selected for determining the modulus of elasticity. Therefore, it is recommended that the modulus for confined concrete be equal to the value attained for unconfined concrete. The recommended equation is presented in Equation 5-6.

- Within the material testing of A706 steel a number of conclusions were drawn about the behavior when subjected to seasonal freezing conditions. Based on the information presented in Chapter 6, these conclusions are provided below:
  - A706 mild steel experienced an increase in yield and ultimate tensile strengths of 5.1 and 6.3 percent, respectively, when the temperature was reduced from 20°C (68°F) to -40°C (-40°F). These increases varied in a non-linear manner. The recommended equations for defining these increases are presented in Eqs. (6-1) and (6-3).
  - The magnitude of temperature increases for the yield and ultimate tensile strengths of A706 mild steel are generally lower than that suggested by previous research on other types of steel. They are also lower than the maximum increases observed in Sloan's research (2005) for A706 steel.
  - The impact of temperature on the ultimate tensile strength is greater than that of the yield strength, which is opposite to the trends of the previous research presented in this paper on other steels.
  - Material behavior is altered even at temperatures higher than 0°C (32°F). An increase of around 1.0 and 1.6 percent for the yield and ultimate tensile strengths were observed between 20°C (68°F) and 5°C (41°F).
  - The impact of changing the strain rate from 0.003 to 0.03 /min showed a 3 percent increase in the yield strength and 1.67 percent increase in the ultimate tensile strength at both -1°C (30.2°F) and -20°C (-4°F).
  - The yield plateau generally shortened as the strain rate increased and completely disappeared upon reaching a strain rate of 0.3 /min. A total dissipation of 0.00084 strain (34.7 percent) was experienced in the yield plateau length when varying the strain rate from 0.003 /min. to 0.3 /min. This reduction appeared to be dependent upon temperature, but should be further researched for validation.
  - The modulus of elasticity and ultimate tensile strain of A706 were not significantly affected by temperature and strain rate.
  - Although a complete conclusion on the effects of bar size could not be made due to the use of two bar sizes, it appeared that bar size may affect the magnitudes of the yield and ultimate tensile strength increases with larger changes occurring in the smaller bar size.

- Although a complete conclusion on the combined effects of strain rate and temperature could not be made due to the scope limits of this study, strength increases associated with strain rate changes may be dependent upon the testing temperature used. It appeared that a slightly greater strength increase occurred for specimens at a lower temperature when varying the strain rate from 0.003 /min to 0.3 /min.
- The cyclic loading, consisting mainly of inelastic tensile strains and zero compressive strains, led to no change in the cold temperature effects of parameters from that established from the monotonic testing except for the exclusion of the onset of strain hardening. It is recommended that the initially proposed cyclic loading path, involving both inelastic compression and tensile strains, be performed on a higher diameter/length ratio so that buckling does not occur and more useful data can be collected.

- A number of conclusions were drawn from the soil testing performed on soils typical of the State of Alaska by MRCE in New York. Based on the information presented in Chapter 7, the results from the investigation are as follows:
  - The failure strength of the five soil types significantly increased when subjected to freezing temperatures. At -1 °C (30.2 °F), the increase was typically by a magnitude of ten whereas at -20 °C (-4 °F) the soil samples typically experienced a magnitude of one hundred increase. It is suggested that the relative increase in strength of magnitude 10 and 100 be used to account for seasonal freezing at -1 °C (30.2 °F) and -20 °C (-4 °F) if actual testing of specimens in the frozen state is not possible. These relationships are shown in the equations below.

    $$(\sigma)_{-1} = 10(\sigma)_{20} \quad (8\text{-}1)$$

    $$(\sigma)_{-20} = 100(\sigma)_{20} \quad (8\text{-}2)$$

  - To more accurately define the p-y curves additional testing is needed on sandy soils to examine the effect of cold temperatures on the effective friction angle. This data would be used to define the modulus of horizontal subgrade reaction. It is believed that the friction angle increases at temperatures decreases and an estimate on the friction angle. Therefore, the designer can estimate a friction angle such the ultimate strengths of the p-y curves agree with the relationships in Equations (7-1) and (7-2).

- Although a correlation for the strain at the ultimate compressive stress of the soil could not be established, the data suggests that a decrease in strain is experienced as temperatures decrease from 20 °C (68 °F) to -23 °C (-9.4 °F).
- The modulus of elasticity increased according to a polynomial or exponential curve as temperature of the tested soil specimens decreased from 20 °C (68 °F) to -23 °C (-9.4 °F). A direct correlation was not established due to the scatter in the test data because of the multiple soil types tested in this investigation. The cold temperature modulus of elasticity increased by 200 times for the Type I soil and 1400 times for the Type II soil.
- As the density of the specimen increased the undrained shear strength of an alluvial deposit of CH soil increased in a linear manner in a frozen state when the moisture content was held constant. The increase in undrained shear strength experienced at -20 °C (-4 °F) was a factor of 2.75 from a density of 15.7 kN/m^3 (100 pcf) to 19.0 kN/m^3 (121 pcf)
- The effects of moisture content on the undrained shear strength of an alluvial deposit of CH soil at -20 °C (-4 °F) was found to increase in a linear manner when the density of the specimens were maintained at a constant level. The increase in strength was a factor of 2 from a moisture content of 17% to a moisture content of 40%.
- The effects of strain rate on the monotonic testing of soils was found to agree with previous studies and have an impact on the stress-strain behavior of a Type I (CH) soil tested at -20 °C (-4 °F). The ultimate compressive strength of the soil was found to increase linearly increase by 33% between an applied loading rate of 0.1% and 10% strain per minute. The strain at the ultimate compressive strength of the soil was found to linearly increase by 26% between an applied loading rate of 0.1% and 10% strain per minute. Although slight increase in the secant modulus of elasticity was noted, the difference was found to be negligible thus suggesting that modulus of elasticity was unaffected by a change in the applied rate of loading during testing.
- The effects of temperature on cyclic testing on a Type I soil produced similar results to the monotonic testing. The strength of the specimens tested at -20 °C (-4 °F) increased by 22 times the strength of the specimens tested at -1 °C (30.2 °F). The modulus of elasticity was also noted to increase as the temperature decreased.

- The cyclic testing found that the unloading and reloading moduli of the soil at the frozen state were equivalent to the initial modulus of loading (see Figure 7-18).
- Residual strains of 93% and 84% of the peak strain during a given cycle were present during the cyclic testing of a Type I soil at -1 °C (30.2 °F) and -20 °C (-4 °F). Additionally, the second and third cycles at a given strain experienced an 80% drop in strength from the first loading cycle applied to the soil specimens.
- The effects of strain rate on the cyclic testing were found to agree with the results found for the monotonic testing. The compressive strength increased and the modulus of elasticity remained unchanged. Also, the unload and reload moduli were not affected by the variable loading rates of 1% strain per minute and 10% strain per minute.

8.4 Design Guidelines and Recommendations

Throughout the duration of the project, a number of challenges were identified within codes and guidelines when determining the seismic response of deep bridge bridge pier foundations in seasonally frozen ground. These challenges led the author to develop a simplified model that would determine a bilinear force-displacement response for a bridge column supported by a CIDH shaft in cohesive soils using minimal input parameters thus reducing the need for a detailed computer based analysis. This proposed model was verified against available experimental data and analytical techniques in LPILE (Reese et al., 2004). In addition to the model development, material testing at cold temperatures was performed on confined/unconfined concrete, A706 mild steel reinforcement and soils typical of the state of Alaska. Using the results of this project, design guidelines were constructed for using the new simplified model along with a number of recommendations for future research.

8.4.1 Design Guidelines

To meet the scope of research requirements specified in Chapter 1, a series of guidelines were created to allow for the seismic design of CIDH shafts in both a simplified and sophisticated method. This process was completed by creating a series of flowcharts dependent on the type of soil present at the site and the design method desired. The process starts in Figure 8-1 where the input parameters are defined and the analysis method is selected. After going

through this flowchart, the designer is referred to the appropriate flowchart for completion of the design process. These series of charts are presented herein as Figure 8-2 through Figure 8-6.

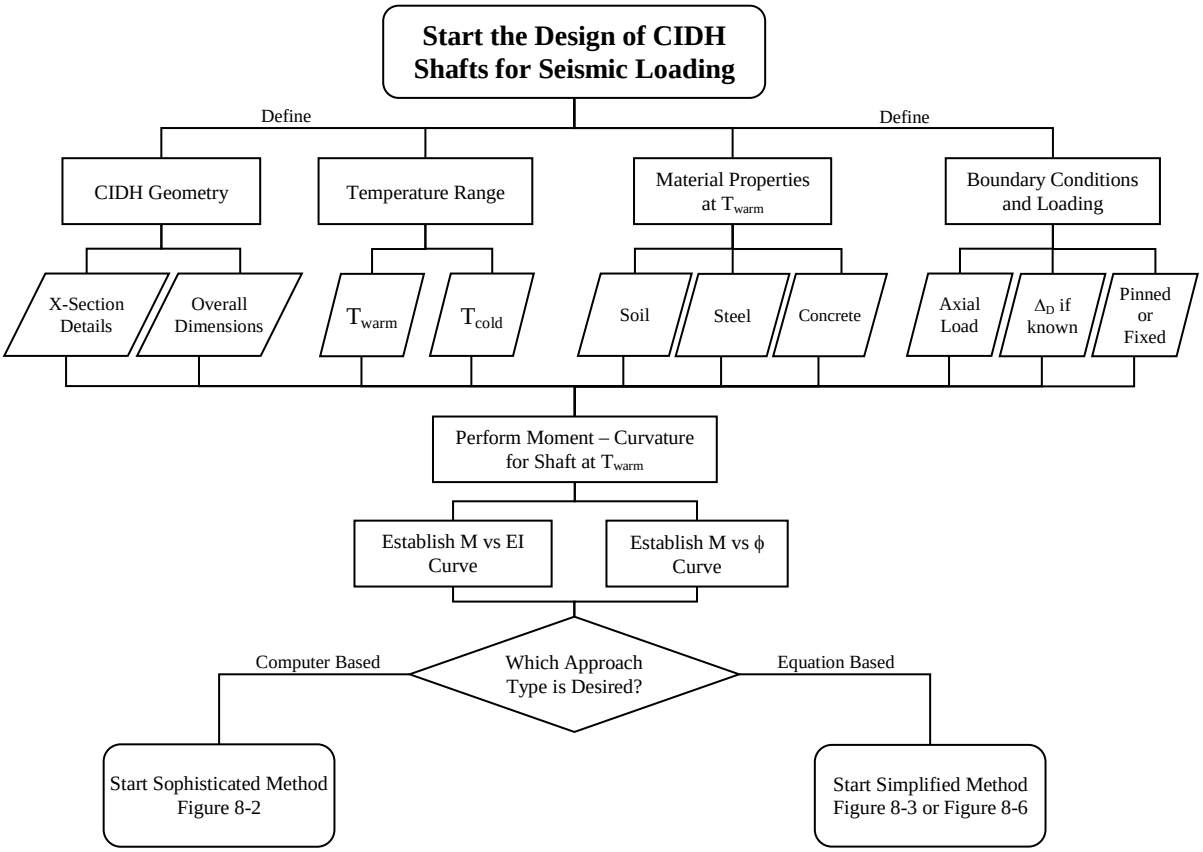

Figure 8-1: Initial design flow chart for the seismic design of CIDH shafts

Sophisticated Method (All Soil Types)

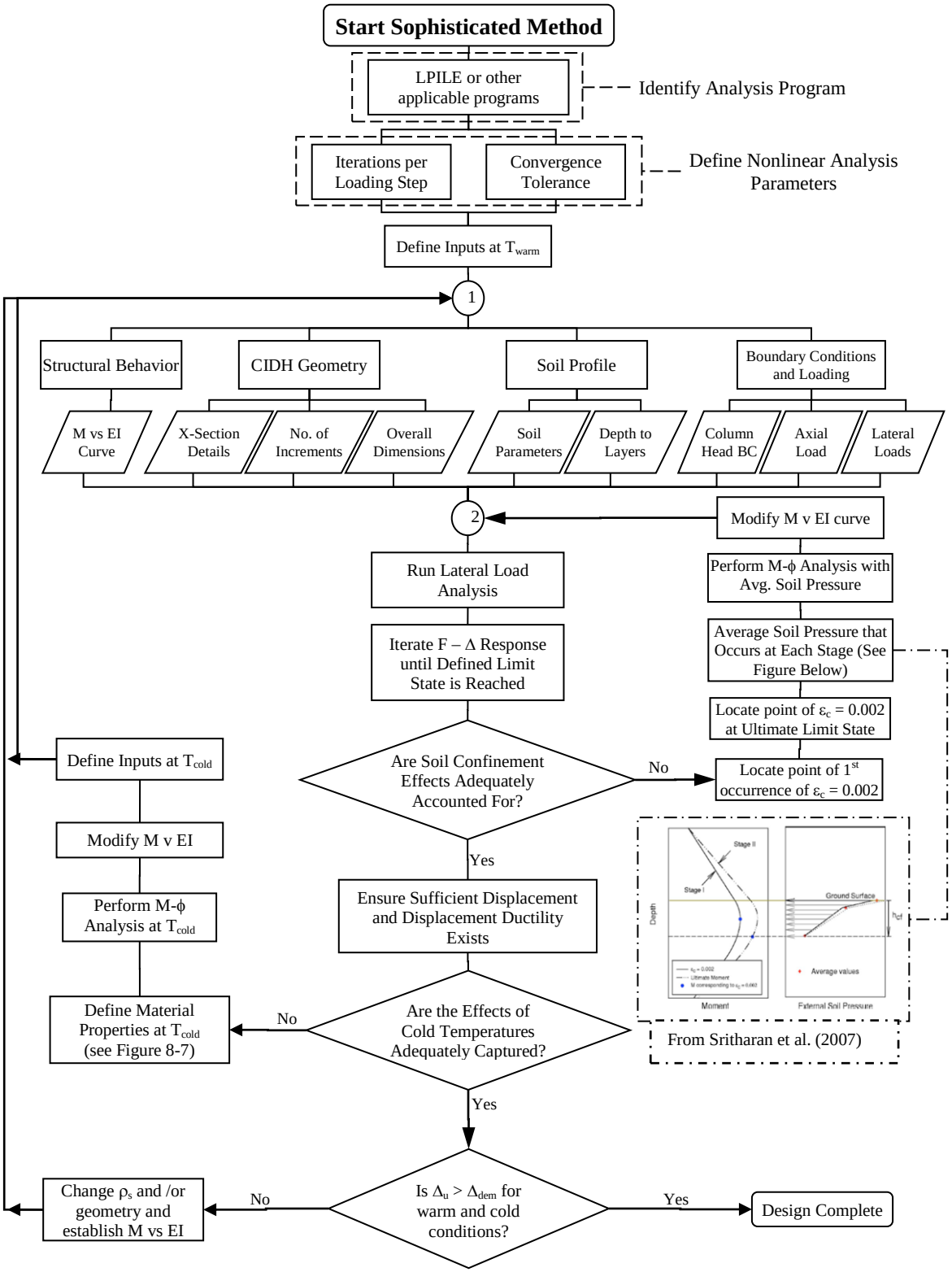

Figure 8-2: Sophisticated design method flowchart in all soil types

Simplified Method for Drilled Shafts in Cohesive Soils

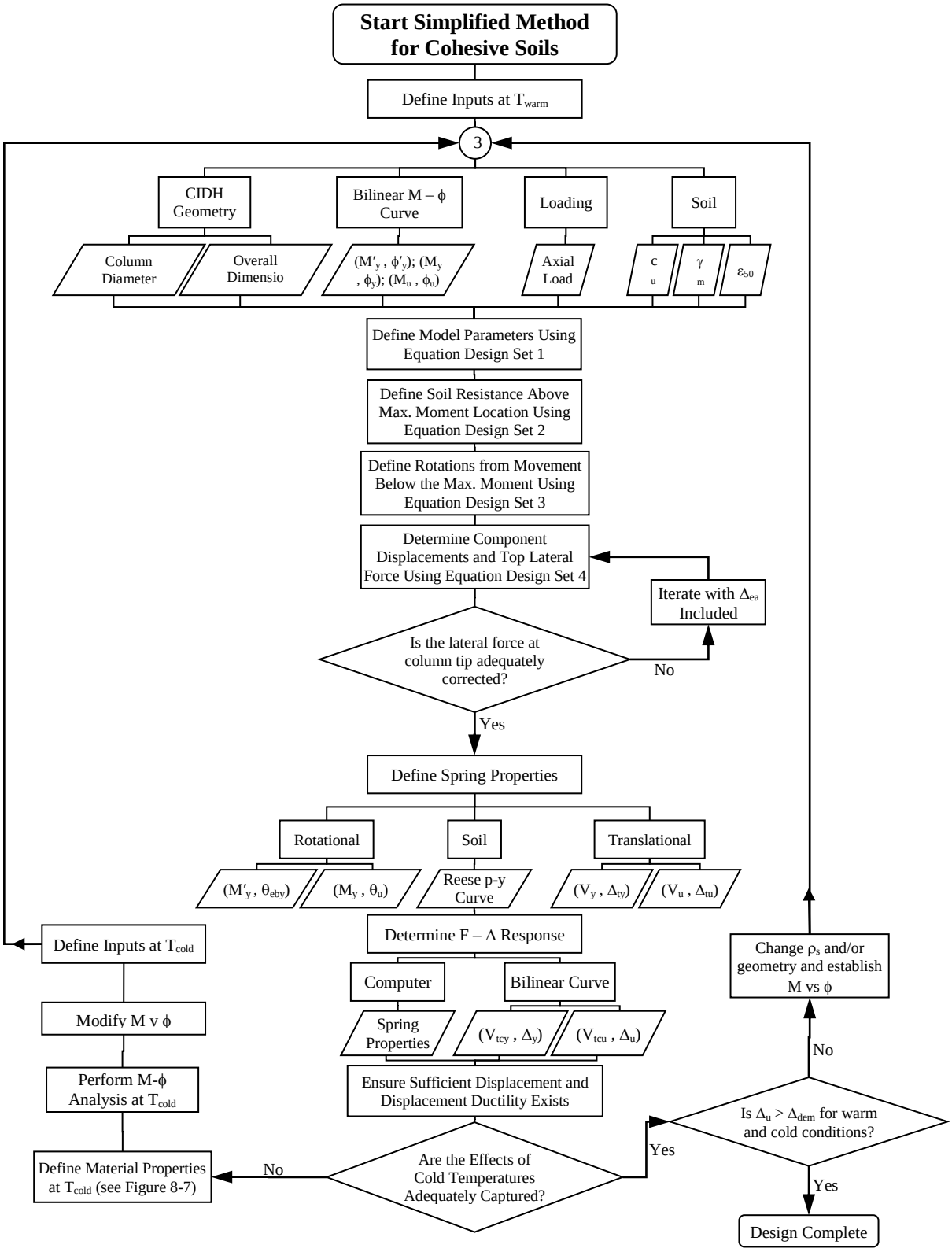

Figure 8-3: Simplified method design flowchart in cohesive soils

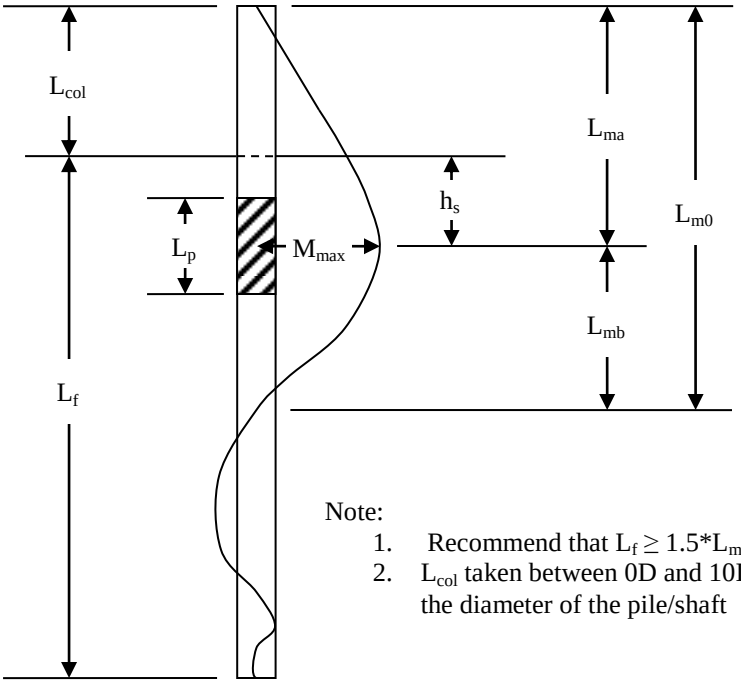

Figure 8-4: Description of the terminology used within the simplified method for cohesive soils provided in Figure 8-3

Equation Design Set #1

$$L_{ma} = D\left[\alpha_{ma}\left(\frac{L_{col}}{D}\right)^2 + \beta_{ma}\left(\frac{L_{col}}{D}\right) + \chi_{ma}\right]$$

$$\alpha_{ma} = -0.000005ac_u^{\,2} + 0.0003bc_u + 0.028$$

$$\beta_{ma} = 0.0038bc_u + 0.3247$$

$$\chi_{ma} = -1.28\ln[c_u(\text{kPa})] + 9.6021$$

$$\chi_{ma} = -1.28\ln[c_u(\text{psi})] + 7.1307$$

$a = 0.021$ for c_u in kPa and 1.0 for c_u in psi

$b = 0.145$ for c_u in kPa and 1.0 for c_u in psi

$$L_{m0} = D\alpha_{m0}[c_u(\text{psi})]^{\beta_{m0}}, \text{or}$$

$$L_{m0} = D\alpha_{m0}[0.145c_u(\text{kPa})]^{\beta_{m0}}$$

$$\alpha_{m0} = 0.11\left(\frac{L_{col}}{D}\right) + 22.3$$

$$\beta_{m0} = 0.021\left(\frac{L_{col}}{D}\right) - 0.33$$

$$L_{mb} = L_{m0} - L_{ma}$$

$$L_{pb} = 0.16L_{mb}$$

$$L_p = 2(0.16L_{mb}) = 0.32L_{mb}$$

Equation Design Set #2

$$p_u = \left(3 + \frac{\gamma x}{c_u} + 0.5\frac{x}{b}\right)c_u b$$

$$p_u = 9c_u b$$

γ = unit weight of soil
x = depth from ground surface to point of spring
b = width or diameter of foundation

$$V_{su} = p_u h_s$$

p_u = ultimate soil subgrade reaction, minimum of above equations
h_s = height of soil being effected for the soil spring

$$V_{sy} = \eta V_{su}$$

η = modification factor to determine a yield soil reaction

$$\eta = -0.03\ln[c_u(\text{psi})] + 0.7536$$

$$\eta = -0.03\ln[c_u(\text{kPa})] + 0.8115$$

If using one soil spring only,

$$h_s = L_{ma} - L_{col}$$

Equation Design Set #3

$$\theta_{eby} = 0.002\left(\frac{L_{mb}}{D}\right) + 0.00001$$

$$\theta_{ebu} = 0.0031\left(\frac{L_{mb}}{D}\right) + 0.0006$$

$$\theta_p = L_p\phi_p = L_p(\phi - \phi_e)$$

ϕ = curvature at a given point past the first yield point
ϕ_e = elastic curvature component

$$\phi_e = \frac{M}{M'_y}\phi'_y$$

M = moment at a given point past the first yield point
M'_y = moment at first-yield for concrete cross-section
ϕ'_y = curvature of concrete cross-section at first-yield moment

Equation Design Set #4

$$\Delta_{tu} = D\left[0.0255\psi\left(\frac{L_{mb}}{D}\right) - 0.0652\right]$$

$$\psi = 0.0157\left(\frac{L_{col}}{D}\right) + 0.9342 \qquad \text{For } c_u \le 70\,\text{kPa}(10\,\text{psi}).\ \text{Else } \psi = 1$$

$$\Delta_{ty} = \frac{\Delta_{tu}}{4.37}$$

$$\Delta_{eby} = \theta_{eby} L_{ma}$$

$$\Delta_{ebu} = \theta_{ebu} L_{ma}$$

$$\Delta_{p} = \theta_{p} L_{ma}$$

$$V_{t1} = \frac{M_{max} - P\left(\Delta_p + \Delta_{eb}\right) + V_s\left(h_s/2\right)}{L_{ma}}$$

$$\Delta_{ea} = \frac{V_{t1} L_{ma}^{\ 3}}{3EI_e}$$

The above value needs to be corrected for P-Δ effects using the following:

$$V_t = \frac{M_{max} - P\left(\Delta_p + \Delta_{eb} + \Delta_{ea}\right) + V_s\left(h_s/2\right)}{L_{ma}}$$

$$\Delta_{ea} = \frac{V_t L_{ma}^{\ 3}}{3EI_e}$$

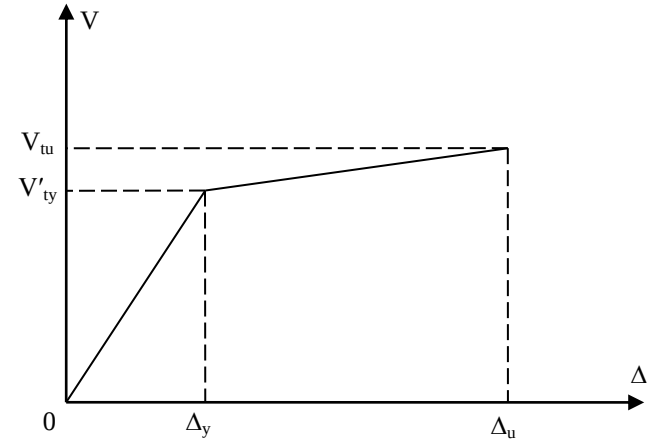

Note:

1. V'_{ty} and V_{tu} correspond to values in design set 4
2. $\Delta_u = \Delta_{ea} + \Delta_{ebu} + \Delta_p + \Delta_{tu}$
3. $\Delta_y = \Delta_{ea} + \Delta_{eby} + \Delta_{ty}$

Figure 8-5: Final bilinear force-displacement response attained using the simplified method for cohesive soils

Simplified Method for Drilled Shafts in Cohesionless Soils (Equations in Section 2.2.4)

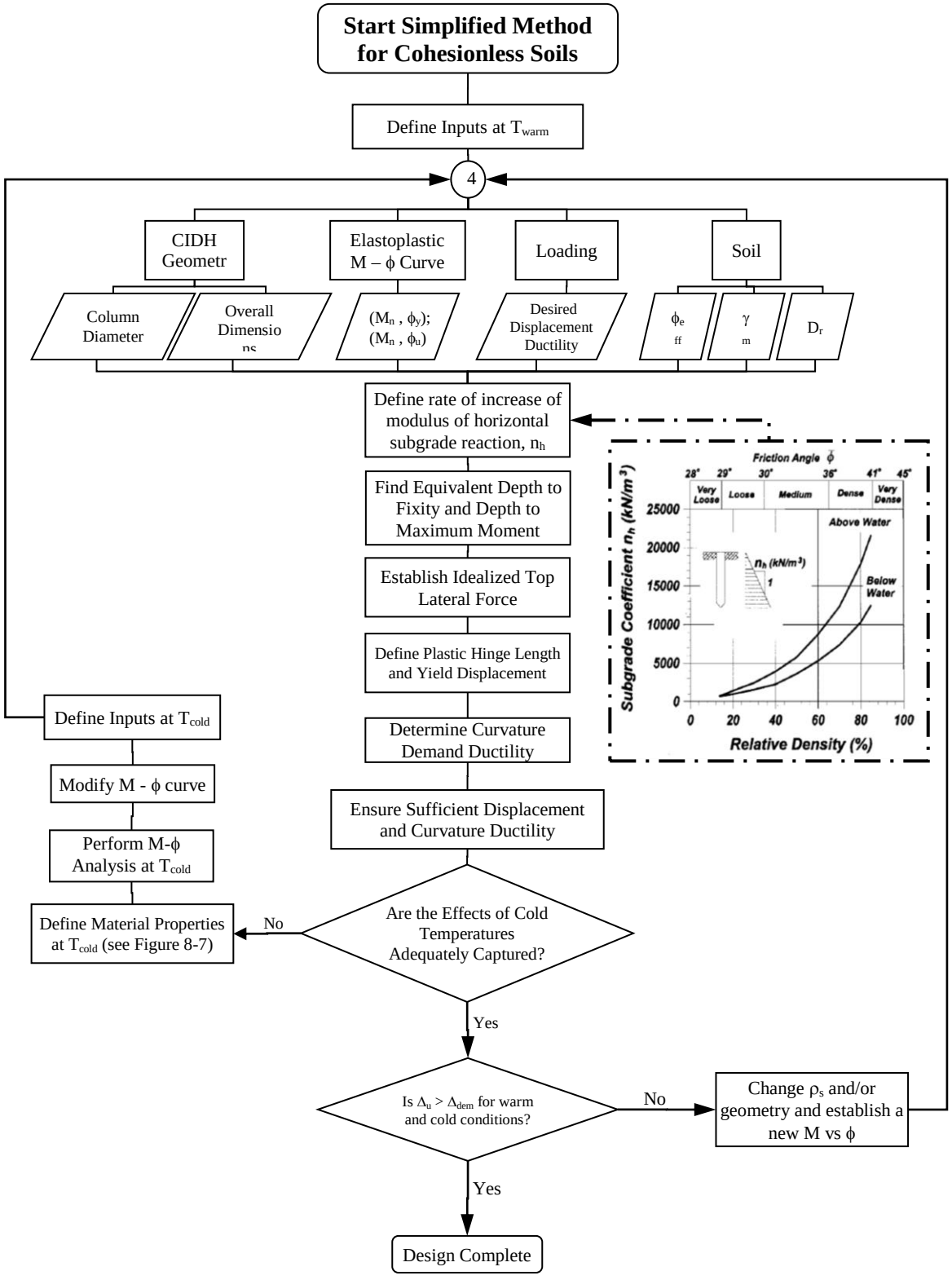

Figure 8-6: Simplified method design flowchart in cohesionless soil

Definition of Cold Temperature Material Properties

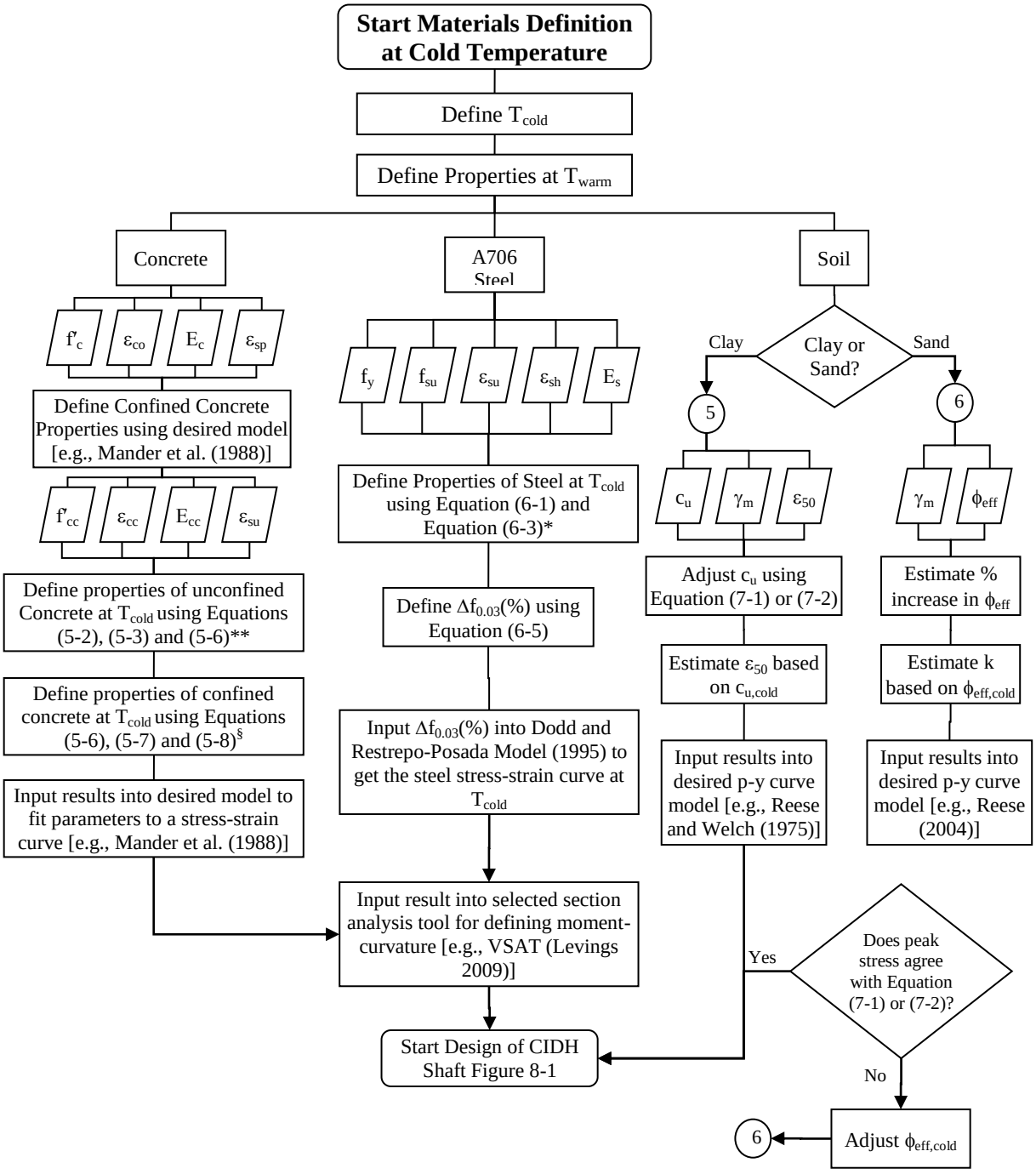

Notes:
* The other steel properties remain unchanged or can be computed based on these two equations
** Test data was not available for ε_{sp} therefore assume remains unchanged
§ Ultimate compressive strain does not change

Figure 8-7: Flowchart for defining concrete, steel and soil material properties at cold temperatures

8.4.2 Recommendations for Future Research

During the development of the proposed simplified model, the following recommendations were established:

- the use of a tri-linear curve in determining the lateral response could be investigated to more accurately capture the shear demands experienced by the system;
- further full-scale experimental testing should be performed in cohesive soils to verify the effectiveness of the model and the design guidelines suggested in Section 8.4.1;
- additional analyses should be run with differing structural parameters to better define the sensitivity of the simplified model; and
- an examination into cohesionless soils should be performed in the future to determine whether or not the same model may be used with this soil type thus creating a more coherent method for all soil types.

During the experimental investigations into the effects of seasonal freezing on the response of material properties a number of recommendations arose for future research into the material properties area. The recommendations are as follows:

- additional confined/unconfined concrete specimens should be constructed and tested so that a larger data set can be obtained to further verify the equations presented within this report that account for cold temperatures;
- larger specimens should be constructed and tested with the inclusion of longitudinal reinforcement to verify the approach with this reinforcement. This will also calibrate the equations for any possible size effect issue;
- additional testing should be performed on multiple bar sizes as it appears to effect the magnitude of increase of the yield and ultimate strengths of A706 mild steel reinforcing bar. In order to provide a better result a larger data set is required including more than two bar sizes;
- it is recommended that the initially proposed cyclic loading path be performed on a higher diameter/length ratio so that buckling does not occur and more useful data can be collected for mild steel reinforcement;
- it is recommended that future testing should be performed to provide a larger data set of results so that the effects of density and moisture content can be better examined for all soil types; and,

- testing should be performed on all soil types in order to provide equations for each specific soil to determine the ultimate compressive strength, strain at ultimate compressive strength and modulus of elasticity as a function of temperature.

REFERENCES

American Association of State and Highway Transportation Officials (AASHTO). (1998). *LRFD bridge design specifications, 2nd edition.* Washington D.C.: AASHTO.

AASHTO. (2007). *LRFD bridge design specifications with 2008 interim revisions, customary U.S. units, 4th edition.* Washington D.C.: AASHTO.

AASHTO. (2009). *Guide specifications for LRFD seismic bridge design.* Washington D.C.: AASHTO.

American Concrete Institute (ACI). (2008). *Building code requirements for structural concrete (ACI 318-08) and commentary (ACI 318R-08).* Farmington Hills, MI: ACI.

Andersland, O. B. and Anderson, D. M. (1978). *Geotechnical engineering for cold regions.* U.S.A.: McGraw-Hill Inc.

Anderson, J. B., Townsend, F. C. and Grajales, B. (2003). "Case history evaluation of laterally loaded piles." *Journal of geotechnical and geoenvironmental engineering* 129(3): 187-196.

Applied Technology Council (ATC). (1996). *Improved seismic design criteria for California bridges: provisional recommendations.* Redwood City, California: Applied Technology Council.

Ashour, M., Norris, G. and Pilling, P. (1998). "Lateral loading of a pile in layered soil using the strain wedge model." *Journal of geotechnical and geoenvironmental engineering* 124(4): 303-315.

ASTM Standard A615. (2009). "Standard specification for deformed and plain carbon-steel bars for concrete reinforcement." West Conshohocken, PA: ASTM International.

ASTM Standard D7300. (2006). "Standard test method for laboratory determination of strength properties of frozen soil at a constant rate of strain." West Conshohocken, PA: ASTM International.

ASTM Standard E8. [2004 (2006)]. "Standard test methods for tension testing of metallic materials." West Conshohocken, PA: ASTM International.

Bowles, J. E. (1988). *Foundation analysis and design, 4th edition.* United States of America: McGraw-Hill Book Company.

Broms, B. B. (1964a). "Lateral resistance of piles in cohesive soils." *Journal of soil mechanics foundation division, American Society of Civil Engineers* 90(SM2), 27-63.

Broms, B. B. (1964b). "Lateral resistance of piles in cohesionless soils." *Journal of soil mechanics foundation division, American Society of Civil Engineers* 90(SM3), 123-156.

Bruneau, M., Uang, C-M. and Whittaker, A. (1997). *Ductile design of steel structures.* New York: Mc-Graw Hill.

Budek, A. M., Priestley, M. J. N. and Benzoni, G. (2000). "Inelastic seismic response of bridge drilled-shaft rc pile/columns." *Journal of structural engineering* 126(4): 510-517.

Bureau of Transportation Statistics. (Accessed Online: 2007). "Conditions of U.S. Highway Bridges By State." Washington D.C.: United States Department of Transportation. http://www.bts.gov/current_topics/2007_08_02_bridge_data/html/bridges_by_state.html

Butkovich, T. R. (1954). "Ultimate strength of ice." *Report No. 11.* U.S. Army Res.

California Department of Transportation (Caltrans). (1990). *Bridge design aids: pile shaft design*: 12-30 to 12-49. (Accessed online: 2009 through http://www.dot.ca.gov).

Caltrans (2006). *Seismic design criteria version 1.4.* Sacramento, CA: Caltrans

Carr, A. J. (2005) *3D Ruaumoko: inelastic three-dimensional analysis program*. Christchurch, NZ: University of Canterbury – Department of Civil Engineering.

Chai, Y. H. (2002). "Flexural strength and ductility of extended pile-shafts I: Analytical model." *Journal of structural engineering* 128(5): 586-594.

Chai, Y. H. and Hutchinson, T. C. (2002). "Flexural strength and ductility of extended pile-shafts II: Experimental study." *Journal of structural engineering* 128(5): 595-602.

Concrete Reinforcing Steel Institute (CRSI). (1990). *ASTM A706 reinforcing - bars technical information with commentary on usage and availability.* Schaumburg, IL: CRSI

Crowther, G. S. (1990). "Analysis of laterally loaded piles embedded in layered frozen soil." *Journal of geotechnical engineering* 116(7): 1137-1152.

Das, B. M. (2004). *Principles of Foundation Engineering, 5th Edition.* United States of America: Thomson, Brooks/Cole.

Davisson, M. T. and Robinson, K. E. (1965). "Bending and buckling of partially embedded piles." *Proceedings of the sixth international conference S. M. and F. E.* Montreal, Canada: University of Toronto Press. pp. 243-246.

DeGaetano, A. T., and Wilks, D. S. (2001). "Development of Frost Depth Maps for the United States." *Research report.* Upper Marlboro, Maryland: National Association for Home Builders (NAHB) Research Center, Inc.

Dodd, L. L. and Restrepo-Posada, J. I. (1995). "Model for predicting cyclic behavior of reinforcing steel." *Journal of structural engineering* 121(3): 433-445.

ENSR (2002). " Fort Wainwright hydrological data network." Alaska: University of Fairbanks. (Accessed Online November 2007). http://www.uaf.edu/water/projects/ftww/gwdata/gwdata.html.

Filiatrault, A. and Holleran, M. (2001a). "Stress-strain behavior of reinforcing steel and concrete under seismic strain rates and low temperatures." *Materials and structures* 34: 235-239.

Filiatrault, A. and Holleran, M. (2001b). "Characteristics of reinforced concrete bridge components under seismic strain rates and low temperatures." *Proceedings of the 18th US-Japan bridge engineering workshop, St. Louis.* FHWA: 49-63.

Gustafson, D. (2007). *Revisiting Low-Alloy Steel Reinforcing Bars.* (Accessed online: May 5, 2009 through BNET at: http://findarticles.com/p/articles/mi_qa5363/is_200701/ai_n21290713/?tag=content;col1)

Harris, J. S. (1995). *Ground freezing in practice.* London, England: Thomas Telford Services Ltd.

Hetenyi, M. (1946). *Beams on elastic foundation.* Ann Arbor, Michigan: University of Michigan Press.

Hose, Y., Brestel, D., Seible, F. and Dowell, R. (2001). *Assessment of hoop strains in the flexural plastic hinge region of typical bridge columns.* San Diego, CA: University of California

Iowa Department of Transportation (Accessed Online: September 2009). http://www.i235.com/ped_bridge_2.htm

Japanese Meteorological Agency. (Accessed Online: August 2008). http://www.jma.go.jp/jma/indexe.html

Kumar, S. and Lalvani, L. (2004). "Lateral load-deflection response of drilled shafts in sand." *Journal of the institution of engineers (India): civil engineering division* 84(4): 282-286.

Lee, G. C., Shih, T. S. and Chang, K. C. (1988a). "Mechanical properties of concrete at low temperature." *Journal of cold regions engineering* 2(1): 13-24.

Lee, G. C., Shih, T. S. and Chang, K. C. (1988b). "Mechanical properties of high-strength concrete at low temperature." *Journal of cold regions engineering* 2(4): 169-178.

Levings, J. C. (2009). "Development of a versatile section analysis tool for use in seismic design." *Master's Thesis.* Ames, Iowa: Iowa State University.

Levings, J. C. and Sritharan, S. (2010: In Progress). "Stress-strain characteristics of ASTM A706 mild steel reinforcement at low temperatures." *To be submitted to: Journal of materials in civil engineering.*

Mander, J. B., Priestley, M. J. N. and Park, R. (1988a). "Theoretical stress-strain model for confined concrete." *Journal of structural engineering* 114(8): 1804-1826.

Mander, J. B., Priestley, M. J. N. and Park, R. (1988b). "Observed stress-strain behavior of confined concrete." *Journal of structural engineering* 114(8): 1827-1849.

Merriam-Webster. (Accessed Online: October 22, 2008). Bridge definition. http://www.merriam-webster.com/dictionary.

Montejo, A., Kowalsky, M. and Hassan, T. (2008). *Seismic behavior of reinforced concrete bridge columns at sub-freezing temperatures.* Springfield, Illinois: North Carolina State University, FHWA.

Parametric Technology Corporation (PTC). (2007). *Mathcad, version 14.0.0.163.* Needham: PTC.

Poulos, H. G. and Davis, E. H. (1980). *Pile foundation analysis and design.* New York: Wiley.

Priestley, M. J. N., Seible, F. and Calvi, G. M. (1996). *Seismic design and retrofit of bridges.* New York: John Wiley & Sons, Inc.

Priestley, M. J. N., Calvi, G. M. and Kowalsky, M. J. (2007). *Displacement-based seismic design of structures.* Pavia, Italy: IUSS Press

Reese, L. C. and Welch, R. C. (1975). "Lateral loading of deep foundations in stiff clay." *Journal of geotechnical engineering division* 101(GT7): 633-649.

Reese, L. C., Wang, S. T., Isenhower, W. M. and Arrellaga, J. A. (2000). *LPILE plus 4.0, technical manual.* Austin: Ensoft, Inc.

Reese, L. C., Wang, S. T., Isenhower, W. M., Arrellaga, J. A. and Hendrix, J. (2004). *LPILE plus 5.0, user's manual.* Austin: Ensoft, Inc.

Reese, L. C., Wang, S. T.. Isenhower, W. M. and Arrellaga, J. A. (2004). *LPILE plus 5.0, technical manual.* Austin: Ensoft, Inc.

Robertson, P. K. and Campanella, R. G. (1983). "Interpretation of cone penetration tests. Part II: Clay." *Canadian geotechnical journal* 20(4): 734-745.

Sayles, F. H. (1966). "Low temperature soil mechanics." *Technical note.* Hanover, N.H.: Cold regions research and engineering laboratory.

Sayles, F. H. (1968). "Creep of frozen sands." *Technical Report 190.* Hanover, N.H.: Cold regions research and engineering laboratory.

Sehnal, Z. A., Kronen, H. and Marshall, A. L. (1983). "Factors influencing the low temperature strength of concrete." *Proceedings 2nd international conference on cryogenic concrete, Amsterdam.* London: Concrete Society of UK. pp. 1-11.

Sloan, J. E. (2005). "The seismic behavior of reinforced concrete members at low temperatures." *Master's Thesis.* Raleigh, NC: North Carolina State University.

Sritharan, S., Suleiman, M. T. and White, D. J. (2007). "Effects of seasonal freezing on bridge column-foundation-soil interaction and their implications." *Earthquake spectra* 23(1): 199-222.

Sritharan, S. and Shelman, A. (2008). "An assessment of broad impact of seasonally frozen soil on seismic response of bridges in the U.S. and Japan." *Proceedings of the 24th US-Japan bridge engineering workshop, Minneapolis.* FHWA: 429-440.

State of Alaska (2006). "Department of Transportation/Department of Labor" (Accessed online October 2007 from http://www.state.ak.us/).

Suarez, V. and Kowalsky, M. J. (2007). "Displacement-based seismic design of drilled shaft bents with soil-structure interaction." *Journal of earthquake engineering* 11: 1010-1030.

Suleiman, M. T., Sritharan, S. and White, D. J. (2006). "Cyclic lateral load response of bridge column-foundation-soil systems in freezing conditions." *Journal of structural engineering* 132(11): 1745-1754.

Thiemann, Z. J. (2009). "Pretest three-dimensional finite element analysis of the girder-to-cap-beam connection of an inverted-tee cap beam designed for seismic loadings." *Master's Thesis.* Ames, Iowa: Iowa State University.

Tsytovich, N. A. (1975). *The mechanics of frozen ground.* U.S.A.: Scripta Book Company

United States Department of Agriculture, Natural Resources Conservation Service (2006). "Land resource regions and major land resource areas of the United States, Caribbean, and the Pacific Basin." *U.S. Department of Agriculture Handbook 296.*

United States Geological Survey (USGS). (Accessed Online: 2009) http://www.usgs.gov.

United States Geological Survey (USGS). (Accessed Online: July 6, 2009) About earthquakes: earthquake facts. *Earthquake hazards program web site.* http://earthquake.usgs.gov/learning/facts.php.

United States Geological Service. (2002). (Accessed Online: August 2008). "0.2 second spectral acceleration with a 10 percent probability of exceedance in 50 years seismic hazard map." *USGS*. http://earthquake.usgs.gov/research/hazmaps/products_data/2002/maps/.

University of Florida (UF). (2009). *FB-Pier v 3.2.1*. Florida: University of Florida.

Wahrhaftig, C. (1965). "Physiographic Divisions of Alaska." Geological *Survey Professional Paper 482*. Washington D.C.: U.S. Government Printing Office.

Weaver, J. S. and Morgenstern, N. R. (1981). "Pile design in permafrost." *Canadian geotechnical journal* 18: 357-370.

Williams, P. J. (1988). "Thermodynamic and mechanical conditions within frozen soils and their effects." *Proceedings of the 5th International Conference on Permafrost, Trondheim.* International Permafrost Association: 493-498

Wotherspoon, L. M., Sritharan, S. and Pender, M. J. (2010a). "Modeling the response of cyclically loaded bridge columns embedded in warm and seasonally frozen soils." *Engineering structures journal* 32:933-943.

Wotherspoon, L. M., Sritharan, S., Pender, M. J. and Carr, A. J. (2010b). "Investigation on the impact of seasonally frozen soil on the seismic response of bridge columns." *Journal of bridge engineering* 15(5):473-481.

Zhu, Y. and Carbee, L. (1984). "Uniaxial compressive strength of frozen silt under constant deformation rates." *Cold regions science and technology*. 9:3-15

APPENDIX A: ADDITIONAL INFORMATION FOR PROPOSED NEW MODEL

Example Calculations for SS1

- Input Parameters

Soil Input Variables:

Undrained Cohesive Strength, c_u =	21.79	psi
Soil Moist Unit Weight, γ_m =	0.078	lb/in^3
Strain at 1/2 max princ stress dif., ε_{50} =	0.005	in/in

Pile Input Variables:

Column Diameter, D =	24	in
Aboveground Column Height, L_{col} =	106	in
Length of Foundation, L_f =	410	in
Axial Load to Column, P =	0	lb

Inputs from Moment Curvature Analysis:

Moment at First Yield, M'_y =	3852720	lb-in
Curvature at First Yield, ϕ'_y =	0.00015002	1/in
Idealized Moment at Yield, M_y =	6002005	lb-in
Idealized Curvature at Yield, ϕ_y =	0.00023371	1/in
Moment at Ultimate, M_u =	7094760	lb-in
Curvature at Ultimate, ϕ_u =	0.003527164	1/in
Effective Flexural Rigidity, EI_e =	25681375817	lb-in^2

- Output Parameters

Ultimate Limit State Calculations

Maximum Moment Location using Equation (4-2):

Coef. for Max Moment Location, α_{ma} =	0.032	
Coef. for Max Moment Location, β_{ma} =	0.408	
Coef. for Max Moment Location, χ_{ma} =	3.186	
Maximum Moment Location, L_{ma} =	134.727	in

First Zero Moment Location using Equation (4-5):

Coef. for Zero Moment Location, α_{m0} =	22.786	
Coef. for Zero Moment Location, β_{m0} =	-0.237	
First Zero Moment Location, L_{m0} =	263.254	in

Length Between Maximum Moment and Zero Moment Location:

Dist. btwn Max M and Zero M Location, L_{mb} =	128.526	in

Soil Resistance Outputs at Ultimate Condition using Equation (4-12):

Height of Soil Above Max Moment, h_s =	28.727	in
Soil Resistance at Ultimate, p_u =	1749.786	lb/in
Soil Shear Force Resistance, V_s =	50.267	kip

Translation at Maximum Moment Location (Ultimate) using Equation (4-18):

Soft Soil Correction Factor, ψ =	N/A	
Translation at Max M Location, Δ_{TRANS} =	1.713	in

Displacement due to Elastic Rotation Below Max M (Ultimate) using Equations (4-11) and (4-22):

Elastic Rotation Below Max Moment, θ_{ebu} =	0.017	rad
Displacement due to θ_{ebu}, Δ_{ebu} =	2.317	in

Plastic Displacement of the System at Ultimate Condition using Equations (4-7), (4-9) and (4-21):

Analytical Plastic Hinge Length, L_{pb} =	20.564	in
Elastic Curvature at Ultimate, ϕ_e =	0.000276	1/in
Plastic Curvature at Ultimate, ϕ_p =	0.00325	1/in
Plastic Rotation below Max M, θ_{pb} =	0.067	rad
Plastic Displacement at Ultimate, Δ_p =	18.014	in

Determine Lateral Displacement due to Cantilever Action using Equations (4-23) thru (4-25):

Initial Lateral Force at Column, V_{t1} =	58.019	kip
Cantilever Displacement, Δ_{ea} =	1.842	in
Corrected Lateral Force at Column, V_t =	58.019	kip
Corrected Cantilever Displacement, Δ_{eac} =	1.842	in

Determine Ultimate Displacement and Force at top of Column using Equations (4-20) and (4-25):

Lateral Force at Top of Column, V_t =	58019.205	lb
Ultimate Displacement, Δ_u =	23.885	in

Yield Calculations

Translation at Maximum Moment Location (Yield) using Equation (4-17):

Translation at Max M Location, Δ_{TRANSy} =	0.392	in

Displacement due to Elastic Rotation Below Max M (Yield) using Equations (4-10) and (4-22):

Elastic Rotation Below Max Moment, θ_{eby} =	0.011	rad
Displacement due to θ_{eby}, Δ_{eby} =	1.444	in

Determine Lateral Displacement due to Cantilever Action using Equations (4-13), (4-14) and (4-23) thru (4-25):

Correction Factor for Soil Resistance, η =	0.661	
Initial Lateral Force at Column, V_{t1y} =	32.140	kip
Cantilever Displacement, Δ_{eay} =	1.020	in
Corrected Lateral Force at Column, V_{ty} =	32.140	kip
Corrected Cantilever Displacement, Δ_{eacy} =	1.020	in

Determine Yield Displacement and Force at top of Column using Equations (4-20) and (4-25):

Lateral Force at Top of Column, V_{ty} =	32139.612	lb
Ultimate Displacement, Δ_y =	2.856	in

Initial Values for Force Displacement Curve

Lateral Force at Top of Column, V_{ti} =	0.000	lb
Ultimate Displacement, Δ_i =	0.000	in

Spring Properties

Rotational Spring Properties:

Initial Rotation, θ_i =	0.00000	rad
Initial Moment, M_i =	0.00000	kip-in
Yield Rotation, θ_{eby} =	0.01072	rad
Yield Moment, M_y =	3852.72000	kip-in
Ultimate Rotation, $\theta_{eb} + \theta_p$ =	0.15091	rad
Ultimate Moment, M_u =	7094.76000	kip-in

Translational Spring Properties:

Initial Displacement, Δ_{ti} =	0.00000	in
Initial Force, V_{ti} =	0.00000	kip
Yield Displacement, Δ_{ty} =	0.39190	in
Yield Force, V_{ty} =	-1.09468	kip
Ultimate Displacement, Δ_{tu} =	1.71262	in
Ultimate Force, V_{tu} =	7.75229	kip

Soil Spring Properties:

Disp. at ε_{50} Value, y_{50} =	0.30000	in
Ultimate Soil Resistance, p_u =	1749.78577	lb/in

Soil Spring Values using Equation (2-5)

y in	p lb/in	Vs kip
0.00	0.35	0.010042
0.1	664.7748	19.0973
0.2	790.555	22.71064
0.3	874.8929	25.13346
0.4	940.1336	27.00766
0.5	994.0702	28.55712
1	1182.155	33.96033
1.5	1308.27	37.58328
2	1405.828	40.38587
2.5	1486.482	42.70286
3	1555.804	44.69431
3.5	1616.931	46.45034
4	1671.82	48.02716
4.5	1721.78	49.46238
4.75	1745.211	50.1355
4.8	1749.786	50.26691
5	1749.786	50.26691
5.5	1749.786	50.26691

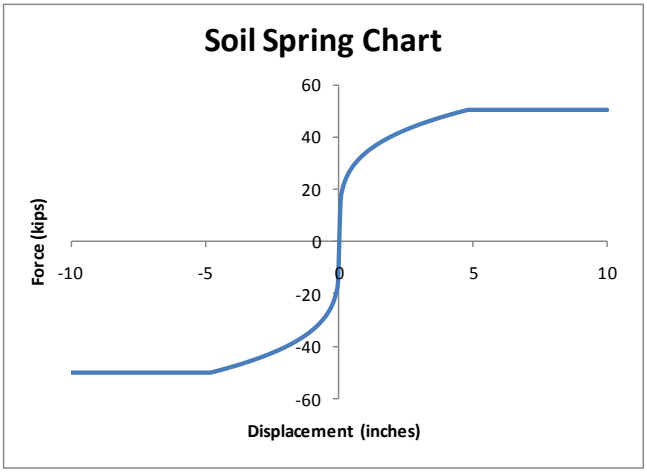

- Additional Analytical Verification #1

Table A-1: Input parameters for additional analytical verification #1

Soil Properties		
c_u	48.3 kPa	7 psi
γ_m	21.2 kN/m^3	0.078 lb/in^3
ε_{50}	0.007	
Structural Properties		
D	0.61 m	24 in.
L_{col}	2.69 m	106 in.
L_f	10.4 m	410 in.
ALR	5 %	
M-ϕ Response	See Section 4.3.2	

Table A-2: Comparison of critical parameters at the ultimate limit state for additional analytical verification #1

	Detailed Analysis		Proposed New Model		
Property	SI	English	SI	English	Error
L_{ma}	4.11 m	161.7 in.	4.13 m	162.6 in.	0.49%
L_{m0}	8.71 m	342.9 in.	8.75 m	344.6 in.	0.49%
L_{mb}	4.60 m	181.2 in.	4.63 m	182.1 in.	0.65%
p_u	110.2 kN/m	629.1 lb/in	108.3 kN/m	618.4 lb/in	-1.71%
V_s	155.7	35.0 kip	155.7 kN	35.0 kip	0%
Δ_t	8.28 cm	3.26 in.	9.96 cm	3.92 in.	20.29%
θ_{eb}	0.0244 rad		0.024 rad		-1.64%
Δ_{eb}	10.01 cm	3.94 in.	9.96 cm	3.92 in.	-0.50%
L_{pb}	0.83 m	32.87 in.	0.74 m	29.13 in.	-10.84%
θ_{pb}	0.106 rad		0.094 rad		-11.32%
θ_p	0.199 rad		0.188 rad		-5.53%
Δ_p	0.83 m	32.59 in.	0.78 m	30.57 in.	-6.02%
Δ_{ea}	6.68 cm	2.63 in.	4.09 cm	1.61 in.	-38.77%
V_t	113.4 kN	25.5 kip	116.1 kN	26.1 kip	2.35%
Δ_u	1.03 m	40.37 in.	0.99 m	39.14 in.	-3.05%

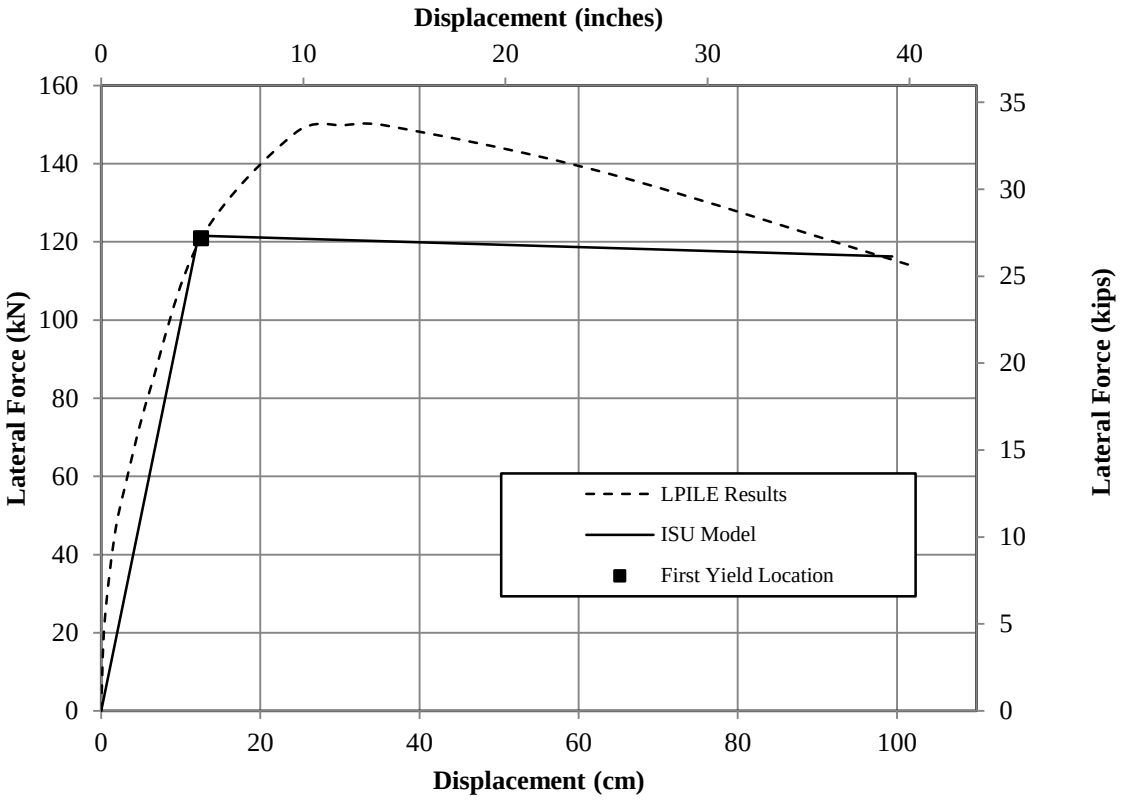

Figure A-1: Global response comparison of new methodology with additional analytical verification #1

- Additional Analytical Verification #2

Table A-3: Input parameters for additional analytical verification #2

Soil Properties		
c_u	48.3 kPa	7 psi
γ_m	21.2 kN/m^3	0.078 lb/in^3
ε_{50}	0.007	
Structural Properties		
D	0.61 m	24 in.
L_{col}	6.10 m	240 in.
L_f	10.4 m	410 in.
ALR	5 %	
M-ϕ Response	See Section 4.3.2	

Table A-4: Comparison of critical parameters at the ultimate limit state for additional analytical verification #2

	Detailed Analysis		Proposed New Model		
Property	SI	English	SI	English	Error
L_{ma}	6.71 m	264.3 in.	6.79 m	267.3 in.	1.19%
L_{m0}	11.48 m	452.1 in.	11.29 m	444.6 in.	-1.66%
L_{mb}	4.77 m	187.8 in.	4.50 m	177.3 in.	-5.66%
p_u	94.2 kN/m	537.9 lb/in	97.95 kN/m	559.3 lb/in	3.98%
V_s	58.3 kN	13.1 kip	68.1 kN	15.3 kip	16.81%
Δ_t	9.14 cm	3.60 in.	8.56 cm	3.37 in.	-6.35%
θ_{eb}	0.0256 rad		0.024 rad		-6.25%
Δ_{eb}	17.20 cm	6.77 in.	15.95 cm	6.28 in.	-7.27%
L_{pb}	0.87 m	34.37 in.	0.72 m	28.37 in.	-17.24%
θ_{pb}	0.111 rad		0.092 rad		-17.12%
θ_p	0.221 rad		0.183 rad		-17.19%
Δ_p	1.48 m	58.3 in.	1.24 m	48.95 in.	-16.22%
Δ_{ea}	16.76 cm	6.60 in.	4.01 cm	1.58 in.	-76.1%
V_t	6.81 kN	1.53 kip	26.4 kN	5.94 kip	288%
Δ_u	1.86 m	73.08 in.	1.53 m	60.18 in.	-17.65%

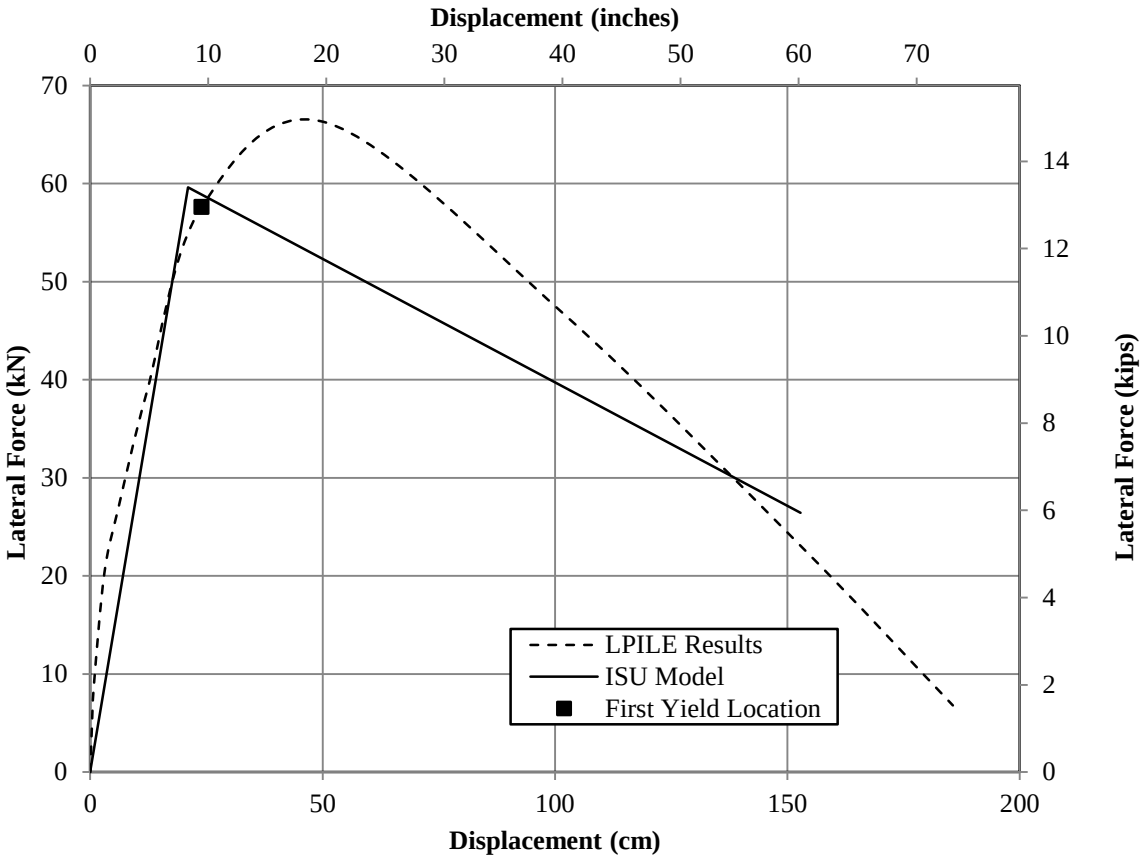

Figure A-2: Global response comparison of new methodology with additional analytical verification #2

- Additional Analytical Verification #3

Table A-5: Input parameters for additional analytical verification #3

Soil Properties		
c_u	168.6 kPa	24.455 psi
γ_m	21.2 kN/m^3	0.078 lb/in^3
ε_{50}	0.005	
Structural Properties		
D	0.61 m	24 in.
L_{col}	0 m	0 in.
L_f	10.4 m	410 in.
ALR	5 %	
M-ϕ Response	See Section 4.3.2	

Table A-6: Comparison of critical parameters at the ultimate limit state for additional analytical verification #3

	Detailed Analysis		Proposed New Model		
Property	SI	English	SI	English	Error
L_{ma}	1.87 m	73.8 in.	1.85 m	72.93 in.	-1.07%
L_{m0}	4.80 m	189.0 in.	4.73 m	186.4 in.	-1.46%
L_{mb}	2.93 m	115.2 in.	2.88 m	113.4 in.	-1.71%
p_u	374.7 kN/m	2139.5 lb/in	398.6 kN/m	2276.2 lb/in	6.38%
V_s	702.4 kN	157.9 kip	738.4 kN	166.0 kip	5.13%
Δ_t	3.35 cm	1.32 in.	3.38 cm	1.33 in.	0.90%
θ_{eb}	0.0156 rad		0.015 rad		-3.85%
Δ_{eb}	2.92 cm	1.15 in.	2.82 cm	1.11 in.	-3.48%
L_{pb}	0.53 m	20.72 in.	0.46 m	18.15 in.	-12.40%
θ_{pb}	0.067 rad		0.059 rad		-11.94%
θ_p	0.13 rad		0.117 rad		-10.00%
Δ_p	0.24 m	9.53 in.	0.22 m	8.54 in.	-8.33%
Δ_{ea}	1.55 cm	0.61 in.	2.18 cm	0.86 in.	40.98%
V_t	676.1 kN	152.0 kip	708.2 kN	159.2 kip	4.75%
Δ_u	0.30 m	11.79 in.	0.30 m	11.84 in.	0.42%

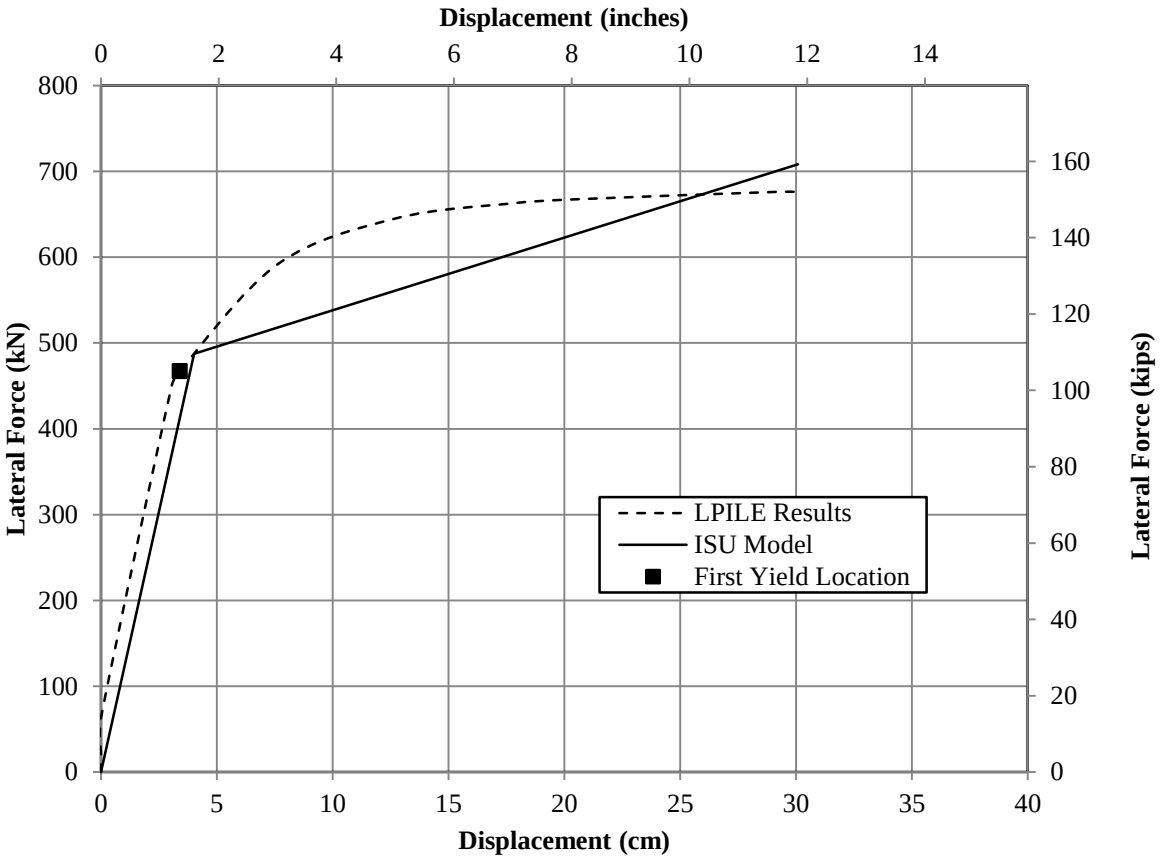

Figure A-3: Global response comparison of new methodology with additional analytical verification #3

- Additional Analytical Verification #4

Table A-7: Input parameters for additional analytical verification #4

Soil Properties		
c_u	168.6 kPa	24.455 psi
γ_m	21.2 kN/m^3	0.078 lb/in^3
ε_{50}	0.005	
Structural Properties		
D	0.61 m	24 in.
L_{col}	2.69 m	106 in.
L_f	10.4 m	410 in.
ALR	5 %	
M-ϕ Response	See Section 4.3.2	

Table A-8: Comparison of critical parameters at the ultimate limit state for additional analytical verification #4

	Detailed Analysis		Proposed New Model		
Property	SI	English	SI	English	Error
L_{ma}	3.32 m	130.7 in.	3.36 m	132.3 in.	1.20%
L_{m0}	6.50 m	256.0 in.	6.50 m	256.1 in.	0.04%
L_{mb}	3.18 m	125.3 in.	3.14 m	123.8 in.	-1.26%
p_u	301.6 kN/m	1722.4 lb/in	341.0 kN/m	1946.9 lb/in	13.06%
V_s	189.5 kN	42.6 kip	228.2 kN	51.3 kip	20.42%
Δ_t	4.34 cm	1.71 in.	4.04 cm	1.59 in.	-6.91%
θ_{eb}	0.0174 rad		0.017 rad		-2.30%
Δ_{eb}	5.77 cm	2.27 in.	5.59 cm	2.20 in.	-3.12%
L_{pb}	0.61 m	24.15 in.	0.50 m	19.81 in.	-18.03%
θ_{pb}	0.078 rad		0.064 rad		-17.95%
θ_p	0.14 rad		0.128 rad		-8.57%
Δ_p	0.48 m	18.8 in.	0.43 m	16.92 in.	-10.42%
Δ_{ea}	4.19 cm	1.65 in.	3.30 cm	1.30 in.	-21.24%
V_t	174.8 kN	39.3 kip	179.7 kN	40.4 kip	2.80%
Δ_u	0.59 m	23.36 in.	0.56 m	22.01 in.	-5.08%

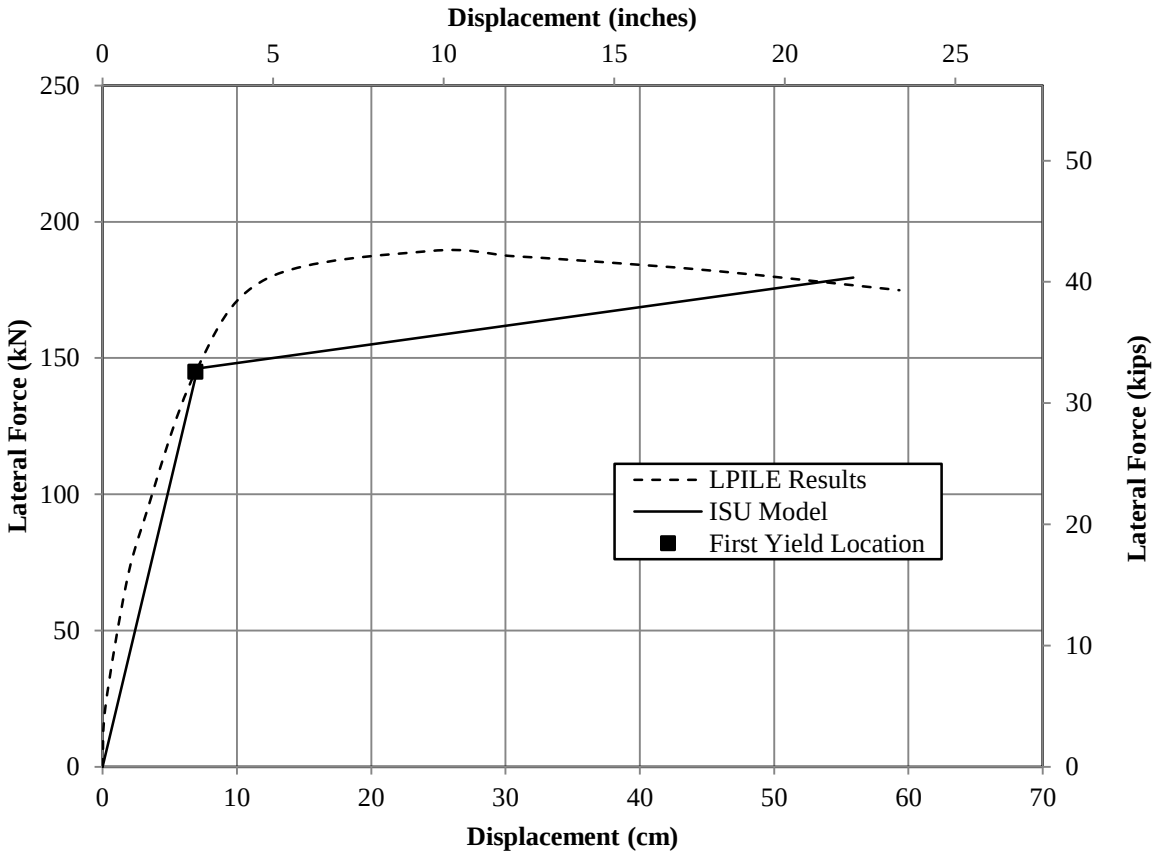

Figure A-4: Global response comparison of new methodology with additional analytical verification #4

- Additional Analytical Verification #5

Table A-9: Input parameters for additional analytical verification #5

Soil Properties		
c_u	168.6 kPa	24.455 psi
γ_m	21.2 kN/m^3	0.078 lb/in^3
ε_{50}	0.005	
Structural Properties		
D	0.61 m	24 in.
L_{col}	6.10 m	240 in.
L_f	10.4 m	410 in.
ALR	5 %	
M-ϕ Response	See Section 4.3.2	

Table A-10: Comparison of critical parameters at the ultimate limit state for additional analytical verification #5

	Detailed Analysis		Proposed New Model		
Property	SI	English	SI	English	Error
L_{ma}	6.38 m	251.3 in.	6.37 m	250.8 in.	-0.16%
L_{m0}	9.61 m	378.4 in.	9.72 m	382.7 in.	1.14%
L_{mb}	3.23 m	127.1 in.	3.35 m	131.9 in.	3.72%
p_u	263.8 kN/m	1506.6 lb/in	321.7 kN	1837.0 lb/in	21.95%
V_s	75.6 kN	17.0 kip	88.1 kN	19.8 kip	16.53%
Δ_t	4.19 cm	1.65 in.	4.57 cm	1.80 in.	9.07%
θ_{eb}	0.0174 rad		0.018 rad		3.45%
Δ_{eb}	11.10 cm	4.37 in.	11.23 cm	4.42 in.	1.17%
L_{pb}	0.59 m	23.33 in.	0.54 m	21.1 in.	-8.47%
θ_{pb}	0.075 rad		0.068 rad		-9.33%
θ_p	0.17 rad		0.136 rad		-20.00%
Δ_p	1.06 m	41.6 in.	0.87 m	34.16 in.	-17.92%
Δ_{ea}	15.01 cm	5.91 in.	6.43 cm	2.53 in.	-57.12%
V_t	35.7 kN	8.03 kip	51.6 kN	11.6 kip	44.54%
Δ_u	1.33 m	52.5 in.	1.09 m	42.9 in.	-18.05%

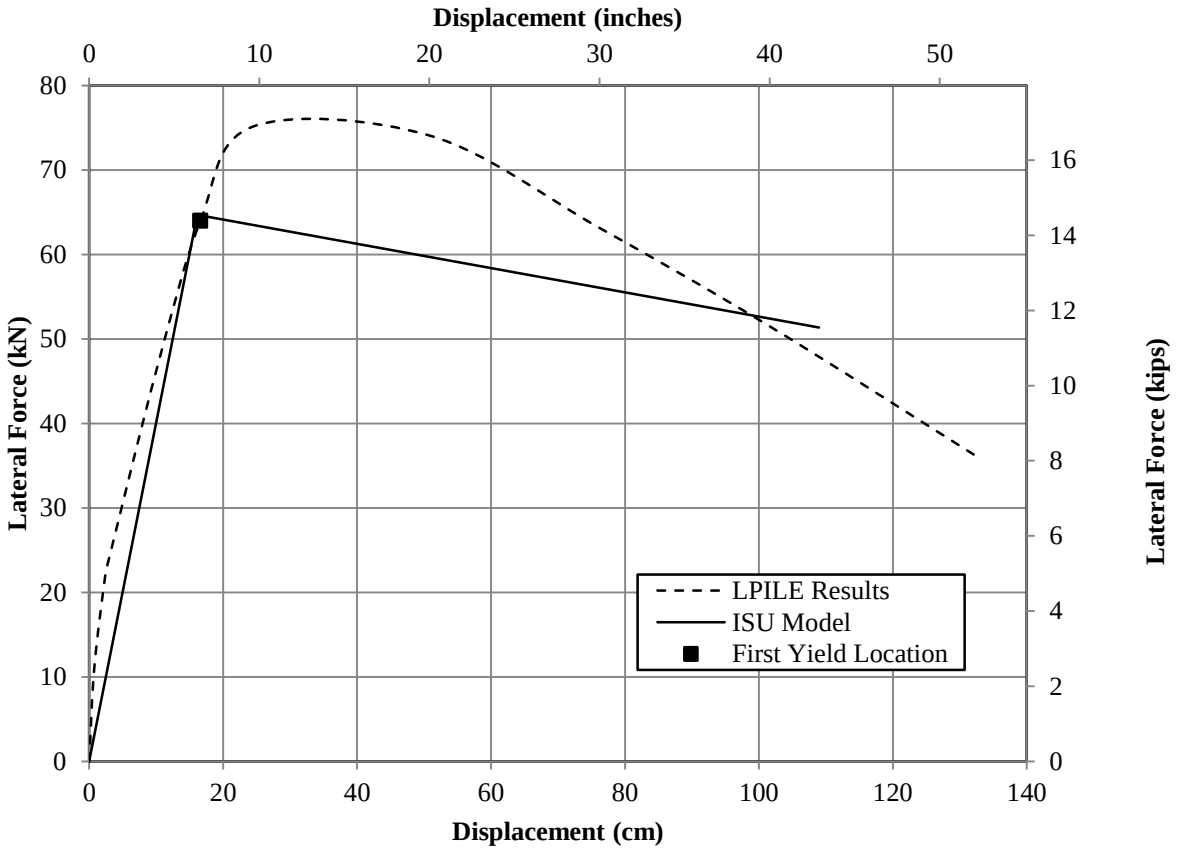

Figure A-5: Global response comparison of new methodology with additional analytical verification #5

- Additional Analytical Verification #6

Table A-11: Input parameters for additional analytical verification #6

Soil Properties		
c_u	379.2 kPa	55 psi
γ_m	21.2 kN/m^3	0.078 lb/in^3
ε_{50}	0.004	
Structural Properties		
D	0.61 m	24 in.
L_{col}	0 m	0 in.
L_f	10.4 m	410 in.
ALR	5 %	
M-ϕ Response	See Section 4.3.2	

Table A-12: Comparison of critical parameters at the ultimate limit state for additional analytical verification #6

	Detailed Analysis		Proposed New Model		
Property	SI	English	SI	English	Error
L_{ma}	1.39 m	54.67 in.	1.22 m	48.03 in.	-12.15%
L_{m0}	3.60 m	141.8 in.	3.62 m	142.6 in.	0.56%
L_{mb}	2.21 m	87.14 in.	2.40 m	94.59 in.	8.55%
p_u	748.8 kN/m	4276 lb/in	827.2 kN/m	4723.5 lb/in	10.47%
V_s	1040.0	233.8 kip	1009.3 kN	226.9 kip	-2.95%
Δ_t	1.85 cm	0.73 in.	2.16 cm	0.85 in.	16.44%
θ_{eb}	0.0117 rad		0.013 rad		11.11%
Δ_{eb}	1.63 cm	0.64 in.	1.57 cm	0.62 in.	-3.68%
L_{pb}	0.38 m	15.13 in.	0.38 m	15.14 in.	0.07%
θ_{pb}	0.0488 rad		0.049 rad		0.41%
θ_p	0.10 rad		0.0977 rad		-2.30%
Δ_p	0.14 m	5.32 in.	0.12 m	4.69 in.	-11.84%
Δ_{ea}	0.86 cm	0.34 in.	0.97 cm	0.38 in.	11.76%
V_t	1014.2 kN	228.0 kip	1060.0 kN	238.3 kip	4.52%
Δ_u	0.17 m	6.57 in.	0.17 m	6.52 in.	-0.76%

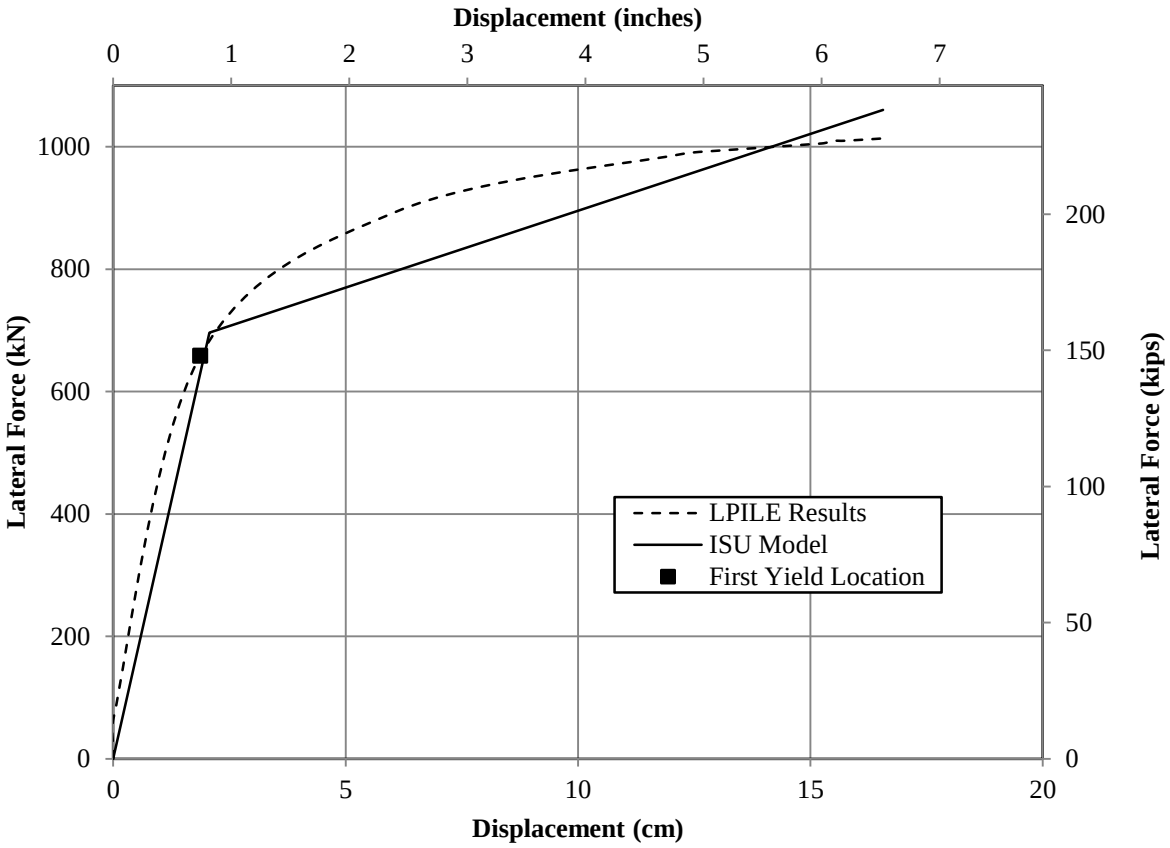

Figure A-6: Global response comparison of new methodology with additional analytical verification #6

- Additional Analytical Verification #7

Table A-13: Input parameters for additional analytical verification #7

Soil Properties		
c_u	379.2 kPa	55 psi
γ_m	21.2 kN/m^3	0.078 lb/in^3
ε_{50}	0.004	
Structural Properties		
D	0.61 m	24 in.
L_{col}	2.69 m	106 in.
L_f	10.4 m	410 in.
ALR	5 %	
M-ϕ Response	See Section 4.3.2	

Table A-14: Comparison of critical parameters at the ultimate limit state for additional analytical verification #7

	Detailed Analysis		Proposed New Model		
Property	SI	English	SI	English	Error
L_{ma}	3.06 m	120.4 in.	3.01 m	118.4 in.	-1.66%
L_{m0}	5.45 m	214.6 in.	5.37 m	211.3 in.	-1.54%
L_{mb}	2.39 m	94.20 in.	2.36 m	92.98 in.	-1.30%
p_u	572.3 kN/m	3268.0 lb/in	727.9 kN/m	4156.4 lb/in	27.18%
V_s	209.5 kN	47.1 kip	228.6 kN	51.4 kip	9.12%
Δ_t	2.29 cm	0.90 in	2.06 cm	0.81 in.	-10.00%
θ_{eb}	0.0129 rad		0.013 rad		0.78%
Δ_{eb}	3.94 cm	1.55 in.	3.78 cm	1.49 in.	-3.87%
L_{pb}	0.44 m	17.37 in.	0.38 m	14.88 in.	-14.34%
θ_{pb}	0.0561 rad		0.048 rad		-14.44%
θ_p	0.11 rad		0.096 rad		-12.73%
Δ_p	0.33 m	13.1 in.	0.29 m	11.37 in.	-13.21%
Δ_{ea}	3.51 cm	1.38 in.	2.74 cm	1.08 in.	-21.74%
V_t	203.7 kN	45.8 kip	209.1 kN	47.0 kip	2.62%
Δ_u	0.42 m	16.39 in.	0.37 m	14.75 in.	-10.01%

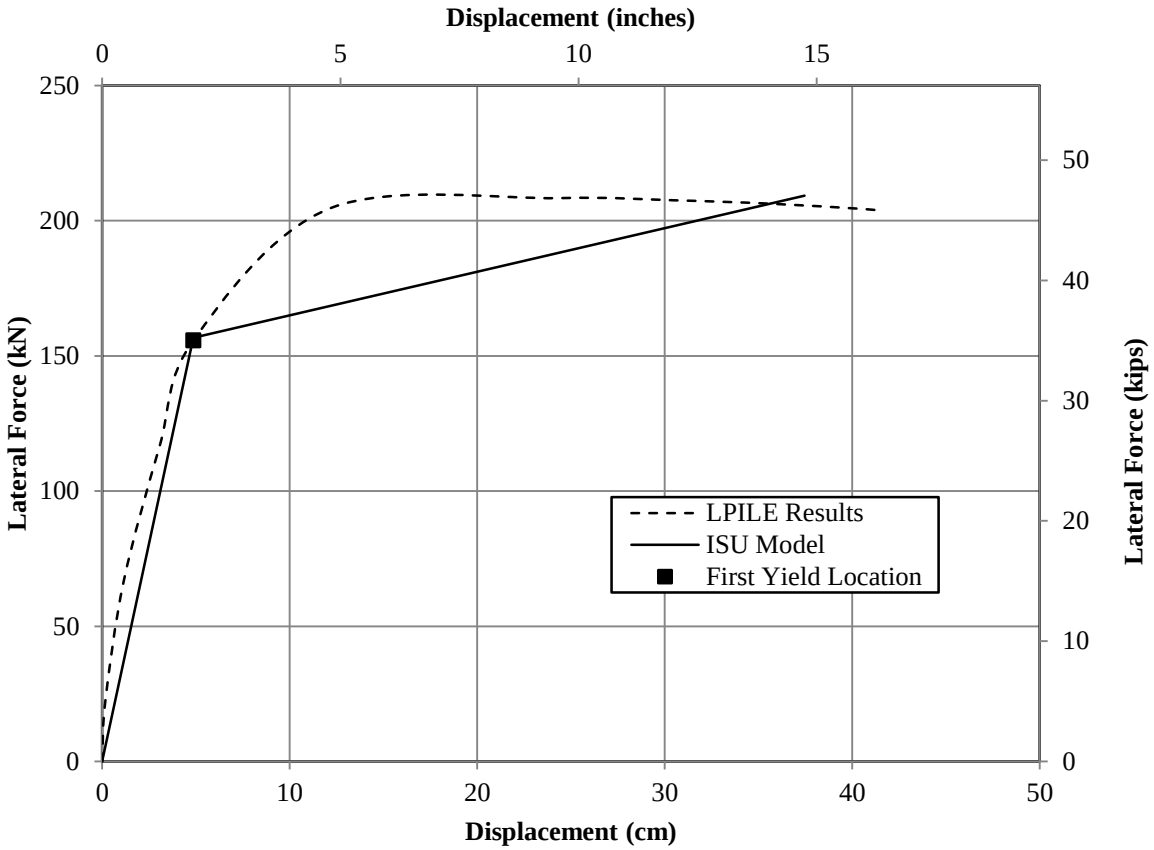

Figure A-7: Global response comparison of new methodology with additional analytical verification #7

- Additional Analytical Verification #8

Table A-15: Input parameters for additional analytical verification #8

Soil Properties		
c_u	379.2 kPa	55 psi
γ_m	21.2 kN/m^3	0.078 lb/in^3
ε_{50}	0.004	
Structural Properties		
D	0.61 m	24 in.
L_{col}	6.10 m	240 in.
L_f	10.4 m	410 in.
ALR	5 %	
M-ϕ Response	See Section 4.3.2	

Table A-16: Comparison of critical parameters at the ultimate limit state for additional analytical verification #8

	Detailed Analysis		Proposed New Model		
Property	SI	English	SI	English	Error
L_{ma}	6.27 m	247.0 in.	6.26 m	246.6 in.	-0.16%
L_{m0}	8.68 m	341.9 in.	8.82 m	347.2 in.	1.55%
L_{mb}	2.41 m	94.87 in.	2.36 m	100.6 in.	6.04%
p_u	516.4 kN/m	2948.9 lb/in	711.9 kN/m	4065.2 lb/in	37.85%
V_s	91.6 kN	20.6 kip	119.7 kN	26.9 kip	30.58%
Δ_t	2.21 cm	0.87 in.	2.54 cm	1.00 in.	14.94%
θ_{eb}	0.0129		0.014 rad		8.53%
Δ_{eb}	8.10 cm	3.19 in.	8.51 cm	3.35 in.	5.02%
L_{pb}	0.43 m	16.94 in.	0.41 m	16.09 in.	-5.02%
θ_{pb}	0.0547 rad		0.052 rad		-4.94%
θ_p	0.14 rad		0.104 rad		-25.71%
Δ_p	0.86 m	33.9 in.	0.65 m	25.62 in.	-24.42%
Δ_{ea}	14.33 cm	5.64 in.	7.90 cm	3.11 in.	-44.86%
V_t	49.8 kN	11.2 kip	66.3 kN	14.9 kip	33.04%
Δ_u	1.09 m	43.08 in.	0.84 m	33.08 in.	-23.21%

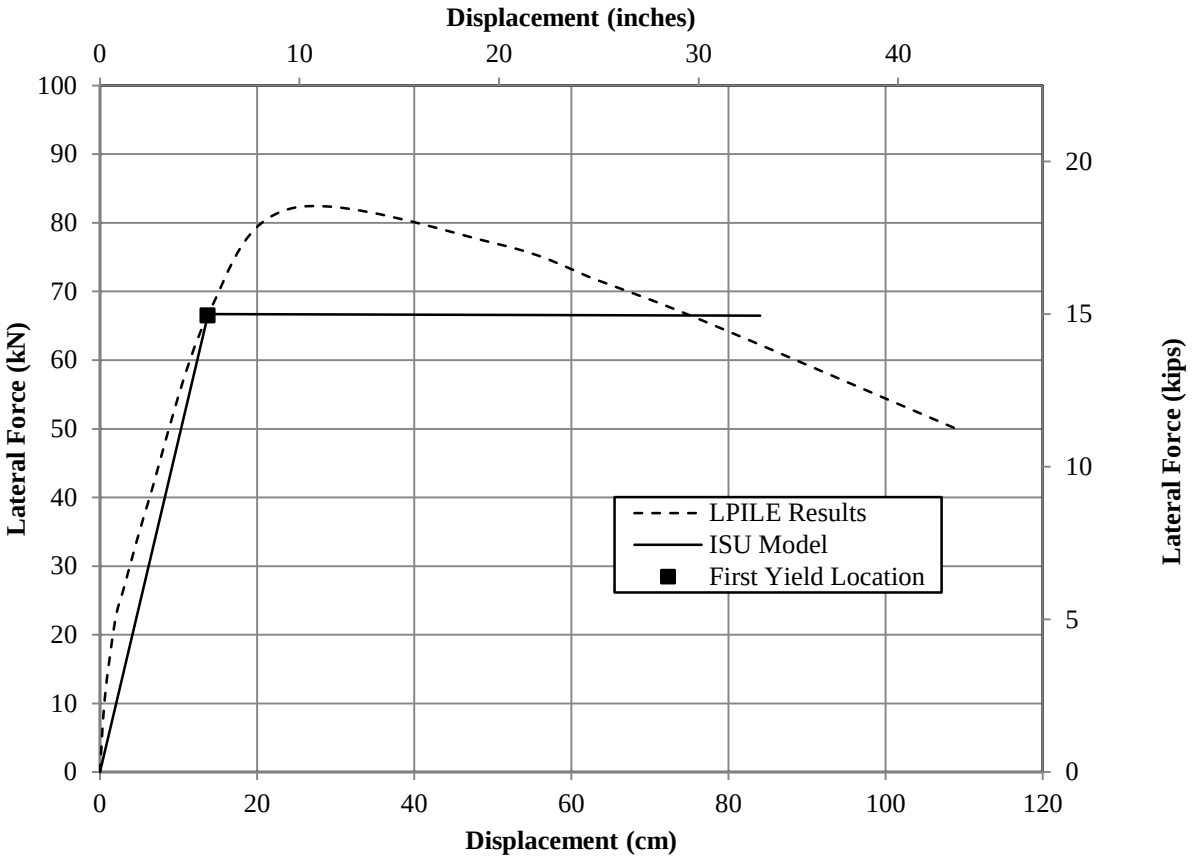

Figure A-8: Global response comparison of new methodology with additional analytical verification #8

APPENDIX B: ADDITIONAL CONCRETE TESTING INFORMATION

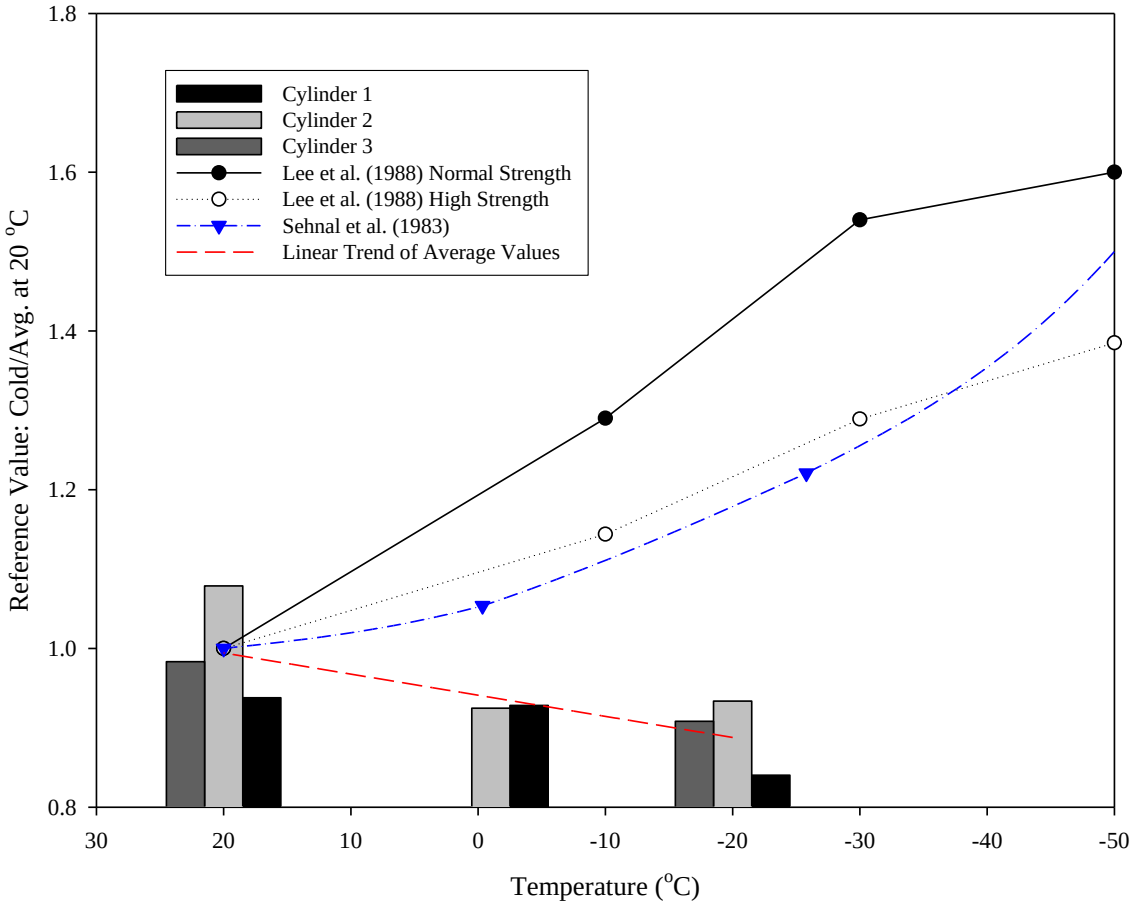

Figure B-1: Comparison of SGF obtained from experimental testing of Man C concrete mix and past studies

Notes:

1. Data is not indicative of strength increases associated with past studies and other data within this experiment. Therefore, the data will not be used in the establishment of trends.

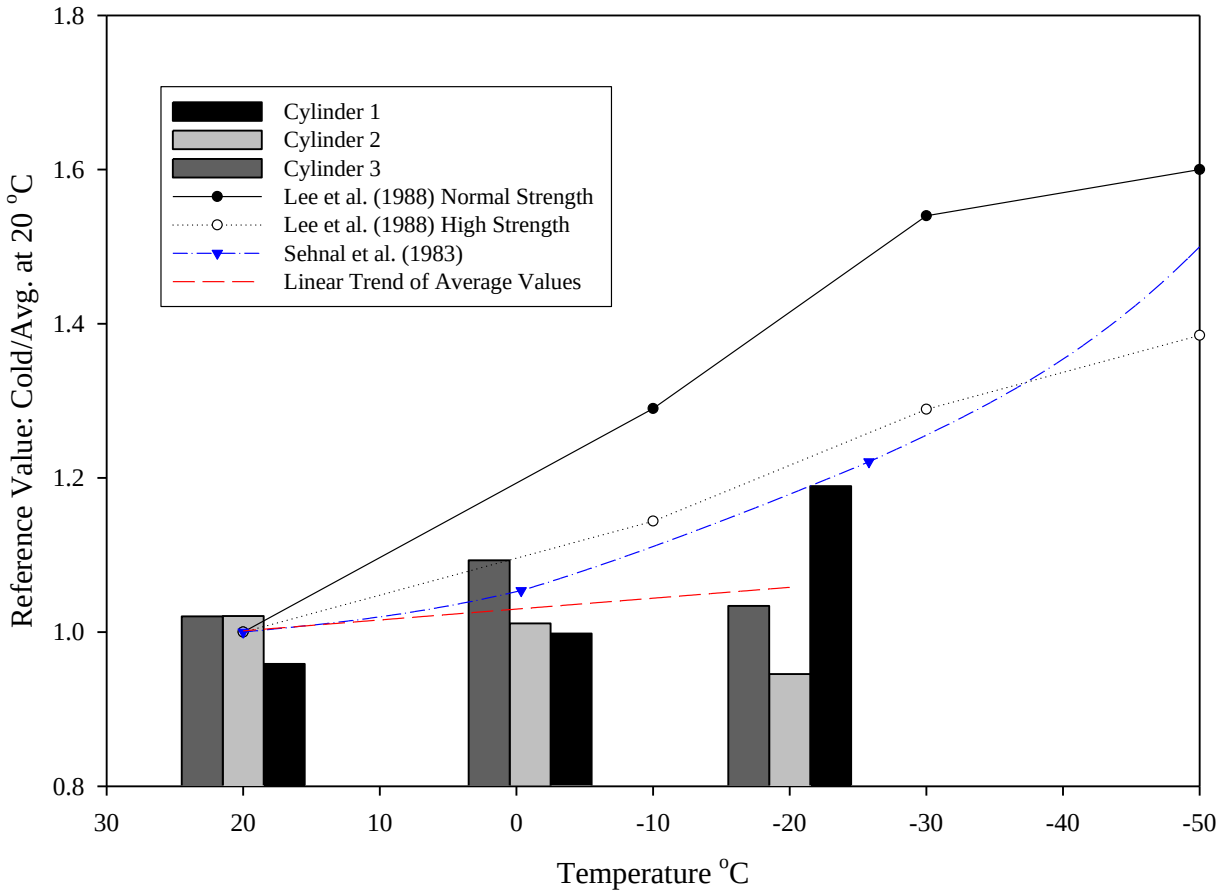

Figure B-2: Comparison of SGF obtained from experimental testing of IF concrete mix and past studies

Notes:

1. High strength data by Lee et al. (1988b) and data from Sehnal (1983) adequately capture the increase in strength found in the experimental testing at ISU as an upper bound.
2. The normal strength concrete data suggested by Lee et al. (1988a) does not sufficiently capture the behavior of the experimental data and will not be included in the average value charts.
3. The average values of the experimental data set follow a linear trend better than that of a curvilinear trend and will be used in determining a recommendation for strength increase.

APPENDIX C: ADDITIONAL A706 MILD STEEL REINFORCING BAR TEST DATA

The following section provides additional results from the testing of A706 mild steel reinforcement. The results depict the effects of temperature on the elastic modulus, yield plateau length, and ultimate strain, along with the effects of strain rate on the elastic modulus and ultimate strain. The last portion of this section provides a comparison between the recommended and recorded stress-strain curves to show how closely the Equations capture the measured response.

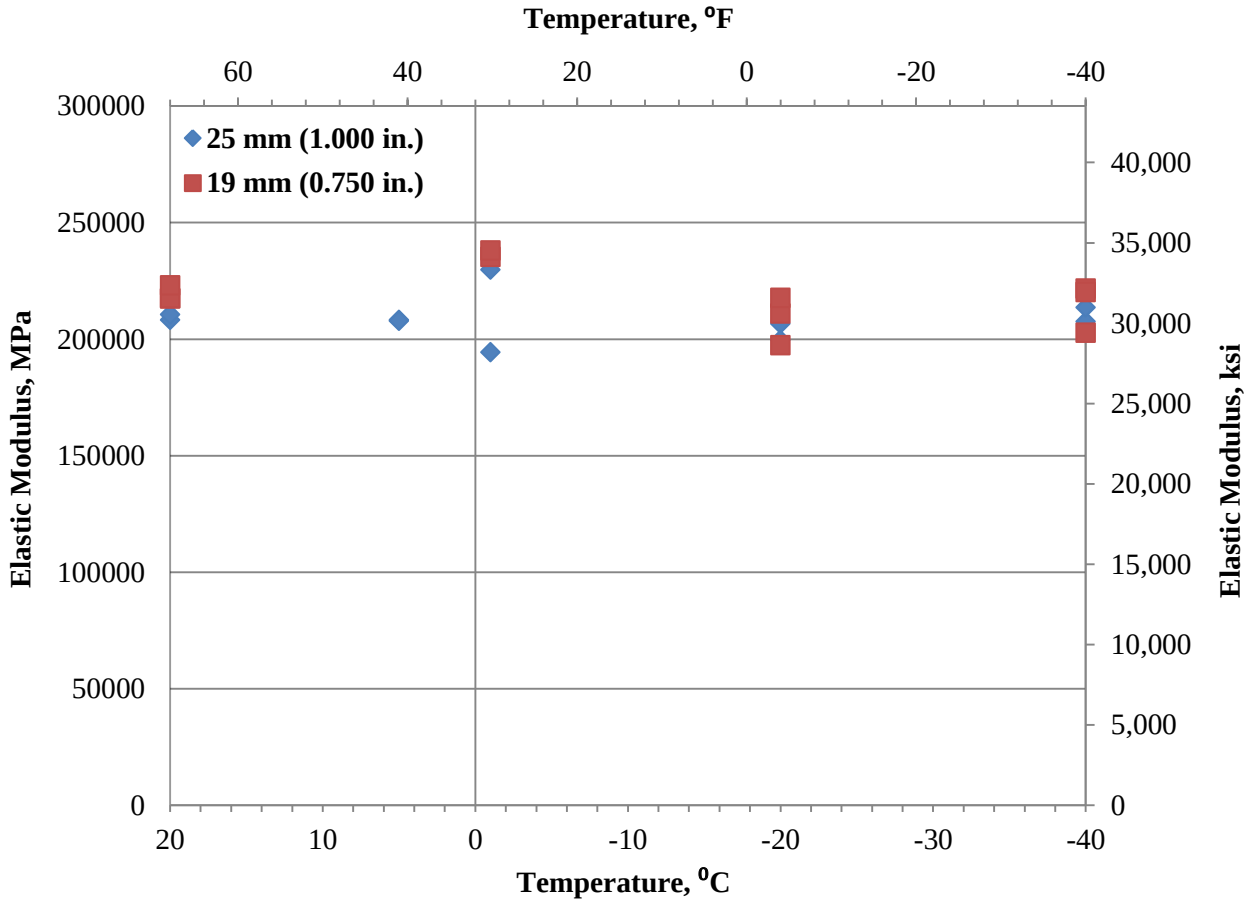

Figure C-1: Modulus of elasticity vs. temperature obtained at a strain rate of 0.001896 ε/min.

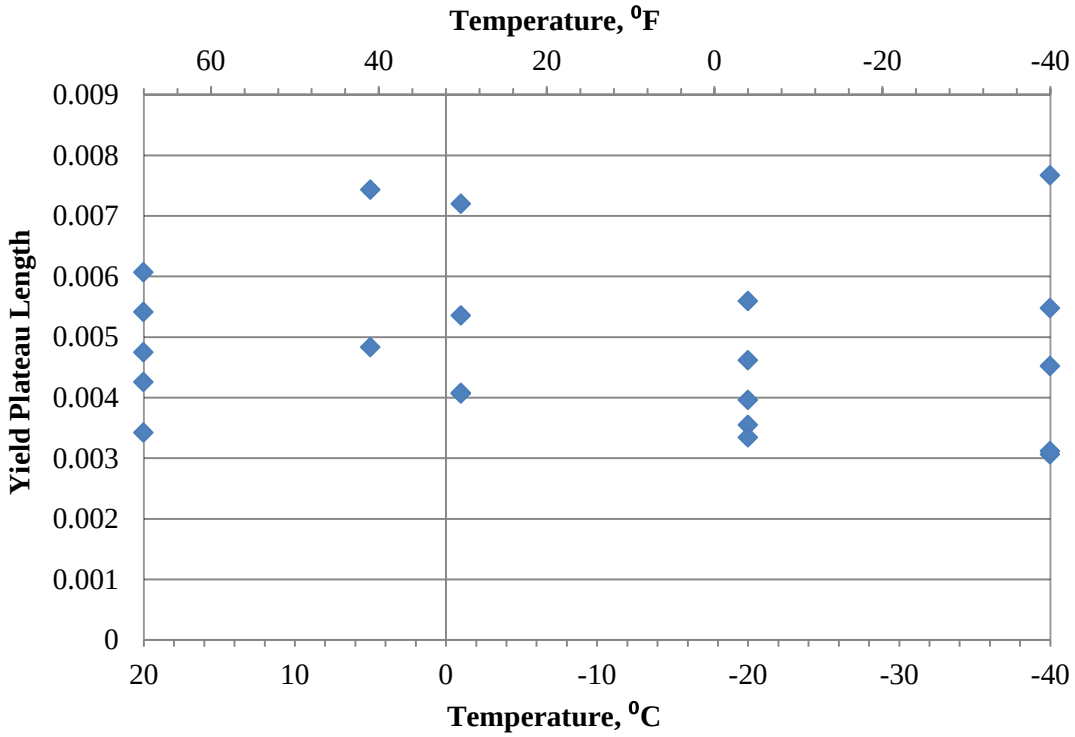

Figure C-2: Yield plateau length vs. temperature obtained at a strain rate of 0.001897 ε/min. for all tested bar sizes

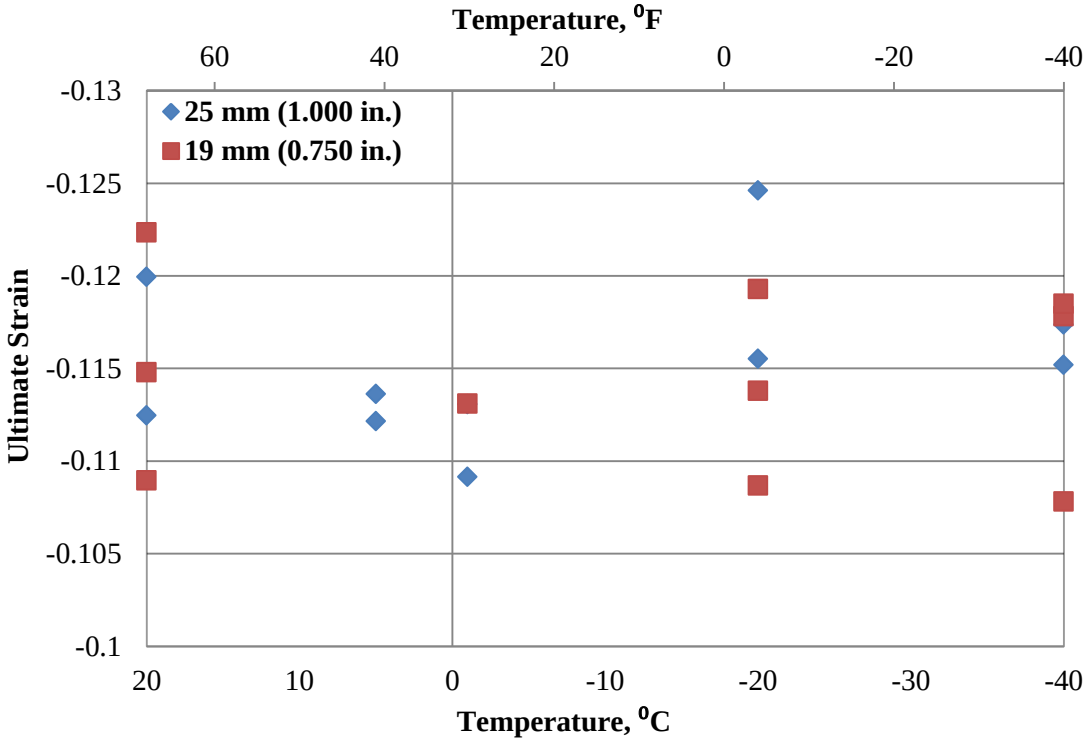

Figure C-3: Ultimate strain vs. temperature at a strain rate of 0.275 ε/min.

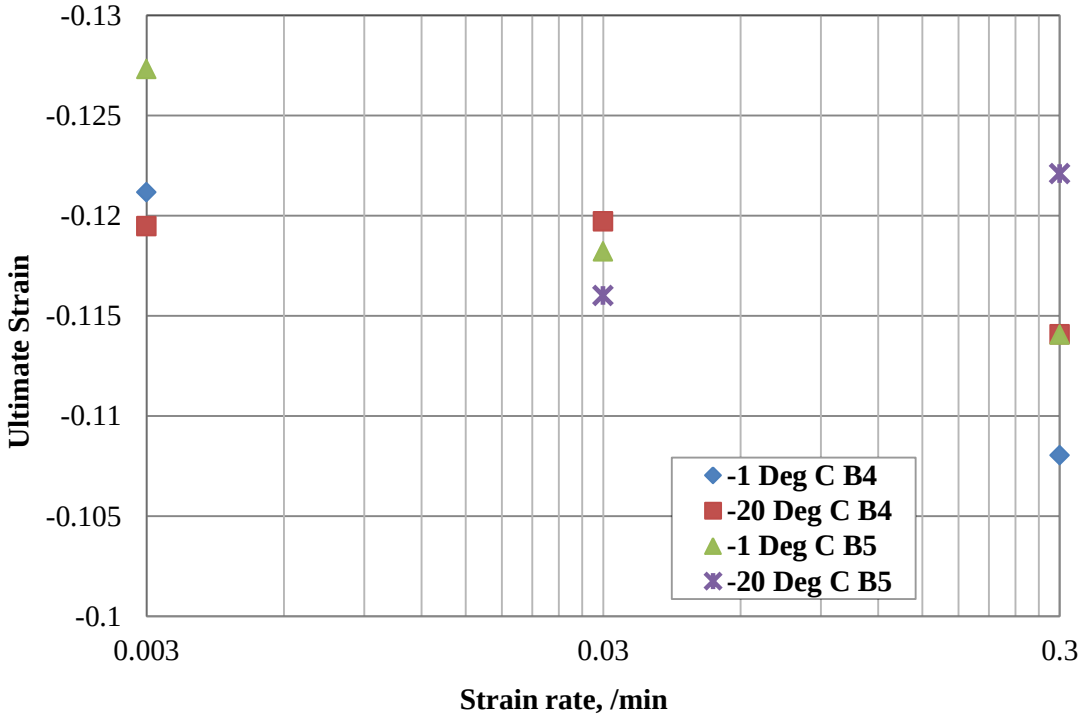

Figure C-4: Ultimate strain vs. strain rate at various temperatures

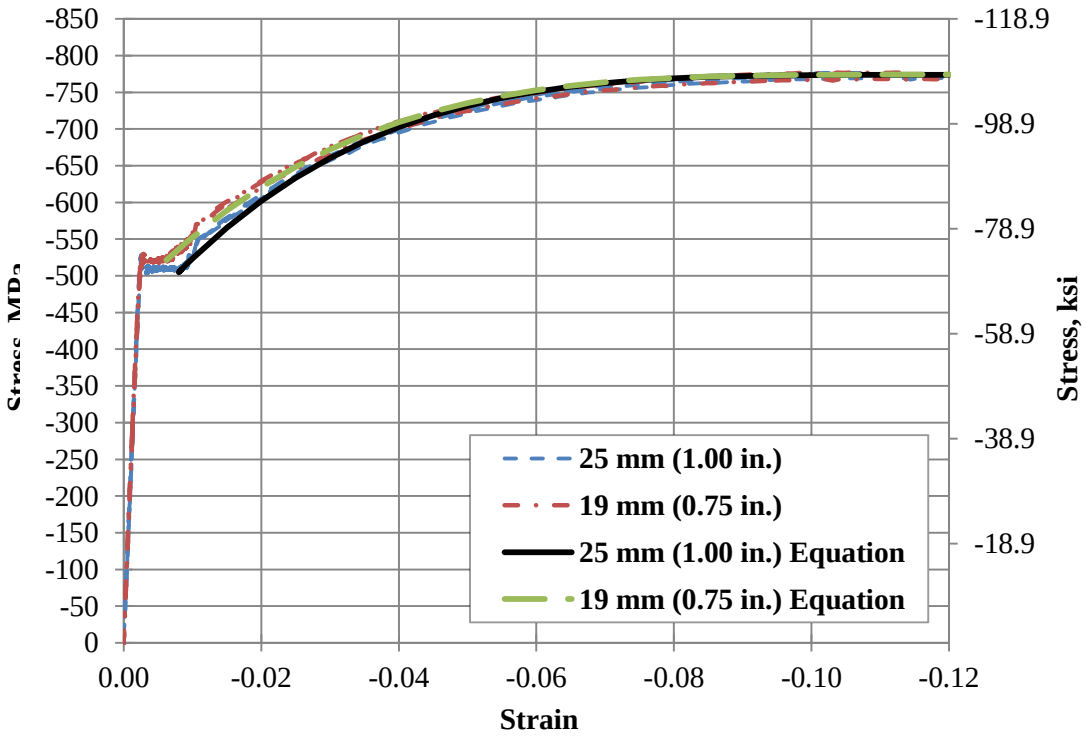

Figure C-5: Strain-hardening strength increase equation 6-5 validation at 20 °C (68 °F)

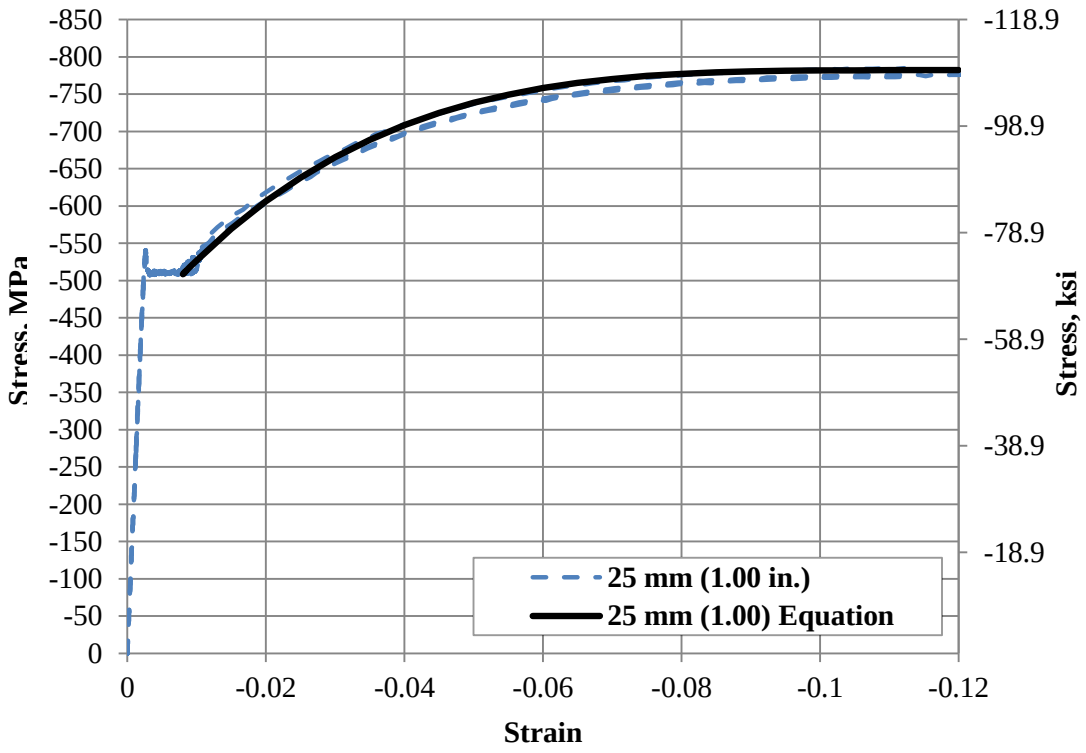

Figure C-6: Strain-hardening strength increase equation 6-5 validation at 5 °C (41 °F)

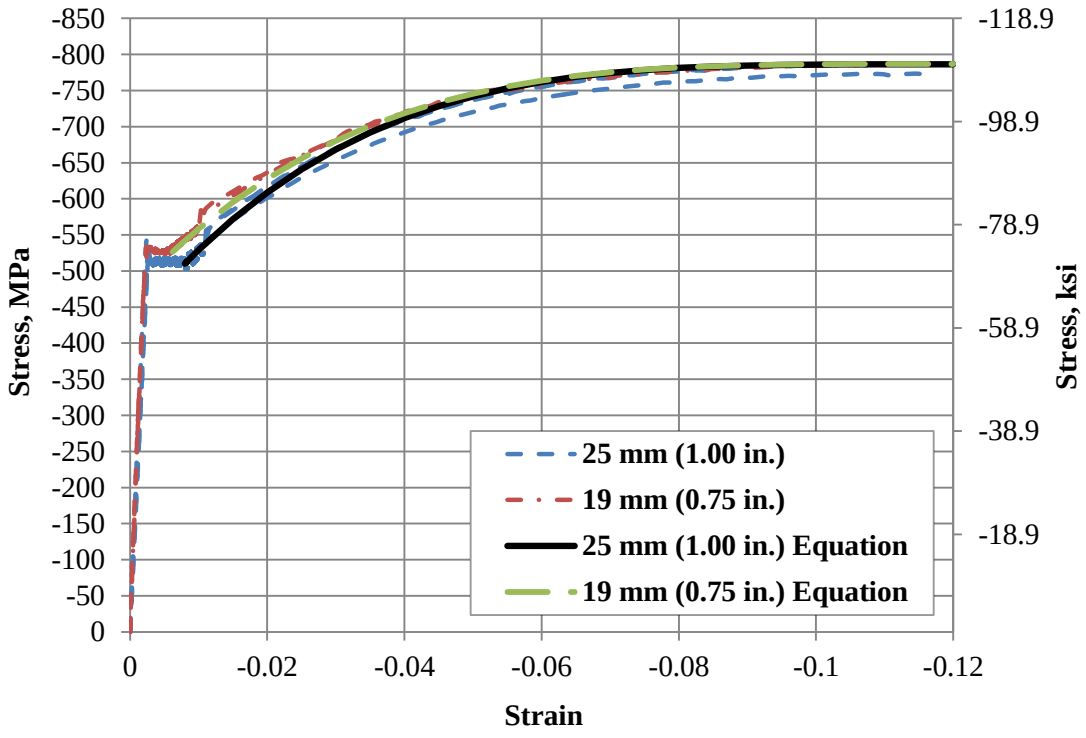

Figure C-7: Strain-hardening strength increase equation 6-5 validation at -1 °C (30.2 °F)

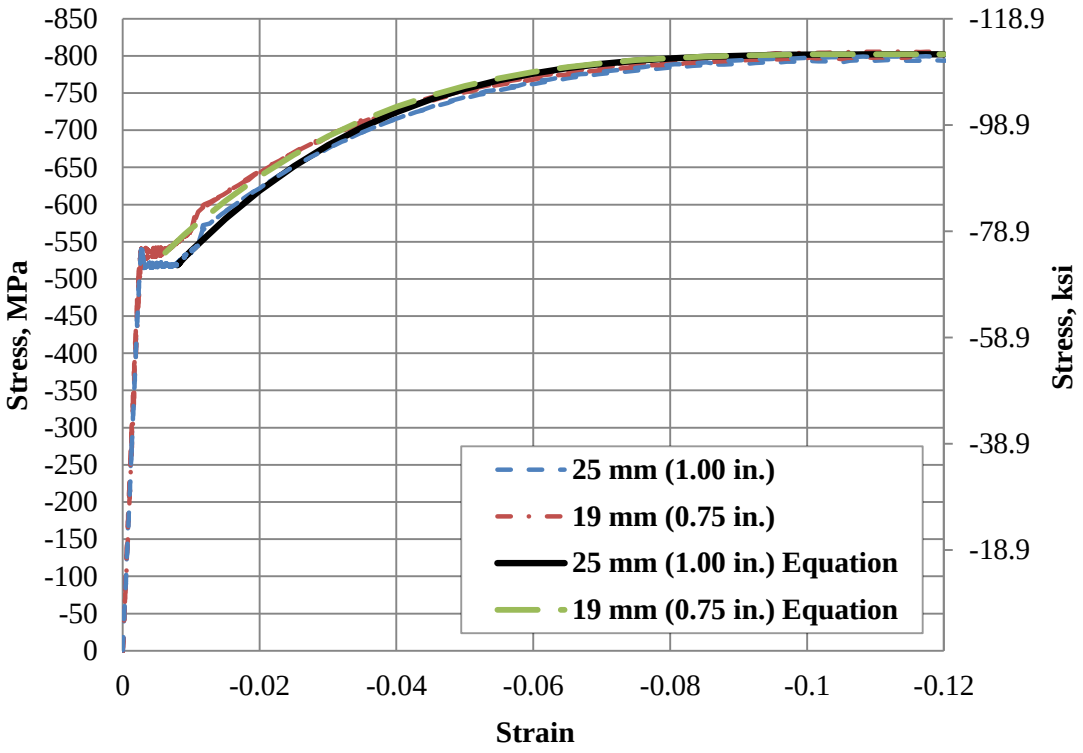

Figure C-8: Strain-hardening strength increase equation 6-5 validation at -20 °C (-4 °F)

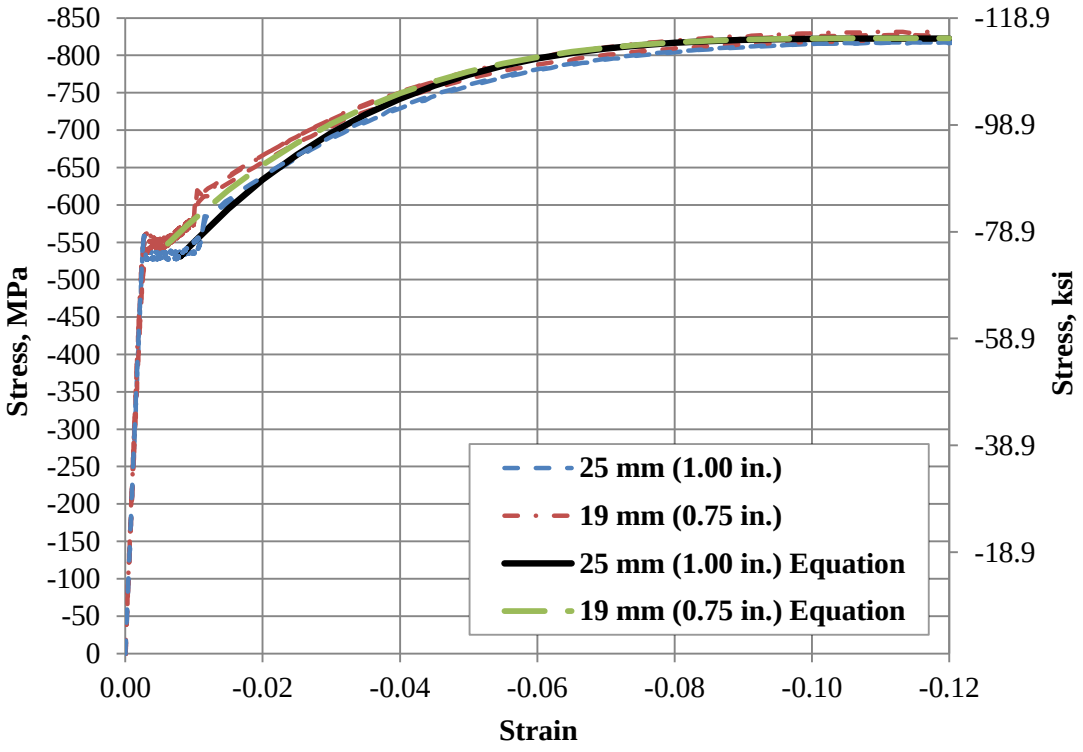

Figure C-9: Strain-hardening strength increase equation 6-5 validation at -40 °C (-40 °F)

APPENDIX D: ADDITIONAL FROZEN SOIL TESTING INFORMATION

The following section provides additional information from the frozen soil investigation. Included within this section are the individual figures constructed for the failure strength reference values as well as the individual failure strain comparisons.

- Additional Type II Soil Information

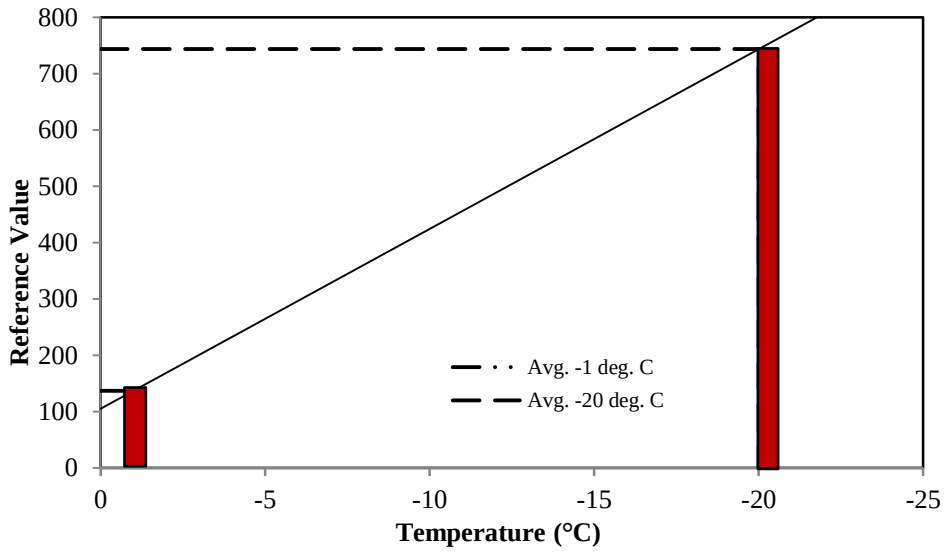

Figure D-1: Refernce value comparison for failure strength on a Type II soil

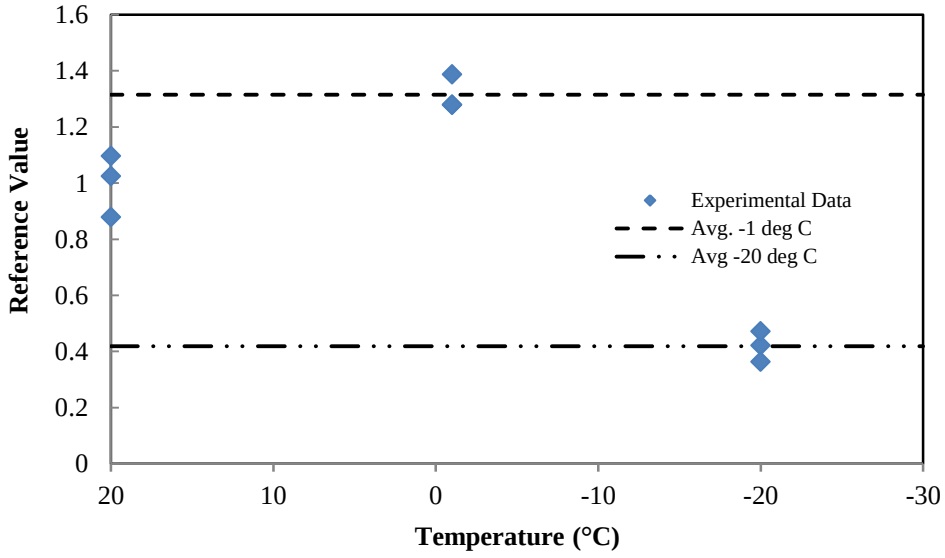

Figure D-2: Reference value comparison for failure strain on a Type II soil

- Additional Type III Soil Information

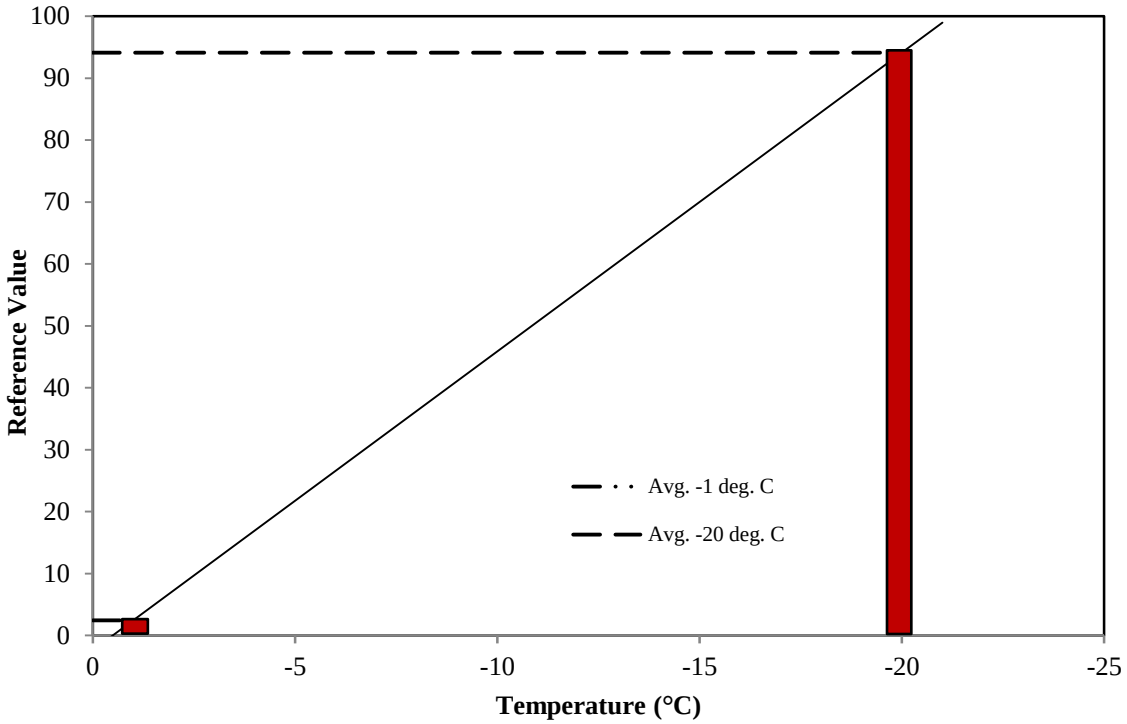

Figure D-3: Reference value comparison for failure strength on Type III soil

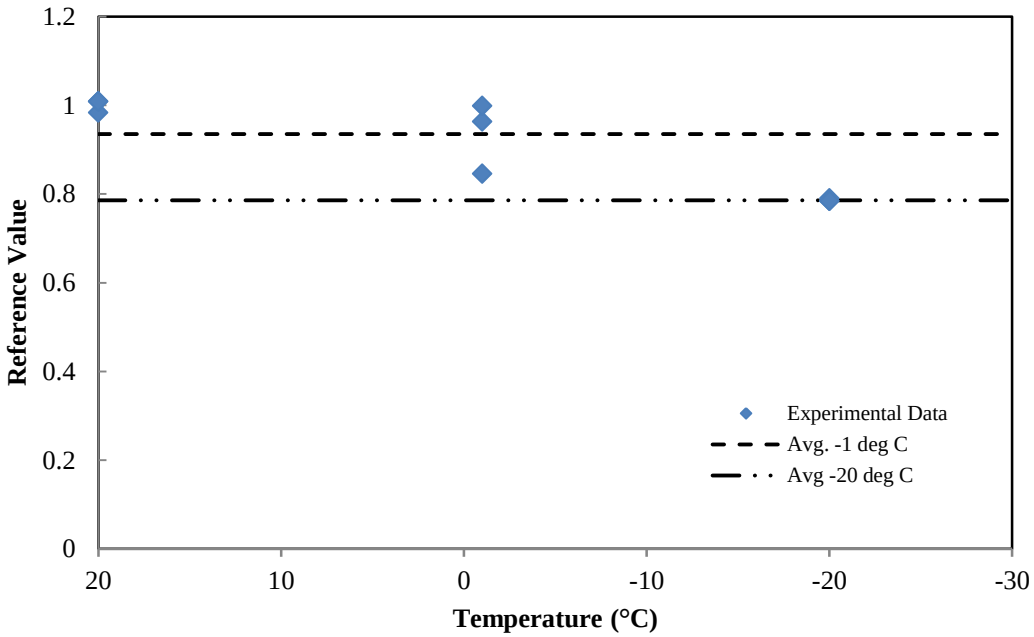

Figure D-4: Reference value comparison for failure strain on Type III Soil

- Additional Type IV Soil Information

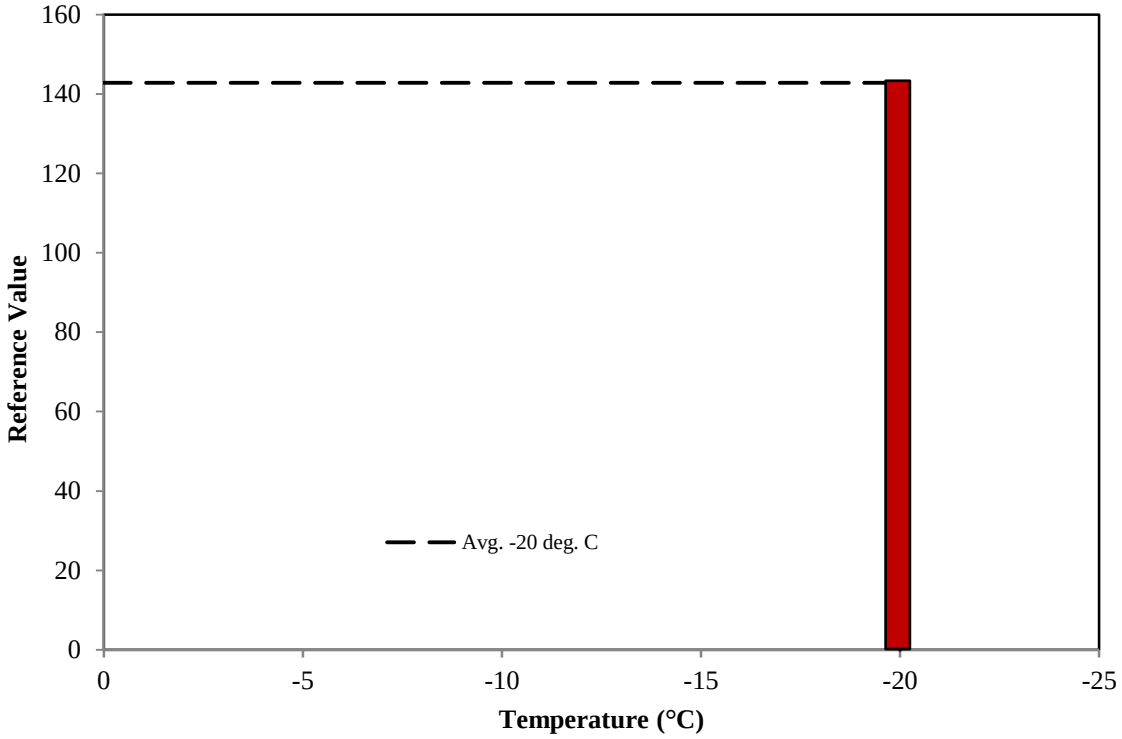

Figure D-5: Reference value comparison for failure strength on Type IV soil

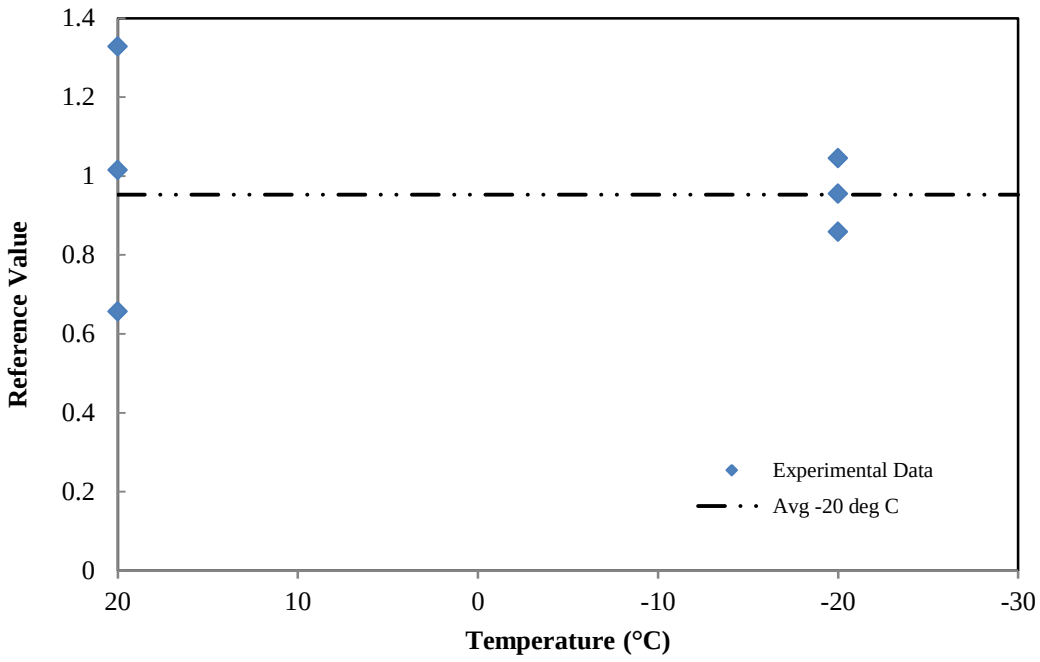

Figure D-6: Reference value comparison for failure strain on Type IV soil

- Additional Type V Soil Information

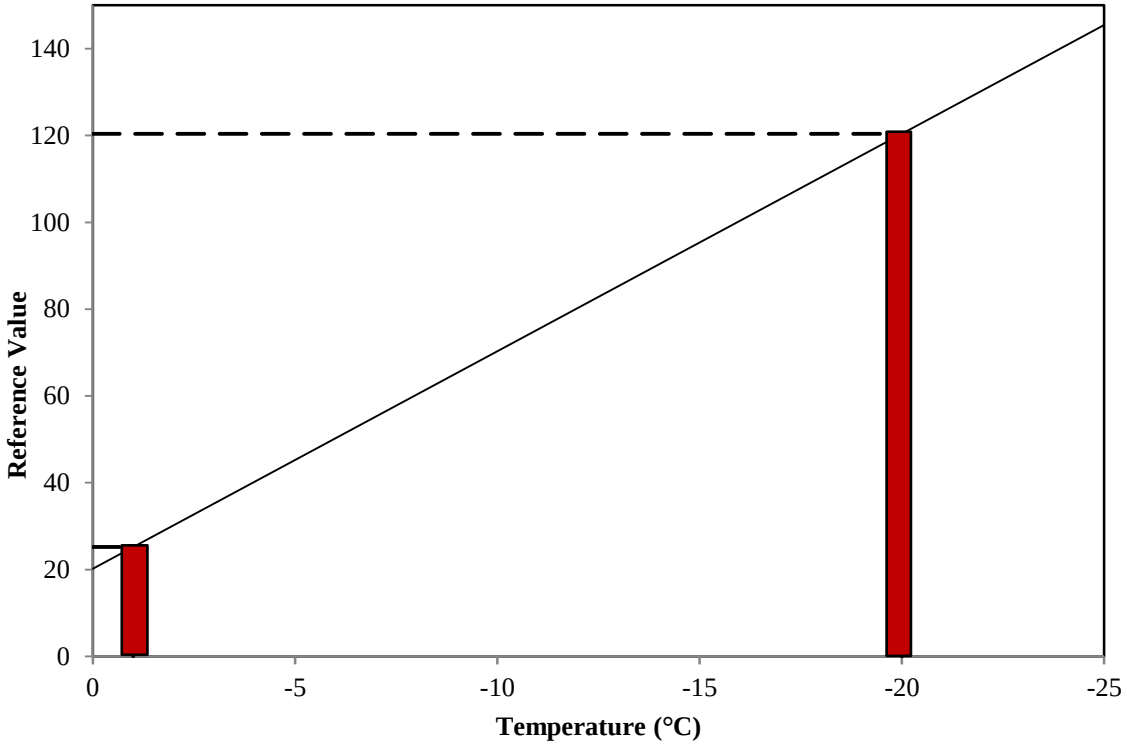

Figure D-7: Reference value comparison for failure strength on Type V soil

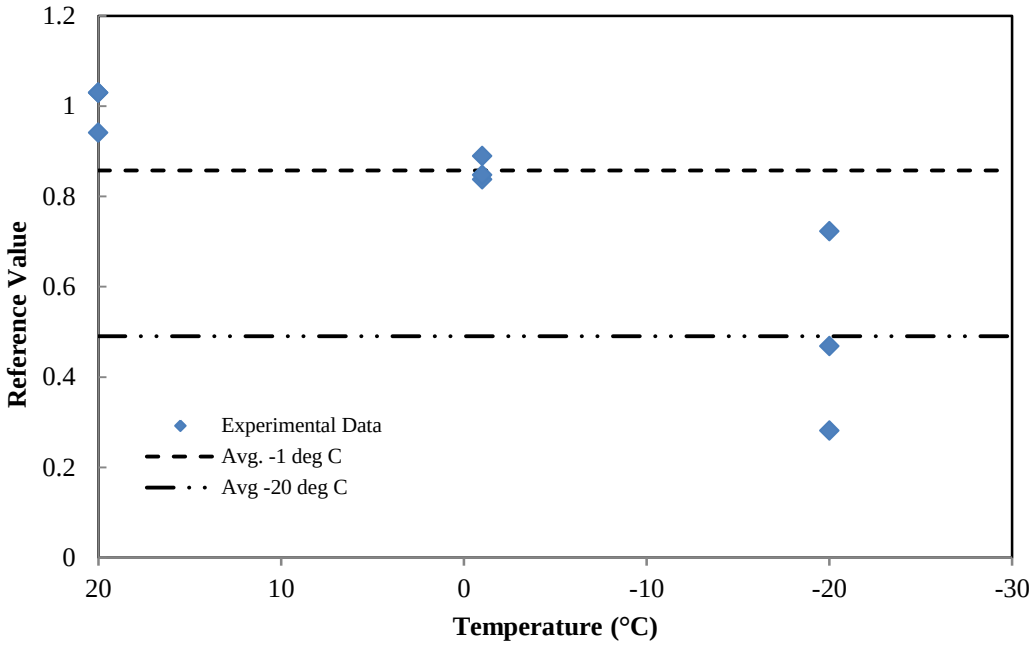

Figure D-8: Reference value comparison for failure strain on Type V soil